technische universität dortmund

MAX PLANCK INSTITUTE OF MOLECULAR PHYSIOLOGY

Structural Insights into Muscle Organisation by Electron Cryo-tomography

Dissertation

zur Erlangung des akademischen Grades eines Doktors
der Naturwissenschaften
der Fakultät für Chemie und Chemische Biologie
der Technischen Universität Dortmund

angefertigt am
Max-Planck-Institut für Molekulare Physiologie in Dortmund

vorgelegt von
Zhexin Wang

1st referee: **Prof. Dr. Stefan Raunser**
Department of Structural Biochemistry
Max-Planck Institute of Molecular Physiology

Faculty of Chemistry and Chemical Biology
Technical University Dortmund

2nd referee: **Prof. Dr. Roland Winter**
Department of Physical Chemistry I
Faculty of Chemistry and Chemical Biology
Technical University Dortmund

Date of submission: 20.09.2022

Formal declaration

The work described in this dissertation was carried out from December 2016 to September 2022 under the guidance of Prof. Dr. Stefan Raunser at the Max-Planck-Institute of Molecular Physiology, Dortmund.

I hereby declare that I carried out the work independently and did not use any aid, other than the ones mentioned.

Eidesstattliche Erklärung

Die vorliegende Arbeit wurde in der Zeit von Dezember 2016 bis September 2022 am Max-Planck-Institut für Molekulare Physiologie in Dortmund unter der Anleitung von Prof. Dr. Stefan Raunser durchgeführt.

Hiermit erkläre ich, dass ich die vorliegende Arbeit selbstständig und nur mit den angegebenen Hilfsmitteln angefertigt habe.

Table of Contents

List of Figures

List of Tables

List of Abbreviations

2D	2-dimensional
3D	3-dimensional
A-band	anisotropic band
ABD	actin-binding domain
ADP	adenosine diphosphate
Arp2/3	actin related protein 2/3
ATP	adenosine triphosphate
B-state	blocked state
BSE	backscattered electrons
C-state	closed state
CEMOVIS	cryo-EM of vitreous sections
cryo-EM	electron cryo-microscopy
cryo-ET	electron cryo-tomography
cryo-FIB	cryo-focused ion beam milling
CTF	contrast transfer function
D-loop	DNase-I-binding loop
DTT	dithiothreitol
EGTA	ethylene glycol tetraacetic acid
ELC	essential light chain
EM	electron microscopy/microscope
EMDB	electron microscopy data bank
ET	electron tomography
F-actin	filamentous actin
FEG	field-emission gun
Fn	fibronectin-like
FSC	Fourier shell correlation
G-actin	globular actin
GIS	gas-injection system
HC	heavy chain
HEPES	4-(2-hydroxyethyl)-1-piperazineethanesulfonic acid
HMM	heavy meromyosin

HPF	high-pressure freezing
I-band	isotropic band
Ig	immunoglobin-like
IHM	interacting-head motif
L50	lower 50 kDa
LMM	light meromyosin
M-band	*mittel* band
M-state	myosin state
Mito	mitochondria
MyBP-C	myosin-binding protein C
PDB	protein data bank
PFIB	plasma focused ion beam
P_i	phosphate group
PPS	pre-power stroke
RLC	regulatory light chain
SART	simultaneous algebraic reconstruction technique
SD	sub-domain
SE	secondary electrons
SEM	scanning electron microscopy/microscope
SH3	Src homology-3
SIRT	simultaneous iterative reconstruction technique
SPA	single-particle analysis
SR	spectrin-like repeat/sarcoplasmic reticulum
TEM	transmission electron microscopy/microscope
TnC	troponin C
TnI	troponin I
TnT	troponin T
U50	upper 50 kDa
Z-disc	*zwischen* band

CHAPTER 1 ABSTRACT AND ZUSAMMENFASSUNG

1.1 Abstract

Movement is the essence of life in the animal realm. Skeletal muscle is an essential tissue specialised for movement. Muscle cells are multi-nucleated cells containing bundles of myofibrils, which are segmented into the smallest contractile units, named sarcomeres. While sarcomeres are known to contain thin (actin) and thick (myosin) filaments, the detailed architecture, especially the high-resolution and 3-dimensional (3D) information, remains obscure. In addition to actin and myosin, other structural proteins such as nebulin are also essential for contraction and their mutations are related to debilitating or even life-threatening diseases. However, how these proteins function and interplay with actin and myosin remains elusive due to a lack of structures.

In this thesis, I obtained the first high-resolution 3D pictures of the sarcomere using cryo-focused ion beam milling (cryo-FIB-milling) and electron cryo-tomography (cryo-ET). Furthermore, from these native 3D images, I determined the first structures of the ruler protein, nebulin, to a resolution of 4.5 Å and the myosin in an active double-head state using sub-tomogram averaging.

The 3D molecular picture of the sarcomere unexpectedly reveals a pseudo-regular actin-myosin interaction pattern in the A-band, an irregular rearrangement of the thin filaments in the I-band, and a heterogeneous mesh-like network formed by actin and α-actinin in the Z-disc. The sarcomere organisation highlights a molecular plasticity which ensures efficient muscle contraction in different environments.

The *in situ* structure of nebulin not only reveals its organisation in a sarcomere, but also establishes the molecular basis for its functions in thin filament stabilisation, length control and myosin-binding regulation. This structure explains the pathogenicity of nebulin mutations in a common skeletal muscle disease, nemaline myopathy. The structure of double-head myosin demonstrates how the two heads cooperate inside a sarcomere and function simultaneously, and reveals inherent variability that increases myosin's capability to bind to the thin filaments.

Collectively, my thesis research provides unique insights into muscle structures that allow improved dynamic modelling of muscle contraction and muscle diseases. This research also establishes a new cryo-FIB-ET approach for structurally characterising muscle components in different types of muscles and diseased states.

1.2 Zusammenfassung

Bewegung ist die Essenz des Lebens im Tierreich. Die Skelettmuskulatur ist ein wesentliches Gewebe, das auf Bewegung spezialisiert ist. Muskelzellen sind mehrkernige Zellen, die Bündel von Myofibrillen enthalten, die in kleinste kontraktile Einheiten, die Sarkomere, unterteilt sind. Obwohl bekannt ist, dass Sarkomere dünne (Aktin) und dicke (Myosin) Filamente enthalten, ist die detaillierte Architektur, insbesondere die hochauflösende und dreidimensionale (3D) Information, nach wie vor unklar. Neben Aktin und Myosin sind auch andere Strukturproteine wie Nebulin für die Kontraktion wichtig, deren Mutationen in Zusammenhang mit teils lebensbedrohlichen Muskelschwäche-Erkrankungen stehen. Allerdings ist aufgrund fehlender Strukturen immer noch unklar, wie diese Proteine funktionieren und mit Aktin und Myosin zusammenwirken.

In dieser Arbeit habe ich die ersten hochauflösenden 3D-Bilder des Sarkomers mit Hilfe von Kryofokussiertem Ionenstrahl-Ätzen (Kryo-FIB) und Elektronen-Kryotomographie (Kryo-ET) erstellt. Außerdem habe ich mit Hilfe von Subtomogramm-Mittelung aus diesen nativen 3D-Bildern die ersten Strukturen von Nebulin, das die Länge des Sarkomers festlegt, mit einer Auflösung von 4,5 Å und des Myosins im aktiven Doppelkopfzustand bestimmt.

Das molekulare 3D-Bild des Sarkomers zeigt unerwartet ein pseudoreguläres Aktin-Myosin-Interaktionsmuster im A-Band, eine unregelmäßige Umordnung der dünnen Filamente im I-Band und ein heterogenes, maschenartiges Netzwerk aus Aktin und α-Aktinin in der Z-Scheibe. Die Organisation der Sarkomere weist auf eine molekulare Plastizität hin, die eine effiziente Muskelkontraktion in unterschiedlichen Umgebungen gewährleistet.

Die In-situ-Struktur von Nebulin offenbart nicht nur seine Organisation in einem Sarkomer, sondern schafft auch die molekulare Grundlage für seine Funktionen bei der Stabilisierung der dünnen Filamente, der Längenkontrolle und der Regulierung der Myosinbindung. Diese Struktur erklärt die Pathogenität von Nebulin-Mutationen bei einer häufigen Skelettmuskelerkrankung, der nemalinen Myopathie. Die Struktur des Doppelkopf-Myosins zeigt, wie die beiden Köpfe innerhalb eines Sarkomers zusammenarbeiten und gleichzeitig funktionieren, und deckt eine inhärente Variabilität auf, welche die Fähigkeit des Myosins zur Bindung an die dünnen Filamente erhöht.

Insgesamt bietet meine Dissertation einzigartige Einblicke in Muskelstrukturen, die eine verbesserte dynamische Modellierung von Muskelkontraktion und Muskelkrankheiten ermöglichen. Mit dieser Forschung wird außerdem ein neuer Kryo-FIB-ET-Ansatz zur strukturellen Charakterisierung von Muskelkomponenten in verschiedenen Muskeltypen und Krankheitszuständen etabliert.

CHAPTER 2 INTRODUCTION

This thesis investigated and revealed the structure of the skeletal muscle sarcomere and sarcomeric proteins using electron cryo-tomography (cryo-ET). This chapter first introduces the organisation of a muscle sarcomere and its protein components (section 2.1). Then, it summarises previous structural studies in the muscle field and demonstrates the limitation of currently available structural methods (section 2.2). Next, the technique of electron microscopy and cryo-ET is introduced (section 2.3). In the end, the aims of this thesis are established with the undetermined questions in the muscle field when this thesis research started (section 2.4).

2.1 Sarcomere and sarcomeric proteins

Muscle is a sophisticated tissue that converts chemical energy into mechanical energy to produce forces. In humans, there are three types of muscles: skeletal muscle (responsible for movement), cardiac muscle (responsible for pumping blood through the body), and smooth muscle (comprising the walls of internal organs and blood vessels). Among the three kinds of muscle, skeletal muscle is the most abundant type, constituting around 40% of the total body mass in humans (Mukund and Subramaniam, 2020). Muscle tissues are made of muscle fibres, which are specialised multi-nucleated cells that contain bundles of contractile myofibrils (Fig. 2.1A). Surrounding the myofibrils, other organelles such as sarcoplasmic reticulum and mitochondria are responsible for the calcium-dependent regulation and energy production. Both skeletal and cardiac muscles are known as striated muscles. In these muscles, individual myofibrils, with diameters of 1-2 μm and lengths of up to several centimetres, are axially segmented into sarcomeres – the smallest force-generating and load-bearing units (Fig. 2.1B).

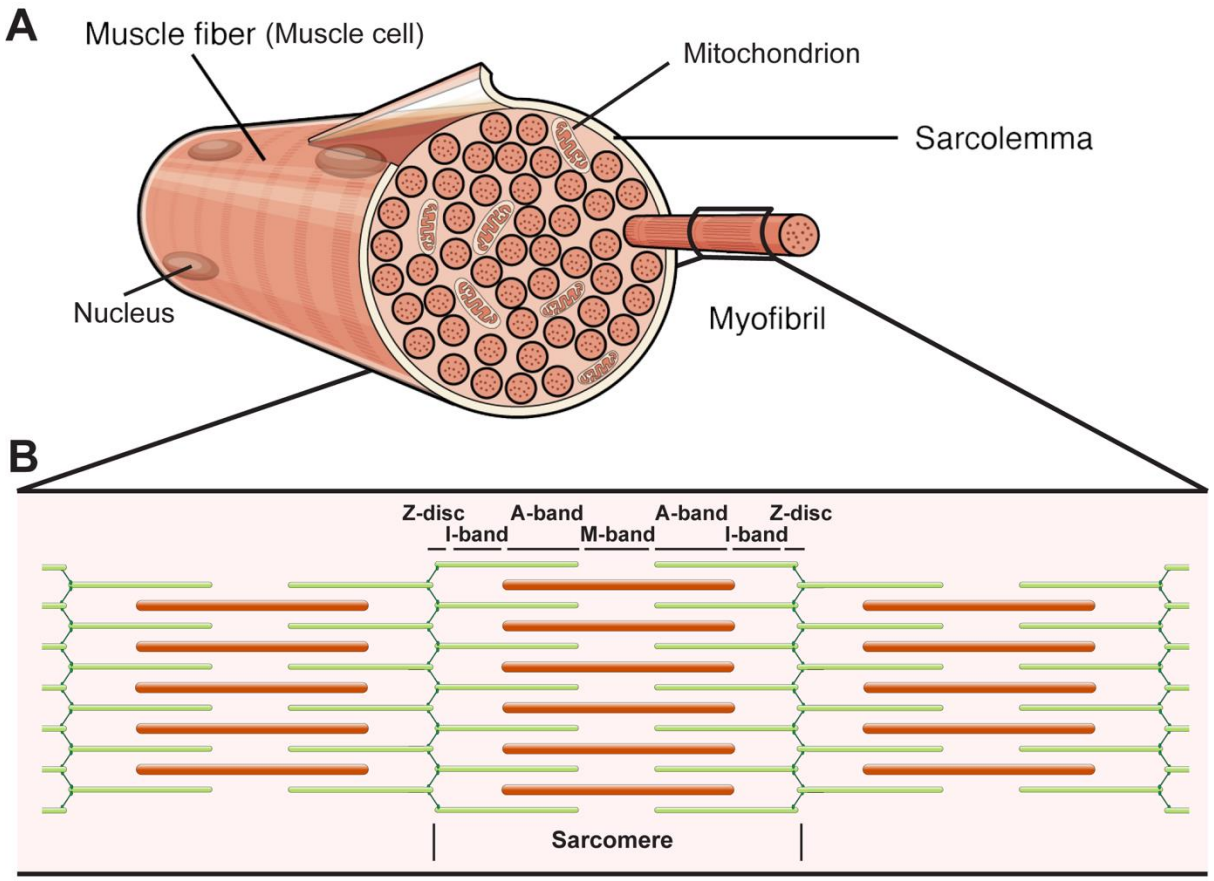

Fig. 2.1 The hierarchical organisation of a muscle cell

*(**A**) Schematic drawing of a muscle cell composed of bundles of myofibrils. (**B**) Schematic drawing of a myofibril segmented into consecutive sarcomeres. The thin and thick filaments are represented in green and dark red, respectively. Panel (A) adapted from* (Betts et al., 2013) *under license CC BY 4.0.*

A sarcomere is composed of two main types of filaments: the actin-containing thin filaments and the myosin-containing thick filaments. The organisation of the two types of filaments lead to morphologically different zones along the long axis of a sarcomere (Fig. 2.1). The A (anisotropic)-band consists of overlapping thin and thick filaments, between which myosin forms cross-bridges. The I (isotropic)-band contains only the thin filaments. The Z ("zwischen", *between* in German)-disc forms the border of a sarcomere and anchors the ends of thin filaments from adjacent sarcomeres. The M ("mittel", *middle* in German)-band marks the centre of a sarcomere where only the thick filaments are present and cross-linked (Fig. 2.1).

Muscle contraction is the result of the shortening of sarcomeres. In 1954, two breakthrough studies using interference microscopy (Huxley and Niedergerke, 1954) and phase contrast microscopy together with electron microscopy (Huxley and Hanson, 1954) revealed that the length of the dark region (corresponding to the A-band and the M-band) remained the same during contraction, while the light region (corresponding to the I-band) became shorter. It has been established since then that the basis for muscle contraction is the relative movement between the thin and the thick filaments within a sarcomere. This is the so-called sliding filament theory (Huxley and Hanson, 1954; Huxley and Niedergerke, 1954) (Fig. 2.2). This sliding movement, as later discovered, results from the binding of myosin cross-bridges to the actin filaments and a subsequent "swinging" conformational change (Huxley, 1969; Spudich, 2001).

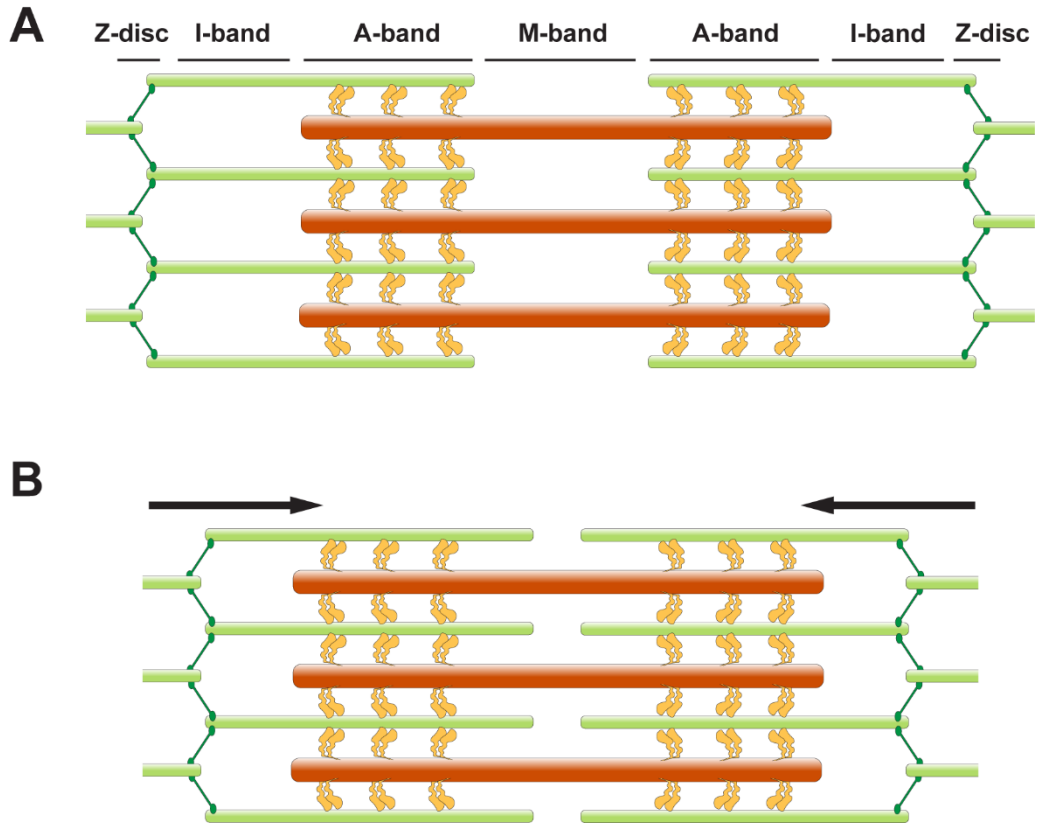

Fig. 2.2 The sliding filament theory

*Schematic representation of the stretched (**A**) and contracted (**B**) state of a sarcomere. The thin and thick filaments are depicted in green and dark red, respectively. Myosin cross-bridges are depicted in orange. Arrows indicate the direction of the sliding of the thin filaments during contraction.*

In addition to actin and myosin, a number of other proteins play regulatory or structural roles in muscle contraction (Fig. 2.3). The thin filament includes actin (section 2.1.1.1), tropomyosin, and troponin (section 2.1.1.2). Furthermore, nebulin (section 2.1.1.3) is present on the entire length of the thin filament in skeletal muscle while nebulette, a short homolog of nebulin, binds to the region of the thin filament close to the Z-disc in cardiac muscle (Moncman and Wang, 1995). The thick filament includes myosin (section 2.1.2.1), titin (section 2.1.2.2), and myosin-binding protein C (MyBP-C) (section 2.1.2.3). In the A-band, the thin filaments and the thick filaments interlace with each other, forming hexagonal patterns in cross-section views (Huxley, 1957). In the M-band (section 2.1.3) and Z-disc (section 2.1.2), myomesin and α-actinin cross-link the thick and the thin filaments, respectively (Gautel and Djinović-Carugo, 2016). Altogether, these sarcomeric proteins constitute an intricate network that requires their concerted functions for efficient muscle contraction (Fig. 2.3). The following sections introduce the main sarcomeric proteins in different regions and their coordination to maintain a proper muscle contraction.

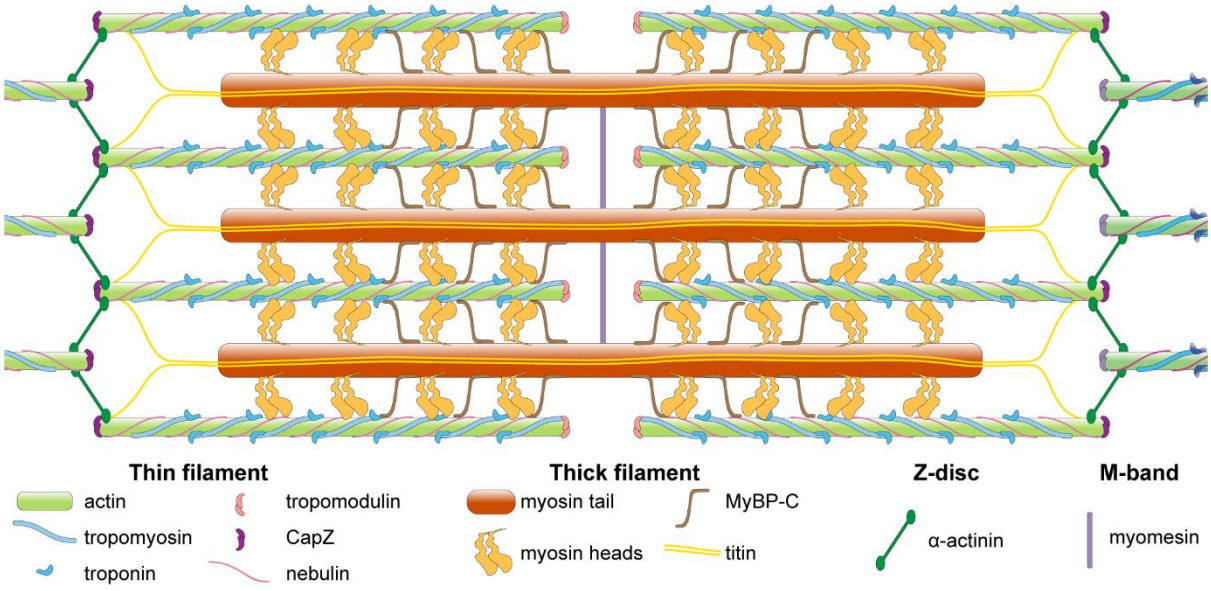

Fig. 2.3 Schematic representation of a sarcomere and major sarcomeric components

2.1.1 Thin filament

2.1.1.1 Actin

Actin is the core and the backbone of the thin filament. Although actin was initially discovered in muscle (Straub, 1942), it is abundant in all cell types and crucial to a variety of cellular events such as organelle transport, cell division, and motility (reviewed in (Pollard and Cooper, 2009)). Actin can exist in a monomeric form (G(globular)-actin) (Fig. 2.4) or a filamentous form (F(filamentous)-actin) (Fig. 2.5). In vertebrates, six different isoforms of actin are expressed: three α-actin isoforms in skeletal, cardiac, and smooth muscles, β-actin in non-muscle cells and two γ-actin isoforms in non-muscle cells and smooth muscles (reviewed in (Perrin and Ervasti, 2010)). Different actin isoforms, although sharing more than 90% sequence identity, have different spatial and temporal expression patterns and functions with some overlaps (Perrin and Ervasti, 2010). $\alpha_{skeletal}$-actin is the major component in the thin filament from skeletal muscle in a healthy state. However, $\alpha_{cardiac}$-actin can also replace $\alpha_{skeletal}$-actin when $\alpha_{skeletal}$-actin is knocked-out in postnatal skeletal muscle (Nowak et al., 2009).

The polymerisation of G-actin into F-actin is reversible and remains dynamic in cells. Actin polymerises into filaments when its concentration is higher than a critical concentration (Blanchoin et al., 2014). The critical concentration can be largely reduced to facilitate polymerisation by high ionic strength (Pollard, 1986) or other regulatory proteins such as formin and the actin related protein 2/3 (Arp2/3) complex (Chesarone and Goode, 2009). F-actin is a polar filament with one end termed the barbed end, or the "+" end, and the other end termed the pointed end, or the "-" end (Blanchoin et al., 2014) (Fig. 2.5A). In the cytoplasm, F-actin has a higher association rate on the barbed end and a higher dissociation rate on the pointed end (Pollard, 1986). This leads to a net growth on the barbed end and a shrinkage from the pointed end, resulting in a "treadmilling" process (Wegner, 1976). Inside a muscle sarcomere, on the contrary, F-actin remains static with the barbed end and pointed end located in the Z-disc and M-band, respectively. The dynamic polymerisation/depolymerisation of F-actin is prevented by proteins capping the two ends of the thin filament: tropomodulin on the pointed end and CapZ on the barbed end (Casella et al., 1987; Weber et al., 1994), which both function by sterically blocking the exposed surface of the end actin protomers (Funk et al., 2021; Rao et al., 2014).

G-actin has a molecular weight of 42 kDa and contains four sub-domains, SD1-4. SD2 contains a DNase-I-binding loop (D-loop) that is flexible in G-actin (Kudryashov and Reisler, 2013) and can adopt different discrete conformations in F-actin (Merino et al., 2018). The four domains form a "U" shape that harbours a nucleotide-binding cleft in the centre which contains adenosine triphosphate (ATP), adenosine diphosphate (ADP), or ADP + phosphate group (P_i) (Fig. 2.4A). Upon polymerisation, SD1 and SD2 rotate relative to SD3 and SD4, leading to a flattening of the molecule (von der Ecken et al., 2015; Oda et al., 2009) (Fig. 2.4B). This conformational change brings the catalytic residues closer to the ATP γ phosphate (Chou and Pollard, 2019; von der Ecken et al., 2015; Merino et al., 2018; Oosterheert et al., 2022), thus drastically increasing the ATPase activity of F-actin (Blanchoin and Pollard, 2002).

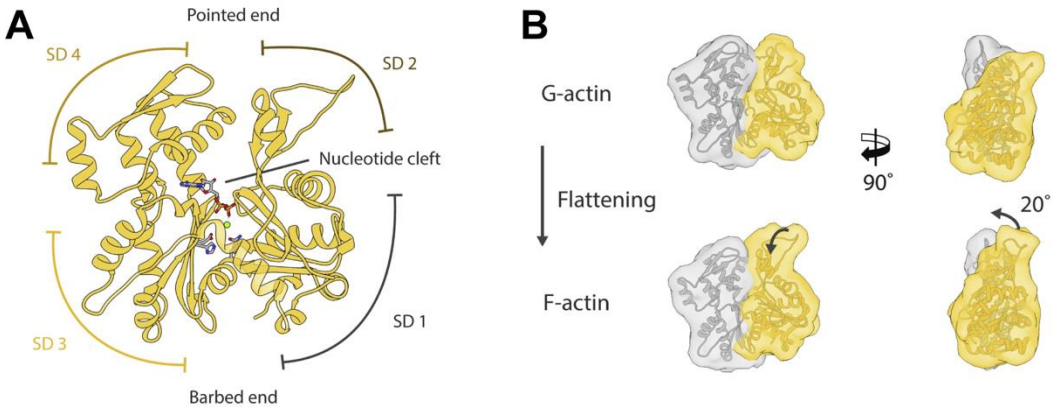

Fig. 2.4 Actin structure and conformational change upon polymerisation

*(**A**) Actin domain organisation depicting four subdomains and the central nucleotide cleft. (**B**) Structural change of an actin subunit from the globular form to the filamentous form. Figure adapted from* (Merino et al., 2020) *under license CC BY NC ND.*

F-actin can be considered as a double-stranded right-handed helix or a single-stranded left-handed helix with a helical twist of -166.7° and helical rise of 27.5 Å (Fig. 2.5). Between axially adjacent actin subunits on the same strand, tight interactions are formed between SD3 and SD2/4. On the contrary, the two strands are held together by only a few salt bridges (von der Ecken et al., 2015). Several ligands can bind between the two strands to stabilise F-actin such as phalloidin, a mushroom toxin that is commonly used for staining actin, and jasplakinolide, a drug from a marine sponge (Pospich et al., 2020).

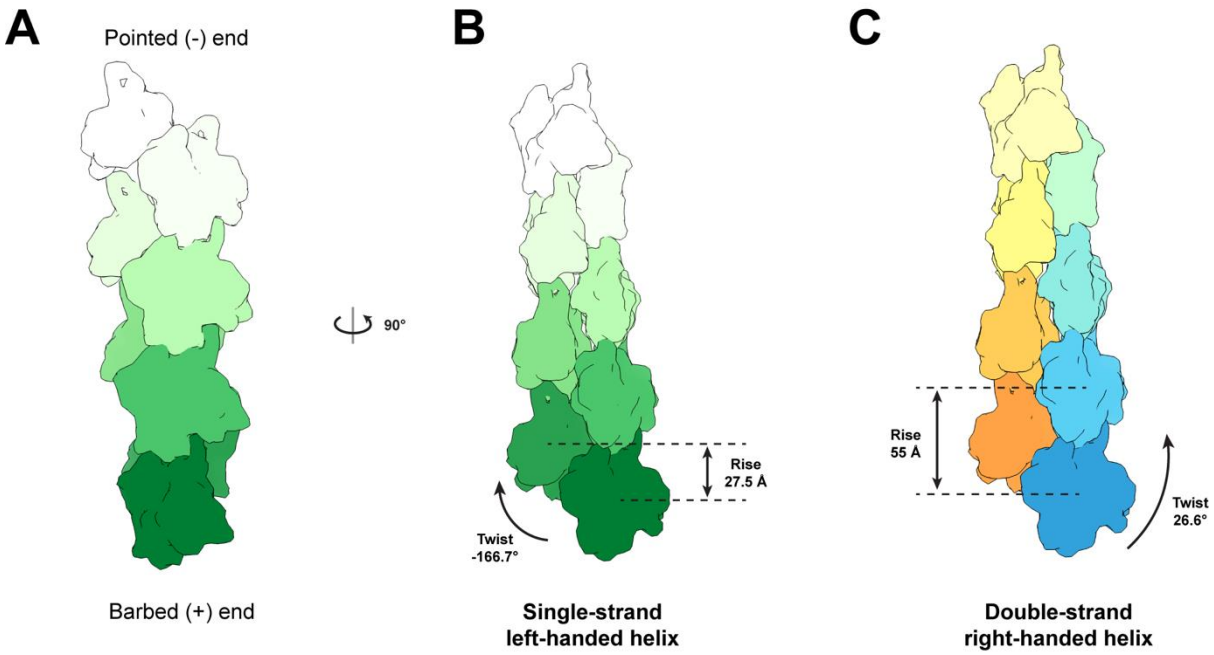

Fig. 2.5 Helical arrangement of F-actin

*(**A**) Schematic structure of F-actin. Different actin subunits are coloured in different shades of green. (**B**) Helical symmetry of F-actin when it is represented as a single-strand left-handed helix. Consecutive actin subunits are coloured in different shades of green. (**C**) Helical symmetry of F-actin when it is represented as a double-strand right-handed helix. Actin subunits in one strand are coloured in different shades of orange, while the ones in the other strand are in different shades of blue.*

ATP hydrolysis in actin is not coupled to any force generation. Instead, the nucleotide states of F-actin mark its molecular age (Merino et al., 2020). In the cytoskeleton, actin subunits that are freshly added to the barbed end of F-actin have ATP bound in their nucleotide pocket while the ATP in the "older" subuits is hydrolysed to ADP and P_i. The even older subunits, typically located around the pointed end, only contain ADP (Carlier and Pantaloni, 1988). In a mature muscle sarcomere, F-actin stays in the ADP state. In the cytoplasm, this ADP state has a higher rate of depolymerisation and is susceptible to being severed by cofilin (Merino et al., 2020). However, in the sarcomere, F-actin is decorated by additional proteins such as tropomyosin, troponin, and nebulin, which can stabilise F-actin and protect F-actin against cofilin (von der Ecken et al., 2015; Tanaka et al., 2018).

2.1.1.2 Tropomyosin and troponin

Tropomyosin is an elongated coiled-coil protein that forms head-to-tail polymers along F-actin. In the thin filament, F-actin is fully decorated by two tropomyosin molecules every 37 nm (one per actin strand) (Fig. 2.6A), except in the Z-disc (Luther, 2009) (section 2.1.2). The interactions between tropomyosin and the outer surface of the actin strands stabilise F-actin (von der Ecken et al., 2015). In addition to its stabilisation role, tropomyosin together with troponin regulate muscle contraction based on the Ca^{2+} concentration. Tropomyosin can adopt multiple positions on the thin filament (McKillop and Geeves, 1993; Vibert et al., 1997). When the Ca^{2+} concentration is low, tropomyosin is located in a position that sterically blocks myosin binding. Therefore, this position of tropomyosin is termed the B(blocking)-state (Fig. 2.6B). At a high Ca^{2+} concentration, tropomyosin moves azimuthally towards a C(closed)-state, which allows partial binding of myosin. Eventually, myosin binding further moves tropomyosin to a fully open state, termed the M(myosin)-state (McKillop and Geeves, 1993; Vibert et al., 1997).

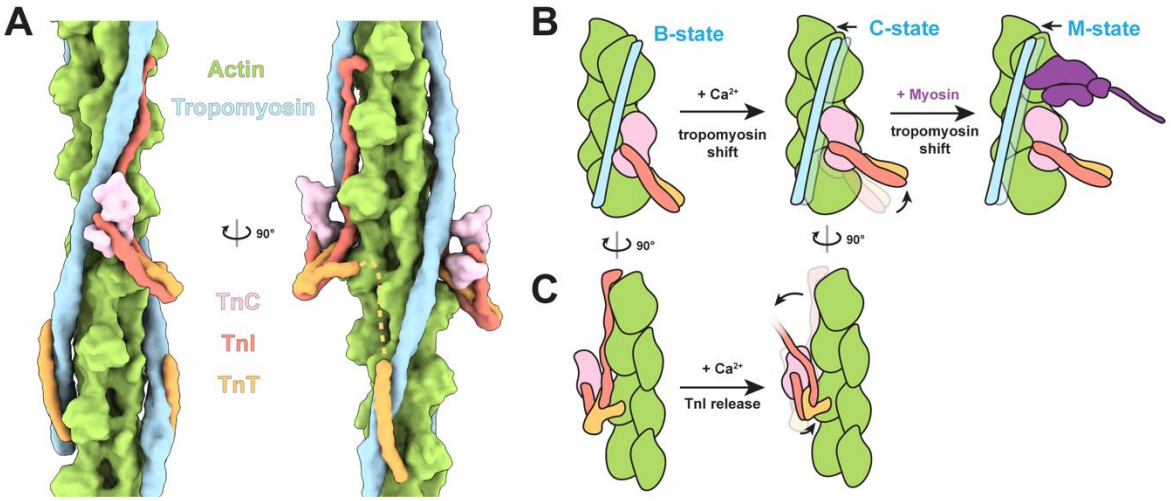

Fig. 2.6 Structure and regulation of the troponin-tropomyosin complex

*(**A**) Structure of the cardiac thin filament in the Ca^{2+}-free state, containing actin, tropomyosin and the troponin complex (PDB: 6KN7)* (Yamada et al., 2020) *(**B**) Schematic representation demonstrating the regulation of myosin binding controlled by the tropomyosin position. Simplified conformational changes are marked as arrows. The prior conformation is depicted in transparency. (**C**) Schematic representation demonstrating the mechanism by which TnI controls myosin binding through the steric blocking of the binding sites.*

The transition of tropomyosin from the B-state to the C-state is a result of conformational changes of the troponin complex upon binding to Ca^{2+}. The troponin complex is composed of three components: troponin T (TnT, involved in binding to tropomyosin), troponin I (TnI, involved in the inhibition of myosin binding), and troponin C (TnC, involved in Ca^{2+}-sensing) (reviewed in (Marston and Zamora, 2020)). Similar to tropomyosin, two troponin complexes decorate the thin filament every 37 nm. As such, troponin, tropomyosin and actin have a 1:1:7 stoichoimetry (Potter, 1974). The troponin complex has a "L"-shaped core (Takeda et al., 2003; Vinogradova et al., 2005) (Fig. 2.6A). The short arm is composed of two TnC lobes, while the long arm contains coiled-coil structures formed by both TnI and TnT. The N-terminus of TnT extends from the core through a flexible linker and binds to the tropomyosin on the other actin strand (Yamada et al., 2020). When the Ca^{2+} concentration is low, the C-terminal of TnI stretches along the thin filament next to the tropomyosin, blocking the myosin binding site (Fig. 2.6A,C). This TnI region and the B-state tropomyosin together prevent myosin binding and the subsequent muscle contraction. An increasing Ca^{2+} concentration leads to a conformational change in TnC that rotates the core, eventually pushing the tropomyosin into the C-state (Vinogradova et al., 2005; Yamada et al., 2020) (Fig. 2.6B). In addition, the binding of Ca^{2+} also causes TnI to bind to the TnC lobes, and thus to be released from blocking myosin binding sites on the thin filament (Yamada et al., 2020) (Fig. 2.6C).

2.1.1.3 Nebulin

Nebulin is an elongated protein with a molecular weight of ~800 kDa that spans the entire thin filament in skeletal muscle. Being identified in 1980, nebulin is one of the longest structural proteins in the skeletal sarcomere and essential for the sarcomere integrity (Wang and Williamson, 1980). Abnormities in the gene of nebulin, NEB, are the major cause of nemaline myopathy, which is one of the most common congenital skeletal muscle diseases (Romero et al., 2013; Ryan et al., 2001; Sewry et al., 2019). The symptoms of nemaline myopathy range from muscle weakness, hypotonia to, in severe situations, respiratory failure and death.

A single nebulin molecule is able to interact with both tropomodulin close to the M-band (McElhinny et al., 2001) and CapZ in the Z-disc (Pappas et al., 2008) (Fig. 2.7). The major part of nebulin contains 22-27 tandem super repeats, each consisting of seven simple repeats (Donner et al., 2004; Labeit and Kolmerer, 1995). The super repeat region is flanked by several additional simple repeats on both the N- (M1-M8) and C-termini (M163-M185) (Fig. 2.7B).

Each simple repeat is composed of 31 to 38 amino acid residues and contains a conserved SDxxYK sequence motif, while each super repeat contains a conserved WLKGIGW sequence motif (Labeit and Kolmerer, 1995). The modular sequence of nebulin suggested that each simple repeat binds to actin and each super repeat binds to tropomyosin or the troponin complex (Labeit and Kolmerer, 1995). *In vitro* experiments indicated that segments of nebulin were able to interact with both actin and tropomyosin (Marttila et al., 2014). However, the full-length nebulin appeared to not interact with tropomyosin or troponin (Chitose et al., 2010). It has remained a mystery how nebulin is incorporated into the thin filament until this thesis research.

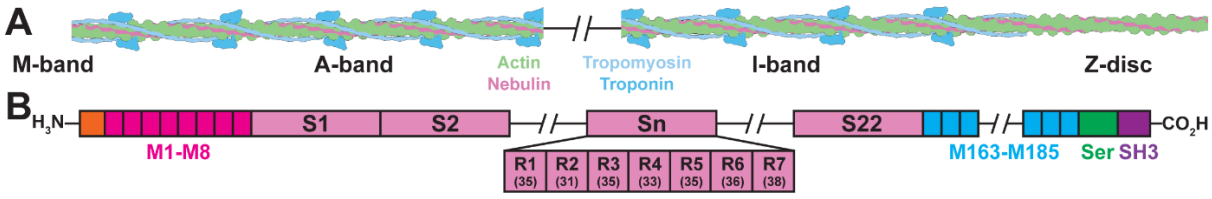

Fig. 2.7 Modular primary sequence of nebulin.

*(**A**) Schematic representation of a skeletal thin filament depicting nebulin. (**B**) Modular primary sequence demonstrating the simple and super repeats. From the N-terminus to the C-terminus, nebulin consists of a N-terminal sequence (orange), repeats 1-8 (M1-M8, bright magenta), a large super repeat region (S1-S22, magenta), repeats 163-185 (M163-M185, blue), a serine-rich region (Ser, green), and a Src homology-3 domain (SH3, purple). Each super repeat contains seven simple repeats (R1-R7). The most common number of amino acids of each simple repeat is indicated in brackets. Figure was adapted from* (Wang et al., 2022).

Nebulin has been proposed to regulate the length of the thin filaments (Kruger et al., 1991; Labeit et al., 1991). The size of nebulin is positively correlated to the thin filament length across different species and different muscle types in human (Gokhin et al., 2012; Labeit et al., 1991). Mice expressing larger or smaller nebulin exhibited corresponding longer or shorter thin filaments (Kiss et al., 2020; Pappas et al., 2010). Moreover, nebulin knock-out caused a loss of thin filament length control in mice and eventually led to death (Bang et al., 2006; Witt et al., 2006). In cardiac muscle, only nebulette, a short homolog located close to the Z-disc, is present instead of nebulin (Moncman and Wang, 1995). As a result, thin filaments in cardiac muscle

have a larger distribution in length (Burgoyne et al., 2008). Therefore, nebulin is considered as a "molecular ruler" of the thin filament in skeletal muscle.

In addition to regulating thin filament length, nebulin also stabilises and stiffens the thin filament (Kiss et al., 2018; Pappas et al., 2010). A reduced nebulin level resulted in an increased turnover rate of actin in the thin filament (Pappas et al., 2010). The extensibility in the thin filaments were three-fold higher in a nebulin knock-out model compared to normal muscle (Kiss et al., 2018). Furthermore, nebulin has been shown to regulate myosin binding. It promotes myosin binding and cross-bridge formation, thus increases muscle contraction efficiency (Bang et al., 2009; Chandra et al., 2009; Kiss et al., 2018). *In vitro* studies suggested that nebulin fragments could directly interact with myosin (Jin and Wang, 1991; Root and Wang, 1994). Despite extensive experiments demonstrating the functions of nebulin, the molecular mechanism underlying the role of nebulin as a molecular ruler, in stabilising the thin filament and regulating myosin binding still remained "nebulous".

2.1.2 Thick filament

2.1.2.1 Myosin

The backbone of the thick filament is constituted by myosin. Myosin is a motor protein that uses the energy from ATP hydrolysis for force generation. The protein "myosin" was the first muscle component discovered back in the 19th century (Kühne, 1864), which was later shown to be a mixture of both actin and myosin (Straub, 1942; Szent-Györgyi, 1943). In the cytoplasm, the interaction between actin and myosin is the key to a variety of cellular activities such as cell division, cell movement, and cargo transport (Pollard and Cooper, 2009). The myosin family can be divided into a number of different classes, responsible for its diverse functions (Hartman and Spudich, 2012). In muscle contraction, the myosin class involved in force generation is myosin II, also referred to as conventional myosin. Myosin II contains two heavy chains (HCs), two essential light chains (ELCs), and two regulatory light chains (RLCs) (Fig. 2.8A,B). The N-terminus of the HC folds into a motor domain, followed by a lever arm that is bound by an ELC and an RLC. The motor domain and the lever arm together constitute the myosin S1 domain (also referred to as the myosin head). The C-terminal regions of the two myosin HCs intertwine and form a long coiled-coil tail. The initial segment of the tail is termed as the S2 domain. The S1 and S2 domains together compose the so-called heavy meromyosin

(HMM), while the rest of myosin is termed the light meromyosin (LMM), as derived from limited proteolysis (Szent-Györgyi, 1953) (Fig. 2.8A).

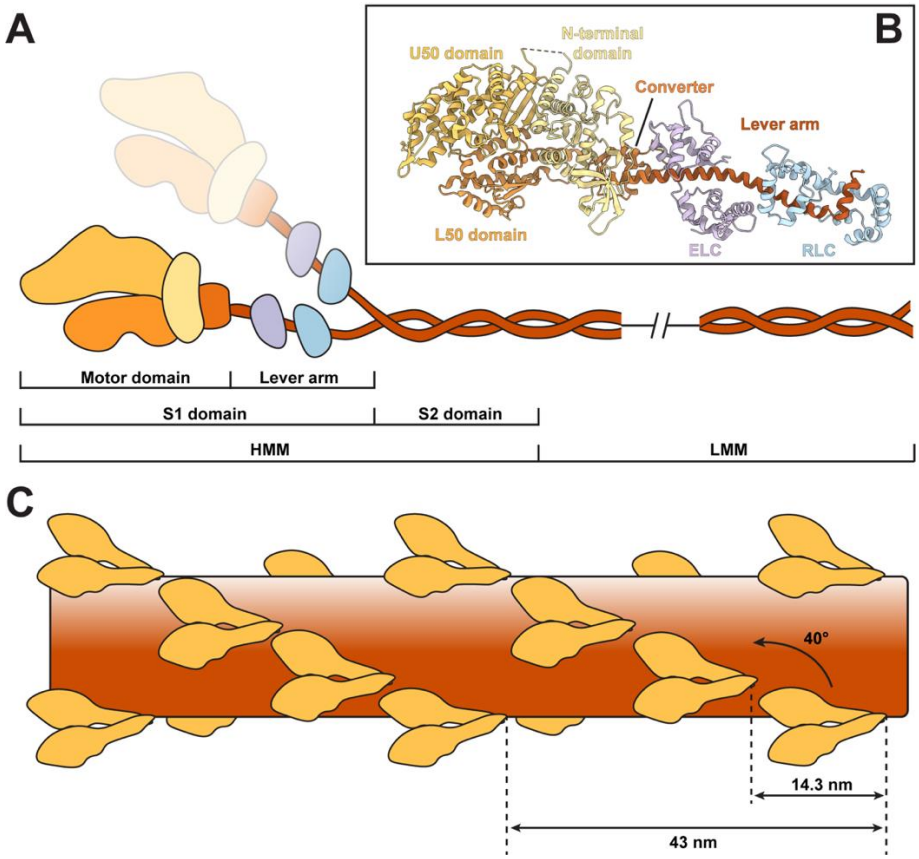

Fig. 2.8 Myosin and the thick filament

*(**A**) Schematic representation of a myosin II molecule. The domains from the N-terminus to the C-terminus are coloured from light yellow to dark brown (in the order of N-terminal domain, U50 domain, L50 domain, converter, the lever arm and tail). ELC and RLC are coloured in purple and blue, respectively (**B**) Crystal structure of the S1 domain of myosin II from scallop muscle in the rigor state (PDB: 3I5G) (**C**) Organisation of pairs of myosin heads (orange) on a thick filament (dark red).*

The thick filament is a bi-polar filament with the myosin tails pointing to the centre. The myosin heads lie on the surface of the thick filament and are arranged in a helical pattern. In vertebrate muscle, myosin heads are organised in a 3-start helix with a helical rise of 14.3 nm and helical twist of 40° (Squire, 2009). As such, the thick filament has a 3-fold rotational symmetry with a 43 nm axial repeat of the myosin heads (Fig. 2.8C). During muscle contraction,

the myosin heads reach out and interact with actin on the thin filament, constituting a cross-bridge between the two types of filaments (Huxley, 1969; Spudich, 2001).

Myosin interacts with actin via its motor domains. Each motor domain contains a 50-kDa domain that is divided into upper (U50) and lower sub-domains (L50) by a central cleft, an N-terminal domain, and a converter domain that continues to the lever arm (Yang et al., 2007) (Fig. 2.8B). The force generation by myosin is coupled to cyclic interactions with actin and ATP hydrolysis, referred to as the myosin ATPase cycle, also known as the Lymn-Taylor cycle (Lymn and Taylor, 1971). It was later refined to the swinging lever-arm hypothesis with the determination of myosin structures (Holmes, 1997). The cycle starts from a detached myosin state harbouring ATP in its nucleotide pocket, known as the **post-rigor state** (Fig. 2.9i). In this state, the cleft between U50 and L50 is open, resulting in a low binding affinity for actin (Fisher et al., 1995). The bound ATP is quickly hydrolysed to ADP and P_i, leading to a series of conformational changes from the active site to the converter. These conformational changes eventually result in a large swing (~70°) of the lever arm (Dominguez et al., 1998; Houdusse et al., 2000), called the **recovery stroke** (Fig. 2.9i-ii). Therefore, the energy from ATP hydrolysis primes myosin into a high-energy **pre-power stroke** (PPS) state (Fig. 2.9ii). While myosin in the PPS state still has low affinity for actin due to its open actin binding cleft, a surface loop between U50 and L50, called loop 2, is thought to bind first to actin (Joel et al., 2001; Onishi et al., 2006). This enables initial binding of the L50 domain to actin through mainly hydrophobic interactions (Behrmann et al., 2012; von der Ecken et al., 2016), which causes the cleft to partially close (Fig. 2.9ii-iii). The initial interactions between myosin and actin have been proposed to open a tunnel for P_i release (Llinas et al., 2015). Thus, this state is termed the **P_i-release state** (Fig. 2.9iii). The release of P_i through the tunnel is suggested to cause the full closure of the cleft and a swing of the lever arm in opposite direction to the recovery stroke, called the **power stroke** (Fig. 2.9iii-iv). In muscle contraction, the large swing of the lever arm while the motor domains are attached to F-actin generates the force to pull the thin filaments towards the M-band, leading to the shortening of the sarcomere. The state of myosin after the power stroke contains ADP in its active site, and is thus called the **ADP-bound state** (Fig. 2.9iv). The release of ADP further leads to a small movement of the lever arm as shown in myosin Ib and myosin V (Mentes et al., 2018; Pospich et al., 2021) and results in the so-called **rigor state** of myosin (Fig. 2.9v). In the end of the cycle, upon binding of ATP, myosin returns to the post-rigor state through a proposed intermediate post-rigor transition state identified in myosin V where ATP-bound myosin is still attached to F-actin (Pospich et al.,

2021) (Fig. 2.9vi). *In vitro* studies showed that around 5% of myosin are in the ADP-bound or rigor state for muscular myosin II (O'Connell et al., 2007). Despite being a small proportion of the entire cycle, these states, especially the rigor state, are the key to understand the interactions between actin and myosin. The rigor state is also the state in which myofibrils are typically extracted as most cross-bridges are attached to the thin filaments, stabilising the integrity of the myofibrils (Knight and Trinick, 1982).

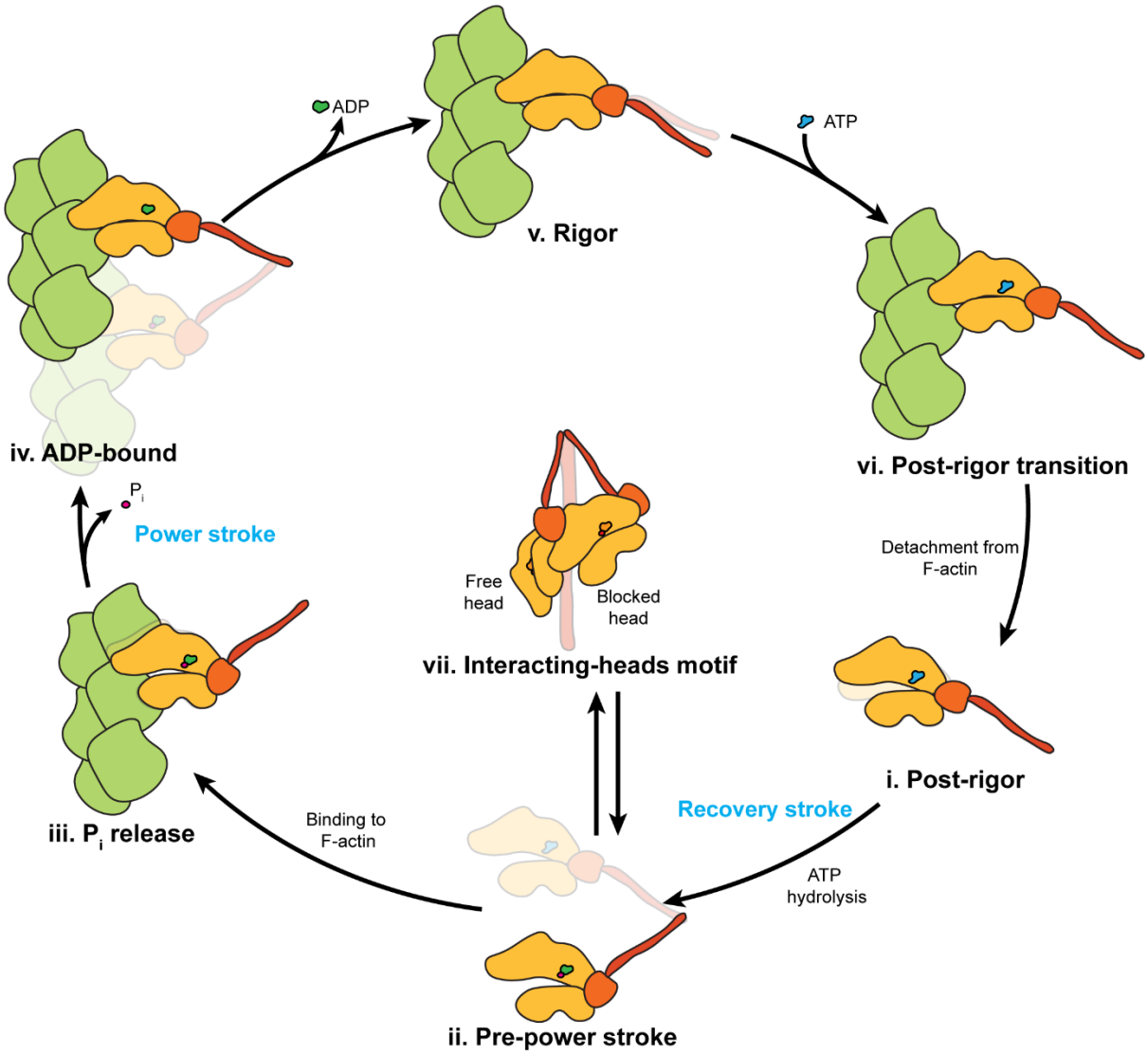

Fig. 2.9 Myosin ATPase cycle

Schematic representations of different states of myosin during muscle contraction. Actin is coloured in green. Myosin motor domain, converter, and lever arm are coloured in orange, dark orange, and dark red, respectively. ELC and RLC are not illustrated. The prior state of every state is depicted as transparent background. In the IHM state (vii), the myosin tail is shown as transparent background.

Myosin can also enter an "energy-saving" super-relaxed state (Stewart et al., 2010). In fact, in resting muscle, it was estimated that ~50% of the myosin is in the super-relaxed state, where the ATP turnover rate is significantly lower (Hooijman et al., 2011; Stewart et al., 2010). The structural basis of the super-relaxed state is generally believed to be a special configuration of the two myosin heads, called the interacting-head motif (IHM) (Nag and Trivedi, 2021). In the IHM state, one of the two myosin heads (called the blocked head) bends around the converter and interacts with the other head (called the free head), forming a triangular shape folded back to the S2 domain (Heissler et al., 2021; Scarff et al., 2020; Yang et al., 2020) (Fig. 2.9vii). Both heads in this configuration are locked by each other as well as the S2 domain, and thus unable to interact with actin. The motor domain in the IHM state structurally resembles the PPS state and also contains ADP and P_i in its active site (Heissler et al., 2021; Scarff et al., 2020; Yang et al., 2020). The IHM state is thereby considered as an inactive branched state from the PPS state in the cross-bridge cycle. Multiple factors control the activation and deactivation of myosin, including phosphorylation of the RLC and MyBP-C, Ca^{2+} binding, and thick filament stress, yet the detailed mechanism remains to be uncovered (reviewed in (Nag and Trivedi, 2021)).

2.1.2.2 Titin

Myosin is not the only component in the thick filament. Another major protein present in the thick filament is titin. As the largest protein (~3 MDa) in the human body, titin spans across a complete half sarcomere including the A-band, I-band, M-band, and Z-disc (reviewed in (Krüger and Linke, 2011)). This gigantic protein has its N-terminus anchored in the Z-disc while its C-terminus reaches the M-band (Fig. 2.10A). In the A-band, titin closely associates with myosin on the thick filament (AL-Khayat et al., 2013; Zoghbi et al., 2008), yet the structural details are unknown. The A-band titin consists of tandem repeats of immunoglobin-like (Ig) and fibronectin-like (Fn) domains, mostly arranged in 11-domain super repeats. The length of each 11-domain super repeat was suggested to be 43 nm, consistent with the 43-nm axial repeat of myosin heads on the thick filament (Labeit et al., 1992). Therefore, titin was proposed to be a "molecular ruler" for the thick filament during the assembly of the sarcomere (Labeit et al., 1992). The I-band titin contains tandem Ig domains as well as a PEVK region (rich in proline (P), glutamate (E), valine (V), and lysine (K)) and, in cardiac muscle, an N2B domain (Fig. 2.10A). The I-band region of titin has been proposed to act as a "molecular spring" through the stretching of the linker between Ig domains (Fig. 2.10B) and the straightening of

unstructured coils in the PEVK region (reviewed in Granzier and Labeit, 2004). This elastic property of titin contributes to the passive tension of the sarcomere. The N-terminus of titin in the Z-disc consists of up to seven 45-amino acid modules called the Z-repeats (Gautel et al., 1996). The titin Z-repeats interact with a major component in the Z-disc, α-actinin, and have been proposed to control the number of layers of α-actinin (Gautel et al., 1996). However, the detailed molecular mechanism is yet to be determined as the distance between α-actinin layers appears to be different from the length of the Z-repeats (Luther and Squire, 2002). The M-band titin contains a kinase domain and other Ig domains that can interact with various M-band components such as myomesin and obscurin (section 2.1.3). It remains unclear whether the kinase domain is active or acts only as part of the structural scaffold (Gautel and Djinović-Carugo, 2016).

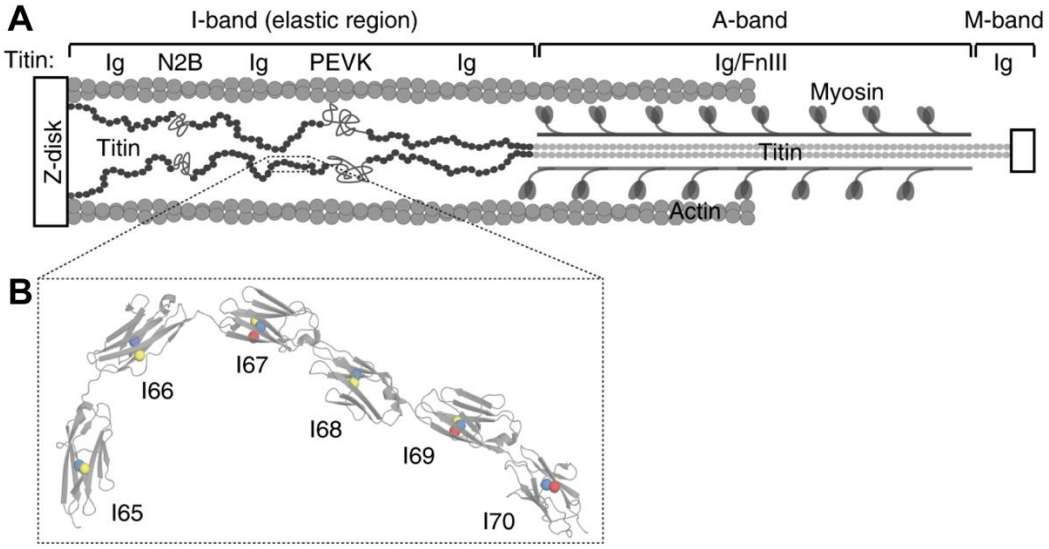

Fig. 2.10 Titin domain organisation

*(**A**) Schematic representation of titin in a half sarcomere from the M-band to the Z-disc. (**B**) Crystal structure of a 6-module titin in the I-band (PDB: 3B43). Figure adapted from* (Giganti et al., 2018) *under license CC BY 3.0.*

2.1.2.3 Myosin-binding protein C (MyBP-C)

MyBP-C is another thick filament component that interacts with myosin. In skeletal muscle, MyBP-C consists of 10 tandem Ig and Fn domains (C1-C10) and one M domain between C1 and C2 (reviewed in Heling et al., 2020). In cardiac muscle, one additional Ig domain is present

on the N-terminus, termed C0 (Yasuda et al., 1995). MyBP-C interacts with myosin and potentially titin through its C-terminal domains C7-C10, while its N-terminal domains, C0-C2, interacts with actin on the thin filament (Heling et al., 2020). Thus, it can form a cross-link between the thin and thick filaments in an A-band region that is close to the M-band, termed the C-zone (Fig. 2.3). The cross-links formed by MyBP-C were initially observed as stripes with a periodicity of 43 nm (Craig and Offer, 1976) and later visualised in a reconstruction of the relaxed muscle using freeze-substitution electron tomography (Luther et al., 2011). While initial structural studies suggested that the C-terminal domains of MyBP-C are positioned along the long axis of the thick filament (AL-Khayat et al., 2013; Zoghbi et al., 2008), the organisation of other domains remains elusive. Structural studies confirmed the binding of the N-termainl C0-C2 domains to F-actin (Risi et al., 2018, 2021a). Meanwhile, these domains are also able to interact with myosin light chains and the S2 domain (Ababou et al., 2008; Gruen et al., 1999; Ratti et al., 2011). These experiments indicate a complex and dynamic role of MyBP-C in muscle contraction that needs to be uncovered. As MyBP-C can interact with both actin and myosin, it has been proposed to regulate the activation of both the thin filament, potentially through shifting tropomyosin (Mun et al., 2014), and the thick filament, potentially through destabilising the IHM state of myosin upon phosphorylation (McNamara et al., 2019). However, the full structure and detailed function mechanisms of MyBP-C remain to be investigated.

2.1.2 Z-disc

The core component of the Z-disc besides actin is α-actinin, which cross-links the thin filaments in two to seven layers depending on the muscle type (Luther, 2009). The thin filament region in the Z-disc does not contain tropomyosin or troponin, as shown by immunostaining EM studies (Ohtsuki, 1974; Trombitas et al., 1993), but still incorporates nebulin in skeletal muscle or nebulette in cardiac muscle (Millevoi et al., 1998). The perception into the Z-disc started from EM projection images acquired from chemically fixed muscle samples (Goldstein et al., 1990; Luther, 2009). The longitudinal section view of the Z-disc showed a zigzag pattern of each layer of cross-links between the thin filaments from adjacent sarcomeres (Luther, 2009). The transverse section view depicted two different states: a “small-square” pattern representing the relaxed form and a “basket-weave” pattern representing the active form (Goldstein et al.,

1990) (Fig. 2.11A). In both forms, the thin filaments are organised in a squared pattern, in contrast to the hexagonal arrangement in the A-band.

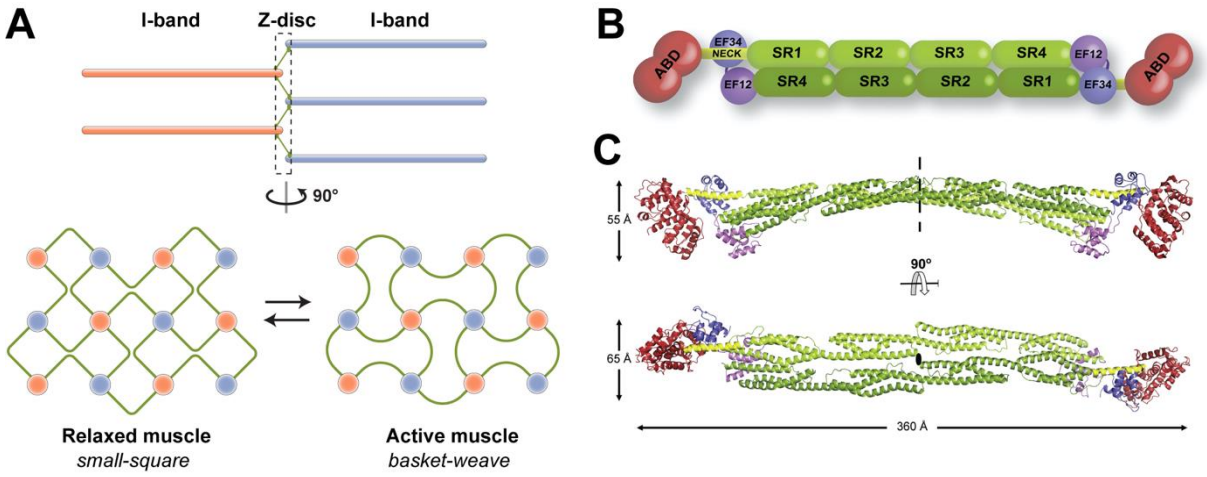

Fig. 2.11 Models of the Z-disc and structure of α-actinin.

*(**A**) Models of the two states of the cross-section view of the Z-disc. (**B**) Schematic representation of the structure of an α-actinin dimer. (**C**) Crystal structure of an α-actinin dimer in a closed conformation (PDB: 4D1E). Panel (B) and (C) reprinted from* (Ribeiro et al., 2014) *with permission from Elsevier.*

The Z-disc cross-links are formed by antiparallel α-actinin homodimers (Ribeiro et al., 2014). The centre of the dimer is a rod domain composed of four spectrin-like repeats (SR) from each protomer (Fig. 2.11B,C). The spectrin repeats in each protomer are flanked by an N-terminal actin-binding domain (ABD) and a C-terminal calmodulin-like domain (Ribeiro et al., 2014). The ABD and the rod domain are connected by an α-helical neck domain, which accounts for the flexibility of α-actinin as observed in smooth muscle α-actinin (Winkler et al., 1997) and *in vitro* reconstituted actin-α-actinin raft (Hampton et al., 2007).

In addition to acting as a structural component, the Z-disc is also able to sense strain/stress within the sarcomere (Gautel, 2011). The Z-disc conformation can be affected by temperature, osmotic pressure, ionic strength, and the activation state of the thin filaments (Perz-Edwards and Reedy, 2011). It is believed that this plasticity of the Z-disc helps not only to resist the mechanical forces during muscle contraction and relaxation but also to translate stress into biochemical signals potentially through other Z-disc components such as LIM proteins, myopalladin, ZASP, FATZ, myotilin etc (Pyle and Solaro, 2004).

2.1.3 M-band

In the M-band, the thick filaments are cross-linked and anchored by a number of proteins including myomesin, titin, and obscurin (Gautel and Djinović-Carugo, 2016; Lange et al., 2019) (Fig. 2.12). It has been proposed that the stable network formed by the thick filament and these proteins maintains the stability of the sarcomere through absorbing the misbalanced forces generated on the two halves of the sarcomere (Agarkova and Perriard, 2005). Potential deformation of the M-band by shear forces allows the M-band to also act as a strain sensor to translate mechanical information into biochemical signals (Gautel, 2011).

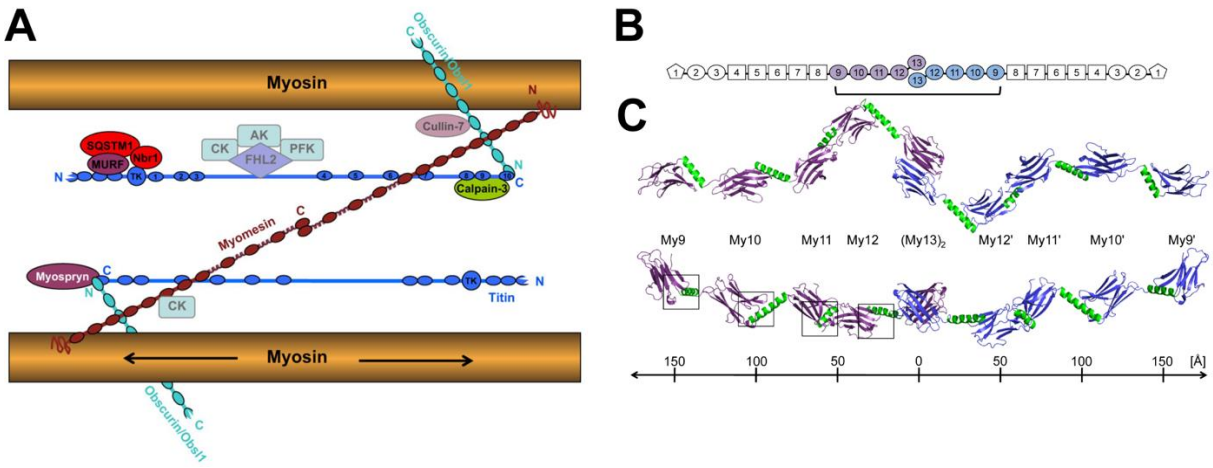

Fig. 2.12 Model of the M-band organsiation and partial structure of myomesin.
*(**A**) Schematic representation of a proposed model of the M-band describing the organisation of myomesin, titin, and obscurin, together with components of the protein turnover machinery MURF, SQSTM1, Nbr1, Cullin-7, myospryn and metabolic enzymes CK, AK, PFK mediated by FHL2. (**B**) Schematic representation of the myomesin dimer. Coloured domains have their structures characterised by X-ray crystallography. (**C**) Crystal structures of myomesin My9-My13 (PDB: 2Y23, 2Y25). Figure reprinted from* (Gautel and Djinović-Carugo, 2016) and (Pinotsis et al., 2012) *under licences CC BY 3.0 and CC BY 4.0*

As the thick filament is a bi-polar filament with myosin tails orientated towards the centre, the thick filament in the M-band is a bare zone without myosin heads. Previous EM projection images have shown that the centre of the M-band contains multiple transverse lines, termed M-lines (Pask et al., 1994). It has been generally accepted that the M-lines, i.e. the cross-links between the thick filaments, are formed by the myomesin family, including myomesin-1

(initially called myomesin), myomesin-2 (initially called M-protein), and myomesin-3 (Agarkova and Perriard, 2005). All three myomesin proteins share a similar domain organization despite their exact role and localisation in the M-band is not clear. Each myomesin contains 13 tandem repeats of Ig or Fn domains (My1-My13). The C-terminal Ig domain, My13, is able to dimerise, resulting in an anti-parallel homodimer (Pinotsis et al., 2012) (Fig. 2.12B,C). Myomesin has been shown to be an elongated elastic ribbon as the linkers between Ig domains are able to be stretched to increase its length (Pinotsis et al., 2012). In addition to myomesin, the C-terminal titin and obscurin are also major components in the M-band. Obscurin is another large protein mainly consists of series of Ig and Fn domains and interacts with both titin and myomesin (Young et al., 2001). It is suggested to provide the structural integrity of the M-band and serve as a scaffold for other components (Manring et al., 2017). These proteins add further complexity to the M-band network that remains to be revealed.

2.2 Structural investigation of the sarcomere

The understanding of muscle contraction is built upon centuries of structural evidence. The development of light microscopy and electron microscopy as well as X-ray diffraction, in their initial stage, shed light on the overall organisation of sarcomere (section 2.2.1). As individual muscle components were identified and isolated, structural investigations on these components using primarily X-ray crystallography and recently single-particle electron cryo-microscopy (cryo-EM) provided more insights into the protein architecture and the mechanism of their functions (section 2.2.2). However, there are still limitations in the available structural approaches (section 2.2.3), which motivates this thesis research.

2.2.1 Structural studies of the entire sarcomere

The first picture of a muscle fibre was acquired by Antonie van Leeuwenhoek more than 300 years ago (van Leeuwenhoek, 1682), where he observed the striated patterns in fish muscle using a self-made light microscope. Since then, the understanding of muscle organisation has been advanced gradually by the development of microscopy methods. The development of phase-contrast microscopy (Zernike, 1955), interference microscopy (Smith, 1954) and electron microscopy (EM) (Knoll and Ruska, 1931) enabled muscle myofibrils to be observed with greater details and led to the discovery of the sliding filament theory (Huxley and Hanson, 1954; Huxley and Niedergerke, 1954). In the early stage of transmission electron microscopy (TEM), muscle samples were chemically fixed, stained with heavy metals, embedded in plastics, and mechanically sliced using a microtome (Hodge et al., 1954). 2-dimensional (2D) projection images of longitudinal and transverse sections of muscle revealed the basic organisation of muscle filaments including the spacing between the filaments and the hexagonal and tetragonal arrangement in the A-band and Z-disc, respectively (Goldstein et al., 1990; Huxley, 1957). This conventional EM approach remains a powerful tool nowadays for the diagnosis of myopathies and clinical studies (Sewry, 2002).

The projection images from TEM only provided limited 2D information. Therefore, a technique was developed to image biological objects at different tilted angles and reconstruct computationally a 3D volume (Hoppe et al., 1976). This technique is called electron tomography (ET) (details in section 2.3.3). ET studies of thin sections of insect flight muscle provided the first insights into the 3D organisation of invertebrate cross-bridges (Schmitz et al.,

1996; Taylor et al., 1984). In addition, cardiac muscles were also imaged using ET to determine the length of the thin filaments as well as visualise the Z-disc (Burgoyne et al., 2008, 2015). However, the chemical fixation during the sample preparation takes hours and can disturb the internal structures (Steinbrecht and Zierold, 1987). An improved method is cryo-fixation (details in section 2.3), which was in the early days followed by freeze-substitution to exchange water with organic solvents prior to staining and embedding (Steinbrecht and Müller, 1987). This allowed improved imaging of the insect cross-bridges (Liu et al., 2004) and Z-discs from midshipman fish sonic muscle (Burgoyne et al., 2019). The fish sonic muscle, which has an atypical Z-disc that is more than 10 times thicker than the Z-disc of a vertebrate skeletal muscle, revealed the arrangement of Z-disc cross-links between thin filaments with an axial distance of 19.2 nm, consistent with previous studies (Burgoyne et al., 2015; Perz-Edwards and Reedy, 2011).

A later developed method entirely bypassed staining or embedding through directly sectioning the cryo-fixed sample using a cryo-microtome at ~-140°C (reviewed in (Al-Amoudi et al., 2004)). This technique is called cryo-EM of vitreous sections (CEMOVIS). Although CEMOVIS allows the sample to be imaged in a hydrated state for the first time, an initial CEMOVIS study of insect flight muscle demonstrated severe artefacts due to knife marks and compression along the cutting direction (McDowall et al., 1984).

Cryo-fixation combined with ET at cryogenic temperature (cryo-ET, details in section 2.3.3) can also be performed without sectioning when the sample is thin enough. This approach was used to image isolated Z-discs from honeybee flight muscle and isolated small branches of cardiac myofibrils (Oda and Yanagisawa, 2020; Rusu et al., 2017). The latter study determined two averaged structures of the actin-α-actinin complex at ~23 Å, potentially representing the relaxed and the activated states, which show a structural rearrangement of α-actinin pivoting around the neck domain in response to the torque applied by the myosin heads onto the thin filaments (Oda and Yanagisawa, 2020).

In addition, the regularity within muscle samples and the helical properties of the thick and thin filaments give rise to diffraction signals when passing monochrome X-rays through the muscle. Analysing the X-ray diffraction diagram provided ensemble information of the sarcomere structure under hydrated conditions such as the helical repeats of actin and myosin as well as the spacing between filaments (Huxley and Brown, 1967). Structural changes within a sarcomere upon contraction or relaxation are reflected in the change of the diffraction pattern

and can be interpreted with different models (reviewed in (Ma and Irving, 2022)). Numerous X-ray diffraction studies contributed to the proposal of the "swing-lever arm" model describing the cyclic interaction between myosin and the thin filament (Holmes, 1997; Huxley, 1969; Huxley et al., 1981, 1982) and the steric blocking model of tropomyosin regulation (Gordon et al., 2000; McKillop and Geeves, 1993; Vibert et al., 1997). X-ray diffraction of muscle remains an effective approach to detect sarcomere structural changes (Ma and Irving, 2022). However, it does not allow the direct visualisation of proteins.

2.2.2 Structure studies of individual muscle proteins

Since the discovery of the major components of the muscle, such as actin (Straub, 1942), myosin (Kühne, 1864; Szent-Györgyi, 1943), nebulin (Wang and Williamson, 1980), and titin (Maruyama et al., 1976; Wang et al., 1979), muscle contraction could be studied from a "bottom-up" approach through investigating the structures of the individual components. X-ray crystallography has been the primary method for protein structure determination since the 1950s (Green et al., 1954; Kendrew et al., 1958). Crystals formed by purified proteins can be imaged with X-rays, giving rise to diffraction patterns. The diffraction patterns can be computationally analysed to produce an electron density map of the protein, which allows the building of a structural model (Smyth and Martin, 2000). However, crystallisation of proteins is not always reliable and often requires the removal of flexible regions. Also, most large protein complexes and filaments are not capable to form compact crystals. In recent years, single-particle electron cryo-microscopy (cryo-EM) became another major structural biology approach (details in section 2.3.2). In single-particle cryo-EM, purified proteins can be frozen in a thin layer of vitreous ice and imaged by TEM under cryogenic temperature. The projection images of up to millions of proteins allow the computational reconstruction of a 3D protein structure (Quentin and Raunser, 2018).

The first crystal structure of G-actin was determined using X-ray crystallography together with DNase I (Kabsch et al., 1990). Since then, more than 80 G-actin structures were obtained in complex with various actin-binding proteins (reviewed in (Dominguez and Holmes, 2011)). The structure of F-actin, however, required the usage of cryo-EM and was not solved to a high resolution (3.7 Å) until 2015, together with tropomyosin (von der Ecken et al., 2015). This was followed by several F-actin structures in different nucleotide states (Chou and Pollard, 2019; Merino et al., 2018). Recently, F-actin structures were determined to an even higher resolution

of ~2.2 Å that allowed the direct visualisation of EM densities corresponding to water molecules and demonstrated the detailed mechanisms for ATP hydrolysis (Oosterheert et al., 2022).

The first crystal structure of myosin S1 (Rayment et al., 1993a) was determined shortly after the first structure of G-actin. This structure was followed by numerous structures of myosins from different classes and across different species (reviewed in (Sweeney et al., 2020)), most of which contain the S1 domain or only the motor domain. The S2 coiled-coil structure of human cardiac myosin was solved separately (Blankenfeldt et al., 2006). Crystal structures of myosin depict the conformation of single myosin heads in the post-rigor, pre-power stroke, and rigor-like states and have shed light on the P_i-release configuration (Llinas et al., 2015). In addition, myosin structures in the IHM state (also called the inhibited state or the 10S state) were determined in recent years for smooth muscle by cryo-EM to resolutions ranging from 3.4 Å to 6 Å (Heissler et al., 2021; Scarff et al., 2020; Yang et al., 2020).

The overall organisation of the thick filament has been revealed by cryo-EM in multiple species, to different extents of details. Thick filament structures from insect flight muscles were resolved to 5-7 Å (Daneshparvar et al., 2020; Hu et al., 2016), depicting the packing of myosin tails within a thick filament. Thick filaments from tarantula muscle (Alamo et al., 2008; Woodhead et al., 2005; Yang et al., 2016) were resolved to up to 13 Å and demonstrated a IHM conformation of myosin in the relaxed thick filament. The structure of the thick filament from vertebrate cardiac muscle in the relaxes state has also been studied, but only resolved to 28-30 Å (AL-Khayat et al., 2013; Zoghbi et al., 2008). This limited resolution is potentially due to the use of staining instead of cryo-fixation. Nevertheless, these structures still depict a general shape of the myosin heads consistent with the IHM state, and most identified densities corresponding to titin and MyBP-C (AL-Khayat et al., 2013; Zoghbi et al., 2008).

The interaction between actin and myosin was investigated through the structure of a complex formed by F-actin and myosin, referred to as the actomyosin complex. The actomyosin complex obtained through decorating F-actin with the myosin S1 domain in the rigor state *in vitro* depicted arrowhead shapes along the filament (Craig et al., 1985). This structure of actomyosin has been studied extensively already in the early stage of cryo-EM (Behrmann et al., 2012; Holmes et al., 2003; Rayment et al., 1993b; Volkmann et al., 2003). The first high-resolution structure was only available from 2016 (von der Ecken et al., 2016), revealing the details at the interface between actin and myosin. Following the rigor state, structures other

actin-bound states were also solved using cryo-EM. Due to the short lifetime of other actin-bound states of myosin II, actomyosin structures of other non-muscle myosins such as myosin Ib (Mentes et al., 2018), myosin Va (Pospich et al., 2021; Wulf et al., 2016) and myosin VI (Gurel et al., 2017) were determined to characterise the ADP-bound state and the recently discovered post-rigor transition state (Pospich et al., 2021). Combining the crystal structures of single myosin and the cryo-EM structures of the actomyosin complex, we now have a more comprehensive knowledge of the myosin ATPase cycle (section 2.1.2.1).

In addition to actin and myosin, some of the other sarcomeric components have also been structurally characterised. Cryo-EM structures of isolated cardiac thin filaments revealed the conformations of tropomyosin and troponin in the active and inactive form (Oda et al., 2020; Risi et al., 2021b; Yamada et al., 2020) and illustrated the corresponding regulation mechanism (section 2.1.1.2). Furthermore, a structure of CapZ attached to the barbed end of F-actin was determined using cryo-EM (Funk et al., 2021), while a crystal structure of fragments of tropomodulin bound to actin has shed light on pointed end capping (Rao et al., 2014). On the contrary, the structures of nebulin and nebulette are still unknown (details in section 2.2.3). Only their C-terminal SH3 domain has been so far characterised structurally (Eulitz et al., 2013; Politou et al., 1998). Although the full structure of titin has also not been determined, multiple structures of up to 6 modules of titin Ig and Fn domains up have been resolved using X-ray crystallography (reviewed in (Krüger and Linke, 2011)). Moreover, the closed-state structure of the Z-disc cross-linker, α-actinin, was determined using X-ray crystallography (Ribeiro et al., 2014) (section 2.1.2), while its counterpart in the M-band, myomesin, only has its central domains M9-M13 resolved (section 2.1.3) (Pinotsis et al., 2012).

2.2.3 Limitation of current structural approaches in muscle research

Decades of structural research have shaped our understanding of muscle function. Nevertheless, there are still inherent limitations in the existing structural methods.

On the one hand, the structural investigation of the overall sarcomere lacks high-resolution information and usually involves disruptive treatment during sample preparation (section 2.2.1). The conventional EM approach, including conventional ET which uses chemical fixation or freeze-substitution with staining, provides high contrast at the cost of imaging the staining metal instead of the actual biological sample, which limits the achievable resolution

(Steinbrecht and Zierold, 1987). In addition, the dehydration of the sample during the preparation disrupts the hydrogen bonding network and eventually the internal structures. Furthermore, during imaging within a TEM, the thin section of a plastic embedded biological specimen undergoes shrinkage and evaporation (Bennett, 1974). Although cryo-ET can investigate biological specimens in their native state, it is limited to samples thinner than 1 µm (Lučić et al., 2013). However, most native muscle samples, even the single myofibrils, are thicker than 1 µm. Thus, sectioning of the sample is always required. Recent cryo-ET studies of the Z-disc could skip the sectioning using either isolated honey-bee Z-disc or small branches of the myofibril (Oda and Yanagisawa, 2020; Rusu et al., 2017). Nevertheless, the limited contrast in the images as a result of the thick size of these samples did not allow the visualisation of individual proteins. These studies thereby could not reveal the heterogeneity or plasticity within the same or across different Z-discs (section 2.1.2). It is crucial to employ an artefact-free sectioning approach to apply cryo-ET on a native sarcomere.

On the other hand, structures from X-ray crystallography or cryo-EM lack *in situ* information, i.e., how proteins are organised in a native biological environment. For example, it remains a mystery how the hexagonal pattern of the thin filaments in the A-band is rearranged into the tetragonal pattern in the Z-disc. In addition, in all available actomyosin structures solved so far, F-actin is fully decorated with single myosin heads in order to obtain a high-resolution averaged structure. This is, however, not the situation inside a sarcomere (Goody et al., 1985). Which actin subunits are bound by myosin remained an intriguing question, considering the helical mismatch of the thick and thin filaments. Moreover, both myosin heads are required for maximum force generation (Tyska et al., 1999). As the crystal structure of single-head myosin does not allow simultaneous binding of both heads to the thin filament while connected by the S2 domain (Rayment et al., 1993a), the structural basis of the double-head myosin is another mystery.

Finally, the structure of some proteins can only be determined in their native environment, i.e., in complex with their natural binding partners. Nebulin and titin are two examples illustrating the limitations of classical structural approaches. Due to their large sizes and inherent flexible nature, isolated structures of the two proteins are not representative of their native state. Nebulin is especially “nebulous”, as the majority of the protein does not fold into known domains. Isolated full-length nebulin appeared as dense particles in rotary-shadowed images, indicating an aggregated form (Chitose et al., 2010). *In vitro* reconstitution of a complex of F-

actin with nebulin fragments is also challenging as a single nebulin repeat has low affinity towards actin (Pfuhl et al., 1996), whereas multiple nebulin repeats cause bundling of F-actin (Gonsior et al., 1998). As a result, the attempt of reconstitution using a 4-repeat nebulin fragment could not reveal a structure of nebulin, but only proposed three binding sites on actin (Lukoyanova et al., 2002).

A promising approach to overcome the aforementioned limitations and visualise a native sarcomere at a high resolution is to combine cryo-ET (section 2.3.3) with recently developed cryo-focused ion beam milling (cryo-FIB-milling) (section 2.3.4). Adapted from the material science field, cryo-FIB-milling has been shown to be capable of producing thin lamellae from frozen biological samples with minimal artefacts (Marko et al., 2007; Schaffer et al., 2017).

2.3 Electron cryo-tomography (cryo-ET)

2.3.1 Transmission electron microscopy (TEM) and scanning electron microscopy (SEM)

Electron microscopy is a powerful tool to image biological material at high resolution. There are two main types of electron microscopy: transmission electron microscopy (TEM) and scanning electron microscopy (SEM). Both approaches use a beam of accelerated electrons to interact with the specimen and create images. In TEM, the electron beam transmits through the specimen to create an image of its internal structure while in SEM, the electron beam scans the surface of the specimen to portray the surface topology. In this thesis, both TEM and SEM were employed in a workflow of cryo-FIB-ET. TEM was utilised to acquire tomographic data of the sarcomere (section 2.3.3). SEM was used during cryo-FIB-milling to localise the sites for producing lamellae and monitor the process of milling (section 2.3.4).

The composition of both types of microscopes includes an electron source, a series of lenses and apertures, and detectors in a vacuum environment (Fig. 2.13). In TEM, electrons are accelerated to 120-300 keV after being released from tungsten filament or lanthanum hexaboride crystals or extracted from a sharp tip by an electric field in a field emission gun (FEG) (Williams and Carter, 2009). The electron beam passes through stacks of electromagnetic lenses which focus the beam through magnetic fields. The column of a TEM contains three main lens systems: a condenser lens system that focuses the beam onto the specimen, an objective lens system where the image of the specimen is formed and initially magnified, and a projector lens system that further magnifies the image (Fig. 2.13A). Each lens system also includes deflectors for centring the beam along the optical axis, stigmators for compensating asymmetries in the lens magnetic field, and an aperture for removing off-axis electrons and generating amplitude contrast (Williams and Carter, 2009).

The interaction of electrons with the specimen can be described by elastic or inelastic scattering processes dependent on whether the kinetic energy of the electrons is conserved or reduced, respectively. In TEM, image contrast can be attributed to two different mechanisms: the amplitude- and the phase-contrast formation. The amplitude contrast is formed by the removal of inelastically scattered electrons (removed by an energy filter) or elastically scattered electrons with high scattering angles (removed by the objective aperture) when hitting a dense object. The phase contrast is formed by the interference of the elastic scattered electron wave,

which has a different phase, with the unscattered electron wave. A biological specimen itself can only modulate the phase weakly. Therefore, a defocus of a few micrometres is often applied when imaging frozen biological material in order to increase the contrast at a cost of adding certain distortion to the acquired image (details in section 2.3.2). Alternatively, multiple types of phase plates have been developed to increase the phase difference ideally by 90° between scattered and unscattered electron waves and thereby the contrast (Danev and Nagayama, 2001; Danev et al., 2014). However, using a phase plate is still practically challenging for obtaining high-resolution structures at the moment (reviewed in (Wang and Fan, 2019)). The electrons reaching the bottom of the microscope are eventually detected by a camera. High-end detectors also include an energy filter that removes inelastically scattered electrons to enhance the amplitude contrast.

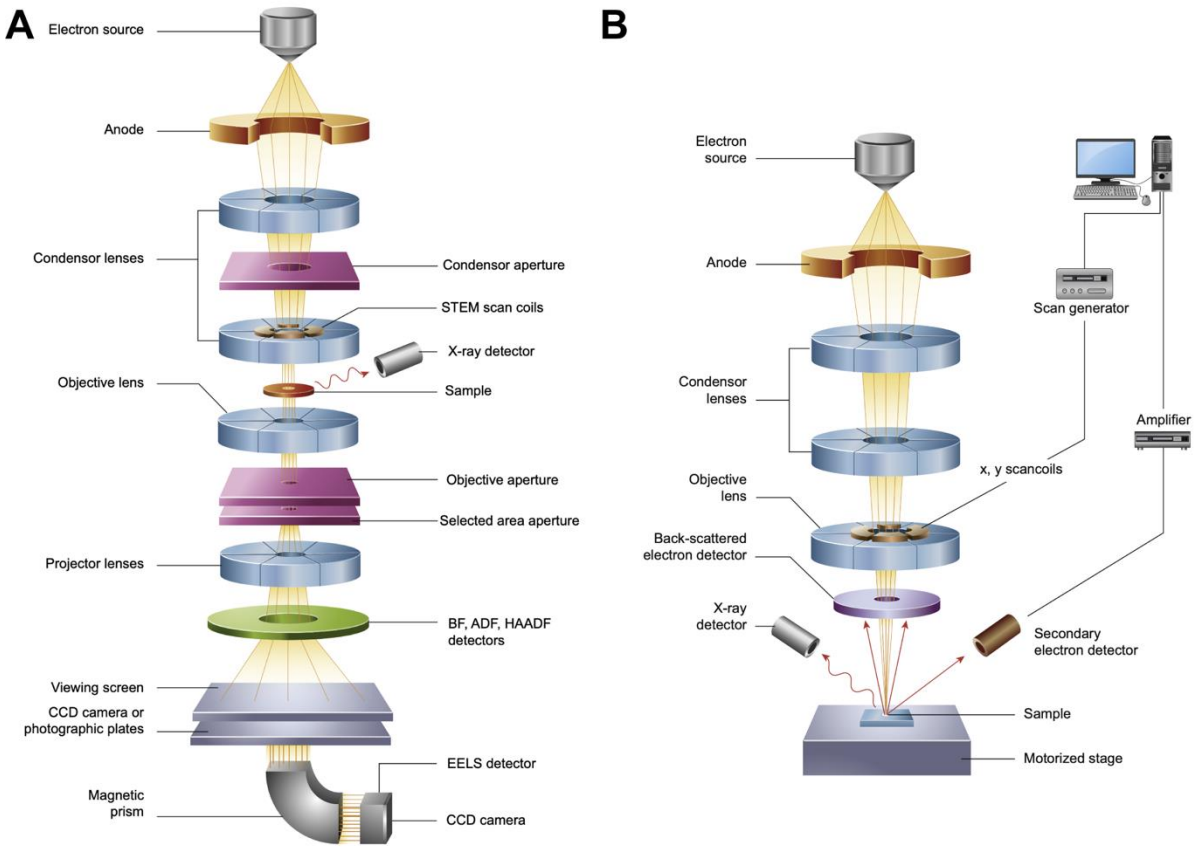

Fig. 2.13 Schematic diagrams of a TEM and an SEM

*Schematic diagrams depicting different lens systems, detectors, and sample positions between a TEM (**A**) and an SEM (**B**). Figure reprinted from* (Inkson, 2016) *with permission from Elsevier.*

In SEM, the electron beam is accelerated to up to 30 keV and focused by the condenser and objective lens system (Goldstein et al., 2003) (Fig. 2.13B). In contrast to TEM, which illuminates the entire field-of-view with a parallel beam with a diameter of a few micrometres, the electron beam of SEM is focused to a small spot with a diameter below 10 nm and raster scans through the field-of-view point by point. The scanning is controlled by deflection coils located in the objective lens system. The SEM electron beam penetrates the specimen to varying depths, called the interaction volume, mainly dependent on its acceleration voltage. The elastic or inelastic interaction between the electrons and the specimen generates various signals including backscattered electrons (BSE), which are primary beam electrons reflected back from the specimen, and secondary electrons (SE), which originate from the specimen upon excitation from the primary beam (Goldstein et al., 2003). Both signals can be measured by different detectors (Fig. 2.13B) for every scanned pixel and used to construct a 2D image computationally. The major contrast when imaging biological specimens is the topographic contrast arising from different numbers of SE detected at different points, as a result of different incidence angles between the beam and the specimen surface. Although SEM has limited magnification and resolution compared to TEM, its unique capability to depict surface shapes makes it an auxiliary imaging tool during cutting samples using a focused-ion-beam in this thesis (section 2.3.4).

2.3.2 Single-particle cryo-EM

Single-particle cryo-EM is a technique of TEM aiming to determine structures of purified proteins. It is also referred to as the single-particle analysis (SPA). While the principles of cryo-EM SPA were established decades ago (Dubochet et al., 1982; Frank, 1975; de Rosier and Klug, 1968), it was until the recent “resolution revolution” (Kühlbrandt, 2014) that cryo-EM SPA started to become a major structural biology technique, which routinely produces structures with global resolutions of better than 4Å. The resolution revolution was driven by the development of fast-readout direct electron detectors, which allowed capturing every image as a movie and thereby made it possible to computationally correct for the movement induced by the electron beam. This hardware improvement also partnered with improved image processing software based on maximum likelihood algorithms (Moriya et al., 2017; Punjani et al., 2017; Scheres, 2012). As cryo-EM SPA does not require protein crystallisation, it has now

become the go-to approach for investigating the structures of large protein complexes, membrane or filamentous proteins.

In SPA, purified proteins are embedded in a thin layer of amorphous ice (Fig. 2.14A,B). To achieve this, firstly, purified protein solution is applied to an EM grid, covered by a thin film of carbon with regular holes. Then, excess liquid is blotted away, leaving only one layer of solution inside the holes. Afterwards, the grid is quickly plunged into liquid ethane or ethane/propane mixture. The speed of the freezing process is so fast that the ice does not form crystals but enters a vitrified state. This allows the proteins to be cryo-fixed in a native conformation where the same hydrogen bond network with water as in solution is kept. The embedded proteins are imaged in a TEM also at cryogenic temperature (<-180°) (Fig. 2.14C). Each image, referred to as a micrograph, contains a number of proteins, referred to as particles, ideally oriented differently (Fig. 2.14D). A cryo-EM dataset typically includes thousands of micrographs, which contain up to millions of particles. These 2D images can be computationally attributed to different views of the protein and used to reconstruct a 3D structure (Fig. 2.14E).

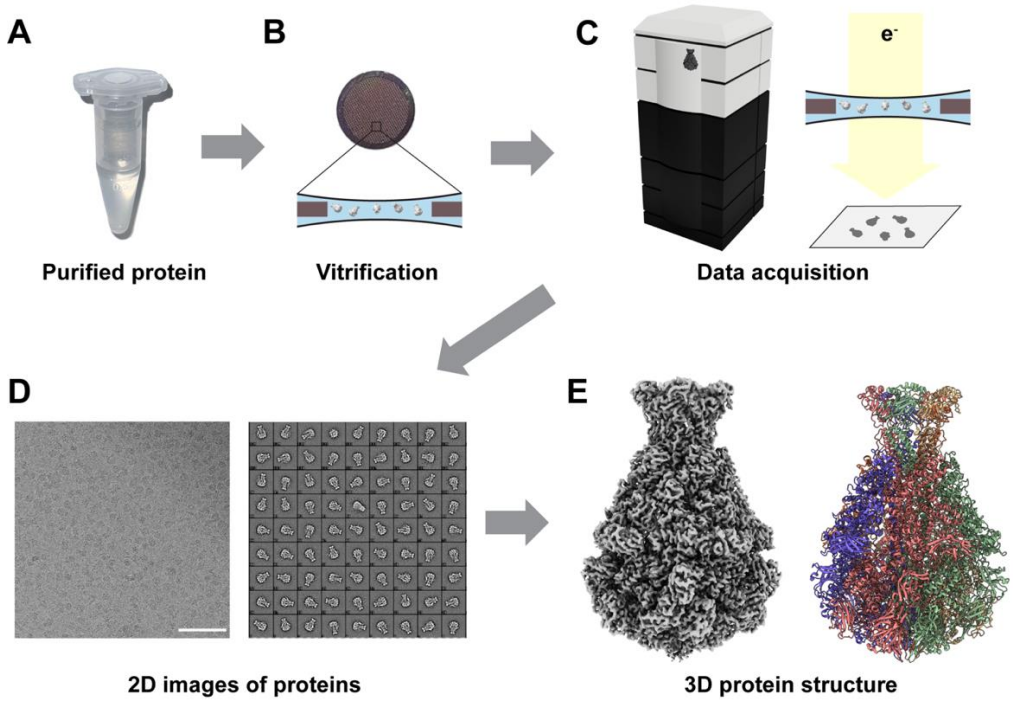

Fig. 2.14 Workflow of single-particle cryo-EM

*(**A-C**) Schematic drawing demonstrating cryo-EM sample preparation and data acquisition. (**D**) A typical micrograph (left) and images of the 2D class averages (right). Scale bar: 100 nm. (**E**) The final EM density map and corresponding structural model of the protein of interest (EMDB-10033, PDB:*

6RW6,). Images of the microscope model in (C) and 2D images in (D) were kindly provided by Dr Sebastian Tacke and Dr Daniel Roderer, respectively.

A typical data processing workflow for SPA starts from motion correction and dose-weighting. The sub-frames within each movie are aligned to remove the motion blur. As high-resolution information is gradually lost during the imaging process upon high radiation damage (Grant and Grigorieff, 2015), the first few sub-frames are weighted more than the rest when creating a final image. Afterwards, the defocus within each image is calculated. The defocus is the major varying parameter that determines the shape of the contrast transfer function (CTF). The CTF describes how the contrast of an image is transferred and modulated by the lens system and strongly depends on lens aberrations and the defocus. Mathematically, the CTF is a sinusoidal curve of the modulation of the contrast versus spatial frequencies. An accurate estimation of defocus allows the CTF to be corrected at spatial frequencies where the contrast is inverted or reduced. The particles in each micrograph are then picked automatically and classified into class averages with higher signal-to-noise ratio (SNR) (Fig. 2.14D). The 2D classification serves as an *in silico* purification that removes false positive proteins. Afterwards, the orientation of each particle is determined by comparing the particle image with the projections of a reference volume. Then a new volume is reconstructed from the particle images based on the orientations and serves as the reference for the next iteration of orientation calculation. This iterative process is referred to as 3D refinement. During 3D refinement, particles are split into two halves, where each half is processed independently of the other half. In the end, two half volumes are reconstructed. The correlation in the Fourier space between the two half volumes at different spatial frequencies, called Fourier Shell Correlation (FSC), is calculated and used to determine the resolution of the final reconstructed map. The heterogeneity within data, such as different conformational states of a protein, can be sorted out with 3D classification. Eventually, the reconstructed map represents the screened Coulomb potential density of a protein, allowing the building of a structural model.

2.3.3 Cryo-ET

Electron cryo-tomography (cryo-ET) aims to obtain the native 3D information of a specific region in a cellular environment instead of purified proteins. In cryo-ET, cells or myofibrils are

cryo-fixed in a vitrified state before imaging through either plunge freezing as in SPA or high-pressure freezing (details in section 4.4.3). At the region of interest, multiple projection images representing different views of the region are acquired (Fig. 2.15). This is achieved by tilting the sample stage to different angles, typically with a range between -60° and 60°, with an increment of 2-3° (Fig. 2.15A). A series of the tilted images, referred to as a tilt series, can be used to computational reconstruct a 3D volume, referred to as a tomogram, using their known orientations (Fig. 2.15B,C).

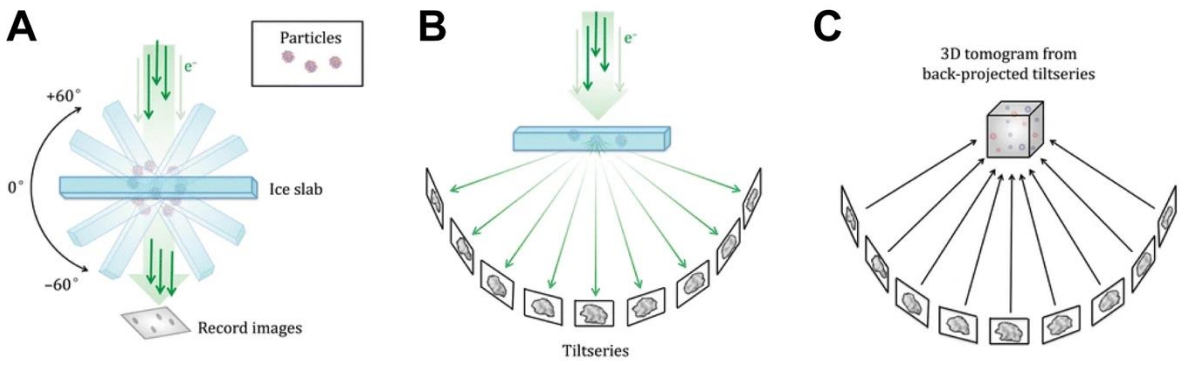

Fig. 2.15 Principle of cryo-ET

*(**A**) In cryo-ET, the sample is tilted to and imaged at different angles. (**B**) A tilt series containing projection images of the sample at different orientations are acquired. (**C**) The images in a tilt series can be back-projected to reconstruct a 3D tomogram. Figure adapted from* (Galaz-Montoya and Ludtke, 2017) *under license CC BY 4.0.*

Since the total number of electrons which can be used for meaningful imaging is limited, cryo-ET has a lower contrast for single images compared to SPA. Cryo-ET requires acquiring 40-60 images on the same position while SPA only needs one. As such, a typical tilt image is illuminated with a dose of ~3 $e^-/Å^2$ while an SPA image is acquired with ~ 60 $e^-/Å^2$. Similar to SPA, the subframes of each image/movie are motion-corrected. However, dose weighting in cryo-ET is not limited within one image, but across the entire tilt series. CTF estimation and correction are also more complex in cryo-ET as the tilted sample has a larger variation in the Z-height. Different positions on a tilted image have different defoci and thereby require different CTF corrections. Therefore, CTF correction in cryo-ET is either strip-based (Xiong et al., 2009), assuming that the height is the same within each strip parallel to the tilt axis, or

more accurately on a per particle basis during sub-tomogram averaging (Tegunov et al., 2021; Turoňová et al., 2017).

Tomogram reconstruction is the key step in processing cryo-ET data. The tilt images are first aligned based on certain fiducial markers in the images. This alignment is used to accurately determine the tilt angle of each tilt image, to correct for shifts between different tilt images, and, if accurate enough, to correct for any magnification change or rotation of the tilt axis. The aligned images are back-projected to generate a tomogram through inverse Radon transform. According to the Fourier slice theorem, each projection image corresponds to a slice in the Fourier space through the origin and perpendicular to the direction of the electron beam. This leads to higher sampling at low spatial frequency compared to high spatial frequency (Fig. 2.16A). Therefore, a filter to reduce the contribution of the low spatial frequency, typically a ramp filter, is applied to the reconstructed tomogram. This is called weighted back-projection. Alternatively, other algorithms such as the simultaneous iterative reconstruction technique (SIRT) (Gilbert, 1972) or the simultaneous algebraic reconstruction technique (SART) (Andersen and Kak, 1984) can be utilised for the final reconstruction. Both SIRT and SART use iterative optimisation to increase the contrast of the final tomogram at a cost of losing high-resolution information (Pyle and Zanetti, 2021).

A tomogram does not cover the entire 3D information of a certain region of interest. The stage typically only tilts between ±60° as limited by its physical proximity to the objective lens and the sample thickness (Fig. 2.16A). As such, certain views are missing, resulting in empty regions in the 3D Fourier space in shapes of wedges. This is thereby called the “missing wedge”. The missing wedge leads to anisotropic resolutions within a tomogram. Specifically, it causes smearing along the Z axis (perpendicular to the tilt axis) (Fig. 2.16B-D). While tomograms suffering from the missing wedge artefacts still can provide valuable information on the overall ultrastructure and the distribution of protein components, the missing wedge artefacts limit the structural information of individual proteins.

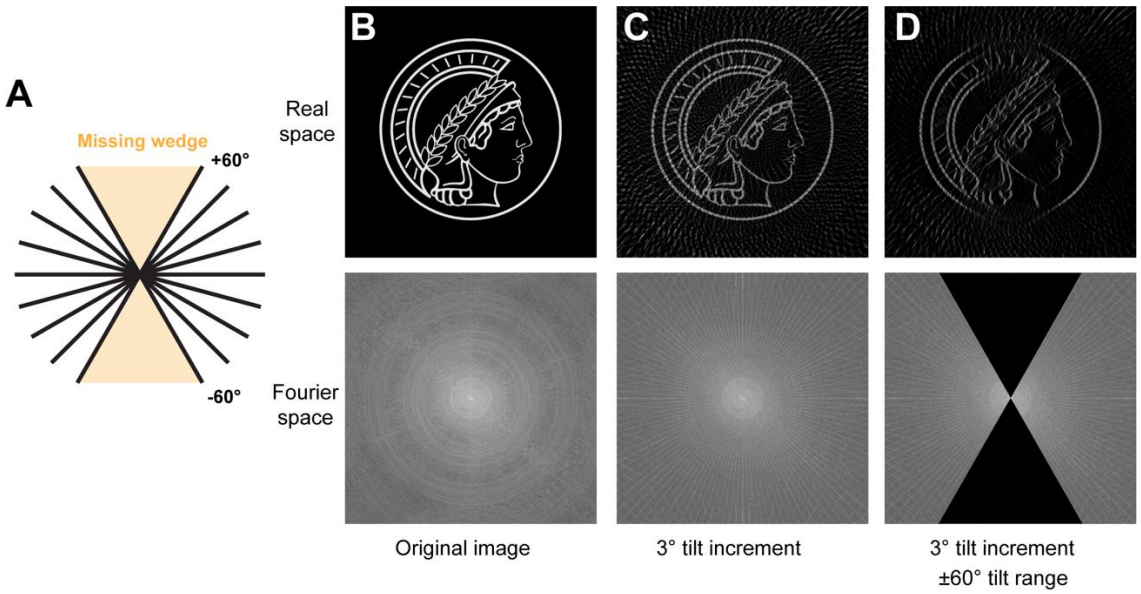

Fig. 2.16 Effect of the missing wedge artefact

*(**A**) Schematic drawing illustrating the cause of the missing wedge. Black lines represent tilt images around a central axis. The orange area is the region with missing information. (**B-D**) Effect of a 3° tilt sampling and the missing wedge simulating the artefacts suffered in the XZ view of a 3D tomogram.*

The artefacts from the missing wedge can be overcome by averaging multiple identical proteins, referred to as sub-tomograms, within tomograms. This approach is called sub-tomogram averaging. The missing information in one sub-tomogram is compensated by other sub-tomograms when they are oriented differently (Fig. 2.17). Sub-tomogram averaging also significantly increases the SNR and thus can reveal high-resolution details of a certain protein. The procedure of sub-tomogram averaging is similar to the iterative 3D refinement in SPA except that every particle now is a 3D volume instead of a 2D image (Fig. 2.17). With the latest development in sub-tomogram averaging software, it is now possible to obtain *in situ* structures of proteins at a resolution comparable to SPA (discussed further in section 4.1).

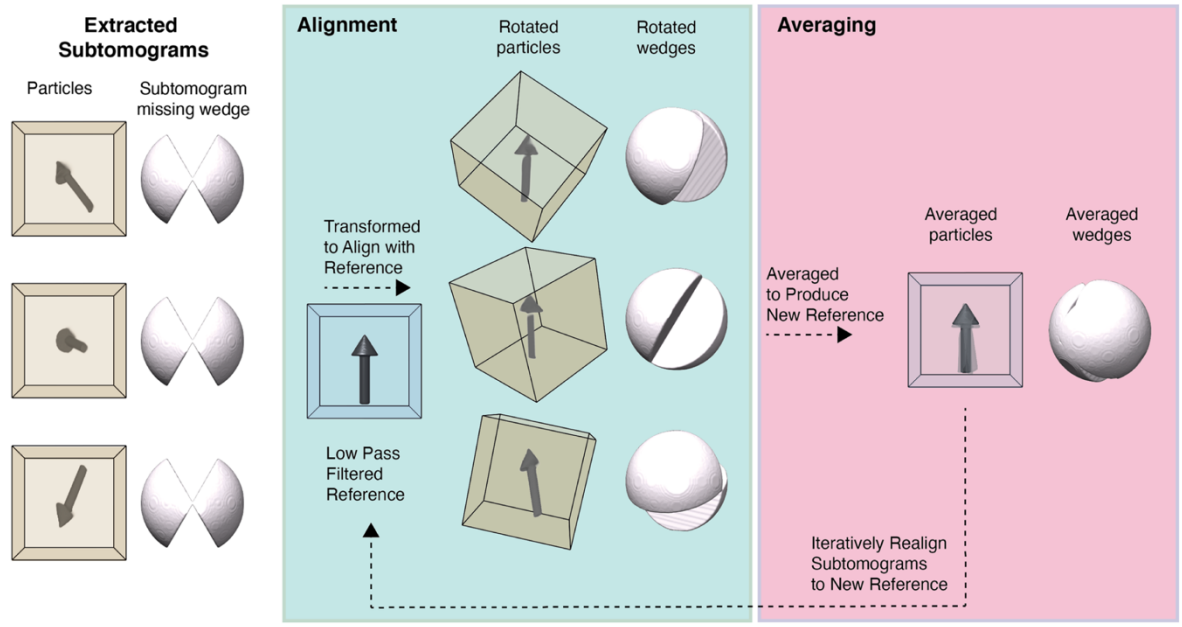

Fig. 2.17 The process of sub-tomogram averaging

During sub-tomogram averaging, sub-tomograms are extracted, aligned and averaged. The volume on the left represents a sub-tomogram in the real space. Its corresponding missing wedge in the Fourier space is depicted on the right. Figure reprinted from (Pyle and Zanetti, 2021) *under license CC BY 4.0.*

2.3.4 Cryo-FIB milling

Most early cryo-ET studies focused on viruses (Grünewald et al., 2003), bacteria cells (Briegel et al., 2006), or small isolated organelles (Nicastro et al., 2000), as these samples are thin enough to be directly imaged by TEM. Investigation of large cellular samples or myofibrils requires sectioning of the sample to a thickness that can be penetrated by a TEM beam (ideally <300 nm). As previously mentioned in section 2.2, mechanical sectioning by ultramicrotome causes a variety of artefacts. A new sectioning technique that almost introduces no artefact is cryo-focused ion beam milling (Cryo-FIB) (Marko et al., 2007). The principle of cryo-FIB is to employ a focused beam of ions (typically Ga ions) at high currents to ablate the material in a defined region. Through the removal of material above and below the region of interest, a thin lamella is produced (Fig. 2.18), which can be later imaged in a TEM using cryo-ET. Although FIB-milling is a mature technique in material science, it has only been recently adapted for processing biological specimens at cryogenic temperatures (Marko et al., 2007; Schaffer et al., 2017). A FIB system works similarly to an SEM which scans the surface of a

specimen. The interaction between FIB and a specimen also produces secondary electrons and ions which can be detected and used for imaging. However, this process is destructive to the specimen. Therefore, a FIB system is integrated into the same chamber as an SEM system and the milled specimen can be imaged by an SEM. In addition, a cryo-FIB/SEM system also involves a gas-injection-system (GIS), which can deposit organometallic platinum for protecting the front of a lamella, and a sputter coater, which allows sputter-coating of conductive platinum to remove charging artefacts (Schaffer et al., 2017).

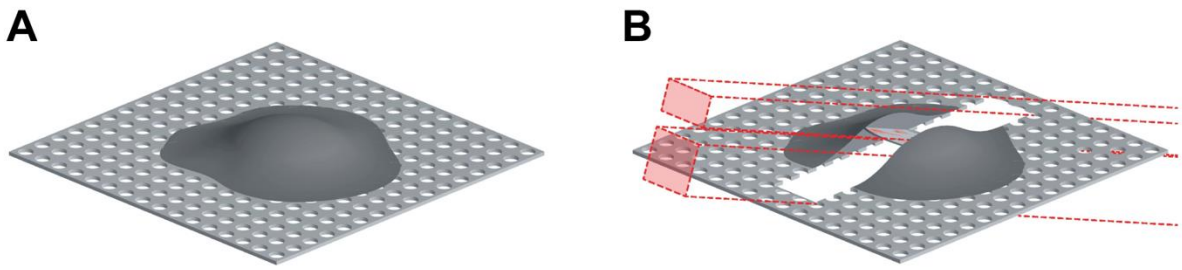

Fig. 2.18 Principle of cryo-focused ion beam milling

Schematic drawing of a frozen cell on an EM grid before (A) and after (B) cryo-FIB milling. The red represents the regions within which an ion beam scans and ablates material. Figure adapted from (Villa et al., 2013) *with permission from Elsevier.*

Lamellae thinner than 200 nm can be reliably produced through cryo-FIB milling. With the development of cryo-FIB, cryo-ET has been successfully employed to visualise a much broader range of biological samples such as mammalian cells (Mahamid et al., 2016), yeast cells (Zachs et al., 2020), and worms (*Caenorhabditis elegans*) (Schaffer et al., 2019).

2.4 Aim of this thesis

Muscle contraction and relaxation is the fundamental activity of a human being. Previous studies on muscle structures lack either high-resolution or *in situ* information, leaving a number of questions still unanswered: Is sarcomere structure a strictly ordered lattice? What is the structural basis of a double-head myosin? How are the thin filaments organised in the I-band to accommodate the hexagonal-to-tetragonal arrangement transition? How does α-actinin cross-link the thin filament in 3D in the Z-disc? What is the native structure of nebulin? How does its mutation cause nemaline myopathy?

To answer these questions, I planned to first implement the cryo-FIB milling and cryo-ET methods for investigating muscle samples using state-of-the-art microscopes. This would grant me access to the structural details of a native muscle sarcomere. A 3D picture of the sarcomere would reveal the organisation and interplay of muscle proteins in different zones. Secondly, I planned to establish a processing workflow of sub-tomogram averaging. This would allow *in situ* structures of muscle proteins to be determined. On the one hand, I aimed to characterise the conformation of muscle myosin with both heads in an active state. On the other hand, I aimed to solve the structure of nebulin, which remained structurally "nebulous" until this thesis. An *in situ* structure of nebulin at high resolution would explain its functions and roles in the disease nemaline myopathy.

Ultimately, the results from this thesis would allow a deeper understanding of muscle organisation and plasticity. The success of this thesis would open a new approach for muscle structure research and pave the way for investigating muscle diseases and ageing.

CHAPTER 3 MATERIALS AND METHODS

3.1. Myofibril preparation

Myofibrils isolated from native source were used throughout this thesis in order to investigate matured sarcomeres that are physiologically functional. As directly obtaining muscle samples from human remains challenging, myofibrils were isolated from mouse (*Mus musculus*) due to their similar genome to human and the common use as an animal model to investigate muscle diseases (van Putten et al., 2020). The myofibrils were isolated and kindly provided by Dr. Ay Lin Kho and Prof Mathias Gautel from King's College London, UK. Skeletal myofibrils and cardiac myofibrils were isolated from psoas major muscle and left ventricular strips of BALB/c mouse, respectively. The details of myofibril isolation protocol can be found in the Method section of the corresponding publications:

Skeletal myofibrils:

Wang, Z., Grange, M., Wagner, T., Kho, A.L., Gautel, M., and Raunser, S. (2021). The molecular basis for sarcomere organization in vertebrate skeletal muscle. *Cell* 184: 2135-2150.e13

Cardiac myofibrils:

Wang, Z., Grange, M., Pospich, S., Wagner, T., Kho, A.L., Gautel, M., and Raunser, S. (2022). Structures from intact myofibrils reveal mechanism of thin filament regulation through nebulin. *Science* 375: eabn1934

Myofibrils were kept in rigor buffers (20 mM HEPES pH7, 140 mM KCl, 2mM $MgCl_2$, 1mM EGTA, 1 mM dithiothreitol (DTT)) and shipped from the Gautel lab on ice. They were then prepared here at MPI Dortmund for cryo-FIB and cryo-ET experiments. Myofibril suspensions can be stored at 4 °C for 2-3 days or at -20°C for several months when 50% glycerol is added to the buffer to prevent the formation of ice crystals. When frozen samples were used for cryo-ET experiment, the buffer needed to be exchanged to remove glycerol. To do this, the suspensions were centrifuged at 3000 xg for 2 minutes to spin down the myofibrils. Then the soft pellet was resuspended in the rigor buffer without glycerol. This process was repeated three times to ensure all glycerol is removed. Typically, due the unavoidable loss of some

myofibrils during the process, half of the initial volume of buffer was used to maintain a similar final concentration of myofibrils. The same protocol was also used to concentrate myofibrils when the concentration is too low for efficient cryo-FIB-milling.

The suitable concentration of the myofibril suspension for cryo-FIB-milling can be determined in different ways. Quantitively, myofibril concentration can be measured based on absorbance at 280 nm using an extinction coefficient of ~0.7 ml mg^{-1} cm^{-1} (Knight and Trinick, 1982). However, this concentration value is not accurate and representative as the suspensions contain different level of aggregations of myofibrils. The concentration can be determined empirically using bright-field light microscopy based on the distribution of myofibrils. Typically, 5 µl of myofibril suspension was added to a glass slide and covered with a coverslip. The myofibrils are visible from even 4 x magnification (Fig. 3.1). Ultimately, the most reliable method to decide a suitable concentration is to screen the myofibrils when frozen on EM grids with the scanning electron microscope (SEM) (see also section 4.1).

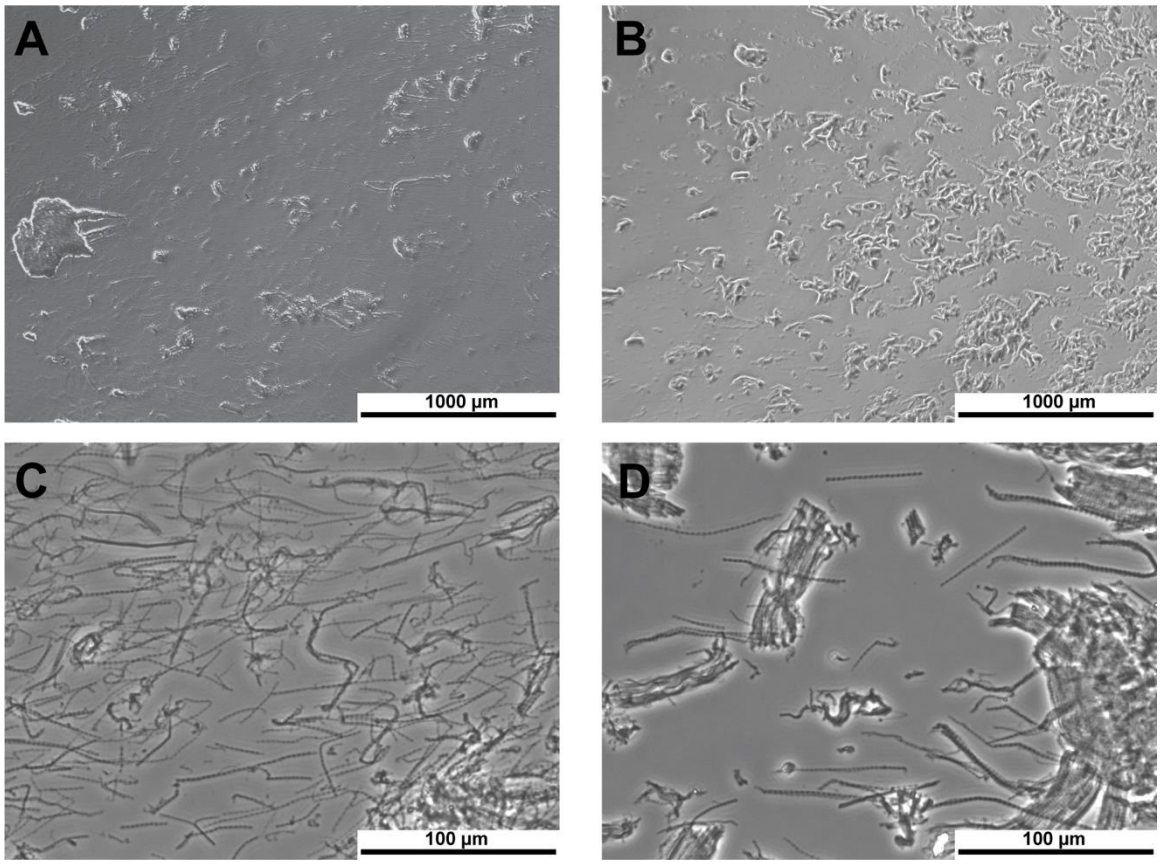

Fig. 3.1 Myofibril suspensions under a bright-field light microscope

*(**A,C**) Mouse psoas muscle myofibrils at 4x (A) and 40x (C) magnification. (**B,D**) Mouse cardiac muscle myofibrils suspension at 4x (B) and 40x (D) magnification.*

3.2. Myofibril vitrification by plunge freezing

Through vitrification, myofibrils are frozen without the formation of crystals which would destroy the structure. Vitrification can be achieved by either plunge freezing or high-pressure freezing. As myofibril bundles are not too thick, plunge freezing is enough to properly vitrify the sample in most situations.

Myofibrils are vitrified on 3-mm-diameter EM grids. For the purpose for cryo-FIB-milling, EM grids with at most mesh 200 (200 squares per inch) should be used to ensure each square is large enough for milling at least one lamella inside. The material of the grid and hole size on the film has little effect while using a SiO_2 film instead of a common carbon film can provide a stronger support that are beneficial for cryo-FIB-milling. Throughout this thesis, different types of grids produced by Quantifoil (Germany) were used and resulted in successful subsequent cryo-FIB-milling (Table 3.1).

Mesh	Grid material	Film material	Hole size/distance (µm)	Rigidity
200	Copper	Carbon	1.2/1.3	More broken film
200	Copper	Carbon	0.6/1	More broken film
200	Gold	SiO_2	1/4	Less broken film
200	Gold	SiO_2	2/2	Less broken film

Table 3.1 Types of EM grids used for cryo-FIB-milling

An EM grid was first glow discharged at 15 mA for 90 s to render its surface hydrophilic and mounted to a pair of tweezers attached to a Vitrobot Mark IV plunger (Thermo Fisher Scientific, USA) (Fig. 3.2). 2 µl of myofibril suspension were applied to the carbon/SiO_2 side of the grid and incubated on grid for 60 s at 13°C with 100% humidity. Excess liquid was blotted for 15-20 s with a blot force of 0. In order to avoid damage to myofibrils due to physical contact of the rough surface of the filter paper, the grid was only blotted from the back side (opposite side from the sample) (Fig. 3.2B). A Teflon sheet was attached instead to the front pad of the Vitrobot. After blotting, the grid was vitrified by rapid plunging into liquid ethane that was cooled by liquid nitrogen to ~185°C (Fig. 3.2C).

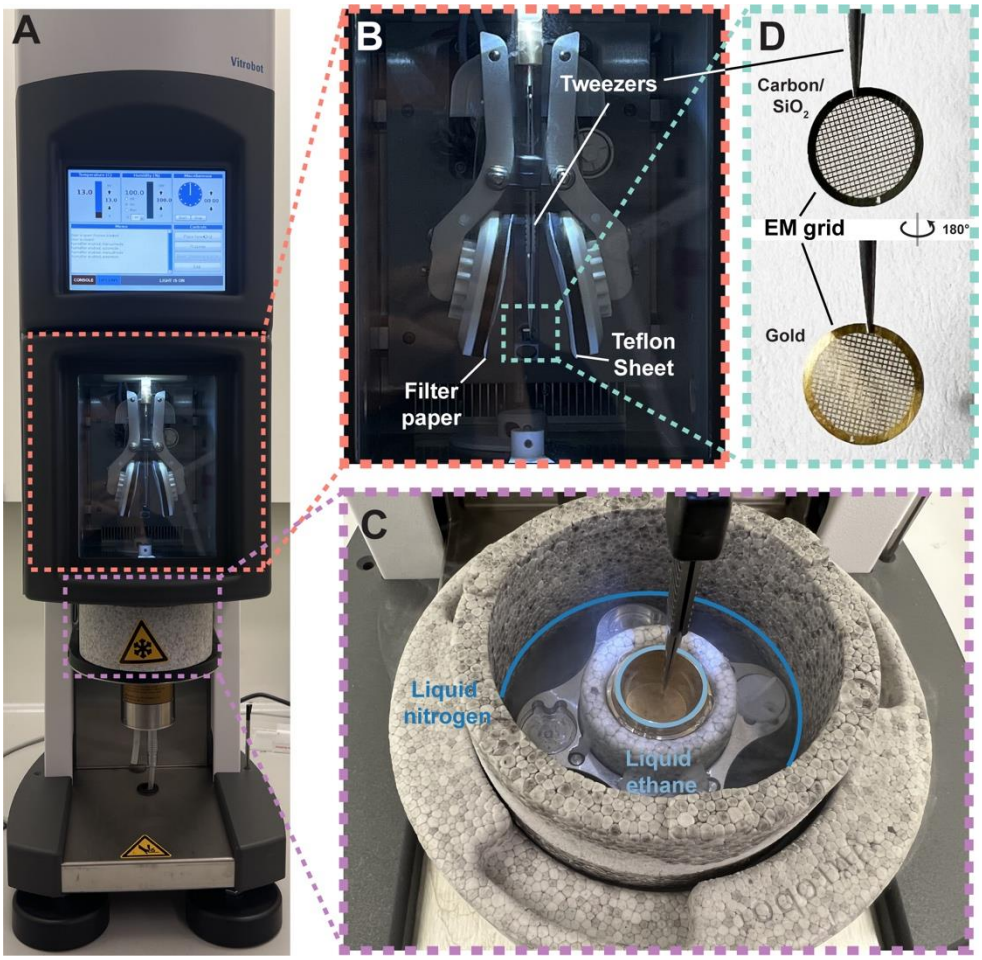

Fig. 3.2 Plunge freezing using a Vitrobot

*(**A**) Image of a Vitrobot with the humidity chamber and cryogen container marked in red and purple, respectively. (**B**) Image of the humidity chamber with the grid on a pair of tweezers marked in green. (**C**) Image of a cryogen container. A grid is plunged into liquid ethane in the centre. Grid boxes are submerged in liquid nitrogen at the periphery. (**D**) Two sides of an EM grid. One side is covered by carbon or SiO_2 film.*

Vitrified grids were clipped into cryo-FIB-specific autogrid rings (Thermo Fischer Scientific) to remain mechanically stable during multiple transfer processes (Fig. 3.3). The autogrid rings are composed of a circular base and a C-ring (Fig. 3.3A,B). A cryo-FIB-specific autogrid base contains a cut-out that allows subsequent milling at a shallow angle and three marks for identifying its orientation. The marks need to be reinforced with a black marker before clipping for better visualisation under liquid nitrogen. During clipping, the carbon/SiO_2 side of the grid that contains myofibrils was facing the base (Fig. 3.3C). The grid was then clipped with a C-

ring on the other side. When loaded into the cryo-FIB-milling shuttle, the cut-out of the clipped autogrids should be facing upside (Fig. 3.3E). Under liquid nitrogen, the cut-out was less visible while the three marks still allowed orientating the clipped gird.

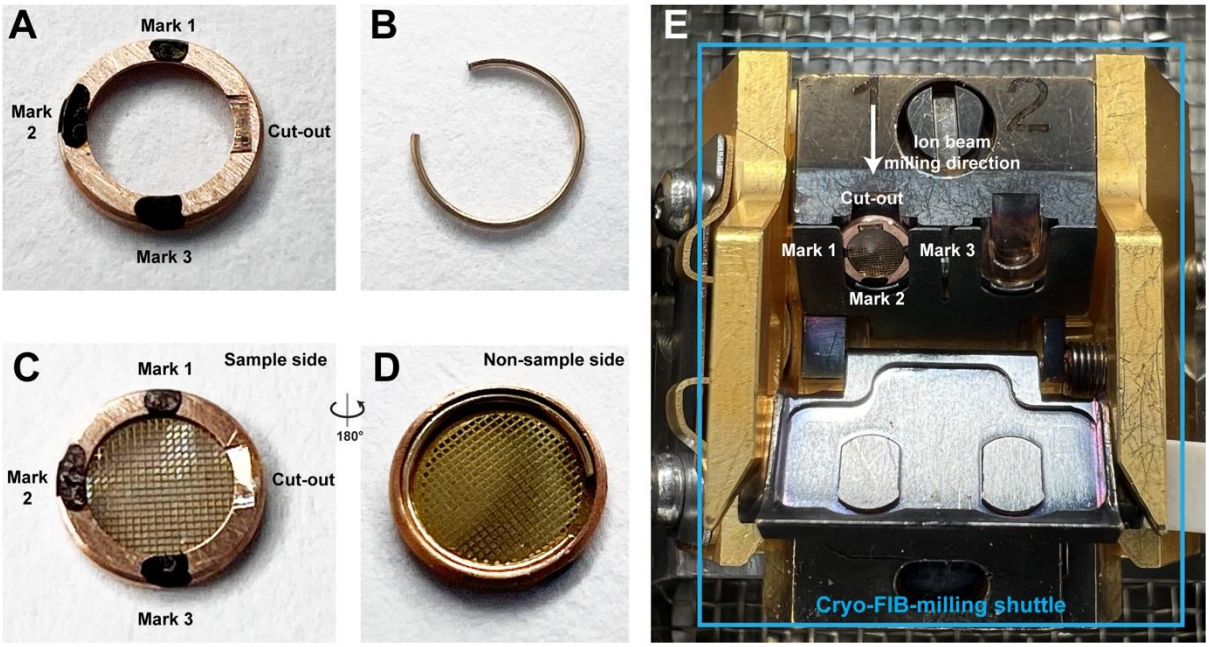

Fig. 3.3 Clipping of grids and loading into cryo-FIB-milling shuttle.

*(**A**) Cryo-FIB-specific autogrid base that contains three marks and a cut-out. (**B**) C-ring of the autogrid. (**C,D**) Front (C) and back (D) side of a clipped autogrid. The sample side of the grid are facing the front side of the autogrid. (E) Loading orientation of the clipped autogrid inside a cryo-FIB-milling shuttle.*

3.3 Cryo-FIB-milling

3.3.1 Transfer into Aquilos

Two clipped autogrids can be loaded into a shuttle at a 45° angle for transferring into a Aquilos cryo-FIB/SEM dual-beam microscope (Thermo Fisher Scientific) (Fig. 3.4A). The shuttle was then picked up by a transfer rod and transferred in a small vacuum chamber (Fig. 3.4B). After the chamber being pumped for 20 s, it was detached from the pumping station and attached to the loading chamber of Aquilos (Fig. 3.4D), where it was pumped again before the shuttle was inserted into the microscope stage through the transfer rod. Before the transfer started, the stage of the Aquilos microscope were cooled down to -190°C. During the transfer process, the grid remained at cryogenic temperature through passive cooling from the cold shuttle. A metal cover of the shuttle and the vacuum chambers prevented the formation of ice contamination. In addition, the use of a zero-humidity glove box that was built in-house by Dr Sebastian Tacke could further reduce potential ice contamination during the transfer process (Tacke et al., 2021) (Fig. 3.4C).

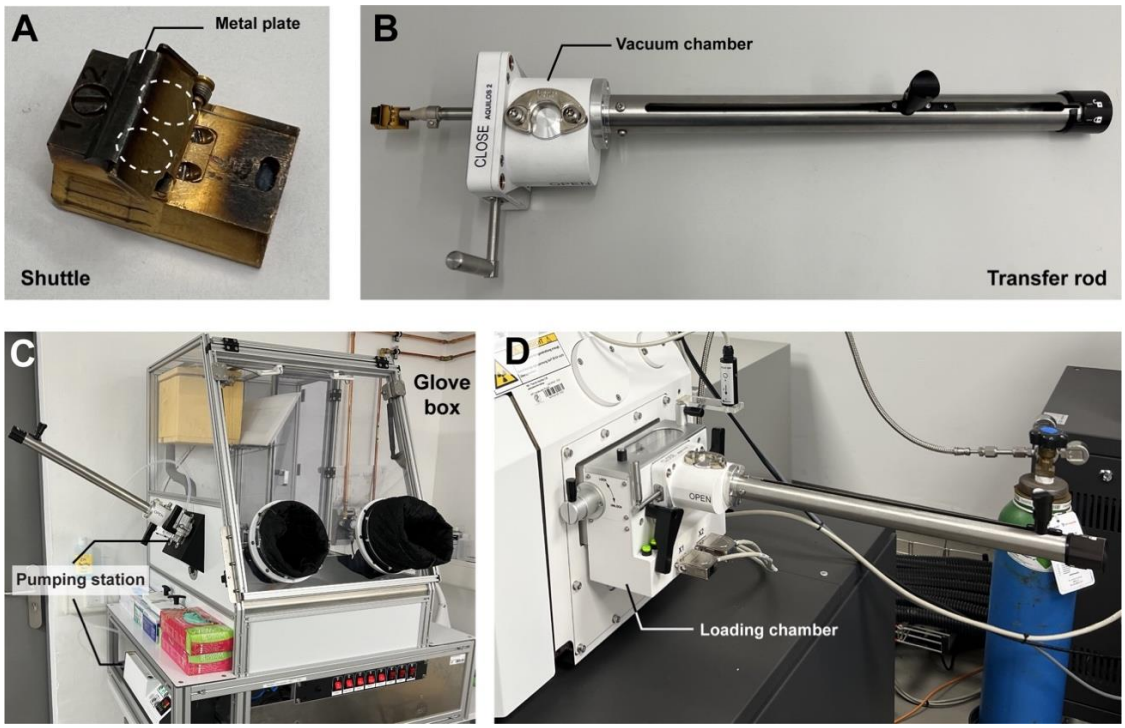

Fig. 3.4 Transfer of a shuttle into a cryo-FIB/SEM

*(**A**) Image of a transfer shuttle containing two grids in positions highlighted in white behind the metal plate. (**B**) Image of a transfer rod with a shuttle attached to the tip. (**C**) Image of a glove box with the transfer rod attached. (**D**) Image of the transfer rod attached to the loading chamber of a cryo-FIB/SEM.*

3.3.2 Preparation for FIB-milling

Inside Aquilos, a gallium ion (Ga^+) beam and an electron (e^-) beam are angled 52° apart, where their incident point is also the eucentric point of the stage. The e^- beam is used for acquiring SEM images to navigate to the milling positions and monitor the milling process while the Ga^+ beam performs actual milling, i.e., ablation of material. To first acquire an SEM image of the entire grid, the stage was moved to the imaging position, where the stage was tilted to 45° to keep the grid horizontal and perpendicular to the e^- beam (Fig. 3.5C). An overview image composed of tiles at 256 x magnification was acquired using MAPS software (Thermo Fisher Scientific) with the e^- beam at 5 kV, 25 pA (Fig. 3.5B). Within MAPS, suitable positions for FIB-milling were selected and marked. Due to the physically obstruction of the clip base, regions close to the side where the Ga^+ beam originates could not be milled and thus should be avoided (Fig. 3.5B). The stage was then tilted to 0° in order to visualise each lamella site from a 45°-tilted perspective to better judge its suitability for FIB-milling (Fig. 3.5D).

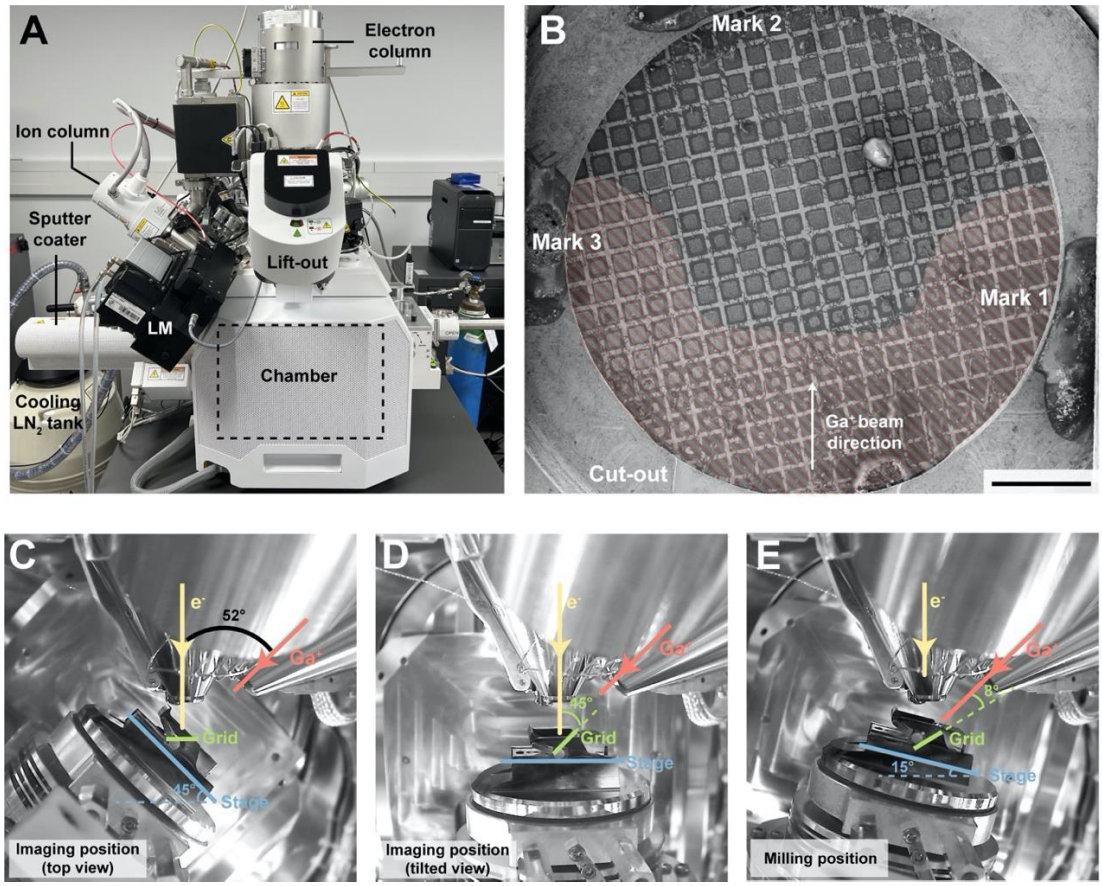

Fig. 3.5 The inside and outside of a cryo-FIB/SEM.

*(**A**) Image of an Aquilos cryo-FIB/SEM. It is also equipped with a lift-out system and a cryo-light microscopy (LM) system that were not used in this thesis. (**B**) Overview image of a clipped grid imaged*

*by SEM. The region that would be obstructed by the clip base during milling is highlighted in red shades. Scale bar: 500 µm. (**C-E**) Different stage positions during imaging from the top (C), imaging at an angle (D), and milling (E). The images of the inside of the Aquilos were taken by a camera mounted at the back of the microscope.*

When a non-conductive material, such as a biological sample, is imaged by an e^- beam, electric charges accumulate on the surface of the specimen. This leads to the so-called "charging artefacts" that deteriorate the quality of acquired SEM images (Fig. 3.6A). To reduce these artefacts, the sample was sputter coated with a layer of conductive platinum with a current of 30 mA for 10 s (Fig. 3.6B). However, in some situations, charging artefacts can be beneficial for identifying myofibrils (Fig. 3.6A) or the determination of thickness during milling (see section 4.1). After sputter coating, an additional layer of metalloorganic platinum was deposited onto the sample through a gas-injection system (GIS, thus the layer is referred as the GIS layer). This served as a protection layer to prevent the surface of the myofibrils from being undesirably damaged by the Ga^+ beam (Fig. 3.6C).

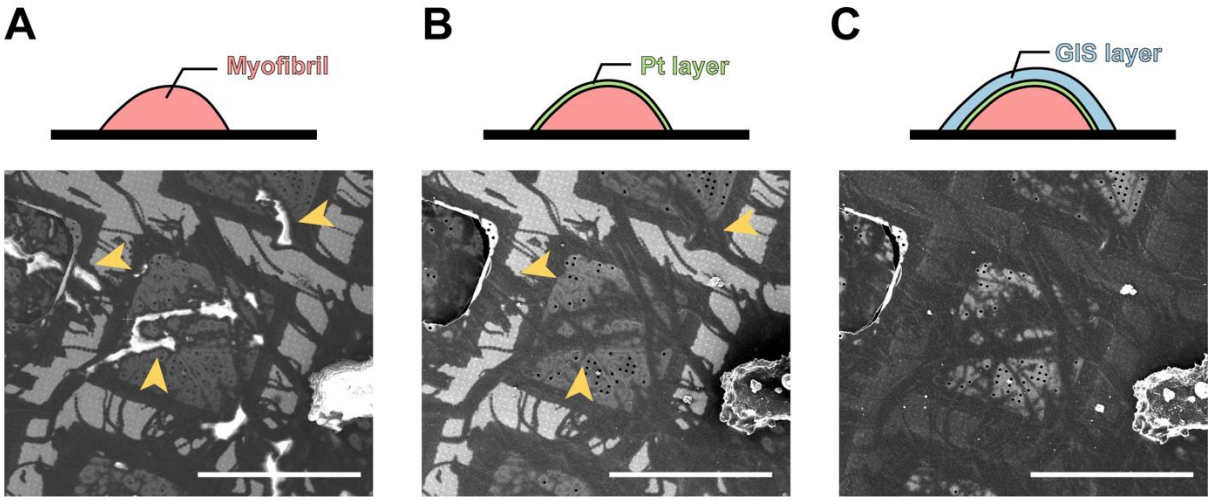

Fig. 3.6 Charging artefacts of frozen myofibrils and the effect of coating.
*Top: Schematic drawings of side views of a frozen myofibril on a grid before coating (**A**), after coating with a Pt layer (**B**), and coating with a GIS layer (**C**). Bottom: SEM images of the top view of myofibrils before coating (**A**), after coating with a Pt layer (**B**), and coating with a GIS layer (**C**). Arrow heads in (A) mark the charging artefacts, which disappear after coating in (B). Scale bar: 100 µm.*

In order to monitor the milling process using the e^- beam, it is essential to ensure that the e^- beam and the Ga^+ beam illuminate the same area. This could be achieved in two ways by determining either the eucentric point or the Ga^+/ e^- beam coincident point at each position. To determine the coincident point between the two beams, a certain feature was first centred using stage XY movement with either beam. Then the feature was brought to the centre with the other beam using stage Z movement. This process was repeated until the feature remained in the centre of the field of view in both beams. Alternatively, the eucentric height could be determined through centring a certain feature at different tilting angles. This could be performed either by manually adjusting the Z height or through calculations in MAPS.

3.3.3 FIB-milling

To perform FIB-milling, the stage was tilted to 13-20° (Fig. 3.5E). At this position, the Ga^+ beam formed an incidence angle of 6-13° relative to the grid. A smaller incident angle often leads to a longer lamella, which provides a larger area for cryo-ET. It also ensures later a small angle between the lamella and the TEM stage later and allows sufficient tilting during cryo-ET data acquisition. The milling process is executed by setting up two rectangular patterns within which the Ga^+ beam scans, one above and the other below the lamella. The lamella was gradually thinned down through decreasing Ga^+ beam current in four steps (Table 3.2) (Fig. 3.7). During the first step, a stress-release pattern (Wolff et al., 2019) was also enabled to reduce the stress built up on the film that would lead to lamella bending (Fig. 3.7C,D). Overtime, up to 50 nm amorphous ice per hour accumulates inside Aquilos on the surface of lamella if no de-contamination method is used (Tacke et al., 2021). Therefore, for each step, all lamellae were milled before proceeding to the next step to prevent too much contamination built up on the lamella. For the same reason, the last step should be finished within an hour. In the final polishing step, the thickness of the lamella was estimated based on the SEM images at either 5 kV or 2kV (see also section 4.1).

	Ga^+ beam voltage	Ga^+ beam current	Thickness of lamella
Step 1	30 kV	500 pA	3 µm
Step 2	30 kV	300 pA	1 µm
Step 3	30 kV	100 pA	500 nm
Step 4 (polishing)	30 kV	50 pA	30-200 nm

Table 3.2 Steps of cryo-FIB-milling.

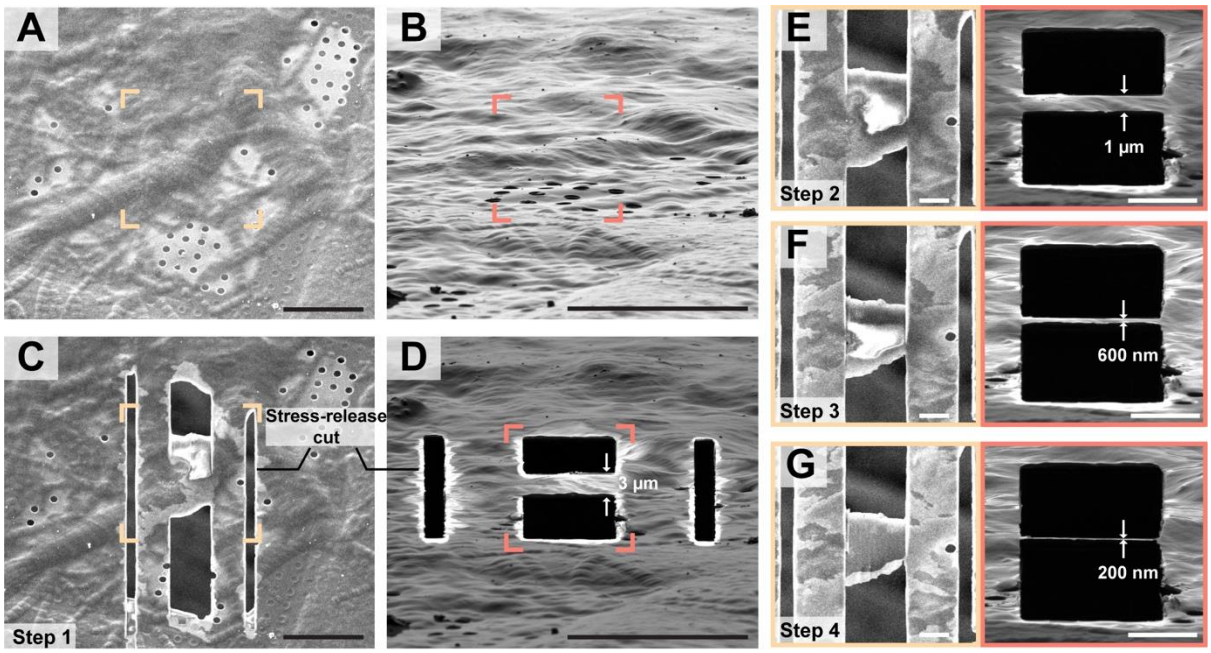

Fig. 3.7 Process of cryo-FIB-milling of a bundle of myofibrils.

*(**A, B**) A bundle of myofibrils before FIB-milling imaged by the electron beam (A) and ion beam (B) and marked in yellow and red, respectively. (**C, D**) The first milling step to open windows and stress-release cuts imaged by the electron (C) and ion beam (D). (E-G) Step-by-step milling process. Left: SEM image. Right: ion beam image.*

Scale bars: 20 µm (A-D), 5 µm (E-G)

3.3.4 Transfer into TEM

Grids containing lamellae after milling were transferred out of Aquilos in the reverse order as the loading procedure. While a glove box was optional during the transfer into Aquilos, it was

necessary when transferring out of Aquilos. The reason is that the lamellae is susceptible to ice contamination. They tend to attract more crystalline ice particles likely due to more charging compared to the rest of the grid. Thus, a zero-humidity environment is critical to prevent losing cryo-ET acquisition area due to contamination. Inside the glove box, the grids were rotated 90° before inserted into a cassette to have the mark 1 or mark 3 pointing upwards. This ensured that later the tilt axis of the TEM stage is perpendicular to the longitudinal axis of the lamella so that during cryo-ET, the tracking/focusing area had the same eucentric height as the acquisition area. Afterwards, the cassette is transferred in a nano-capsule before loaded into a Titan Krios TEM (Thermo Fisher Scientific).

3.4 Cryo-ET data acquisition

The Titan Krios used for this thesis was equipped initially with a K2 Summit direct electron detector and a zero-loss energy filter (Gatan Inc., USA). The camera system was later upgraded to K3 BioQuantum (Gatan Inc.). Different system was employed to acquired different datasets throughout this thesis (Table 3.3). SerialEM software (Mastronarde, 2005) was used to acquire projection images. To localise lamellae under TEM, an overview montage at 175 x magnification was acquired at the beginning of each session (Fig. 3.8A,B). Then, a higher magnification "corner montage" at each lamella position was acquired at 6,300 x or 8,400 x magnification after determining the eucentric height of the lamella automatically in SerialEM (Fig. 3.8C). At this magnification, suitable locations for cryo-ET data acquisition were selected and centred, at which a projection image was acquired and used as a reference image for localisation during batch tomography data acquisition.

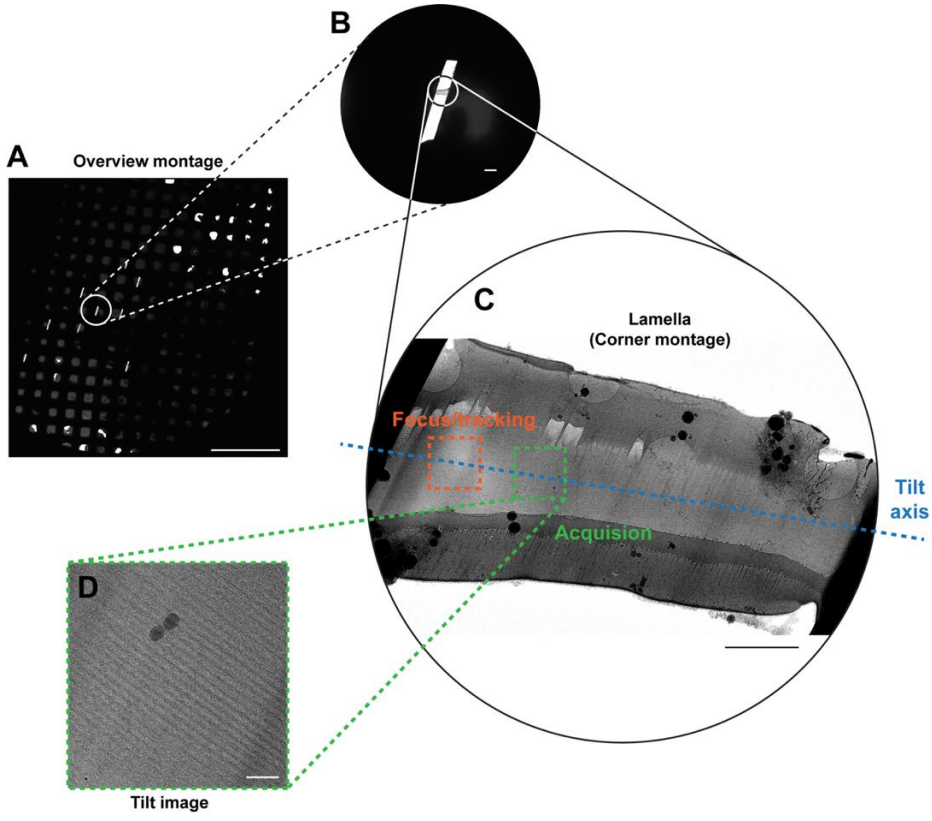

Fig. 3.8 Process of cryo-ET data acquisition

*(**A**) Overview montage of an EM grid after FIB-milling. The white stripes represent the locations of lamellae. (**B**) Zoomed-in view of the inset in (A). (b) Corner montage depicting the overview of the lamella. The tilt axis and one example of the acquisition area and focus/tracking is marked. (b) One*

image of the tilt series acquired from the lamella. Scale bars: 500 µm (A), 10 µm (B), 2µm (C), 100 nm (D).

For each lamella, a pre-tilt angle was determined as the starting angle for data acquisition. As the lamella always forms an angle with the plane of the grid due to the incident angle of the Ga^+ beam during milling, a pre-tilt angle is necessary to ensure that data acquisition starts with 0° with respect to the lamella plane. In theory, the pre-tilt angle could be determined as +incident angle if mark 1 was pointing upwards when loading into the cassette or –incident angle if mark 3 was pointing upwards. However, as in reality the stage and grid itself is often not perfectly flat, a more robust method is to calculate the mid-point angle between a positive high-tilt angle and negative high-tilt angle that show similar brightness and contrast.

Prior to data acquisition, beam illumination was tuned to eliminate objective astigmatism and coma. This was performed automatically in SerialEM based on the thon rings in the power spectrum through the functions "Correct Astigmatism by CTF" and "Coma-free Alignment by CTF". Alternatively, the same aim could be also achieved using AutoCTF (Thermo Fisher Scientific) with the same principle. For this purpose, thin regions at the front of the lamella where the GIS layer is located or at the tail of the lamella where the SiO_2/carbon is present are good positions as they give rise to more thon rings which leads to more accurate calculations. Cryo-ET data were acquired by running a customised SerialEM script (*DS_ultimate.tcl*, Appendix) at every target position through the "Acquired at points" function in SerialEM. Different magnifications and pixel sizes were used for different datasets (Table 3.3). The stage was tilted from -51° to +51° relative to the pre-tilt angle with a 3° increment, using a dose-symmetric tilt scheme (Hagen et al., 2017). At each tilt angle, autofocus and tracking were first performed at a position away from the acquisition area along the tilt axis (Fig. 3.8C). This ensured that the data collected at the acquisition area had consistent defoci and stayed at the same position. Then, each tilt image was recorded with an electron dose of ~3.5 $e^-/Å^2$ that was split into 10 frames, leading to a total dose of around 130 $e^-/Å^2$ per tilt series (Fig. 3.8D).

Datasets	Microscope	Camera	Magnification	Pixel size (Å)	Results
Skeletal muscle A-band	Titan Krios G3	K2	81,000x	1.73	section 4.2, 4.3
Skeletal muscle I-band	Titan Krios G3	K3	81,000x	1.18	section 4.3
Cardiac muscle A-band	Titan Krios G3	K3	42,000x	2.32	section 4.3

Table 3.3 Parameters of different datasets acquired during this thesis.

3.5. Data processing

3.5.1 Pre-processing

Each tilt movie was aligned and averaged into a single tilt image through motion correction. The images within a tilt series were combined into a stack (*.st* file) in the correct order of tilt angles (from – to +) based on the metadata file generated during data acquisition *(.mdoc* file). A file containing the tilt angle information *(.rawtlt* file) was also generated alongside the *.st* file for each tilt series. The pre-processing can be performed in two ways. At early stage of this thesis, a customised script (*serialem2etomo.py*, Appendix) was developed and used. It extracts information from the *.mdoc* file and calls MotionCor2 (Zheng et al., 2017) and EMAN2 (Tang et al., 2007) for motion correction and stacking, respectively. At the later stage of this thesis, Warp software (Tegunov and Cramer, 2019) became available and replaced the customised script for pre-processing. CTF estimation was also involved during pre-processing in Warp that could be used for sub-tomogram averaging later.

3.5.2 Tomogram reconstruction

Stacks of tilt images were reconstructed into 3D tomograms using IMOD package (Kremer et al., 1996). First, the images were roughly aligned based on cross-correlation of the entire images. Images were also 8x binned during this step to speed up calculation and increase accuracy. Then, the alignment is refined based on fiducial models. Here, two approaches were used to generate fiducial models (Fig. 3.9). When there were electron-dense particles (often gold from *in vitro* samples or platinum from lamellae) present in all images, these particles could be used as fiducial markers. Tracing the position of these particles through the tilt series created a fiducial model. Alternatively, each image could be divided into patches and the centre of each patch is considered as a fiducial "marker". These "markers" were tracked by aligning patches from adjacent tilt images. This patch-tracking method can be used universally but only works well when the tomogram is thin (small in Z axis). The comparison of the two approaches is further discussed in section 4.1. Next, an initial downsized tomogram was reconstructed for manually defining the orientation and boundary of the feature-containing slab within the tomogram. A precise determination of these parameters in this step minimises the size of the final volume. Afterwards, a final aligned stack was generated using the refined alignment and

orientation parameters. CTF estimation and correction was performed using *ctfplotter* (Xiong et al., 2009) in IMOD afterwards when the tomogram would be used for sub-tomogram averaging. In the end, a final tomogram was reconstructed from the aligned stack using weighted back projection. Alternatively, the intermediate alignment file from IMOD, namely the <*tomoname*>*.xf* file, could be recognised by Warp and used for generating a tomogram through Warp. However, as Warp does not pick up parameters that are not stored in the *.xf* file such as the tomogram orientation parameters, the tomograms generated in Warp were differently oriented from the ones from IMOD.

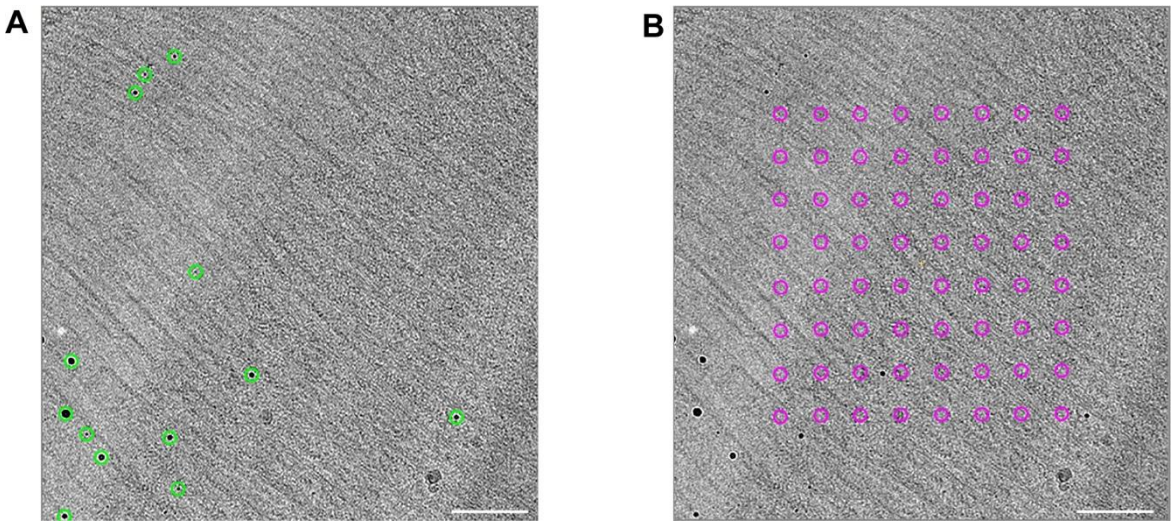

Fig. 3.9 Tilt series alignment by fiducial markers and patch tracking

*(**A**) Fiducial markers in a tilt image, highlighted in green. (**B**) Centres of patches representing the fake "markers" used for alignment.*

Tomogram reconstruction can also be performed automatically using the "Batch Tomograms" function in IMOD, where the same settings are applied to reconstruct all tomograms. However, compared to individual reconstruction, batch reconstruction has certain limitations. As automatic recognition and tracing of fiducial markers was not reliable for markers with varying sizes, only patch tracking could be used in this process. In addition, a number of setting parameters were still missing in the batch mode in the version used for this thesis (version 4.8 or 4.10). Therefore, manual correction and improvement were needed after batch reconstruction to obtain the tomograms at their best quality.

3.5.3 Tomogram segmentation/annotation

Reconstructed tomograms were low-pass filtered, typically to 60 Å or 100 Å, to increase their contrast for better visualisation. This was performed using the *processor* module and *e2proc3d* command in the EMAN2/SPHIRE package (Moriya et al., 2017; Tang et al., 2007). The filtered tomograms were loaded into a 3D visualisation software - Amira (Thermo Fischer Scientific). Segmentation or annotation of a tomogram was performed within Amira manually through selecting the voxels corresponding to the feature of interest. This was carried out on a slice-by-slice basis to produce 2D segmentations that were stacked into 3D volumes. The 3D volumes were rendered for visualisation after surface smoothing within Amira in order to depict distribution of the features. Alternatively the 3D segmentations were exported as binary maps in the *.mrc* format so that structural models could be fit inside using the "Fit in map" function in Chimera/ChimeraX (Goddard et al., 2018; Pettersen et al., 2004). This could be used to illustrate the location and orientation of proteins with known structures such as myosin (see section 4.2).

3.5.4. Sub-tomogram averaging

3.5.4.1 Particle picking

Particle picking is the first step of sub-tomogram averaging to select the X,Y,Z positions of the proteins of interest (particles) within a tomogram. Particles can be picked either manually or automatically. Manual picking was performed in the IMOD package. For single proteins, the centre of each protein was selected on orthogonal or oblique slices. The positions were then saved in *.mod* files, which could be converted to a text file containing the coordinates (typically named as *.coords* files). For filaments, two points marking the start and end of each filament were selected in one "Contour" in IMOD. Each filament can be segmented into a series of particles with the *addModPts* command from the PEET package (Heumann et al., 2011; Nicastro et al., 2006) (Fig. 3.10).

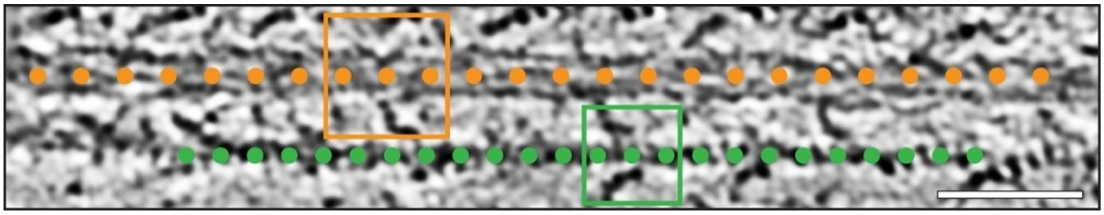

Fig. 3.10 Example of filament picking.

Slice of tomogram depicting a thick and a thin filament in the A-band sarcomere. Yellow and green dots represent the centres of the picked particles. The dimensions of particle boxes of the two types of the filament are represented in coloured squares. Scale bar: 50 nm.

Manual picking is often accurate and reliable. In this thesis, it was used to pick troponin as well as thin filament at the beginning of the thesis to obtain a preliminary structure. However, manual picking is time-consuming and low-throughput. Thus, automatic picking is required for processing large dataset with an objective of reaching high resolutions. Multiple approaches of automatic picking, especially for filaments inside sarcomeres, have been developed in this thesis. The first approach involved first filtering the tomogram with an equator filter, which masks out everything in the Fourier space except for the central line perpendicular to the filament direction, i.e. the equator as termed in fibre diffractions (Fig. 3.11). This filter enhanced the contrast of the filaments and removes any feature that is not in the same direction of the filaments such as the myosin cross-bridges (Fig. 3.11C). As such, in the side view of the tomogram, thin filaments are represented in dots which can be easily recognised. This process of equator filtering was performed in Fiji (Schindelin et al., 2012; Schneider et al., 2012) using a customised script written by Dr Sebastian Tacke. The dots representing the thin filaments in the side views were then traced using the TrackMate plug-in (Tinevez et al., 2017) and used to create the coordinates of the filaments.

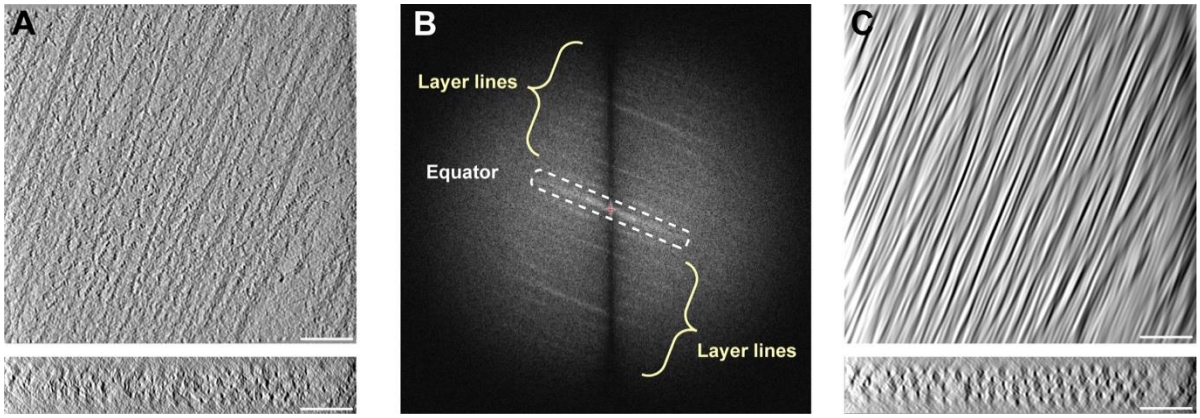

Fig. 3.11 Equator filter for enhancing contrast of the filaments.

(A) *Top (XY) and side (XZ) views of an original tomogram of the sarcomere A-band.* ***(B)*** *Fast Fourier transform of the top image in (A), depicting a line alone the equator and layer lines corresponding to the helical properties of the filaments. The equator filter is marked in the white dotted area.* ***(C)*** *Top (XY) and side (XZ) views of the filtered tomogram in (A).*

The limitation of the first approach is that the TrackMate plug-in can only detect round shapes. Thus, it did not work on filaments with complicated internal features such as the thick filaments. In addition, TrackMate needed manual tuning of parameters for every tomogram and could not be fully automated. Therefore, the second approach was to employ crYOLO (Wagner et al., 2019), a deep-learning based picking software, instead of TrackMate to pick the dots from the side views after equator filtering. Although crYOLO required some manual picking for training in the beginning, the trained model could be applied on multiple tomograms or datasets.

The two aforementioned approaches were designed for picking filaments in the A-band of a sarcomere. However, these approaches were not reliable in the situation where the filaments are not orientated in the same direction, such as in the cytoplasm or the I-band of a sarcomere. Thus, the third approach was developed to pick filaments from the top (XY) views instead of the side (XZ) view. Segments of filaments were picked in 2D slices and traced through the 3D tomogram. This picking strategy has been implemented in the latest version of crYOLO (1.8.0b33) as the tomography-filament mode.

3.5.4.2 Particle extraction and preparation for averaging

Coordinates of the picked filaments were used to extract the sub-tomograms. This could be achieved using either RELION (version 2.0-3.1) (Bharat and Scheres, 2016) or Warp (Tegunov

and Cramer, 2019). In order for subsequent sub-tomogram averaging in RELION, a CTF volume was also required. The CTF volume contained information that was applied during refinement including the missing wedge, dose weighting, and CTF correction (Fig. 3.12). To obtain such CTF volumes, the tomogram itself (*.mrc* file), a stack for the tomogram (*.st* file), a list of tilt angles corresponding to the images in the stack (*.tlt* file), the coordinates of the particles (*.coords* file), and a list of the accumulated dose applied on each tilt image (*.order* file) were required for each tomogram to run the script *relion_prepare_subtomograms.py* and create the volumes. In this thesis, despite the name "CTF volume", it was only used for missing-wedge compensation and dose-weighting but not CTF correction (Fig. 3.12). CTF correction was performed in IMOD during tomogram reconstruction in advance. Alternatively, if Warp was used for pre-processing and particle extraction, a CTF volume for each sub-tomogram would be generated automatically along with the sub-tomograms. The CTF volumes generated from Warp also contained defoci information and used for CTF correction. For RELION-extracted particles, as the last step during tomogram reconstruction in IMOD often applied a rotation around the X-axis (xtilt), the CTF volumes were also rotated accordingly to match the sub-tomograms. In the end, a metadata file (*.star* file) was generated from both methods that could be used later for 3D refinement in RELION. For filamentous particles, the prior Euler angles, ψ and θ, representing their orientations were calculated using a customised script *setpriors.py* (Appendix, see more in section 4.1.5).

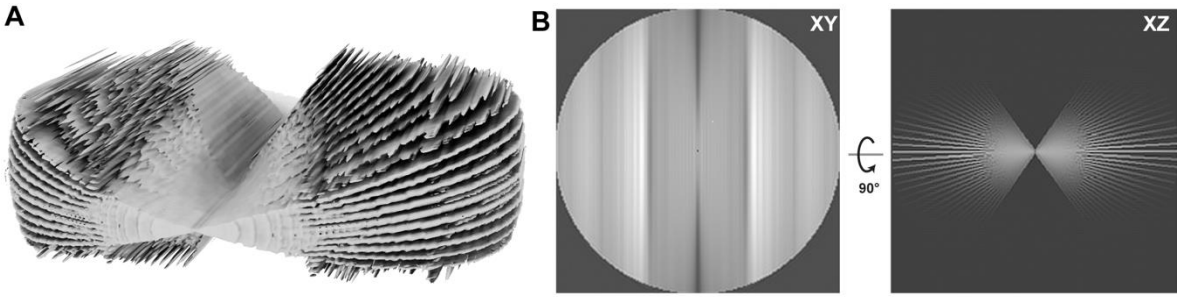

Fig. 3.12 CTF volume for missing-wedge compensation and dose-weighting.
*(**A**) 3D iso-surface view of a CTF volume. (**B**) XY and XZ views of the CTF volume.*

3.5.4.3 *In silico* cleaning by 2D classification

Prior to 3D refinement, it is essential to remove wrongly picked particles by the automatic picking approaches. As 3D classification is time-consuming and inaccurate without refinement, 2D classification is more suitable for the initial cleaning of particles. To generate a 2D image representing the 3D sub-tomogram, a common method is to make projections of the particles along the Z-axis. However, this projection may include unnecessary features, especially when a large box size is used. In this thesis where thin filaments in the sarcomere were picked, neighbouring filaments were also included in a sub-tomogram box (Fig. 3.13A). Therefore, a script *subtomo22d.py* was developed to create projections from only the few central XY slices. As the filaments often appeared tilted in the tomogram, the sub-tomograms were first rotated based on the prior angles calculated so that the filaments are parallel to the XY plane (Fig. 3.13B). The projection images created in this way only contain the filament of interest and better representing the quality of the sub-tomogram. These projection images were then subjected to 2D classification using either RELION or ISAC (Yang et al., 2012) from the SPHIRE package (Moriya et al., 2017). After 2D classification, particles that belong to the classes with high contrast and sharpness were selected as the good particles (Fig. 3.13C).

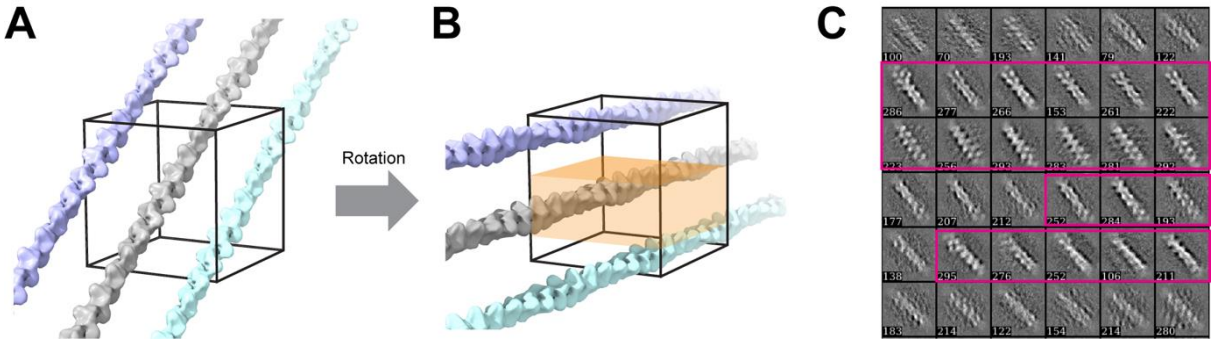

Fig. 3.13 2D classification of the projections of sub-tomogram

*(**A**) Schematic drawing depicting two filaments in addition to the filament-of-interest (grey) in one sub-tomogram. Projection of this sub-tomogram would include all three filaments. (**B**) Filaments are rotated to be parallel to XY plane. The central slices in orange are used for making a projection. This projection image will only contain the central filament (grey). (**C**) Examples of the 2D class averages of the thin filament in the I-band. Classes marked in magenta were selected for further processing.*

3.5.4.4 3D refinement and classification

The good particles were subjected to RELION 3D refinement using a reference. The reference can be either a cylinder or a previous structure filtered to a low resolution. In this thesis, the references were obtained from directly averaging the sub-volumes based on the calculated θ and ψ angles and a random φ angle. This produced a featureless cylinder-like structure with the correct diameter (Fig. 3.14A). 3D refinement in RELION shares the same principle as for single-particle analysis, except that the images are weighted based on the CTF volume. Helical reconstruction was applied when processing the I-band thin filaments but not the A-band thin filaments. The reason was that the I-band thin filaments were not bound by myosin heads and thus lacked surface features for proper alignment. 3D refinement of I-band thin filament without helical reconstruction would lead to an elongated structure suffered from the missing wedge artefacts.

3D refinement was performed in two steps. The first step is a global search of alignment angles (Fig. 3.14A-E). However, as the θ and ψ angles could be calculated, these angles were only refined within a small range while the φ angle were searched in all 360°. One example command for this step is:

relion_refine_mpi --o Refine3D/job013/run --auto_refine --split_random_halves --i particles_all_200box_withpriors_clean.star --ref refs/initial_ref_1.75apix_200box.mrc --firstiter_cc --ini_high 40 --dont_combine_weights_via_disc --no_parallel_disc_io --pool 3 --pad 2 --ctf --ctf_corrected_ref --particle_diameter 340 --flatten_solvent --zero_mask --oversampling 1 --healpix_order 2 --auto_local_healpix_order 4 --offset_range 5 --offset_step 2 --sym C1 --low_resol_join_halves 40 --norm --scale --helix --helical_outer_diameter 300 --ignore_helical_symmetry --sigma_tilt 3.33333 --sigma_psi 2.66667 --j 2

The next step is a local search based on the alignment of the first step (Fig. 3.14F). The structure from the first step was used as the reference. During this step, a mask focused on the desired feature was also applied. One example command for this step is:

relion_refine_mpi --o Refine3D/job013/run --auto_refine --split_random_halves --i Refine3D/job009/run_ct4_data.star --ref Refine3D/job009/run_ct4_class001.mrc --ini_high 15 --dont_combine_weights_via_disc --no_parallel_disc_io --pool 3 --pad 2 --ctf --ctf_corrected_ref --particle_diameter 340 --flatten_solvent --zero_mask --solvent_mask masks/central_actin.mrc --solvent_correct_fsc --oversampling 1 --healpix_order 4 --

auto_local_healpix_order 4 --offset_range 2 --offset_step 2 --sym C1 --low_resol_join_halves 40 --norm --scale --j 2

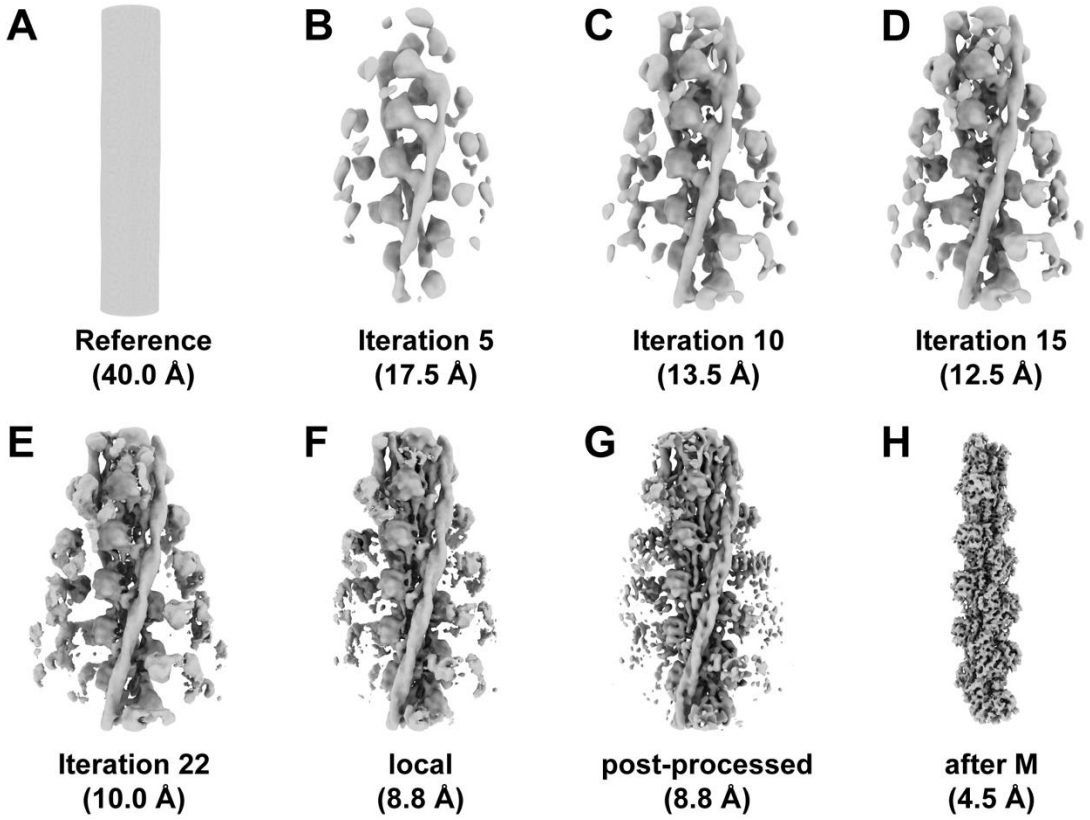

Fig. 3.14 Example of 3D refinement of the A-band thin filament structure using RELION and M. *(**A-E**) Process of global refinement from the first iteration (reference) to the final iteration (iteration 22). (**F**) The structure after local refinement. (**G**) The structure after post-processing using B-factor sharpening. (**H**) The final structure of the core of the thin filament after all refinement steps.*

After 3D refinement, 3D classification was often employed to sort out the heterogeneity within the data. For example, it was employed to separate particles with myosin bound to different positions on the A-band thin filament (section 4.2) and different conformations of myosin (section 4.3). 3D classification was always performed without alignment in this thesis. Depends on the level of detail that needed to be classified, classification was restricted to different resolutions. Different masks were also used to focus classification on different regions. One example command for 3D classification is:

relion_refine_mpi --o Class3D/job019/run --i Refine3D/job001/run_it007_data.star --ref run_it015_half1_bin2_initref.mrc --firstiter_cc --ini_high 30 --

dont_combine_weights_via_disc --no_parallel_disc_io --pool 3 --pad 2 --ctf --ctf_corrected_ref --iter 25 --tau2_fudge 2 --particle_diameter 340 --K 9 --flatten_solvent --zero_mask --strict_highres_exp 30 --skip_align --sym C1 --norm --scale --j 1

In the end, the averaged map is post-processed through B-factor sharpening by boosting the high-resolution signal (Fig. 3.14G).

3.5.4.6 Multi-particle refinement

The resolution of the average can be improved through correcting the errors during tomogram reconstruction (more discussion in section 4.1.6). This was achieved by the multi-particle refinement in M (Tegunov et al., 2021). The two half maps and the metadata file (.*star* file) from the final RELION 3D refinement as well as a tight mask were imported into M. This step also required the metadata files from Warp. If Warp was not used for pre-processing and tomogram reconstruction, these steps needed to be repeated in Warp. In addition, the coordinates of picked particles needed to be converted to match the Warp-reconstructed tomogram coordinate system. Refinement in M generally took 5 iterations. The first three iterations refined particle poses, anisotropic magnification, and stage angles. It also calculated image and volume warping with grids of 4x6 and 8x8x2x10, respectively. The 4th iteration also refined the defoci of the particles in addition to the previous parameters. The last iteration added the refinement of the tilt movie alignment. In the end, the two half maps generated by M were post-processed in RELION (Fig. 3.14H).

CHAPTER 4 RESULTS AND DISCUSSIONS

To achieve the aim of characterising structures of sarcomeres and sarcomeric proteins, I established a cryo-ET-FIB workflow to investigate myofibrils as part of this thesis. The general protocols have been previously described in Methods (Chapter 3). In this chapter, a detailed discussion on the key steps in this workflow and their effects on the quality of the acquired data is presented in section 4.1. With this workflow, I obtained the first high-resolution molecular picture of a sarcomere (section 4.2), describing the overall organisation of filaments and other sarcomeric components. Then I further zoomed in to target *in situ* actomyosin and nebulin on the thin filament by advanced sub-tomogram averaging and characterised multiple structures at sub-nanometre resolutions (section 4.3). In the end, this chapter is completed by a general discussion and future perspective in section 4.4.

4.1 Pushing the resolution limit of cryo-FIB-ET

The resolution of a certain type of protein inside a tomogram can be improved by sub-tomogram averaging as introduced in section 2.3.3. In recent years, sub-tomogram averaging after cryo-ET has shined in resolving *in situ* structures to high resolutions when used for isolated particles, such as viruses, or samples that are thin enough to be imaged without FIB-milling, such as small bacteria or the periphery of mammalian cells (Table 4.1). However, it remains challenging to reach comparable resolutions using cryo-ET for samples after FIB-milling (Table 4.2). In fact, only a handful of structures could be determined from cryo-FIB-milled samples, most of which could not reach sub-nanometre resolutions.

Protein	Resolution	Sample	Citation
apoferritin	2.3 Å	isolated protein	(Tegunov et al., 2021)
HIV-1 capsid-SP1 (spacer peptide 1)	3.0 Å 3.1 Å 3.4 Å 3.9 Å	isolated virus	(Tegunov et al., 2021) (Himes and Zhang, 2018) (Turoňová et al., 2017) (Schur et al., 2016)
ribosome	3.5 Å	bacterial cell	(Tegunov et al., 2021)
S-layer	4.8 Å	bacterial cell	(von Kügelgen et al., 2020)
COPII	4.9 Å	Reconstituted membrane	(Hutchings et al., 2018)

Table 4.1 Recent high-resolution cryo-ET sub-tomogram averaging studies without FIB-milling.

Protein	Resolution	Sample	Citation
orthoreovirus SLP (single-layer particles)	5.6 Å	Viruses inside mammalian cells	(Sutton et al., 2020)
ribosome	11.8 Å	*C. elegans*	(Schaffer et al., 2019)
LRRK2 (leucine-rich repeat kinase 2)	14 Å	mammalian cell	(Pöge et al., 2021)
phycobilisome	15.6 Å	red algae cell	(Li et al., 2021)
thin filament (actin, tropomyosin)	15.7 Å	mammalian cell	(Burbaum et al., 2021)

Table 4.2 Recent cryo-ET sub-tomogram averaging studies after FIB-milling.

There are three major obstacles for reaching a high resolution after cryo-FIB-ET. First, the lamellae after milling (typically 150-200 nm) are much thicker compared to the ice embedding isolated proteins (20-100 nm) and often contain more crowded protein contents. This leads to an overall lower SNR in the data after FIB-milling. Second, cryo-FIB-milling is still an emerging technique. Thus, a limited amount of data can be produced in most facilities

worldwide due to the limited throughput and success rates. Last but not least, the lack of gold fiducial markers for precise alignment during tomogram reconstruction reduces the quality of the sub-tomograms. Therefore, until this thesis, the only structure with sub-nanometre resolution after FIB-milling was from viral proteins in infected cells (Sutton et al., 2020), as the high copy of the viral proteins in each virus helps compensate for the aforementioned obstacles.

In this section, I will present the key steps in the cryo-FIB-ET workflow that are essential to obtaining a high-resolution structure with sub-tomogram averaging. With these crucial steps, a structure of the thin filament containing actin and nebulin resolved to 4.5 Å could be obtained, details of which will be shown in section 4.3, where the biological implications are discussed.

4.1.1 Obtaining the best ice from plunge freezing

The quality of the tomographic data is reduced when vitrification is not complete during plunge freezing (Fig. 4.1). The principle of plunge freezing is to cool down the sample so fast that the water within the sample enters an amorphous vitrified state before it can form ice crystals. However, plunge freezing has a limited freeze rate. It is only possible to completely vitrify pure water thinner than 1 µm through plunge freezing (Dubochet, 2007). Biological specimens such as myofibrils or cells up to a few micrometres thick can be vitrified thanks to the high soluble content. Incomplete vitrification leads to the formation of ice crystals. The diffraction of the electron beam by these crystals results in black and white artefacts in the acquired images (Fig. 4.1D). These artefacts will reduce the quality of acquired cryo-ET data and later hinders tomogram reconstruction (Fig. 4.1C). In the worst situation where large ice crystals are formed, cellular organisations are disrupted and protein structures are destroyed (Fig. 4.1B).

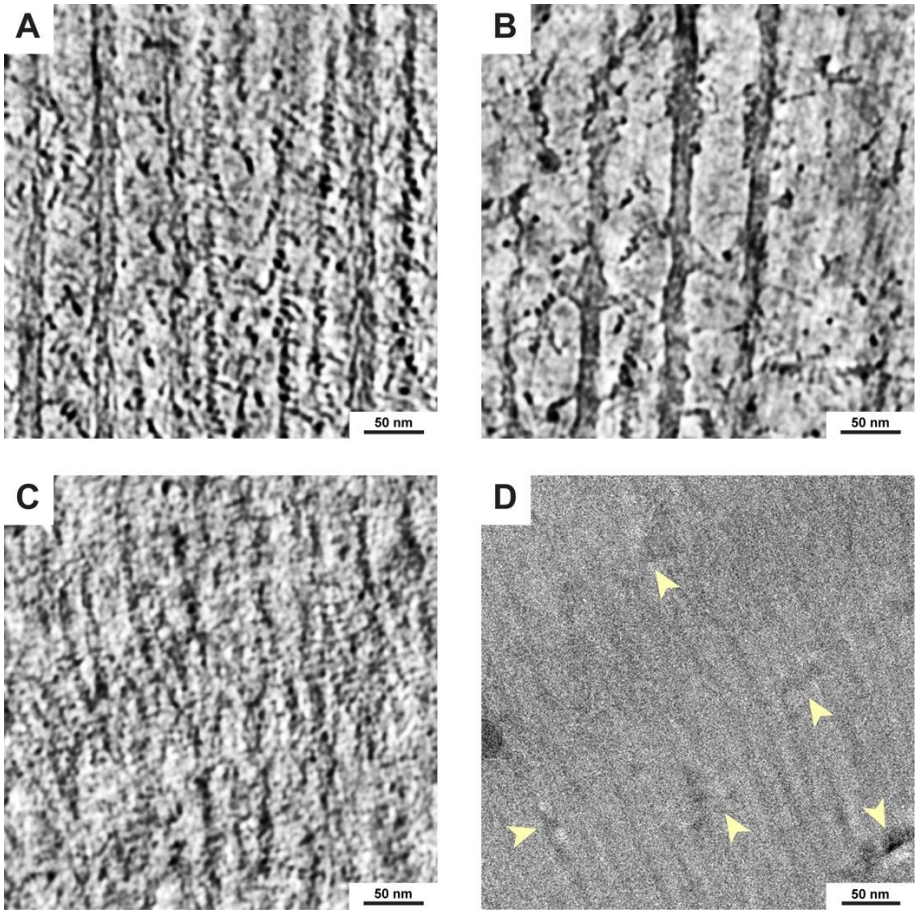

Fig. 4.1 Effect of incomplete vitrification

*(**A**) Slice image of a complete vitrified sarcomere A-band. (**B**) Slice image of a barely vitrified sarcomere A-band. Internal structures were destroyed by ice crystals. (**C**) Slice image of an incompletely vitrified sarcomere I-band. (**D**) A tilt image used to reconstruct the tomogram in (**C**). Black/white artefacts caused by ice crystals are marked by the arrowheads.*

In SPA cryo-EM, good vitrification is achieved by obtaining a thin layer of ice that embeds the proteins (Fig. 4.2A). This can be directly controlled by tuning the blotting time and force during plunge freezing. The situation for freezing FIB-milling samples is more complicated. Cellular specimens such as a bundle of myofibrils retain a layer of water around their shapes (Fig. 4.2A), so the total thickness that needs to be vitrified is the sample itself plus the water layer. While it is not feasible to change the inherent thickness of the specimen, we can ensure only a single layer of the specimen on the grid and minimise the layer of water around the specimen. Therefore, to achieve good vitrification for a FIB-milling sample, both blotting parameters and the sample concentration should be optimised when preparing EM grids.

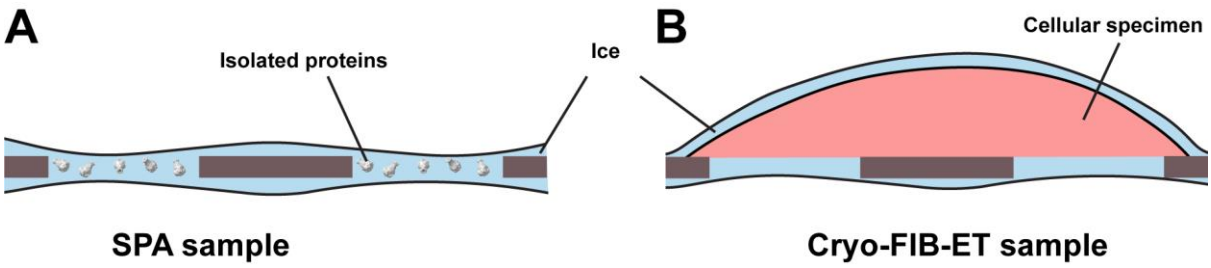

Fig. 4.2 Difference between an SPA grid and a cryo-FIB-ET grid

*(**A**) Schematic drawing of an SPA grid with proteins embedded in a layer of ice. (**B**) Schematic drawing of a cryo-FIB-ET grid depicting the frozen cellular specimen retaining a layer of water around it.*

To minimise the water around the specimens, the grid should be blotted as dry as possible. Typically, 15s blot time with a blot force of 5 is enough. Under such conditions, normal carbon film on an EM grid is likely to have many broken sites. Therefore, a more robust SiO_2 film is preferred to withstand harsh blotting. To prevent multiple layers of specimens, the concentration should be low enough to have sparsely distributed myofibrils/cells. At the same time, the concentration cannot be too low as otherwise the throughput of each FIB-milling session is limited by the available milling sites. As a reference, suitable concentrations for different types of samples are summarised in Table 4.3. However, as the samples are often suspensions with different extent of aggregation, these values only serve as a starting point and the right concentration should always be optimised for each batch of the sample.

Biological sample	Concentration
Myofibrils	5 mg/ml
Yeast cells	OD 0.6
Bacterial cells	OD 20

Table 4.3 Suitable concentrations of different biological specimens for FIB milling.

The most reliable method of accessing specimen concentration as well as grid dryness is through SEM imaging. One should be mindful that ice is formed on both sides of the grid. The ice on the front side can be easily judged from SEM images. As it is not possible to flip a grid during a cryo-FIB session, the ice on the back side can be only determined by the presence of empty holes on the holey film and a round edge within a grid square (Fig. 4.3A). Empty holes are a sign of very thin ice on both sides of the grid. The round edge depicts where the ice starts

to become thick and forms a ramp towards the grid bars on the backside (Fig. 4.3B). Ice on the backside not only reduces the freezing efficiency, but also increases the difficulty of producing lamellae that are close to the grid bars. The optimal ice condition should render a thin layer of ice only around the biological specimens but nowhere else, especially on the backside (Fig. 4.3 green area).

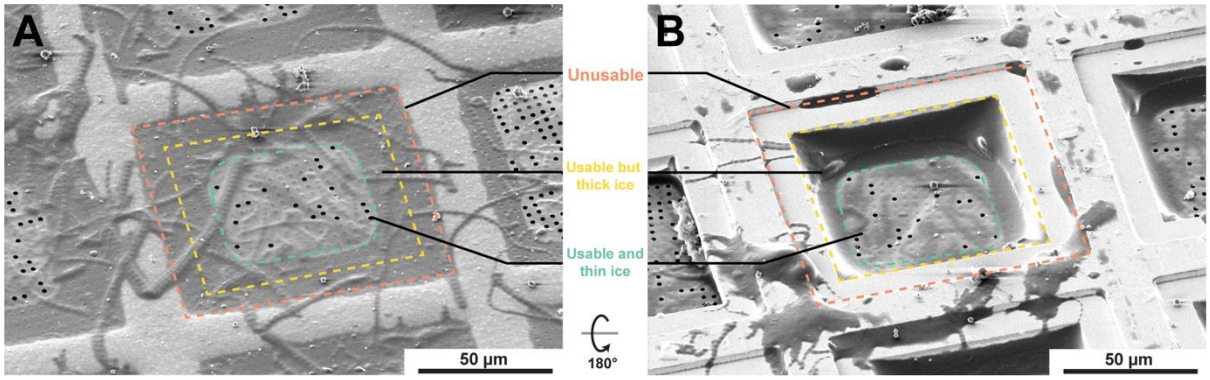

Fig. 4.3 The two sides of a grid containing frozen myofibrils.
*(**A**) SEM image of the front side of a grid used in this thesis. Different area has different suitability for milling. (**B**) The back side of the same grid square as (A). This image usually cannot be obtained as most cryo-FIB/SEM does not allow flipping the grid within its chamber.*

4.1.2 Preparing thin lamella using cryo-FIB

Not only thin ice is desired for proper vitrification, thin lamellae are also essential for achieving good contrast of tomograms. A thick lamella will reduce the quality of tomograms in two aspects: First, more inelastic scattering of the electron beam through the sample leads to a low SNR in the acquired images. Although the use of an energy filter in modern TEMs has reduced noise from inelastically scattered electrons, the features inside a tomogram are still more obscure in thicker samples (Fig. 4.4). Second, a thick sample contains multiple layers of features, which can cause problems in data processing. When using patch tracking to reconstruct a tomogram, features from different layers may dominate the same patch at different tilt angles. This will thereby lead to inaccurate alignment.

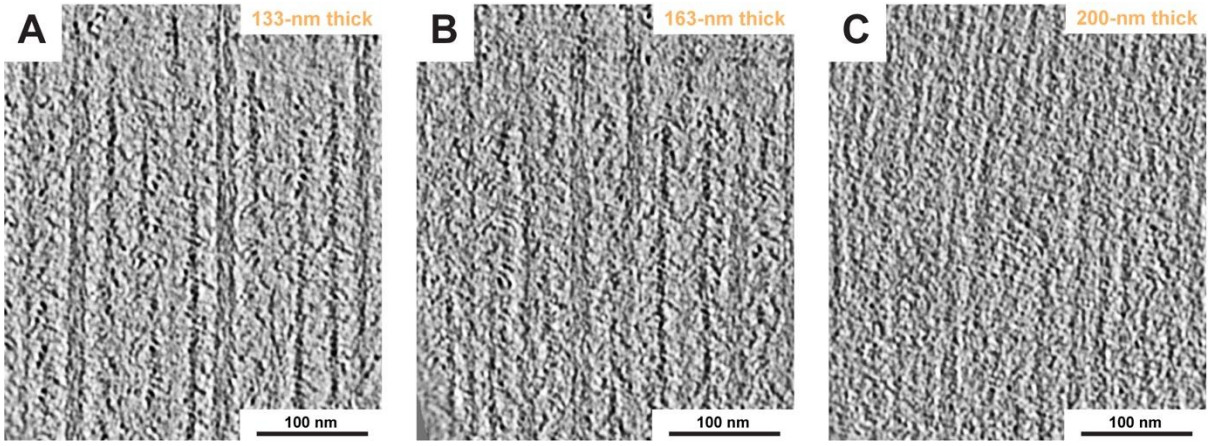

Fig. 4.4 Effect of lamella thickness on the SNR of a tomogram.

*Slices of tomograms depicting the A-band of a sarcomere with thicknesses of 133 nm (**A**), 163 nm (**B**), and 200 nm (**C**).*

In order to produce a thin lamella, the final polishing in a four-step milling procedure is the key. In the first three rough milling steps, two rectangle patterns are typically used, as described in section 3.3.3. In the final polishing, however, different strategies can be used to mill the lamella as thin as possible. The first strategy is the same as used for rough milling, which is through milling in two rectangular patterns (Fig. 4.5A). The spacing between two patterns is reduced gradually to ideally mill the lamella thinner and thinner. The second strategy is to use a single "cleaning cross-section pattern" that covers the lamella and enables milling line by line from top to bottom (Fig. 4.5B). This strategy mills very efficiently yet requires the user to monitor the process after milling every one or two lines as it can easily destroy the lamella if not stopped promptly. The problem with both strategies is that they will mill unevenly when lamella starts warping, which is common when the thickness is below 150 nm. Uneven milling will lead to either a thick lamella or a broken one. Therefore, a more universal strategy is to place a single rectangular pattern covering the lamella (Fig. 4.5C). Compared to a single "clean cross-section pattern", the milling is milder and not limited to a straight line. Although it may seem destructive to lamella integrity, the front GIS layer can protect direct damage to the lamella and only allow removal material from the top and bottom of the lamella (Fig. 4.5C).

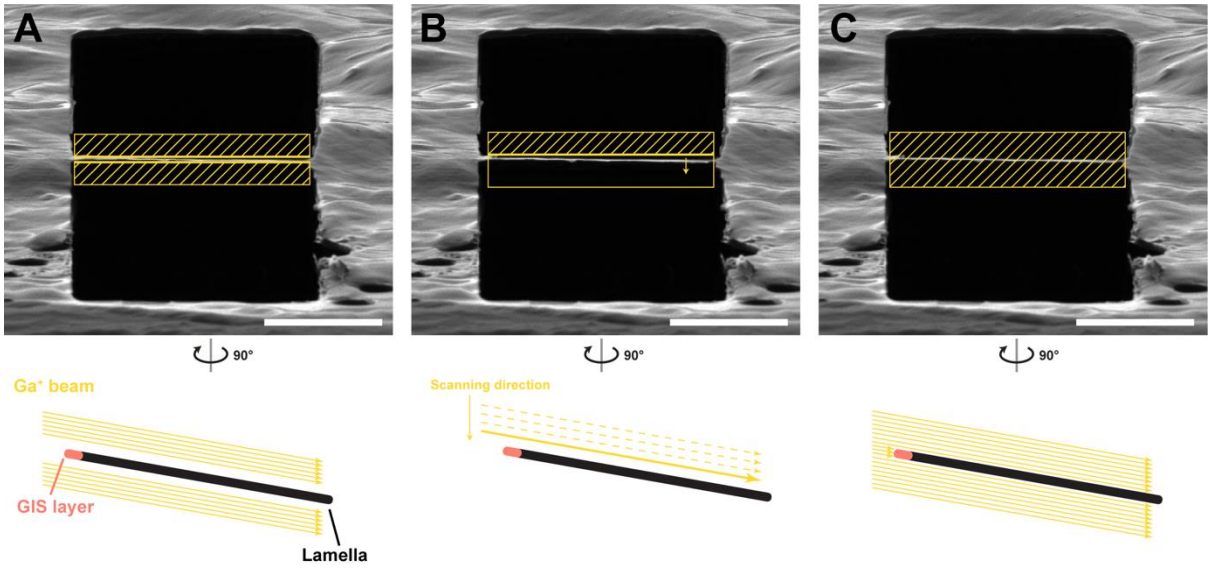

Fig. 4.5 Different strategies for lamella polishing.

*Top: Milling using two rectangular patterns (**A**), single clean cross-section pattern (**B**), and single rectangular pattern (**C**), overlayed on an ion beam image of the lamella. The patterns are coloured yellow. Bottom: Schematic drawings of the three strategies as viewed from the side.*

During final polishing, images taken with SEM can be used to judge lamella thickness based on the visible charging effect (Fig. 4.6). The disappearance of the charging effect imaged using a 5 kV or 2 kV electron beam indicates that the lamella thickness is below 200 nm or 100 nm, respectively (Fig. 4.6). Regardless of the strategy used, milling should be stopped manually when the desired thickness is reached to prevent breakage of the lamella.

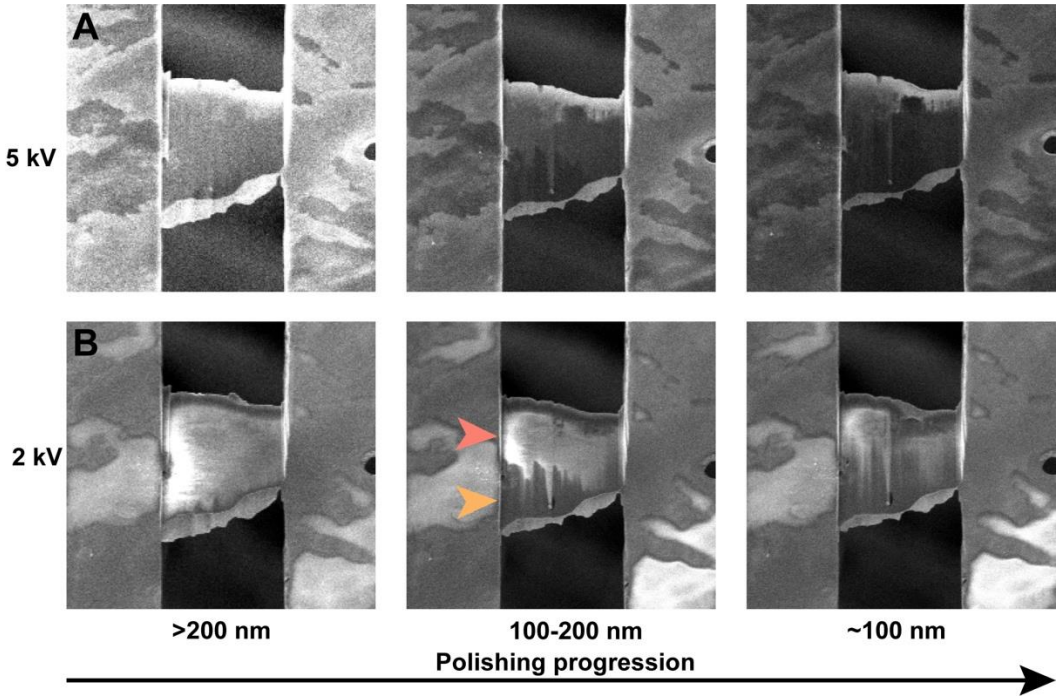

Fig. 4.6 Judging lamellae thickness based on the charging effect.

*SEM images of the lamellae during polishing acquired using a 5 kV electron beam (**A**) and a 2 kV electron beam (**B**). The red arrow head marks a region with charging effect in 2 kV image but not in 5 kV image, indicating a thickness between 100 and 200 nm. The orange arrowhead marks a region without charging effect in either 2 kV or 5kV images, indicating a thickness below 100 nm.*

In addition, automatic cryo-FIB-milling has become possible recently (Tacke et al., 2021; Zachs et al., 2020). The automation of cryo-FIB milling not only saves a considerable amount of human effort, but also provides the potential of milling overnight, thus increasing the throughput at which an EM facility can produce lamellae. However, the accuracy of automatic milling is still limited during final polishing, especially when very thin lamellae are desired. The lack of immediate feedback like a human being to stop milling or change settings in automatic milling often results in destroyed lamellae. In the future, the implementation of image recognition based on machine learning in the automatic milling software may help solve this problem. At the moment, combining automatic milling for rough milling and manual milling for polishing is the most efficient and productive strategy.

4.1.3 High-throughput batch tomography

Acquiring tomographic data fully automatically saves human effort and ensures efficient usage of microscope time. While there have been available SerialEM scripts for acquiring one tomogram using the dose-symmetric tilt scheme (Hagen et al., 2017), a script for batch data acquisition was lacking at the beginning of this thesis. Thus, such a script was developed during this thesis study specifically designed for acquiring tomograms on a lamella (*DS_ultimate.txt*, Appendix) based on the previous script for single tomograms (Hagen et al., 2017). It is common to have regions on a lamella obstructed by ice contaminations or proximity to a grid bar. The script thus allows the user to define different tracking positions and tilting parameters for each data acquisition position and avoid these regions. In addition, the script also allows changing defocus for different tomograms and automatic dark reference correction before each tomogram.

One pitfall during data acquisition is the underestimation of the accumulative radiation damage at low magnification (such as 6400x), where the localisation of acquisition sites and the refinement of eucentric height are performed. At this magnification, the beam covers the entire or most of the lamella. This means the later acquired tomograms will also suffer from the radiation damages from imaging formerly acquired ones. For a large lamella that can accommodate > 10 tomograms, total number of low-magnification images recorded can add up to 200. If each image has been exposed with electron a dose of 0.05 e^-/Å, a total dose of 10 e^-/Å just from low-magnification images is accumulated in the end, which will noticeably reduce sub-nanometre-resolution information (Grant and Grigorieff, 2015). Therefore, the low-magnification radiation should be carefully considered during data acquisition. Using less dose for acquiring low-magnification images or reduce the frequency of eucentric height refinement are effective means of alleviate this type of unnecessary radiation damage. Alternatively, new data acquisition schemes which employ beam shift and geometry calculation to acquire multiple tilt series at the same time only requires the localisation and eucentric height refinement once for every lamella (Bouvette et al., 2021; Eisenstein et al., 2022; Khavnekar et al., 2022). These schemes thereby reduce the radiation damage from low-magnification imaging to a minimum.

4.1.4 Precise alignment during tomogram reconstruction

As described previously, using patch tracking during tomogram reconstruction is not reliable for a thick lamella. For a thin lamella, patch tracking is still less accurate compared to using fiducial markers, especially in a crowded cellular sample (Fig. 4.7A,B). It has been shown recently by Harapin et al. (Harapin et al., 2015) that it is possible to "dip" the lamellae after milling into gold-nanoparticle-containing 2-methylpentane. However, considering the fragility of a lamella thinner than 200 nm, this extra handling step can be detrimental in most situations. So far, a reliable and convenient method to introduce fiducial markers is still lacking. Fortunately, in the FIB-milling process, some dark particles are often generated naturally in the FIB-milling process. During milling, the front platinum gets deposited onto the surface of the lamella. This creates dark particles that has a density gradient from the front to the centre of the lamella, which can be used as fiducial markers (Fig. 4.7C). Therefore, the regions that are close to the front of a lamella should be prioritised during data acquisition. During tomogram reconstruction, fiducial markers should be prioritised to use instead of patch tracking as long as there are more than ~6 of them, especially when the tomogram is thick.

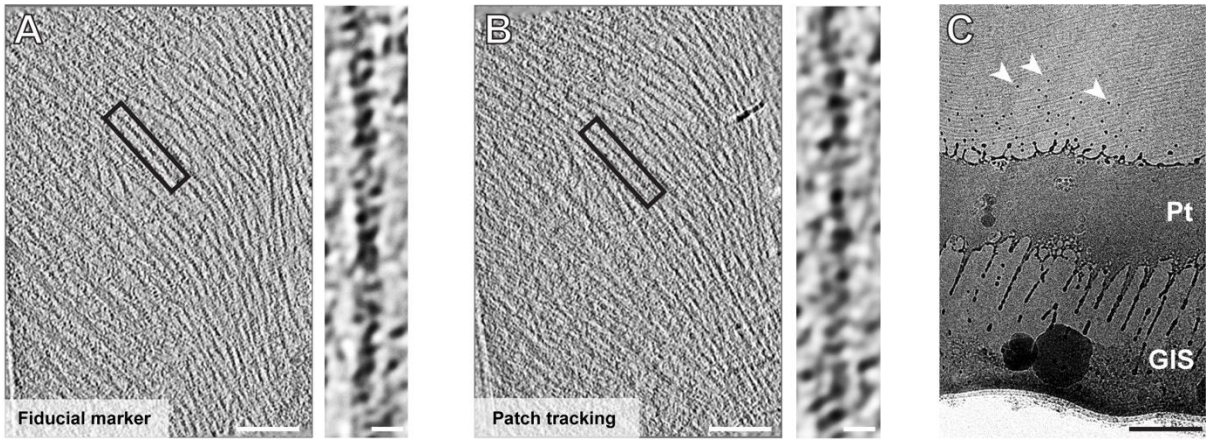

Fig. 4.7 Difference in tomogram quality between using patch tracking and fiducial markers for alignment.

*(**A, B**) Left: slice imges of a 120-nm thick tomogram aligned using fiducial markers (A) or patch tracking (B). Right: zoomed-in view of one thin filament corresponding to the inset on the left showing the difference in SNR. (**C**) The front of a lamella showing a layer of GIS and a layer of platinum in front of the actual biological sample. Examples of platinum particles on the surface of the sample are marked by the arrowheads. Scale bars: 100 nm (A, B left), 10 nm (A, B right), 500 nm (C).*

4.1.5 Prior information of filamentous particles

During sub-tomogram averaging, alignment of filamentous particles is less accurate when they lack surface features. The thin filament in a sarcomere when not bound by myosin is such a case. This can often trap the alignment in a local minimum instead of global minimum, where the filaments are aligned "upside-down" (i.e. with opposite polarities). Fortunately, in a biological context such as the sarcomere, the polarities of the filaments are known and can be determined by the presence of Z-disc or M-band. Therefore, this information can be utilised for sub-tomogram averaging to guarantee the right polarity during alignment. A script was developed to calculate the two alignment Euler angles, ψ and θ, for each sub-tomogram based on a series of coordinates of the filaments (*setpriors.py*, Appendix). These angles can be picked up in sub-tomogram software packages such as RELION and ensure all particles have the same polarity. Knowing the prior angles also allows the generation of a completely bias-free reference. Combining the two prior angles (ψ and θ) and random values of φ, a cylinder-like initial reference can be generated through RELION command *relion_reconstruc*t. Compared to an artificial cylinder with user-defined parameters, this reference has the correct soft edge and diameter that come from the data itself.

In addition to filaments, particles such as membrane proteins or other sarcomeric proteins bridging the filaments, of which the orientation can be determined from the tomogram, could also benefit from this script for initial alignment or generating a bias-free reference.

4.1.6 Structure-based tilt refinement

Although the resolutions of sub-tomogram averages from cryo-FIB samples were limited until this thesis, the resolutions from isolated samples have improved drastically in recent years. This improvement in resolution can be attributed to the development of sub-tomogram averaging software packages. The classic approach of sub-tomogram averaging involves first tomogram reconstruction and then particle extraction from the reconstructed tomograms. This means that the errors that lie in the reconstruction are passed to sub-tomogram averaging. As 3D refinement is downstream of tomogram reconstruction, the errors in tomogram reconstruction can never be reduced by refinement. The more "modern" approaches couple sub-tomogram averaging with tomogram reconstruction. Therefore, the new software packages can refine the alignment of the tilt series iteratively based on an initial structure with good

quality from sub-tomogram averaging and the alignment of sub-tomograms. Until the end of this thesis, four software packages employing this principle are available: M (Tegunov et al., 2021), RELION 4.0 (Zivanov et al., 2022), emClarity (Himes and Zhang, 2018), and EMAN2 (Chen et al., 2019). In this thesis, M was employed to polish various thin filament structures (section 4.3) and improved the resolution from ~8 Å to 4.5 Å.

4.2 Sarcomere organisation in vertebrate skeletal muscle

This section was originally published in *Cell* in 2021:

Wang, Z.*, Grange, M.*, Wagner, T., Kho, A.L., Gautel, M., and Raunser, S. (2021). The molecular basis for sarcomere organization in vertebrate skeletal muscle. *Cell* 184: 2135-2150.e13

Online version: https://www.cell.com/cell/fulltext/S0092-8674(21)00236-1

The investigation of sarcomere organisation in vertebrate skeletal muscle was performed with the help of Dr. Michael Grange. The annotations of the A-band and the Z-disc were performed together with Dr. Michael Grange. In addition, the computational tools for automatic filament picking and statistics analysis were implemented by Dr. Thorsten Wagner. Myofibrils were isolated by Dr. Ay Lin Kho and Prof. Mathias Gautel.

The original publication was reformatted to be adapted in this thesis. Some supplementary figures were integrated into the main text and split when necessary to facilitate reading. Myofibrils were prepared and frozen as described in sections 3.1 and 3.2, respectively. Detailed protocols of FIB-milling, cryo-ET data acquisition and general data processing are provided in sections 3.3, 3.4, and 3.5, respectively. Specific methods for this section and supplementary information was moved to Appendix. Supplementary videos are not included in the thesis but can be downloaded in the online version of the publication. The text and figures of the publication are used in this thesis with the permission from Elsevier.

4.2.1 Abstract

Sarcomeres are force-generating and load-bearing devices of muscles. A precise molecular picture of how sarcomeres are built underpins understanding their role in health and disease. Here, we determine the molecular architecture of native vertebrate skeletal sarcomeres by electron cryo-tomography. Our reconstruction reveals molecular details of the three-dimensional organisation and interaction of actin and myosin in the A-band, I-band, and Z-disc and demonstrates that α-actinin cross-links antiparallel actin filaments by forming doublets with 6-nm spacing. Structures of myosin, tropomyosin, and actin at ~10 Å further reveal two conformations of the ‘‘double-head’’ myosin, where the flexible orientation of the lever arm and light chains enable myosin not only to interact with the same actin filament, but also to split between two actin filaments. Our results provide unexpected insights into the fundamental organization of vertebrate skeletal muscle and serve as a strong foundation for future investigations of muscle diseases.

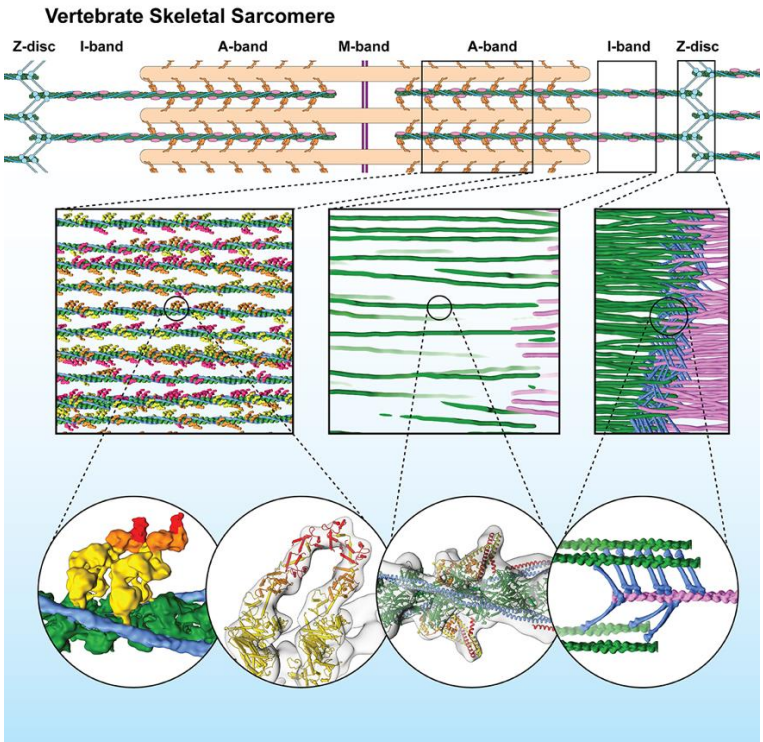

Highlights

- Three-dimensional sarcomere organization and plasticity at the molecular level

- Myosin double heads can adopt two different interactions with actin filaments
- Transition between tropomyosin states happens within one tropomyosin unit
- An irregular mesh of α-actinin doublets cross-links antiparallel actin filaments

4.2.2 Vitrified myofibrils exhibit undisturbed sarcomere ultrastructure in molecular detail

In order to investigate the native organization of an intact sarco- mere, we vitrified mouse psoas myofibrils in the rigor state (i.e., without ATP) by plunge-freezing in liquid ethane and subsequently prepared thin lamellae using cryo-FIB (see also Chapter 3, (Tacke et al., 2020)). The lamellae were 30–150 nm thin and ideally suited for cryo-ET (Fig. 4.8).

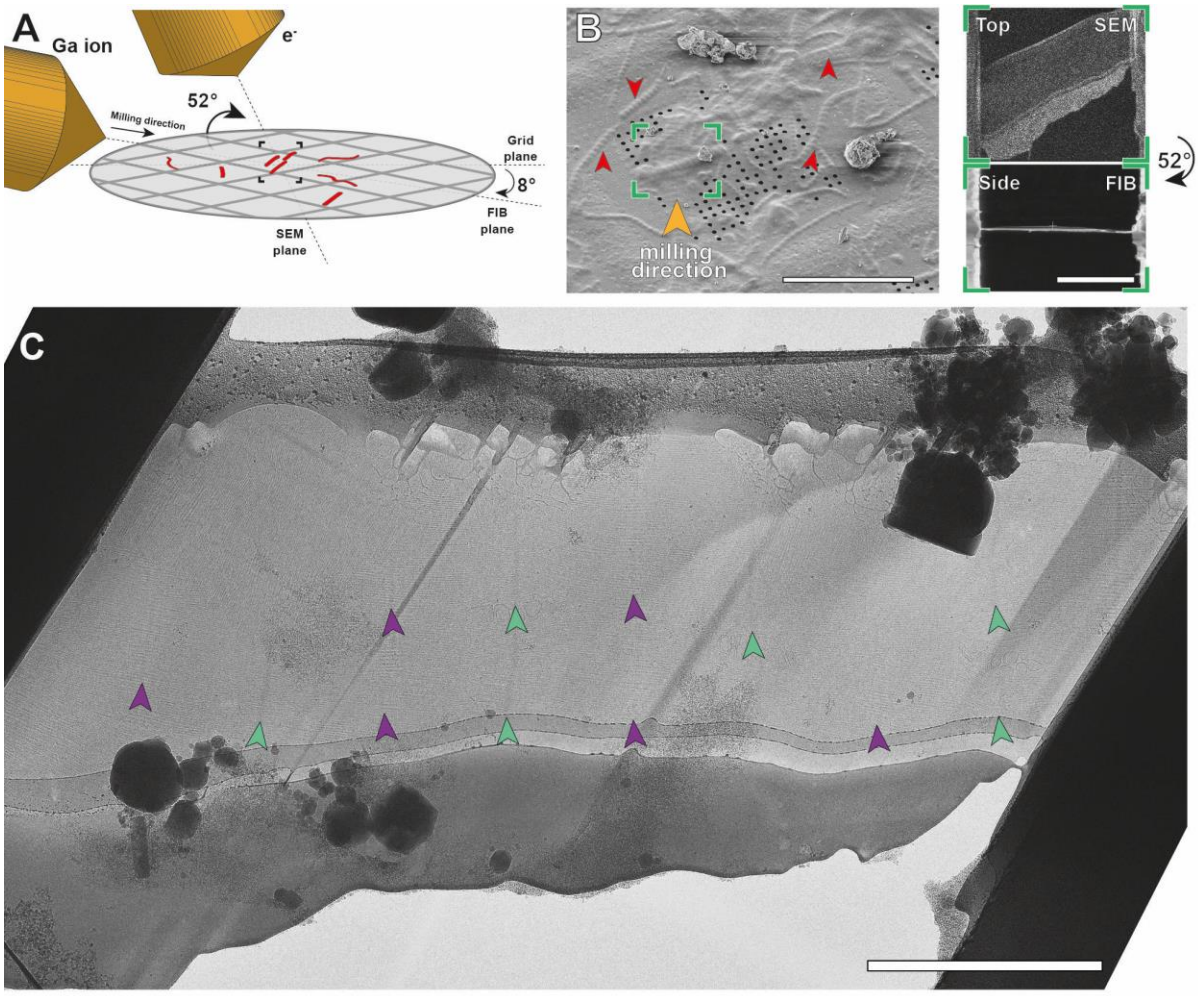

Fig. 4.8 Cryo-FIB-ET of isolated mouse myofibrils reveals sarcomere ultrastructure

*(**A**) Cartoon showing the arrangement of the SEM and FIB ion source with respect to the grid. Myofibrils are depicted in red. (**B**) Left: SEM image taken 45° to the plane of a grid on which myofibrils were vitrified, with red arrow heads pointing toward the myofibrils. The orange arrow head indicates the milling direction. Scale bar, 50 µm. Right: Top (taken with electron beam) and side (taken with ion beam) views of the lamella taken after milling in the FIB-SEM. The top view was taken 60° angle to the plane of the grid. The side view was taken 8° to the plane of the grid, which was also the milling angle. Scale bar: 5 µm. (**C**) Projection image of a lamella after FIB-milling recorded at a TEM at stage 0°.*

Purple arrow heads indicate M-bands of sarcomeres, while green arrow heads indicate Z-discs. Scale bar, 3 µm.

Vitrified myofibrils show an intact sarcomere ultrastructure, including apparent Z-discs, I-bands, A-bands, M-bands, and organelles such as mitochondria and sarcoplasmic reticulum localized between laterally adjacent sarcomeres (Fig. 4.9A). Importantly, the tomograms include structures that could not previously be visualized in situ. Of particular note are myosin double heads forming regular cross-bridges that resemble an “arrow-head”, thin myosin tails mainly composed of coiled-coil structures (Chew and Squire, 1995) protruding from the thick filament, and details of the Z-disc and troponin complexes (Fig. 4.9B-D). The M-band consists of numerous structural proteins other than myosin, such as myomesin, titin, and obscurin as well as accessory proteins with transient localisation, such as FHL-2, Nbr1, MURFs, or calpain-3 (Lange et al., 2006, 2020). Together, they form pleomorphic densities decorating and cross-linking the thick filaments (Fig. 4.9B-D). This heterogeneity hampers identification of individual proteins in this crowded region. Therefore, we focused on the details of the A-band, I-band, and Z-disc in the following sections.

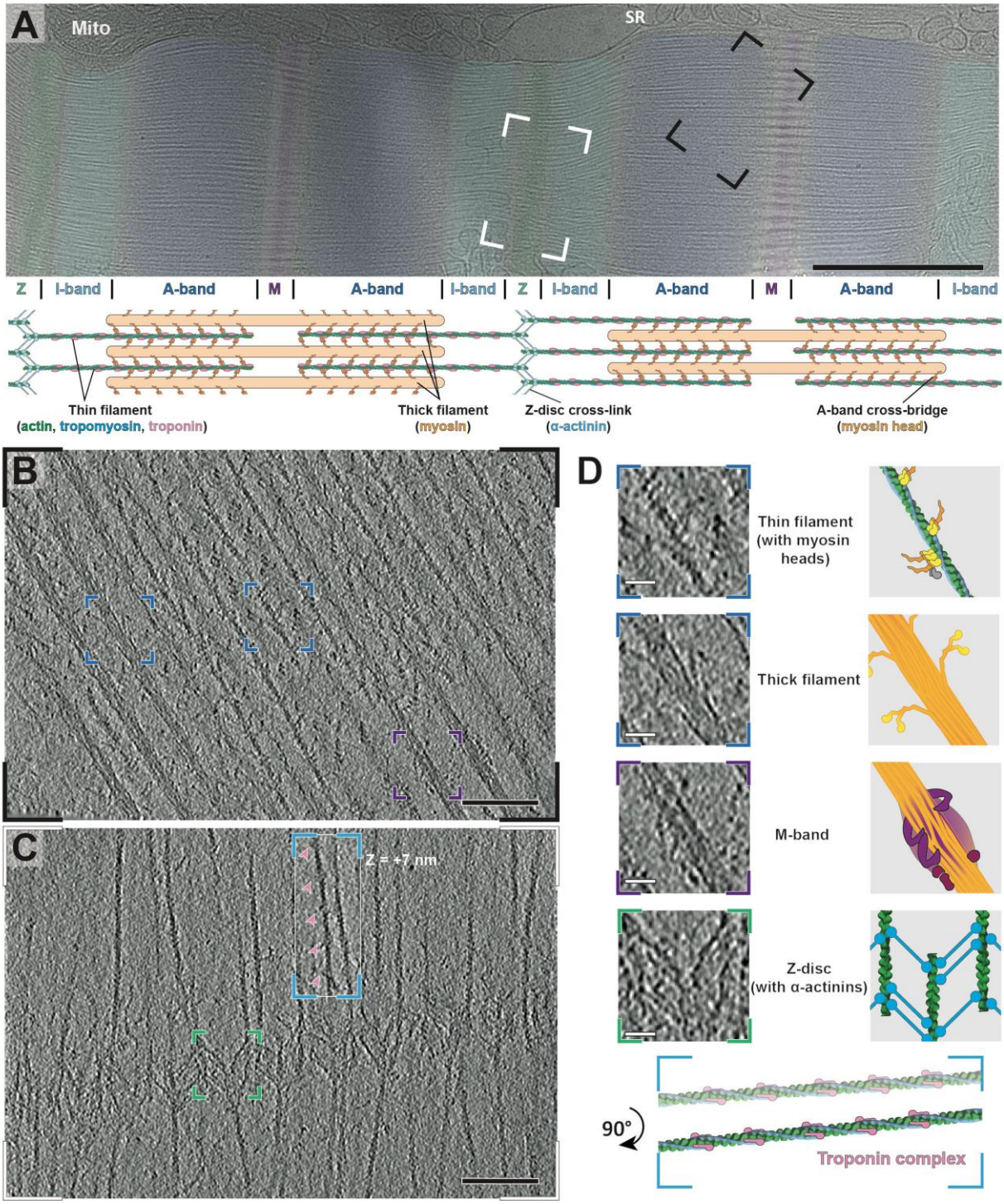

Fig. 4.9 Isolated mouse skeletal myofibrils imaged using electron cryo-tomography.

*(**A**) Projection image of mouse skeletal muscle, with Z-disc, I-, M-, and A-bands visible (green, light blue, dark blue and purple, respectively). A schematic diagram is shown below, highlighting the lateral organisation and cross-links in different zones. Mitochondria (Mito) and sarcoplasmic reticulum (SR) can be identified between sarcomeres. Scale bar, 1 µm. (**B**) Slice through an electron cryo-tomogram spanning A- to M-band. Its representative position on a sarcomere is marked as a black box in (A) (not same sarcomere). In this region, myosin heads bound to the thin filament, myosin tails emanating from*

*the thick filament (dark blue insets) and obscure protein densities at the M-band (purple inset) can be discerned. Scale bar, 100 nm. (**C**) Slice through an electron cryo-tomogram spanning I-band and Z-disc. Its representative position on a sarcomere is marked as white box in (A) (not same sarcomere). The tail-feather-like arrangement of α-actinin molecules cross-bridging thin filaments in a zig-zag manner is visible (green inset). Thin filaments in the I-band have regularly-spaced nodes corresponding to troponin complexes (pink arrow heads, blue inset). A slice of the same location but 7 nm above from the rest of the slice is shown inset. Scale bar, 100 nm. (**D**) Larger view of insets described in (A-C), with cartoon depictions of densities. Scale bar, 20 nm.*

It is well-known from cross-sectional views of myofibrils that thin and thick filaments are hexagonally arranged in the A-band (Huxley, 1957). Interestingly, in immature sarcomeres found within neonatal cardiomyocytes, the hexameric pattern is limited to thick filaments, suggesting that thin filament organisation is a later process of sarcomeric maturation in vivo (Burbaum et al., 2021). In orthogonal views of our tomograms, we can clearly discern this hexagonal pattern in the A-band, demonstrating that our preparations are consistent with previous studies (Fig. 4.10). One thin filament is surrounded by three thick filaments and three other thin filaments at a distance of around 26 nm (Fig. 4.10A-C). Thick filaments form triangular patterns with an average inter-thick-filament distance of 45 nm (Fig. 4.10D-F). This arrangement of thick filaments is maintained from the A-band to the M-band where thin filaments are missing.

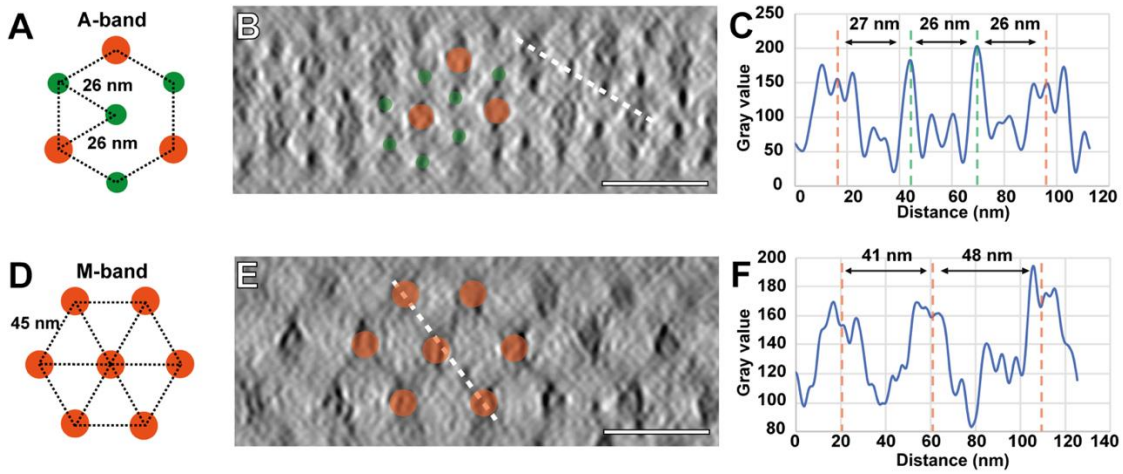

Fig. 4.10 Isolated mouse skeletal myofibrils imaged using electron cryo-tomography.

*(**A** and **D**) Schematic diagrams of the hexagonal arrangement of thin filaments in the A-band (A) and the triangular arrangement of thick filaments in the M-band (D). Thin and thick filaments are represented by green and orange circles, respectively. (**B** and **E**) Slices of the cross-section view of*

*tomograms in the A-band (B) and the M-band (E). The tomograms were previously filtered with an equator filter on XY slices in Fourier space to remove signals from cross-bridges. The thicknesses of lamellae were measured in this view. Scale bar, 50 nm. (**C** and **F**) Distances between filaments were measured using the line profiles of the white dotted lines in (B) and (E), respectively.*

4.2.3 In situ actomyosin structure reveals a myosin double-head with different lever arm conformations

Segmentation of the tomograms enabled us to unequivocally characterise the 3D arrangement of thin and thick filaments and the cross-bridges within a sarcomere. To increase the level of observable detail that we could resolve with our data, we employed sub-volume averaging to determine the structure of the thin and thick filament and cross-bridges. The reconstruction of the thick filament was proved to be difficult due to its heterogeneity, flexibility, and an absence of obvious symmetry. Nevertheless, we obtained a low-resolution reconstruction showing the architecture of the core of thick filaments that we could use for the subsequent analyses (Appendix Fig. 6.1).

The three-dimensional reconstruction of the thin filament and cross-bridges could be resolved to a higher resolution. Segmentation of the tomograms and 3D classification of all sub-volumes of the cross-bridges indicated that the two heads from the same myosin molecule, known as double-heads, mostly bind to two neighbouring actin subunits (see section 4.2.4). Hence, we merged multiple classes after modifying alignment parameters to obtain a structure of a native thin filament with the myosin double-head bound (Fig. 4.11A). The reconstruction has a resolution of 10.2 Å and we could clearly assign tropomyosin and the domains of actin and of the myosin heads and necks, including the essential chains (ELC) and part of the regulatory light chains (RLC) (Fig. 4.11A).

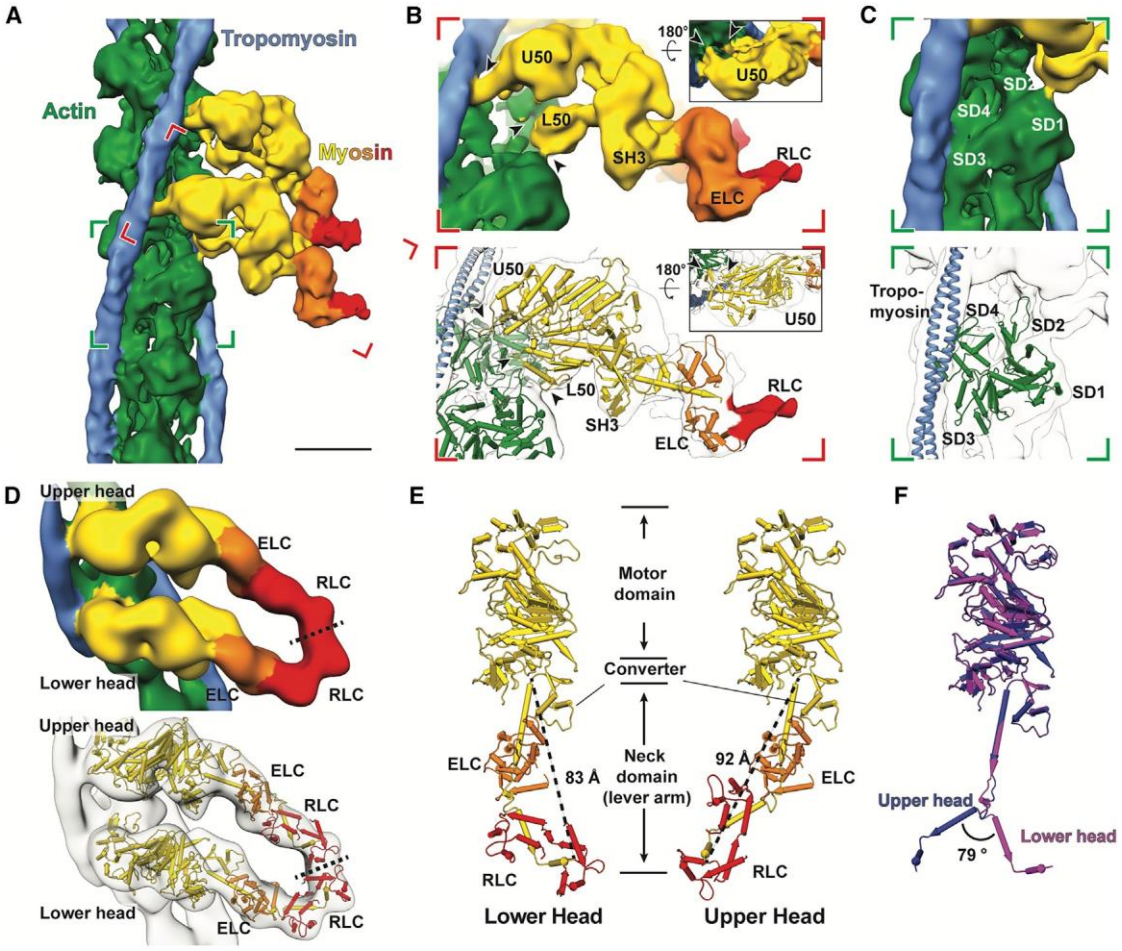

Fig. 4.11 Sub-volume averaging of thin filaments reveals the interaction of a double-head myosin with the thin filament and two conformations of light chain domains within a double-head

*(**A**) Surface view of the in situ actomyosin structure, showing actin filament (green), tropomyosin (blue), and myosin double heads, with motor domains (yellow), essential light chains (orange), and regulatory light chains (red). Scale bar, 5 nm. (**B**) Close-up view of the lower myosin head and homology models based on PDB: 3I5G, 5JLH, and 6KN8. The upper 50 kDa (U50), lower 50 kDa (L50), SH3, and essential light chains (ELC) can be allocated in the map, along with part of the regulatory domain (RLC). Arrow heads indicate the interaction interfaces between actin and myosin at loop 4, helix-loop-helix motif, loop 3 of myosin (top to bottom). Arrow heads in the inset depict interaction interfaces at the cardiomyopathy loop and loop 2 (left to right). (**C**) Close-up of an actin subunit and structural model fitted into the EM map showing the four subdomains of an actin subunit (SD1–SD4). (**D**) Surface view of the structure of a complete myosin double-head including RLCs determined from averaging shifted sub-volumes. Their interface is indicated by a dotted line. (**E**) Comparison between the lower and upper heads within one double head, showing two different conformations in the lever arm that interacts with RLC and ELC. Lengths of the lever arms were measured between G772 and L844. (**F**) Alignment of the lower (purple) and upper (blue) heads heavy chain, showing two different kinks between the ELC-binding region and the RLC-binding region.*

We calculated a homology model using the rigor cytoplasmic actomyosin cryo-EM structure (PDB: 5JLH) (von der Ecken et al., 2016) and the crystal structure of the S1 fragment from squid muscle (PDB: 3I5G) (Yang et al., 2007) as a template and fitted it into the density map using rigid body fitting (Fig. 4.11B,C). We chose this myosin structure because there are no crystal structures of a complete vertebrate myosin S1 fragment in the rigor state available. The model fits well into the density, demonstrating that the in vitro structures resemble well the structures determined in situ. At this resolution, both myosin heads bind to the actin filament in a structurally identical manner with close interactions formed between actin subunits and myosin as well as tropomyosin (Fig. 4.11B,C). Both ELCs bind to the upper parts of the lever arms (residues L788–L800) as is seen in the crystal structure. The density threshold corresponding to the RLCs and RLC binding domains after averaging is considerably lower than the rest of the structure, indicating a higher flexibility or variability in this region.

To improve the quality of the reconstruction in the region of the RLC, we shifted the center of sub-volume averaging from the thin filament to the myosin head. Through further classification, we determined a structure of the complete double-head myosin S1 fragment, including the two heavy chains that are bound to actin, two ELCs and two RLCs (Fig. 4.11D). The S2 fragment that tethers myosin heads to the thick filament was not resolved in this structure, likely due to the different positions and angles it takes in the sarcomere.

Although a homology model of the myosin motor domain and ELC of the squid myosin crystal structure (PDB: 3I5G) fits well into our density, the RLCs and the lower part of the lever arm (residues R811–L844) had to be fitted separately (Fig. 4.11D). Compared with its conformation in the crystal structure, the lever arm is strongly kinked between the ELC and RLC binding regions (residues M801–E810), resulting in a bent conformation (Fig. 4.11E). Interestingly, the kink in the upper head is in the opposite direction compared to the one in the lower head, bringing the RLCs of the two heads in close proximity (Fig. 4.11F). This crucial observation reveals the ability of the myosin double head to accommodate force production, and has not been validated structurally in any previous study in any system. It is also consistent with previous cross-linking and FRET experiments, which suggested a small distance between the two RLCs in a double head (Bower et al., 1992; Chakrabarty et al., 2002; Chantler et al., 1991).

This arrangement, which is probably stabilized by interactions between the ELCs and RLCs, allows for the simultaneous binding of the two heads to actin and at the same time brings their necks close enough together to continue with the coiled-coil structure of the joint S2 fragment.

In addition, the opposite direction of the kinks on the two lever arms leads to a similar length of the two arms. This is important because the length of the lever arm determines the step size of myosin heads on actin (Ruff et al., 2001).

In this context, it is interesting that the hinge in the lever arm together with a hook (residues W824–W826 in molluscan myosin) have previously been shown to be important for regulated myosins (Brown et al., 2011; Himmel et al., 2009). In this case, the light chains control myosin activity even in the absence of actin (Wells and Bagshaw, 1985) and the presence of Ca2+ determines the stability of the ELC/RLC interface. Different ELC/RLC interfaces were also suggested from the latest model of myosin in the relaxed state, where the heads fold back to the thick filament (Hu et al., 2016; Knupp et al., 2019). Notably, the arrangement of the ELC/RLC of the lower head in our model resembles that in the ‘‘blocked’’ head of the off-state myosin while the upper head ELC/RLC is similar to the ‘‘free’’ head (Fig. 4.12). This suggests that there are only two possible angles for the kink in the lever arm, which are likely to be determined by the interaction of the ELCs and RLCs. This interaction probably stabilizes the two conformations to rigidify the lever arm, which is needed for the proper transmission of the force of the power stroke (Holmes, 1997). It will be interesting to visualize how the phosphorylation state of the RLC can modulate the interaction of the ELCs and RLCs and thus modulate muscle contractility.

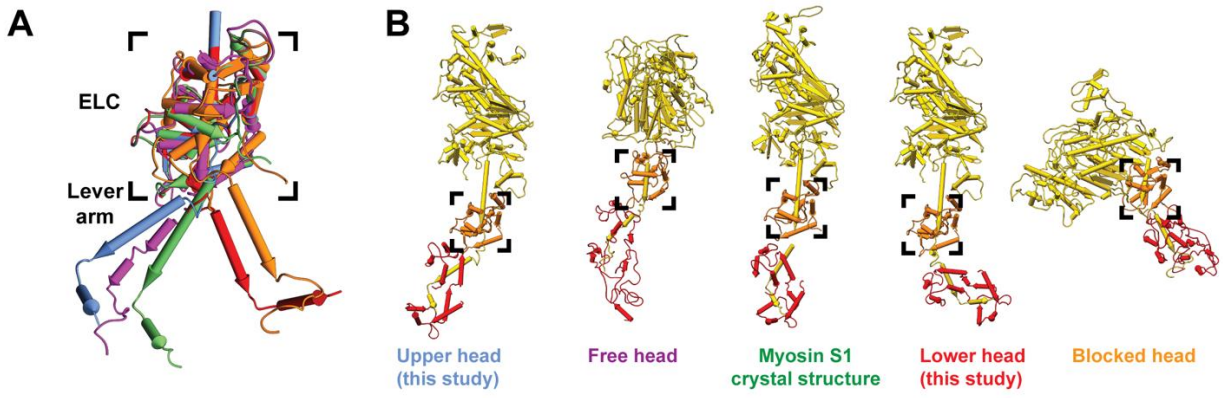

Fig. 4.12 Different “kink” conformations in the lever arm

*(**A**) Alignment of ELCs, together with the ELC-binding region, from different atomic models of myosin heads. Only the RLC-binding helix of the lever arm in each model is shown instead of the complete RLC for clear visualization. Two different groups of conformations are shown. The conformation of the lower head (red) is similar to the relaxed blocked state (orange). The upper head (blue) exhibits a similar conformation to the relaxed free head (purple) and the crystal structure of squid myosin S1 (green). (**B**)*

Side-by-side comparison of the complete myosin atomic models in (A) showing the heavy chain and both light chains.

Various structures for the single isolated myosin head have been determined in different states of the ATP hydrolysis cycle (e.g., (Behrmann et al., 2012; von der Ecken et al., 2016; Houdusse et al., 2000; Mentes et al., 2018; Risal et al., 2004; Yang et al., 2007)). Furthermore, whereas the myosin double-head has also been determined in structures of isolated thick filaments and in 2D crystals of heavy meromyosin (Alamo et al., 2008; Baumann et al., 2012; Knupp et al., 2019; Wendt et al., 2001), our *in situ* actomyosin complex is a structure of the myosin double-head interacting with the thin filament determined directly within fully organised myofibrils. Our analysis of this structure can be used to further inform other states of the myosin double-head, such as the pre-power stroke state and the relaxed state, to further understand the cross-bridge cycle (Spudich, 2001) within a sarcomere in a native context.

4.2.4 Cross-bridges in the A-band depict a pseudo-regular distribution of myosin heads and reveal a split-head conformation

In order to identify the proportion of myosin heads that bind to thin filaments in a rigor state sarcomere, we annotated and isolated the densities corresponding to the cross-bridges as well as thick and thin filaments in the A-band (Fig. 4.13A). Combining annotated filaments with structures determined via sub-volume averaging allowed us to produce a molecular map of the thin and thick filaments and attached myosin heads (Fig. 4.13B).

Of the 30 thin filaments annotated containing 5,664 actin subunits, 2,734 myosin heads were fitted into the cross-bridge densities, corresponding to 82.5% of the total number of myosin heads in this region calculated from the theoretical number of myosin heads per given length of the thick filament (6 heads per 14.3 nm, 294 heads per thick filament [(Bennett et al., 2020)], total heads in our analysis = 3,315). This suggests that not all myosin heads are attached to thin filaments, even in the rigor state.

Similar to sarcomeres from insect muscle, all thin filaments are in helical register (Fig. 4.13B) and cross-bridges appear at regular target regions every ~37 nm on a thin filament between each pair of thick and thin filaments (Fig. 4.13A,B) (Reedy, 1968). However, in contrast to the

‘‘double-chevron’’ arrangement of cross-bridges in an insect sarcomere, the cross-bridges in a vertebrate sarcomere show a higher variability regarding the distance between each other and tend to appear in clusters (Fig. 4.13A,B and Fig. 4.15). Although the most common composition of a cross-bridge is only one myosin double-head (Fig. 4.13C), two consecutive myosin double-heads also appear at many target regions. Occasionally, there are also single heads bound to the thin filament (8.3% of all myosin heads) with their partners not identified within the tomogram. In addition, a rare ‘‘split-head’’ conformation also occurs when the two heads from one myosin binds to two different adjacent thin filaments (10 pairs observed; 0.6% of all heads) (Fig. 4.13D). This conformation has been previously suggested (Offer and Elliott, 1978) and vaguely indicated by 2D projection images (Hirose and Wakabayashi, 1993). Our observation provides direct proof of this conformation in three-dimensions in the rigor state vertebrate sarcomere. The ability of myosin to split its two heads and bind to different thin filaments enhances the plasticity of the sarcomere and allows proper contraction under slight structural deformation due to external forces.

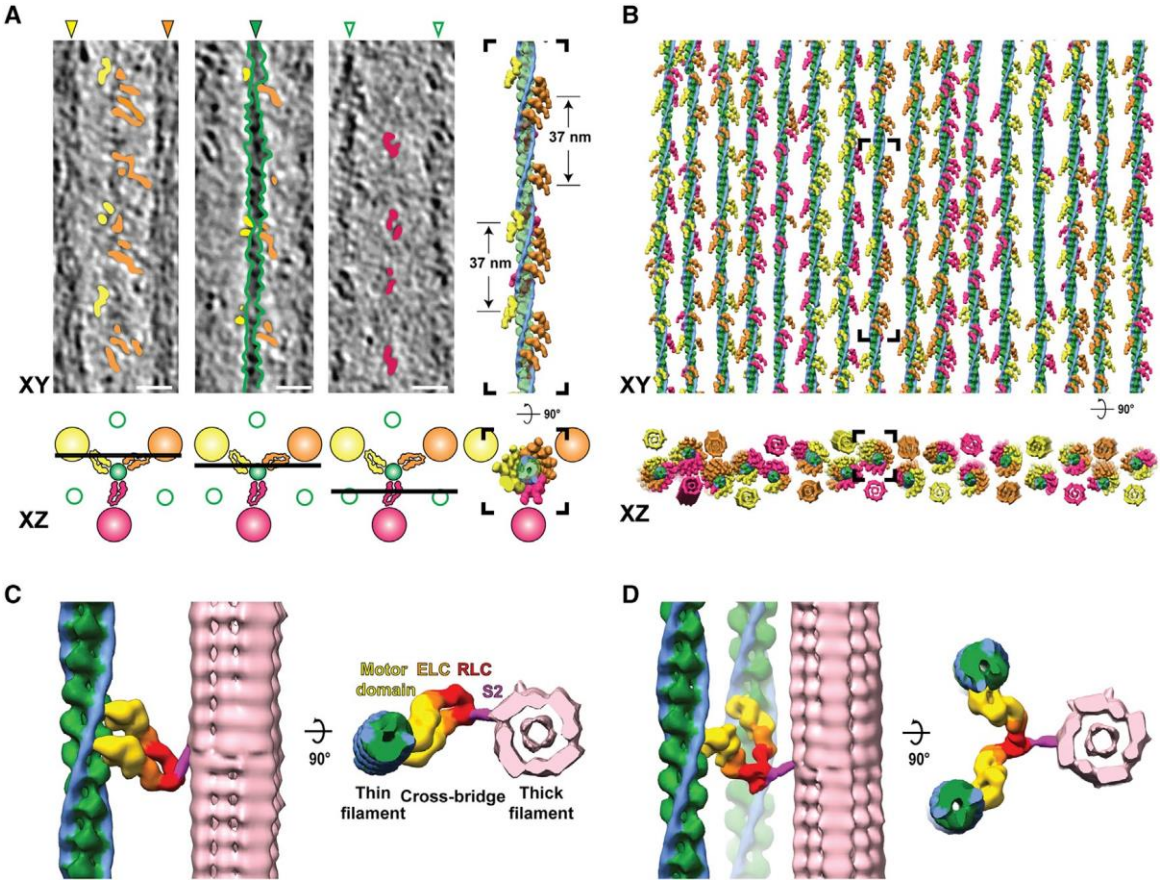

(Figure legend on the next page)

Fig. 4.13 Organization of the A-band in natively isolated myofibrils shows that myosin heads can adopt two interactions with thin filaments

*(**A**)XY-slices through a tomogram at three different Z positions (illustrated by the cartoon below), highlighting the myosin head densities (orange, yellow, and magenta) and the thin filament (green) apparent within the volume. Annotation of densities produces a volume in which filtered actomyosin can be fitted, shown on the right and in (B). The three myosin colors represent the contribution of the myosin head from a respective neighboring thick filament. Scale bars, 20 nm. (**B**) Fitted model of all thin filaments and myosin heads in a tomogram, with the black inset depicting the filament shown in (A) In the XZ view, reconstructions of corresponding thick filaments are also shown. (**C**) A typical cross-bridge with a myosin double-head. (**D**) A rare myosin split-head with two heads from the same myosin molecule binding to two different actin filaments.*

Notably, although we annotated mostly the C-zone of the A- band, where myosin binding protein C (MyBP-C) is present, we did not identify any corresponding densities along the thick filaments with a regularity of 43 nm as seen in previous studies (Craig and Offer, 1976; Luther et al., 2011). In the rigor state sarcomere, the density corresponding to MyBP-C is likely to be overwhelmed by the large number of myosin heads bridging between the thick and thin filaments. Further structural investigation on relaxed myofibrils will shed light on the MyBP-C organisation as retracted myosin heads abolish the cross-bridges, leaving only cross-links formed by MyBP-C between the thick and thin filaments.

To further investigate the variability in myosin binding, we focused on the influence of actin orientation and the distance between thin and thick filaments (Fig. 4.14). We plotted the orientation of the actin subunits bound by myosin heads in terms of their relative angles with respect to a fixed orientation perpendicular to the filament axis. The distribution showed three distinctive groups with a Gaussian distribution corresponding to the three thick filaments from which the myosin heads originate. For a specific thick filament, the orientations of myosin-bound actin sub- units are mostly confined within a range of ~120° (Fig. 4.14A). This indicates that myosin heads tend to bind to actin subunits oriented toward the direction of the thick filament from which it originates. This is also demonstrated by the combined myosin binding profile of all 30 thin filaments (Fig. 4.14B). In addition, this footprint map of myosin binding on a thin filament also exhibits the 37-nm hotspot (~13 actin subunits) of cross-bridge clusters as a consequence of this preferred binding orientation of actin subunits.

Furthermore, the distances between the thin and thick filaments at both myosin-bound and myosin-free actin subunits show a Gaussian distribution with no obvious skewness (Fig. 4.14C). The myosin-bound actin subunits are on average 0.4 nm closer to the thick filaments (95% confidence interval 0.2–0.5 nm) compared to myosin-free actin subunits. This small difference implies only a minor preference for myosin-binding when there is a shorter distance between the thin and thick filaments.

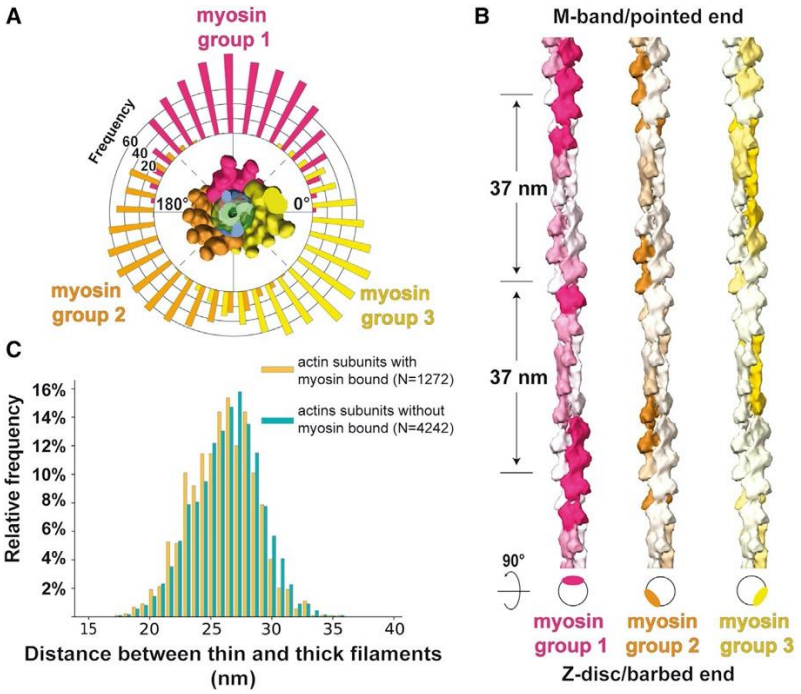

Fig. 4.14 Myosin binding preference is dependent on actin orientation and distance between thin and thick filaments.

*(**A**) Angular distribution of myosin heads shown by a circular histogram of the orientation of the actin subunits bound by myosin heads. The colors indicate three different thick filaments where the myosin heads originate. (**B**) Hotspots of myosin binding from three thick fil- aments shown on actin filaments. Actin filaments are colored with the footprint of the myosin heads according to multiple sequence alignment of the myosin binding profile sequences determined from the annotated volume and the fitted model in Fig. 4.13B. The preferred side on a thin filament for binding of a certain myosin group is shown in the schematic diagram below. (**C**) Histograms of distances between thin and thick filaments at actin subunits with (orange) or without (green) a myosin head bound. Mean distances are 25.9 nm (SD 2.7 nm) and 26.3 nm (SD 2.7 nm), respectively. No skewness was measured in either population, meaning both distributions can be considered Gaussian.*

Our molecular map of myosin head distribution enabled us to determine the arrangement of myosin heads emanating from thick filaments within the rigor state sarcomere (Fig. 4.15A). In the OFF state, when myosin heads are retracted to the thick filament, they are arranged in a 3-start helical pattern with 14.3 nm between layers of crowns as illustrated by cryo-EM and X-ray diffraction studies (AL-Khayat et al., 2013; Squire, 2009). This regular organization is not maintained in sarcomeres in the rigor state, when thick filaments are in the ON state. We could observe that the distance between axially adjacent myosin heads varies (Fig. 4.15B) and found a different binding of myosin heads in different sections of a thick filament (Fig. 4.15D–5G). The S2 fragment, which forms a convex surface with the S1 fragment (Cantino et al., 2000), provides enough flexibility for a myosin head to bind to a random actin subunit within the range of allowed distance and orientation (Fig. 4.15C). This flexibility makes allowance for the mismatch of the 37-nm actin repeat in thin filaments and the 14.3-nm myosin repeat in thick filaments (Squire, 2009) and results in the pseudo-regular arrangement of cross-bridges.

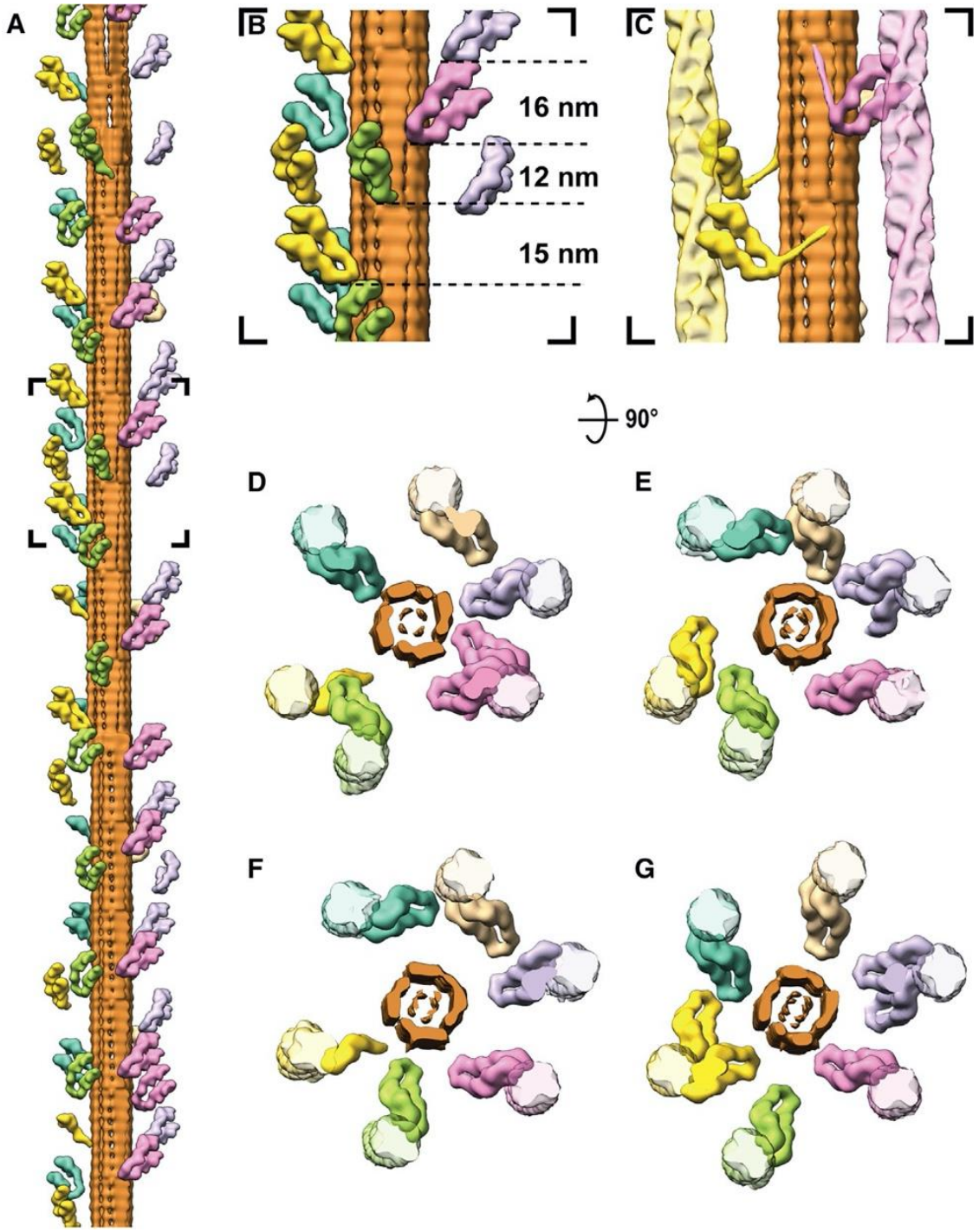

Fig. 4.15 Arrangement of myosin heads around a thick filament

*(**A**) Model of a thick filament with surrounding thin filament-bound myosin heads obtained from fitting into the annotated tomogram. The six different colours represent myosin heads bound to the six adjacent thin filaments. (**B**) Close-up view of the black inset in (A) showing varying spacings between the tips of adjacent myosin heads. (**C**) Different conformations of S2 fragments taken from clearly discernible annotations. (**D–G**) Top view of four segments of the thick filament in (A) together with the thin filaments it binds, highlighting heterogeneity of myosin head organisation. Each image depicts a segment with a depth of ~40 nm.*

Overall, the analysis of myosin heads in the A-band suggests that myosin binding is a stochastic process regulated by physical limitations such as the orientation of actin subunits. Myosin prefers to bind to regions on thin filaments that orient toward the thick filament, creating ~37 nm regular periodic cross-bridge clusters, consistent with previous observations in insect muscle (Reedy, 1968) and single-molecule experiments (Steffen et al., 2001). In insect flight muscle, cross-bridges are formed in distinct lead and rear bridges (Liu et al., 2004; Schmitz et al., 1996; Taylor et al., 1984). However, cross-bridges in vertebrate sarcomere are composed of various myosin double-heads in an irregular pattern. This pseudo-regular organization indicates a certain plasticity within a vertebrate sarcomere, whereby a strictly ordered myosin binding network is unnecessary.

4.2.5 Thin filaments in the I-band are disorganized and bear a different tropomyosin state to those in the A-band

One advantage of our approach is that we can trace single filaments through the sarcomere in 3D, allowing us to follow thin fil- aments from the A-band through the I-band into the Z-disc. The ordered hexagonal pattern of filaments in the A-band breaks down in the I-band, where the thick filaments end (Fig. 4.16D). Consistent with previous studies presenting cross-section images of the I-band (Pepe, 1975) and contrary to a previous model stating an equally distanced arrangement of thin filaments along the A-band to Z-disc transition (Knupp et al., 2002), thin filaments show a transition in the I-band from a hexagonal pattern to an irregular pattern caused by the lack of cross-bridges in this region. The extent of displacement from the hexagonal arrangement varies among filaments (Fig. 4.16D).

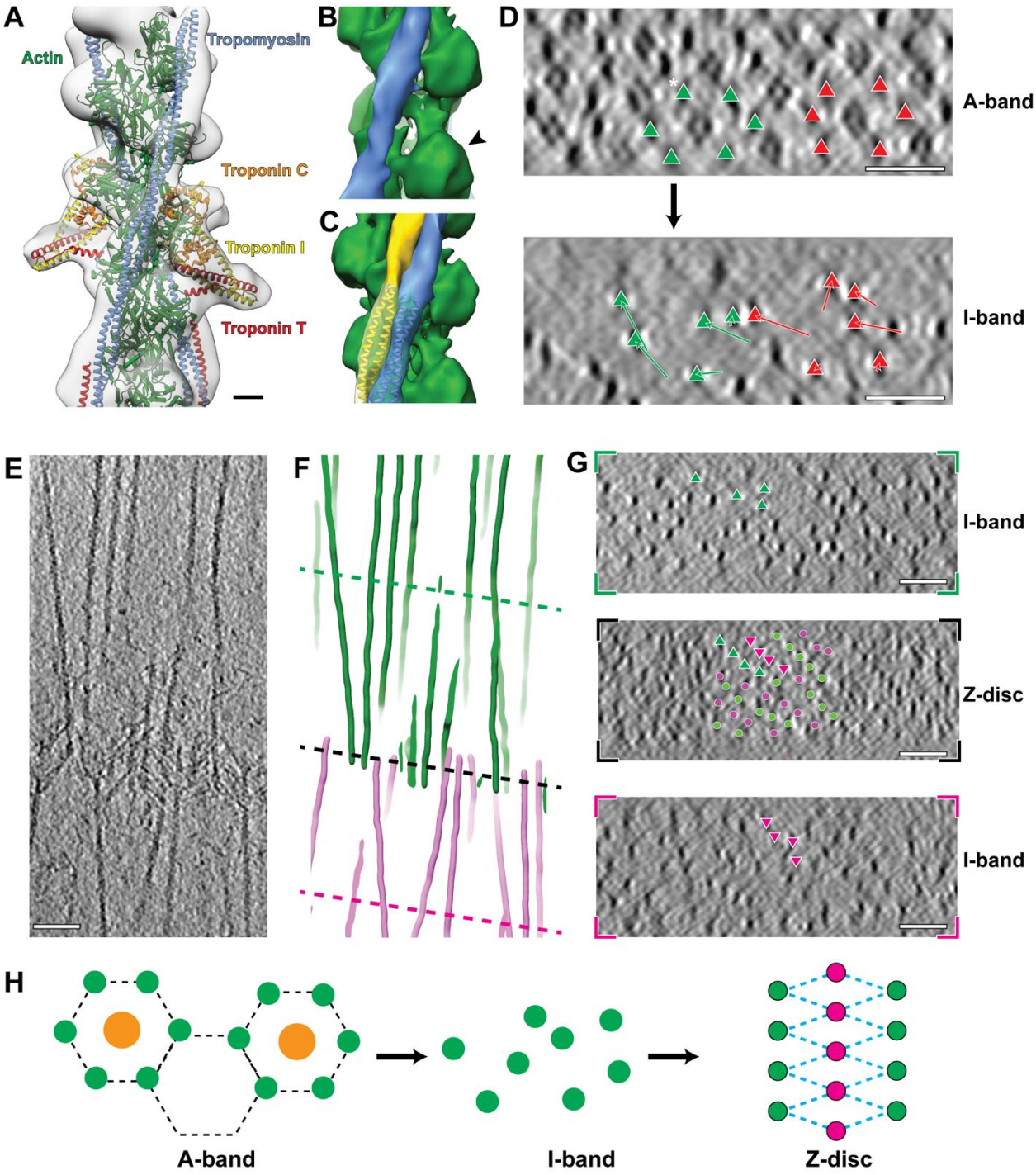

Fig. 4.16 Structure and organization of thin filaments in the I-band

*(**A**) Sub-volume average of the thin filament in the I-band fitted with a homology model of the complete thin filament including troponin. Homology model is based on PDB: 6KN8. (**B**) 3D reconstruction of the thin filament in the I-band excluding troponin. The actin filament is depicted in green and tropomyosin in blue. At this resolution, the four subdomains of actin form a clear ''U'' shape (marked by the arrow head) and indicates actin barbed end faces toward the Z-disc. (**C**) Tropomyosin along thin filaments takes the C-state in the I-band (blue) and the M-state in the A-band (yellow). (**D**) XZ views of sarcomeres at the A-band and I-band highlighting the disappearance of the hexagonal pattern of thin*

*filaments. Two hexagonal units of thin filaments and their corresponding positions in the I-band are indicated by green and orange triangles. Displacement of the filaments from A-band to I-band are shown as arrows. Asterisk denotes a filament that moved out of the field of view during the A–I transition. (**E**) Slice through a tomogram depicting the Z-disc and two I-bands from two adjacent sarcomeres. (**F**) 3D model of thin filaments showing the same region as in (E). (**G**) Cross-section views of the positions indicated by dotted lines in (F), showing the pattern of thin filaments during the I-Z-I transition. Filaments are traced in green triangles from the I-band to Z-disc of the top sarcomere and in magenta triangles from the Z-disc to the I-band of the bottom sarcomere. In the Z-disc image, antiparallel filaments in the center are labeled with green and magenta dots. (**H**) A schematic diagram shows the hexagonal pattern in the A-band, the irregular pattern in the I-band and the rhomboid pattern in the Z-disc. Scale bars, 2 nm (A), 50 nm (D–G).*

Due to the absence of myosin in the I-band, troponin complexes are clearly visible with a periodicity of ~37 nm on the thin filament (Fig. 4.9C, Fig. 4.16D, and Fig. 4.17). We applied sub-volume averaging to determine the structures of the actin-tropomyosin-troponin complex and the actin-tropomyosin complex in the I-band at resolutions of 19.8 Å and 10.6 Å (Fig. 4.16A,B, and Fig. 4.17), respectively. We then calculated a homology model using an in vitro cardiac muscle thin filament cryo-EM structure of the Ca^{2+}-bound state as a template (PDB: 6KN8) (Yamada et al., 2020) and fitted it into the density maps using rigid body fitting. The model fits well into the reconstruction of both structures, demonstrating that the thin filament is in the on-state with tropomyosin in the C (Ca^{2+} induced) state position (Fig. 4.17I,J). This suggests that there is structural similarity between skeletal and cardiac troponin complexes when bound to actin filaments at this resolution, despite differences in respective crystal structures (Takeda et al., 2003; Vinogradova et al., 2005). Interestingly, the position of tropomyosin differs from that in the A-band, where tropomyosin is in the M (myosin-bound) state (Fig. 4.16C, Fig. 4.17A,B) (von der Ecken et al., 2016; McKillop and Geeves, 1993). Thus, the binding of myosin to the thin filament shifts tropomyosin from the C-state to the M-state position in the A-band, whereas tropomyosin remains in the C-state in the I-band. Although different tropomyosin states have been observed separately *in vitro* (von der Ecken et al., 2015, 2016; Poole et al., 2006; Yamada et al., 2020), our *in situ* structures of thin filaments suggest that the tropomyosin position can vary on a local scale within the same sarcomere and even the same thin filament.

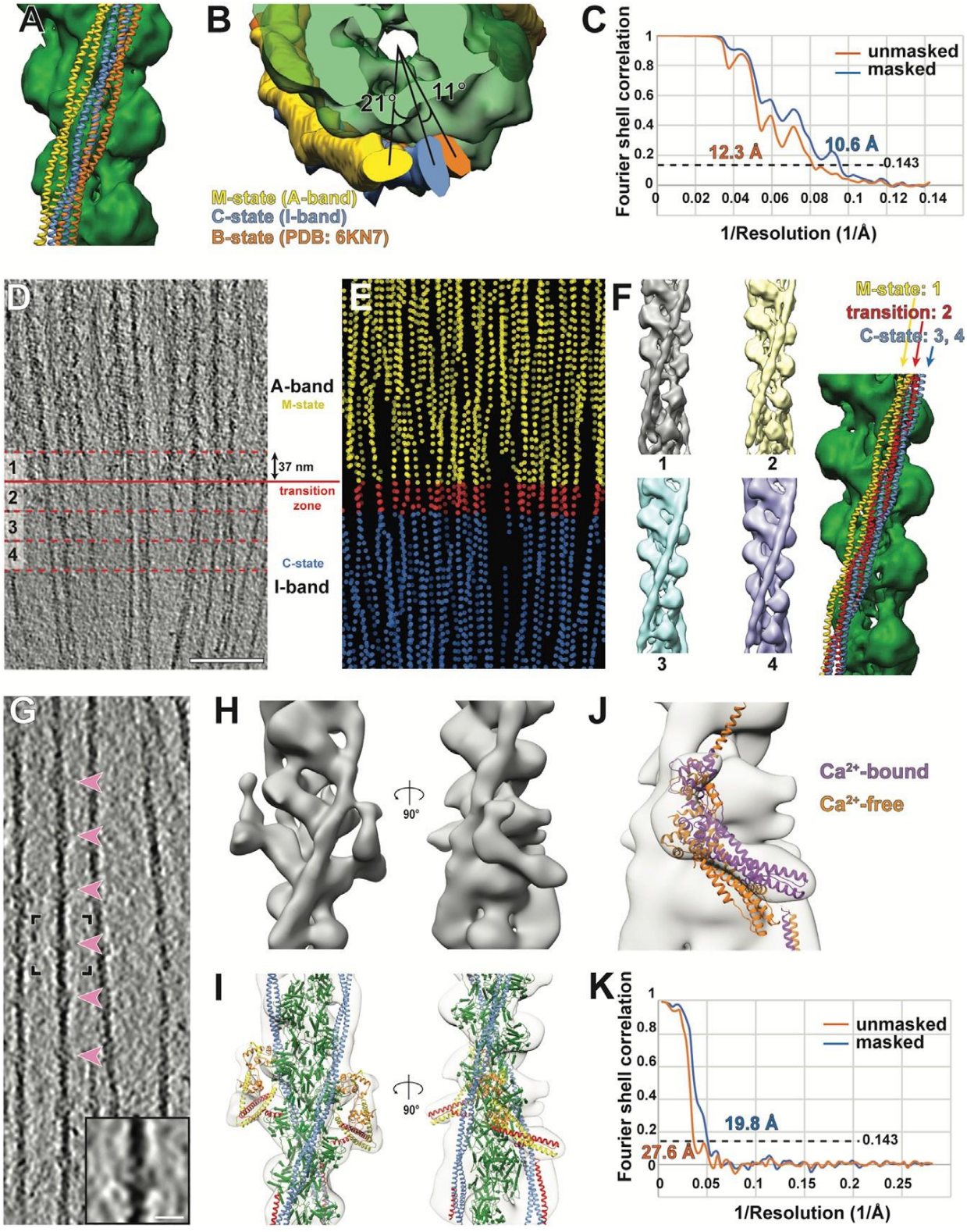

Fig. 4.17 Sub-volume averaging of the thin filaments in the I-band

*(**A** and **B**) Comparison of tropomyosin positions in different regions of the sarcomere. Side (A) and top (B) views of a thin filament with tropomyosin in the A-band (yellow) and I-band (blue). Tropomyosin is in the M state in the A-band and resides in the C-state in the I-band. The two states differ by an azimuthal rotation of ~21°. The B-state tropomyosin from a model of Ca2+-free thin filament (PDB: 6KN7)*

*(orange) is also shown for comparison. (**C**) The estimated resolution of the reconstruction of a thin filament excluding troponin in the I-band is 10.6 Å using the 0.143 criterion. (**D**) Slice from a tomogram showing both A-band and I-band. The solid red line represents the border between the A-band and I-band. 37-nm sections separated by the red dotted lines were selected for separate sub-volume averaging. (**E**) 3D view of particles of the thin filaments in the same region as (D), colored based on the state of their tropomyosin position. All A-band particles exhibit the M- state tropomyosin position (yellow). Most I-band particles exhibit the C-state tropomyosin (blue). The particles in the closest 37-nm section in the I-band to the A- band (section 2 in (D)) exhibit an intermediate position of tropomyosin, and hence define a transition zone. (**F**) Averaged structures corresponding to sections 1-4 as indicated in (D). The structures were aligned to a non-decorated F-actin structure. Tropomyosin models fitted into the structures are shown on the right. Section 1 has the same tropomyosin position as the M-state structure. Section 3 and 4 has the same tropomyosin position as the C-state structure. Section 2 has an intermediate tropomyosin position between the M- and C-state, implying that this is the section where the transition occurs. (**G**) Slice of a tomogram depicting thin filaments in the I-band. Bulges along the filaments appear with a periodicity of ~37 nm (highlighted by pink arrow heads), corresponding to troponin complexes. An enlarged version of a pair of troponin complexes in the black inset is shown at the bottom-right corner, depicting clear extra densities. Scale bar, 10 nm. (**H**) 3D reconstruction of a thin filament decorated by a pair of troponin complexes obtained from sub-volume averaging. (**I**) A homology model based on the structure of the Ca2+-bound cardiac muscle thin filament (PDB: 6KN8) was fitted into the map. Actin, tropomyosin, troponin I, troponin T and troponin C are shown in green, blue, yellow, red, and orange, respectively. (**J**) The structure of troponin in the Ca2+-bound state (PDB: 6KN8) fits much better into the map than the structure of troponin in the Ca2+-free state (PDB: 6KN7). Together with the C-state position of tropomyosin (A and B), this indicates that the I-band thin filament is in the Ca2+-bound state. (**K**) The estimated resolution of the reconstruction of the thin filament including troponin in the I-band is 19.8 Å using the 0.143 criterion.*

To determine the location of this transition, we subdivided the tomograms in 37-nm sections around the A-band/I-band transition and averaged the thin filaments separately (Fig. 4.17D). The averages revealed that tropomyosin is in the M-state in A-band sections. In the first I-band section, tropomyosin is in an intermediate state between the M-state and C-state and from the second I-band section, it occupies the C-state position (Fig. 4.17F). This suggests that, contrary to previous predictions, the M- to C- state transition happens mostly within one tropomyosin unit and occurs at the section immediately after the A-band/I-band transition.

4.2.6 Different forms of the Z-disc and the organization of α-actinin network

The irregular pattern of thin filaments resumes an ordered state when the filaments approach the Z-disc (Fig. 4.16G). In contrast to the exact square patterns observed in Z-discs from midshipman fish sonic muscle (Burgoyne et al., 2019) and rat soleus and cardiac muscle (Goldstein et al., 1990), the Z-discs in our reconstructions are slightly less well ordered and form squared to more rhomboid patterns (Fig. 4.16G,H, and Fig. 4.18). This is likely due to the fact that we used single myofibrils instead of complete muscles, where Z-discs are laterally anchored and stabilised. Antiparallel thin filaments in the Z-disc with opposing polarities are connected by 33-nm long cross-links, which we attribute to α-actinin (Ribeiro et al., 2014; Takahashi and Hattori, 1989) (Fig. 4.18G–I and Fig. 4.19D).

By comparing Z-discs from different reconstructions, we found different Z-discs varied in thickness, ranging from ~80 nm to ~100 nm (Fig. 4.18A–F, Fig. 4.19A,B). Thicker Z-discs are more compact than thinner ones (thin filaments are closer laterally) (Fig. 4.18A–F and Fig. 4.19B). Interestingly, although the mean length of α-actinin is similar in all Z-discs (Fig. 4.19D), the average angle between α-actinin and actin filaments in direction to the pointed end differs considerably, ranging from ~158° in the thickest and ~128° in the thinnest form (Fig. 4.19A).

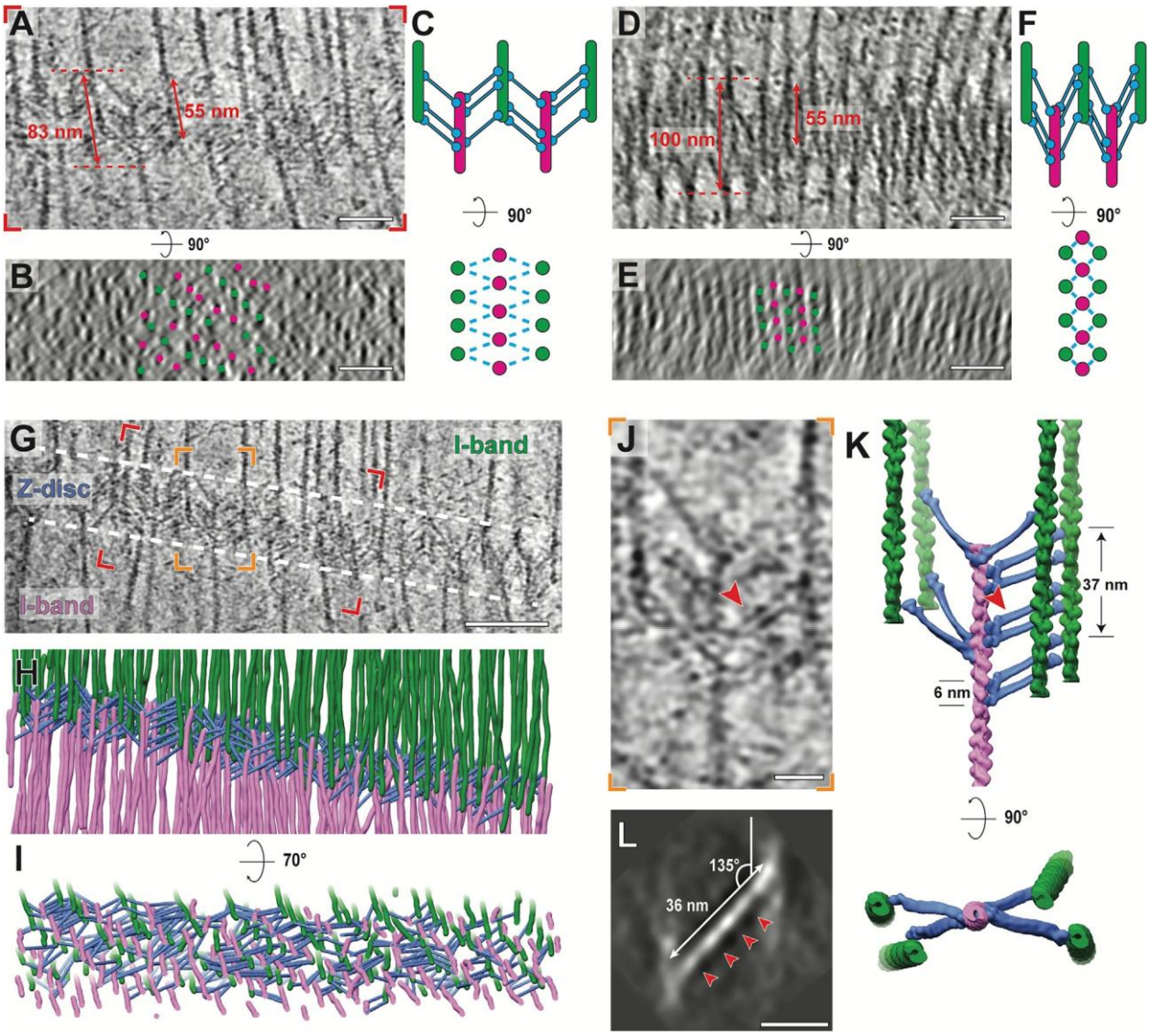

Fig. 4.18 Different types of Z-discs from fast mouse psoas myofibril and α-actinin organization in the thinner form

*(**A**–**C**) XY slice view (A), equator-filtered cross-section view (B), and a schematic diagram showing the pattern (C) of a Z-disc in the thinner form within a tomogram. The thickness of the Z-disc was measured between where α-actinins bind to the antiparallel thin filaments. The length of a single thin filament within the Z-disc was also measured. The organization of the filaments in this Z-disc is rhomboidal, likely resulting from a tilted orientation of the Z-disc on the grid and a slight stretching of the myofibril. We used this Z-disc for our analysis because most of the α-actinin densities could be unambiguously assigned. Scale bar, 50 nm. (**D**–**F**) XY slice view (D), cross-section view (E), and a schematic diagram of a tomogram showing a Z-disc in the thick form with a square pattern (F). This is the predicted organization of a Z-disc from skeletal muscle. However, it is difficult to assign individual α-actinin densities in these tomograms hampering a non- biased annotation. Scale bar, 50 nm. (**G**) Slice through the same tomogram as (A) depicting the thin-form Z-disc and two I-bands. Scale bar, 100 nm. (**H**) Cryo-ET based 3D model of the Z-disc showing antiparallel thin filaments from two adjacent sarcomeres*

*(green and magenta) and the α-actinins (blue) cross- linking the filaments. (**I**) Tilted view of the model shown in (H). (**J**) Slice of an example unit in the Z-disc depicting one thin filament with its neighboring antiparallel thin filaments and the α-actinins connecting them. A doublet of α-actinins is highlighted by a red arrow head. Scale bar, 20 nm. (**K**) Cryo-ET-based 3D model of the same region in (J). Actin filament model is derived from the thin filament reconstruction in Fig. 4.16A, excluding tropomyosin. The α-actinin model is derived from the crystal structure of an α-actinin dimer (PDB: 4D1E). (**L**) Projection image (7-nm thickness) of the 3D reconstruction of α-actinin obtained from averaging the sub-volumes as picked in (H) and (I), depicting four domains (marked by red arrow heads) which correspond to the four spectrin-like repeats (SRs) in the rod region. Scale bar, 20 nm.*

We propose that the different forms of Z-discs represent conformational states of the sarcomeric unit. We hypothesise that post-isolation mechanical factors, such as different on-grid blotting forces before freezing, increase the stress/strain in some myofibrils. The angle between actin and α-actinin becomes more acute and the Z-discs fold together like a parallel hinge, resulting in the thicker appearance of the Z-disc (Fig. 4.18D–F, Fig. 4.19A, B). This situation is likely similar to activated myofibrils under tension (Pavlov et al., 2009). Thinner forms possibly represent the Z-disc under low strain/stress, where the angle between actin and α-actinin is more obtuse (Fig. 4.18A–C, Fig. 4.19A, B). Considering a stable interaction interface between the actin-binding domain of α-actinin and actin filaments (Iwamoto et al., 2018) and the rigidity of the rod region of α-actinin (Ribeiro et al., 2014), the flexibility in the neck be- tween the rod and the actin-binding domain (ABD) of an α-actinin probably serves as the central hinge of this pivot-and-rod structure (Gautel and Djinović-Carugo, 2016). In order to experimentally validate that stress/strain induces different conformations of the Z-disc, activated myofibers will have to be vitrified under defined strain/stress conditions prior to cryo-ET analysis in the future.

We annotated all clearly visible densities in the thinner Z-disc where single α-actinin densities were more apparent to understand the α-actinin organization between antiparallel thin filaments (Fig. 4.18G). Top and side views of the resulting three-dimensional model reveal that α-actinin forms a mesh by cross-linking the actin filaments, which is less well ordered than anticipated from the projection (Fig. 4.18G–I) or from idealized helical models in previous work (Luther, 2009). A prominent and unexpected feature is a doublet of α-actinin cross-links with 6 nm spacing, which is only possible when two α-actinins bind to longitudinally adjacent

actin subunits along the actin filament (Fig. 4.18J, K, and Fig. 4.19F). We observe up to three of these α-actinin pairs connecting two antiparallel thin filaments over ~37 nm, at ~18.5-nm intervals. Thus, although the spacing of these doublets follows the 37-nm actin helical repeat, it places individual α-actinin molecules closer together (maximally 12 nm rather than 18.5 nm) than previously presumed. Doublets have also been observed in an in vitro reconstituted α-actinin-F-actin raft (Hampton et al., 2007). Our analysis shows that this arrangement was not an in vitro artifact but a feature of native sarcomeres. Interestingly, these doublets were not apparent in the recent reconstruction of the F-actin-α-actinin complex from branched cardiac myofibrils obtained through sub-volume averaging, in which the angles between α-actinin and actin resemble the thick-form Z- disc (Oda and Yanagisawa, 2020). Importantly, as single α-actinins were not distinguishable in these tomograms, this study relied strongly on sub-tomogram averaging at certain positions, assuming a highly symmetric Z-disc. However, our visualization of the Z-disc illustrates that it is a heterogeneous, non-symmetrical structure. The doublets, which are not present at regular intervals, were therefore probably lost during sub-volume averaging of the Z-disc or are not present in cardiac myofibrils.

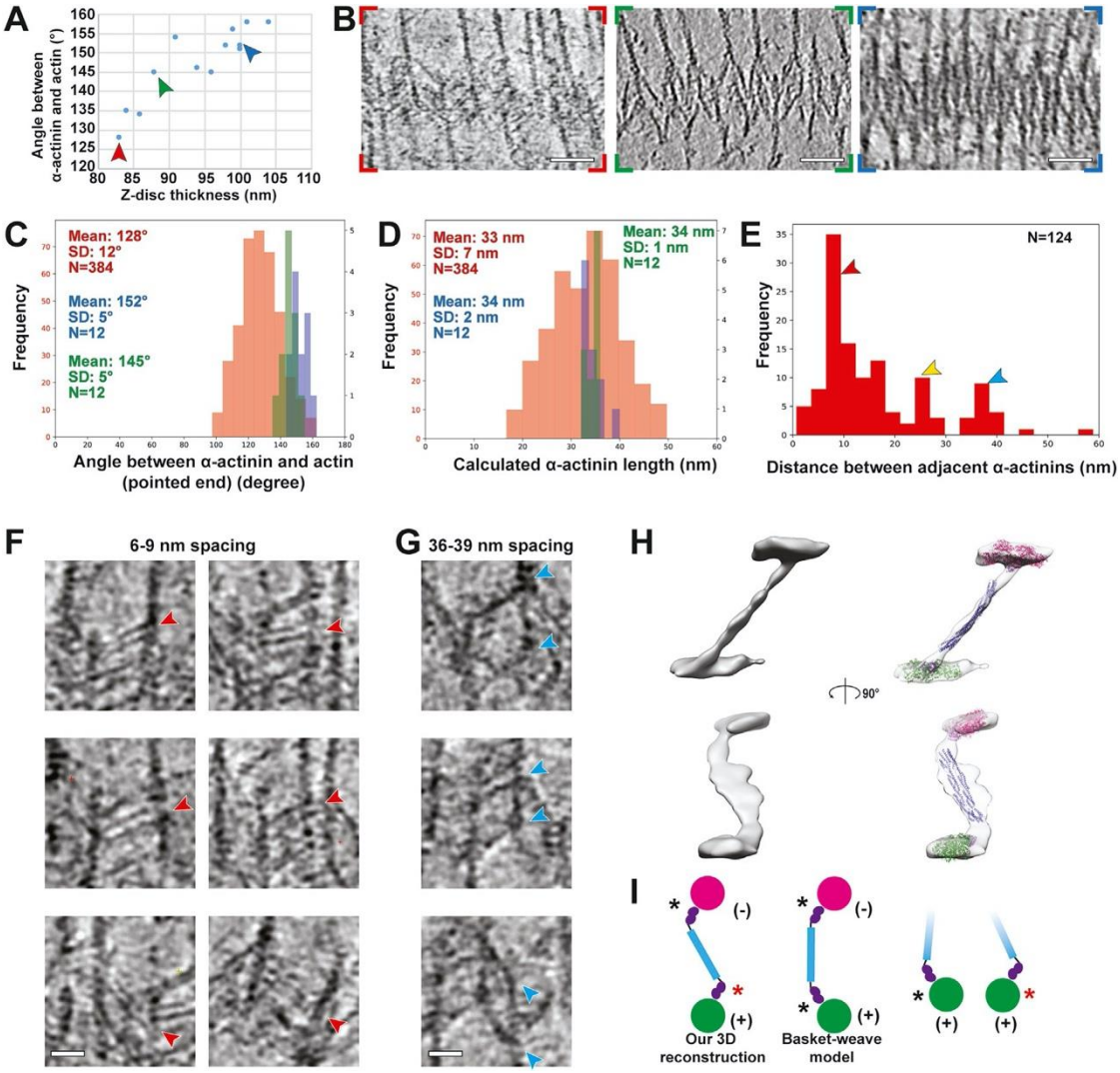

Fig. 4.19 α-Actinin structure and organization in the Z-disc

*(**A**) Plot relating the thickness of Z-discs and the angle between α-actinins and the pointed end of actin filament from different tomograms. The positive correlation implies a parallel hinge mechanism of the Z-disc. (**B**) Slices through tomograms depicting a thin Z-disc (left, red arrow in (A)), a thick Z-disc (right, blue arrow in (A)) and a Z-disc of intermediate thickness (middle, green arrow in (A)). Scale bar, 50 nm. (**C**) Distribution of the calculated angles between annotated α-actinins and actin filaments in direction to the pointed end in the thin (red), thick (blue) and intermediate-thickness (green) Z-discs. The y axis for both the thick and intermediate Z-disc is shown on the right in black. There are more data points for the thin Z- disc as it was completely annotated, while a few examples of α-actinin were selected for the intermediate and thick Z-discs. (**D**) Distribution of the length of annotated α-actinin in the thin (red), thick (blue) and intermediate-thickness (green) Z-discs. The distance along α-actinin between the centres of the connecting actin filaments was measured and the length of α-actinin was calculated by subtracting the diameter of an actin filament (6 nm). The relatively large standard deviation in the thin form Z-disc is likely caused by α-actinins binding to actin filaments at different*

*azimuthal orientations and the error in the precise determination of the central axis of actin filaments. (**E**) Distribution of the calculated spacing between adjacent α-actinins in the thin Z-disc. The red, yellow, and blue arrow heads highlight peaks at 6-9 nm, 24- 27 nm and 36-39 nm, respectively. The 24-27 nm peak appears as a result of the two other types of spacing (36 - 2x6). (**F** and **G**) Example images showing α-actinins with the 6-9 nm spacing (D) and the 36-39 nm spacing (E). Arrow heads highlight the positions and orientations of α-actinins. Scale bar, 20 nm. (**H**) 3D reconstruction of α-actinin obtained from sub-volume averaging. Although there is a strong missing wedge effect resulting in an elongation of the reconstruction in one direction, we were able to manually fit atomic models derived from the crystal structure of α-actinin (PDB: 4D1E) and the cryo-EM structure of actin filaments bound by the first calponin homology domain of the actin binding domain (PDB: 6D8C) into the density. Actin filaments are shown in magenta and green; the actin binding domain and the rod region are depicted in purple and blue, respectively. The flexible neck regions and the C-terminal calmodulin-like domains are not shown. (**I**) Left: Schematic diagram showing the difference between averaged α-actinin structure and the conventional basket-weave model. Right: The two different interactions (marked by the red and black asterisks) between the end of α-actinin and actin filaments (magenta and green) are demonstrated on the right, formed by the flexible neck region between the rod (blue) and actin binding domain (purple).*

Consistent with previous studies (Burgoyne et al., 2019; Luther and Squire, 2002), we observed several ~37 nm spaced α-actinin cross-links (Fig. 4.18E,G), which corresponds roughly to the half-helical pitch of actin filaments. However, we also observed α-actinins that do not follow this pattern (Fig. 4.18J, K, and Fig. 4.19E) suggesting a less ordered organization of the Z-disc than previously assumed or inferred from atypical actin-α-actinin arrays in nemaline rods or midshipman muscle (Burgoyne et al., 2019; Morris et al., 1990). By performing sub-volume averaging of the α-actinin positions, we could show that it connects opposite sides of antiparallel actin filaments, forming a slight ‘‘S’’ shape (Fig. 4.19H). The actin binding domains and the central rod region of an α-actinin from the crystal structure (Ribeiro et al., 2014) fit well into the density (Fig. 4.19H), and the four spectrin-like repeats can be clearly distinguished in a projection of the reconstruction (Fig. 4.19L). This ‘‘S’’ shape fits well to the α-actinin crystal structure (Ribeiro et al., 2014), considering the flexibility in the neck region, but differs from the conventional ‘‘basket-weave’’ model that is derived from observations of transverse sections of Z-discs (Ullrick et al., 1977). In order to form the S shape, the two ends of an α-actinin, where it interacts with actin filaments, need to have different conformations;

one end resembling that of the basket-weave model with the other end in an alternate conformation that interacts with actin differently at the flexible neck region (Fig. 4.19I). Future studies at a higher resolution will elucidate the molecular basis of this interaction and shed light on the organization of other proteins in the Z-disc, such as accessory smaller proteins like ZASP, myotilin or FATZ that may play a role in α-actinin dimerization, or to visualize the position of the α-actinin-binding Z-repeats of titin or the actin-binding repeats of nebulin. The potential contribution of these proteins to the arrangement of α-actinin doublets would also be of fundamental interest for understanding diseases of the Z-disc with aberrant arrangement of α-actinin like actininopathies (Savarese et al., 2019), zaspopathies (Griggs et al., 2007), nemaline myopathies (Wallgren-Pettersson et al., 2011), or myofibrillar myopathies (Selcen and Engel, 2011).

4.2.7 Conclusions and limitations of the study

Cryo-FIB milling combined with cryo-ET enabled us to visualize native vertebrate sarcomeres in three-dimensions with minimal artifacts or damage. Our structure of the actomyosin complex shows the complete myosin double head in the rigor state in molecular detail and pinpoints the ELC/RLC interface as the position within myosin crucial for the structural rearrangement of the double head when bound to the thin filament. In addition, our model of the sarcomere shows a pseudo-regular distribution of myosin cross-bridges in the A-band. An irregular pattern of the I-band thin filaments illustrates the importance of the cross-bridge and the Z-disc in maintaining the regularity of thin filaments within the sarcomere. Our observation that the thin filaments and cross-links of α-actinin within the Z-disc can accommodate different arrangements demonstrates the need for the sarcomere to respond to and accommodate the collective forces exerted on it during muscle contraction. Collectively, our high-resolution structure of the sarcomere, although not yet a complete atomic model of the entire structure, identifies previously unresolved details of the molecular architecture of A-bands, I-bands, and Z-discs and highlights the molecular plasticity of its components. It allows improved dynamic modelling of muscle contraction and will serve to test new concepts on the molecular, cellular, and physiological level, not least for the development of new approaches for investigating muscle diseases.

Although this study provided an overall picture of the skeletal sarcomere, subsequent work needs to be performed to address a number of missing pieces arising from this research. In this study, we focused on sarcomeres from skeletal muscle in rigor, where the myosin cross-bridges are locked in a strong-binding state. Other states of the cross-bridge cycle need to be investigated in order to provide a dynamic understanding of muscle contraction. This study could not include an analysis of M-band proteins, MyBP-C, or other less regularly arranged proteins that also play an essential role in sarcomere regulation, function, and plasticity. Additional *in situ* labelling methods in future studies will help to elucidate the organization of these less common and less organised proteins. In the analysis of Z-discs of different thicknesses, our hypothesis that the different Z-disc conformations may correspond to the different stain/stress states of the sarcomere should be validated experimentally using custom approaches where muscle can be examined under defined load. Future studies using greater numbers of tomograms acquired on myofibrils should help to improve the resolution of structures obtained in this study to achieve insights on the atomic level.

4.3 *In situ* structures of nebulin within native sarcomere

This section was originally published in *Science* in 2022:

Wang, Z., Grange, M., Pospich, S., Wagner, T., Kho, A.L., Gautel, M., and Raunser, S. (2022). Structures from intact myofibrils reveal mechanism of thin filament regulation through nebulin. *Science* 375: eabn1934

Online version: https://www.science.org/doi/10.1126/science.abn1934

The characterisation of *in situ* structures of nebulin and actomyosin was performed with the help of Dr. Michael Grange. Dr. Michael Grange improved the resolution from sub-tomogram averaging using the M software. In addition, atomic models of nebulin, actin and myosin heavy chain was built by Dr. Sabrina Pospich. Computational tools for automatic filament picking and statistcal analysis were implemented by Dr. Thorsten Wagner. Myofibrils were isolated by Dr. Ay Lin Kho and Prof. Mathias Gautel.

The accepted version of the publication was reformatted to be adapted in this thesis. Supplementary figures were integrated into the main text and split when necessary to facilitate reading. Myofibrils were prepared and frozen as described in sections 3.1 and 3.2, respectively. Detailed protocols of FIB-milling, cryo-ET data acquisition and general sub-tomogram averaging are provided in sections 3.3, 3.4 and 3.5, respectively. Specific methods for this section and supplementary information was moved to Appendix. Supplementary videos are not included in the thesis but can be downloaded in the online version of the publication. The text and figures of the accepted manuscript are used in this thesis with the permission from AAAS.

4.3.1 Abstract

In skeletal muscle, nebulin stabilises and regulates the length of thin filaments, but the underlying mechanism remains nebulous. Here, we used electron cryo-tomography and sub-tomogram averaging to reveal structures of native nebulin bound to thin filaments within intact sarcomeres. This in situ reconstruction provided high-resolution details of the interaction between nebulin and actin, demonstrating the stabilising role of nebulin. Myosin bound to the thin filaments exhibited different conformations of the neck domain, highlighting its inherent structural variability in muscle. Unexpectedly, nebulin did not interact with myosin or tropomyosin, but with a troponin-T linker through two potential binding motifs on nebulin, explaining its regulatory role. Our structures support the role of nebulin as a thin filament "molecular ruler" and provide a molecular basis for studying nemaline myopathies.

4.3.2 Structured abstract

INTRODUCTION:

Muscles underpin movement and heart function. Contraction and relaxation of muscles relies on the sliding between two types of filaments - the thin filament (comprising mainly F-actin, tropomyosin, and troponin) and the thick myosin filament. In addition, several other proteins are involved in the contraction mechanism and their mutational malfunction can lead to debilitating and even life-threatening diseases. One such component in skeletal muscle, nebulin, binds to the thin filaments and stabilizes them. It is also responsible for maintaining the length of thin filaments and is involved in regulating myosin binding. Mutations in the nebulin gene are closely linked to a group of muscle diseases called nemaline myopathies.

RATIONALE:

The mechanism underlying nebulin stabilization and regulation of thin filaments remains nebulous due to missing structural information of the protein. To investigate the structure of nebulin in its native environment, we prepared myofibrils from skeletal and cardiac muscle by focused-ion beam milling and imaged them using electron cryo-tomography (cryo-ET). Since nebulin is only present in skeletal but not cardiac muscle, this approach allowed us to unambiguously identify and characterize nebulin in the native muscle.

RESULTS:

We resolved nebulin bound to the thin filament within myofibrils isolated from mouse psoas muscle at near-atomic resolution. The structure reveals a 1:1 binding stoichiometry between nebulin repeats and actin subunits. Different nebulin repeats have the same physical length despite their slightly varying size, supporting the role of nebulin as a "molecular ruler". A nebulin repeat interacts with all three neighbouring actin subunits, which explains how nebulin stabilizes the thin filament. In addition, the position of nebulin on the filament demonstrates that it does not interact with tropomyosin or myosin, but likely with a troponin T (TnT) linker. Our reconstruction of myosin shows that the myosin double-head exhibits inherent variability within a sarcomere, and that nebulin does not alter actin-myosin interactions directly. Therefore, we propose that the myosin-binding regulatory role of nebulin is through its potential interaction with TnT.

CONCLUSION:

Our results show that nebulin is an integral component of the thin filament in skeletal muscle. The interactions between nebulin and the thin filament set the molecular basis for its function and proper muscle contraction. Our structure of nebulin enables the development of experimental models that further help to reveal how mutations responsible for nemaline myopathies impact on nebulin's function in the sarcomere. Our approach, using focused-ion beam milling and cryo-ET to study proteins of muscles at high resolution, paves the way for studying other muscle components in the future to understand muscle diseases at the molecular level.

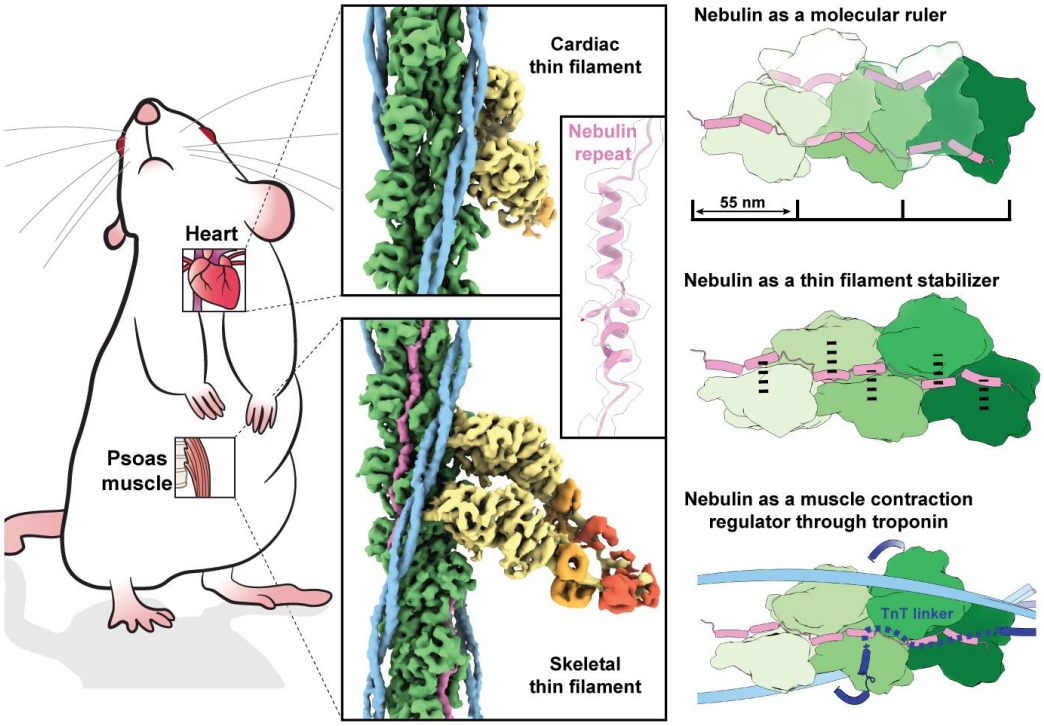

In situ structure of nebulin on the thin filament from mouse skeletal muscle.
Nebulin, resolved at a resolution of 4.5 Å, was identified through comparing cardiac and skeletal thin filament structures. The structure of nebulin reveals the mechanism underlying its function to maintain the length and stability of the thin filament, as well as regulating muscle contraction. Actin, nebulin, tropomyosin, myosin heavy chain, myosin essential light chain and myosin regulatory light chain are coloured in green, magenta, light blue, dark blue, yellow, orange and red, respectively.

4.3.3 In situ position of nebulin on thin filaments

We determined the structure of the core of the thin filament from intact myofibrils isolated from mouse psoas muscle to 4.5 Å resolution (Fig. 4.20) and with actomyosin resolved to 6.6 Å resolution (Fig. 4.21A-C). In the core of the thin filament, two extra continuous densities were visible alongside the actin filament (Fig. 4.21A-C). The elongated structure predicted for nebulin (Pfuhl et al., 1994) suggested that this density might be natively organised nebulin bound to the thin filament. To verify this putative identification, we determined the in situ actomyosin structure in the A-band from cardiac muscle (Fig. 4.21E). Nebulin is barely expressed and only present in small subpopulations of myofibrils in cardiac muscle. The

averaged reconstruction of the cardiac thin filament, determined to an overall resolution of 7.7 Å with the core of the thin filament resolved to 6.3 Å, depicts similar organisations of actin, myosin and tropomyosin. Notably, the extra density observed in skeletal actomyosin was missing (Fig. 4.21E), consistent with this density corresponding to averaged segments of nebulin.

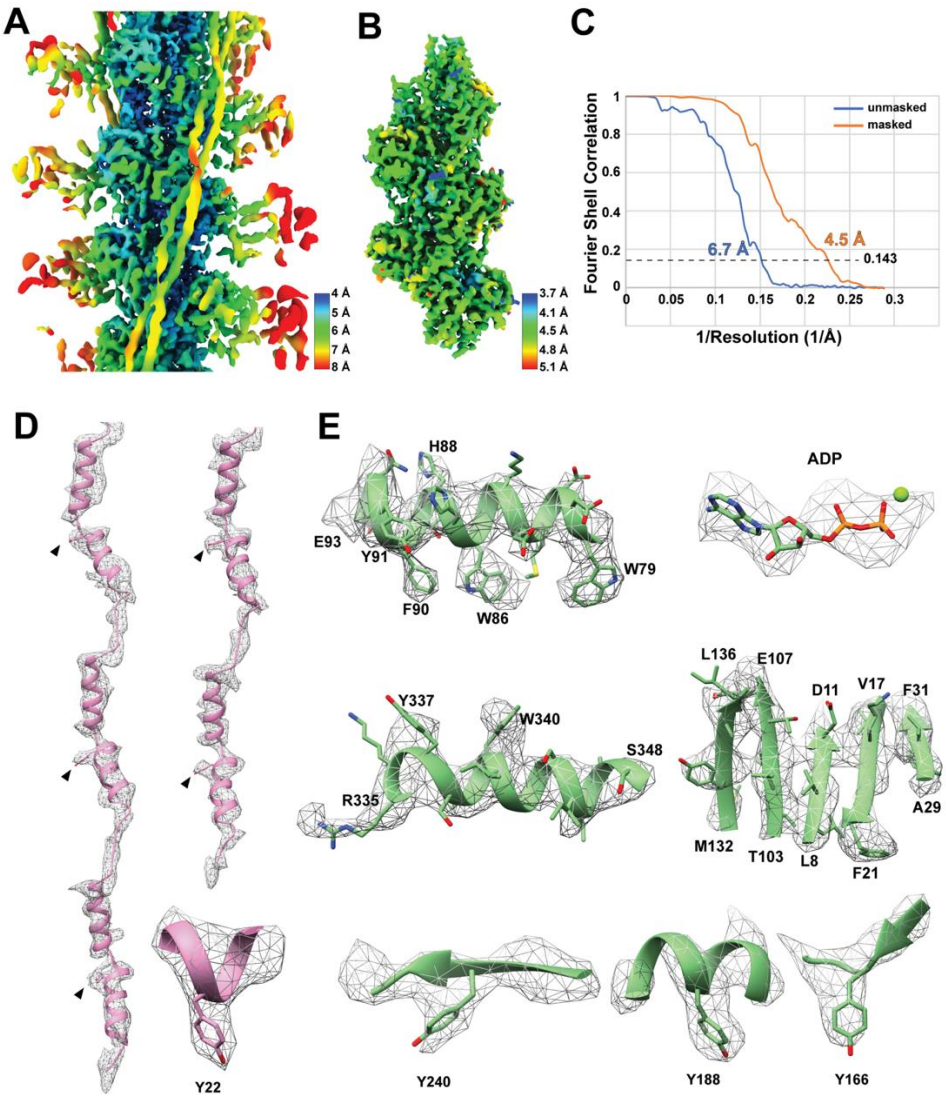

Fig. 4.20 EM density map and structural model of actin and nebulin obtained from sub-tomogram averaging

(A) *Local resolution estimation of the unmasked thin filament. The map is filtered to local resolution.* ***(B)*** *Local resolution estimation of the masked core of the thin filament including actin and nebulin.* ***(C)*** *Gold-standard FSC curve of the actin-nebulin structure. The unmasked and masked structures correspond to the maps in (A) and (B), respectively.* ***(D)*** *Nebulin model and corresponding cryo-EM density map. The conserved tyrosine residues are marked with arrow heads. A zoom-in view of an*

example of tyrosine 22 and corresponding density is shown. ***(E)*** *Examples of side chain density visible in the actin portion of the cryo-EM density map. A few tyrosine residues are selected for comparison with the tyrosine side chain densities in nebulin.*

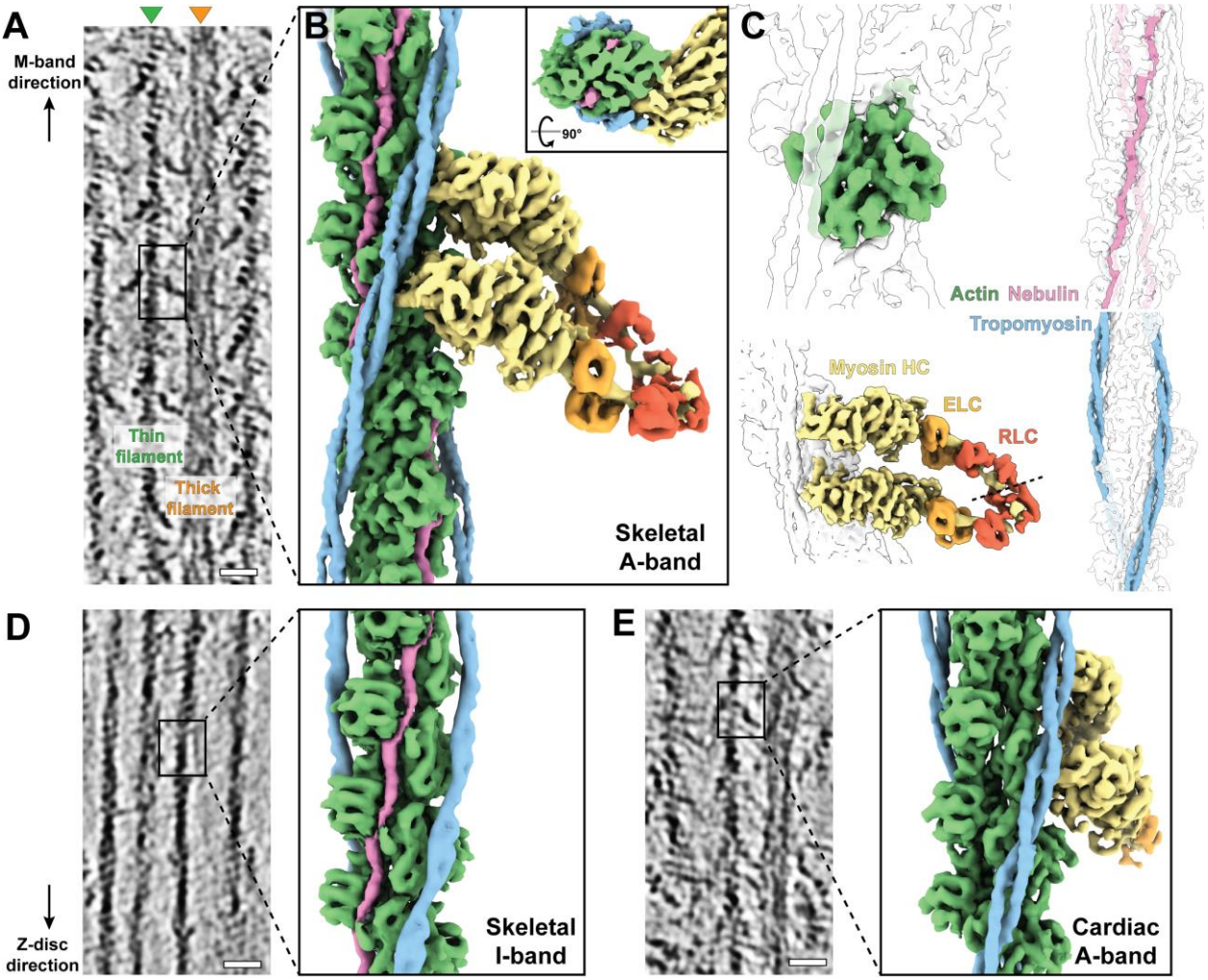

Fig. 4.21 Thin filament structures in striated muscle sarcomeres.

(A) *Tomographic slice of skeletal sarcomere A-band depicting adjacent thin and thick filaments.* ***(B)*** *Actomyosin structure from the skeletal sarcomere A-band consisting of actin (green), myosin (heavy chain (HC): yellow, essential light chain (ELC): orange, regulatory light chain (RLC): red), tropomyosin (blue) and nebulin (magenta). Myosin is a composite map including light chains from different averaged structures (see Fig. 6.7A). Cross-section view of the structure is shown in the inset.* ***(C)*** *Different components of a thin filament and their position highlighted within the structure. The dotted line highlights the interface between the two RLCs of the trailing and leading myosin head.* ***(D)*** *Tomographic slice of a skeletal sarcomere I-band and structure of the thin filament (inset).* ***(E)***

Tomographic slice of a cardiac sarcomere A-band and structure of actomyosin, including a pair of myosin double-heads. All tomographic slices are 7 nm thick. Scale bars: 20 nm

Nebulin was observed in the grooves between the two strands of the actin filament, following their helical turn (Fig. 4.21B). Nebulin occupies a site that is known to be bound by actin-stabilising compounds such as phalloidin and jasplakinolide (Pospich et al., 2020) (Fig. 4.22). This may explain why excessive phalloidin can unzip nebulin from thin filaments (Ao and Lehrer, 1995) and may also suggest a similar mechanism of F-actin stabilisation. Similar to phalloidin, nebulin binding to F-actin did not alter the helical arrangement of F-actin or the conformation of the actin subunits (Fig. 4.23A,B). A single actin filament was decorated by two nebulin molecules on the opposite sides (Fig. 4.21B). In order to ascertain the molecular organisation of nebulin in different regions of a sarcomere, we also determined the structure of the thin filament in the skeletal muscle I-band to a resolution of 7.4 Å (Fig. 4.21D). Nebulin appeared in the I-band at the same position on the thin filament as was observed within the A-band (Fig. 4.21D), indicating that nebulin spans most of the thin filament (Castillo et al., 2009; Kiss et al., 2020). This suggests that nebulin maintains a structural role within the sarcomere. Notably, the position of nebulin bound to actin from native skeletal muscle is different from the three putative sites previously proposed on the outer surface of the actin filament based on reconstituted actin-nebulin fragment complexes (Lukoyanova et al., 2002). The observed differences could represent the limitations of the use of in vitro fragments of nebulin or suggest different interaction patterns during sarcomerogenesis.

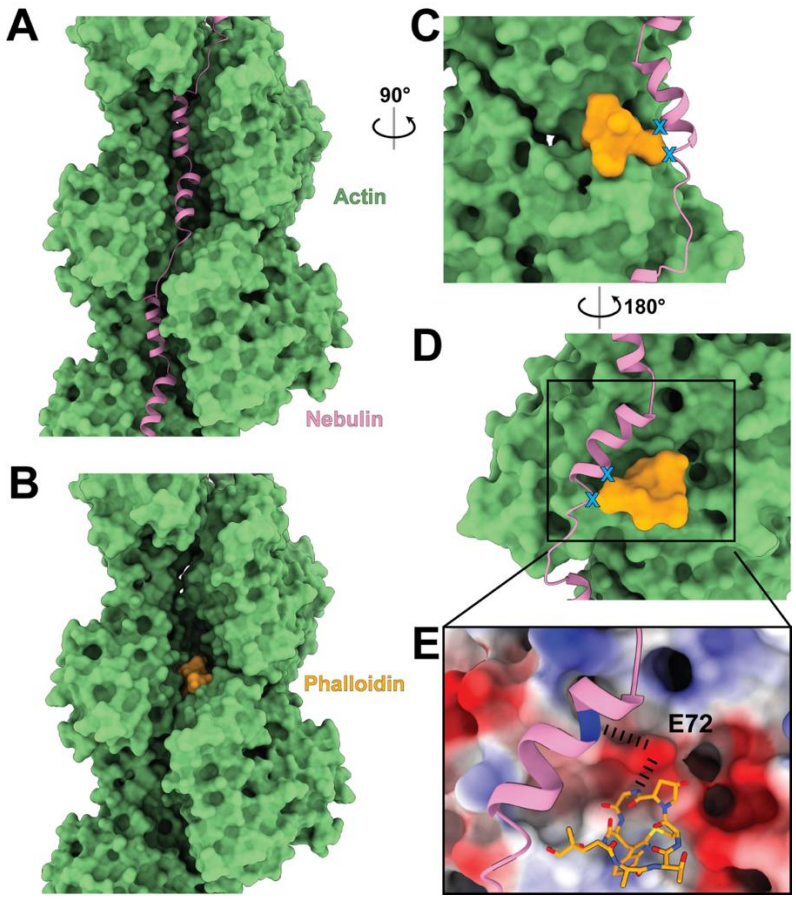

Fig. 4.22 Comparison of nebulin and phalloidin binding sites on the actin filament.
(A,B) *Position of nebulin and phalloidin (from PDB: 6T1Y) on the actin filament, respectively.* ***(C,D)*** *Comparison of the position of both nebulin and phalloidin from different views. Steric clashes would happen at the end of H2 of nebulin if both were present at the same time (marked by blue crosses).* ***(E)*** *E72 on actin is involved in both forming a hydrogen bond with phalloidin and electrostatic interactions with nebulin.*

The position of nebulin implies that it does not interact with tropomyosin (Fig. 4.21B). The subdomain 3 and 4 (SD3, 4) of adjacent actin monomers physically separate nebulin from tropomyosin, regardless of the tropomyosin state at different Ca^{2+} concentrations (Poole et al., 2006) (Fig. 4.23C-F). This is contradictory to previous results from in vitro experiments (Marttila et al., 2014). The discrepancy between our *in situ* structures and in vitro assays again demonstrates that nebulin may have different properties when purified, compared to its native state in a sarcomere. Purified large fragments of nebulin are extremely insoluble when expressed (Chitose et al., 2010; Gonsior et al., 1998; Zhang et al., 1998). Both rotary shadowed images of nebulin (Chitose et al., 2010) and the structure of nebulin predicted by the machine-

learning-based software, AlphaFold (Jumper et al., 2021), suggest non-filamentous structures. These visualisations clearly deviate from the elongated shape of nebulin when bound to actin filaments. Our approach of investigating nebulin inside sarcomeres thus provides in situ structural information about nebulin interactions with the thin filament that are not accessible by sequence-based structure prediction programs or from isolated proteins. Furthermore, during sarcomerogenesis, nebulin integration into the thin filament is likely to require cellular cofactors to prevent the formation of aggregates or large globular structures.

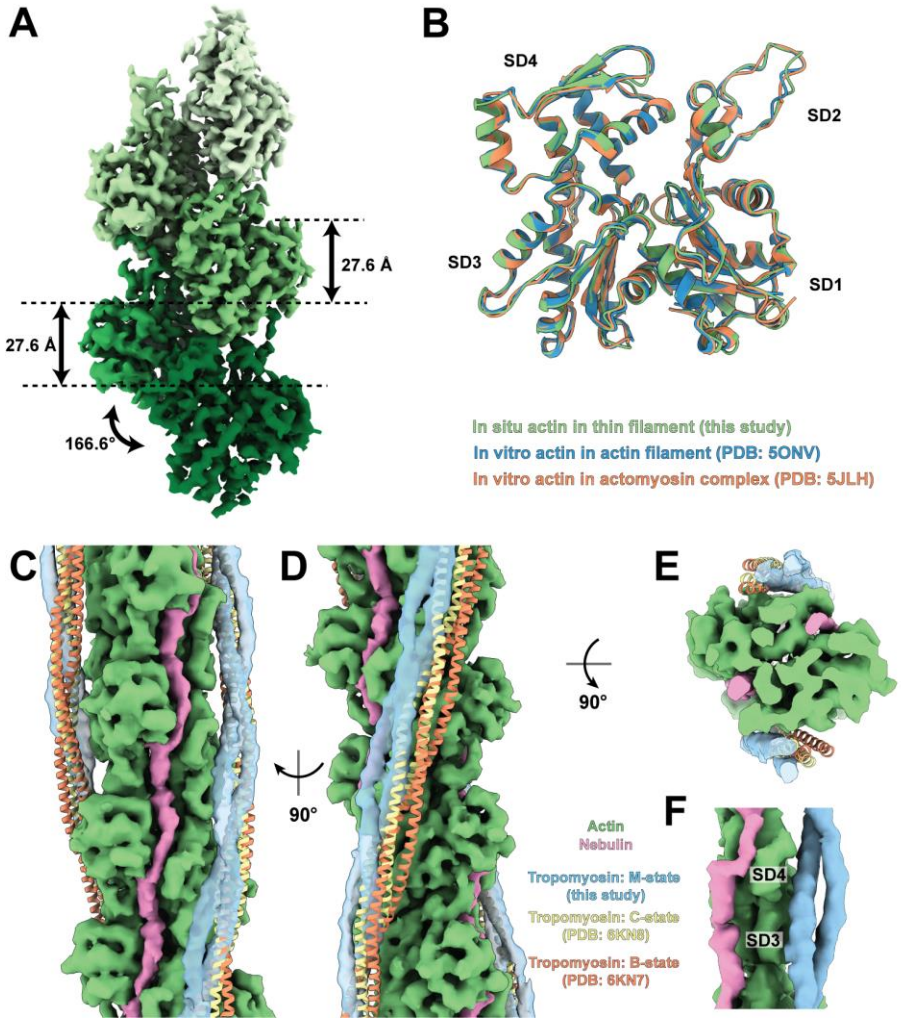

Fig. 4.23 Actin in a thin filament and different tropomyosin states on a thin filament.
(A) *Helical parameters of F-actin determined within a thin filament in a sarcomere.* ***(B)*** *Comparison of the structures of actin subunit from different filamentous structures.* ***(C-E)*** *Different views depicting a thin filament including nebulin and different states of tropomyosin.* ***(F)*** *Zoom-in view of nebulin, tropomyosin and actin depicting the physical separation between nebulin and tropomyosin by the SD3 and 4 of actin subunits.*

4.3.4 Myosin double-head does not interact with nebulin and has high variability

Nebulin has been shown to regulate the actin-myosin cross-bridge cycle. It can increase thin filament activation, promote myosin binding and thus improve the efficiency of contraction (Bang et al., 2009; Chandra et al., 2009; Kiss et al., 2018). In vitro studies have suggested a direct interaction between a nebulin fragment and myosin (Jin and Wang, 1991; Root and Wang, 1994). In our rigor state sarcomere structures, two myosin heads from a single myosin molecule are bound to the thin filament in most cross-bridges, forming a double-head. However, the myosin heads do not interact with nebulin (Fig. 4.21B) nor does nebulin alter the interactions between actin and myosin (Fig. 4.24B).

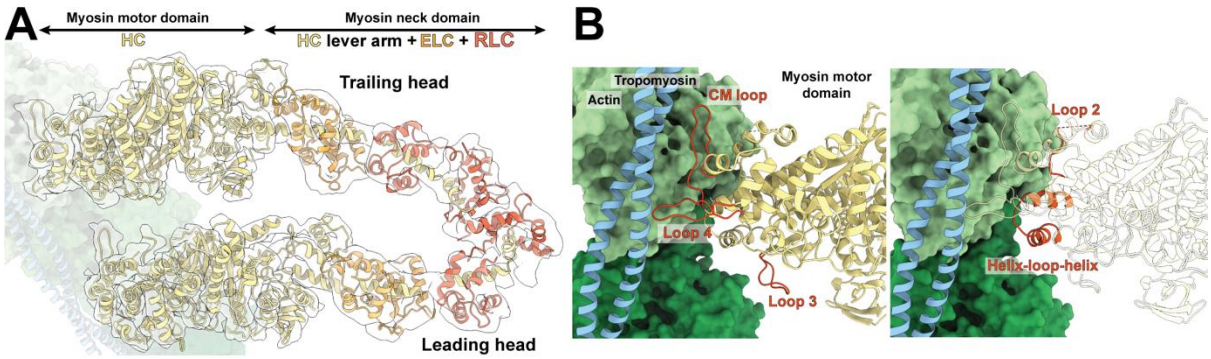

Fig. 4.24 Structure of a myosin double-head

(A) *Composite EM density map and a complete structural model of a myosin double-head when bound to a thin filament.* ***(B)*** *Actin-myosin interaction interface. Loops on myosin involved in the interaction with actin are highlighted in red.*

Having a better-resolved structure available (~9 Å in the neck domain), we were able to accurately fit the lever arms and light chains of myosin based on their secondary structure elements (see Appendix, Fig. 6.7), completing the model of the entire myosin double-head (Fig. 4.25A, Fig. 4.24). Notably, the angles of the kinks in the lever arm helix are different between the two heads (Fig. 4.25A). Especially the kink between the two regulatory light chain (RLC) lobes differs considerably in the two heads, resulting in the clamp-like arrangement of the neck domains (Fig. 4.25B). The RLC-RLC interface resembles that of the RLCs of the free and blocked head in an interacting-head-motif (IHM) of an inactive myosin (Scarff et al., 2020; Yang et al., 2020), but with a rotation of ~20° (Fig. 4.25C). Although the motor domains are similarly arranged in the cardiac muscle (Fig. 4.26A), our 12 Å reconstruction of the neck

domain clearly demonstrates that the interface between the two RLCs is different compared to the skeletal counterpart, resulting in a subtle difference in the arrangement of the two neck domains (Fig. 4.26B). Thus, our structures of myosin in the ON state in skeletal and cardiac muscles and previous structures of myosin in the OFF state (Scarff et al., 2020; Yang et al., 2020) imply natural variabilities within RLCs and at the RLC-RLC interface that allow a dynamic cooperation between the two myosin heads.

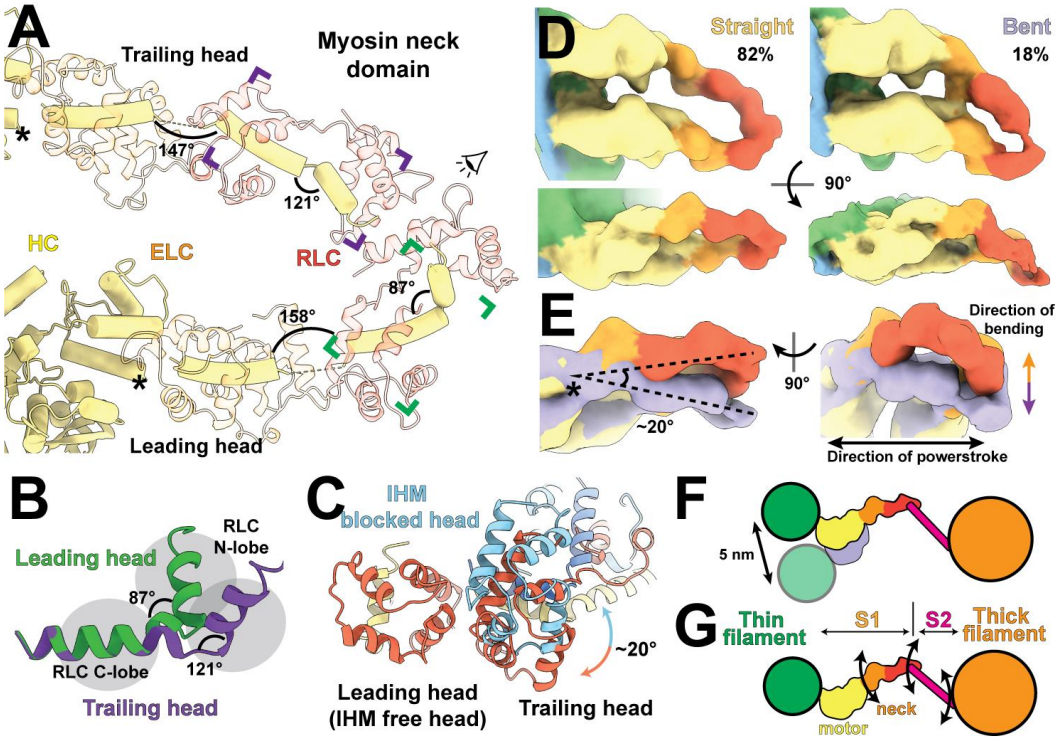

Fig. 4.25 Structural variability within the in situ myosin double-head in skeletal muscle.

(A) *The lever arms of the trailing and leading myosin heads form kinked helices (yellow). Different angles at the kinks between the two heads are labelled. ELCs and RLCs are shown as transparent models.* ***(B)*** *Different conformations of the lever arm at the RLC-binding regions of the trailing head (purple) and the leading head (green).* ***(C)*** *View from the eye symbol in (A) showing the interface between the RLCs from the trailing and leading head (red for RLC, yellow for lever arm helices) compared to the interface of the blocked head (aligned to the leading head) and the free head in the IHM (blue for RLC, dark blue for lever arm helices).* ***(D)*** *Two different conformations, straight and bent forms, of myosin double heads determined by 3D classification. HC, ELC and RLC regions are coloured in yellow, orange and red.* ***(E)*** *Comparison between the straight (orange) and bent (purple) double-head conformation. The origin of bending is marked by an asterisk, also in (A).* ***(F)*** *Schematic drawing describing the increased range of thin filament positions that can be bound by myosin heads due to the bending of double-head.* ***(G)*** *Schematic drawing depicting the three flexible junctions in a myosin head.*

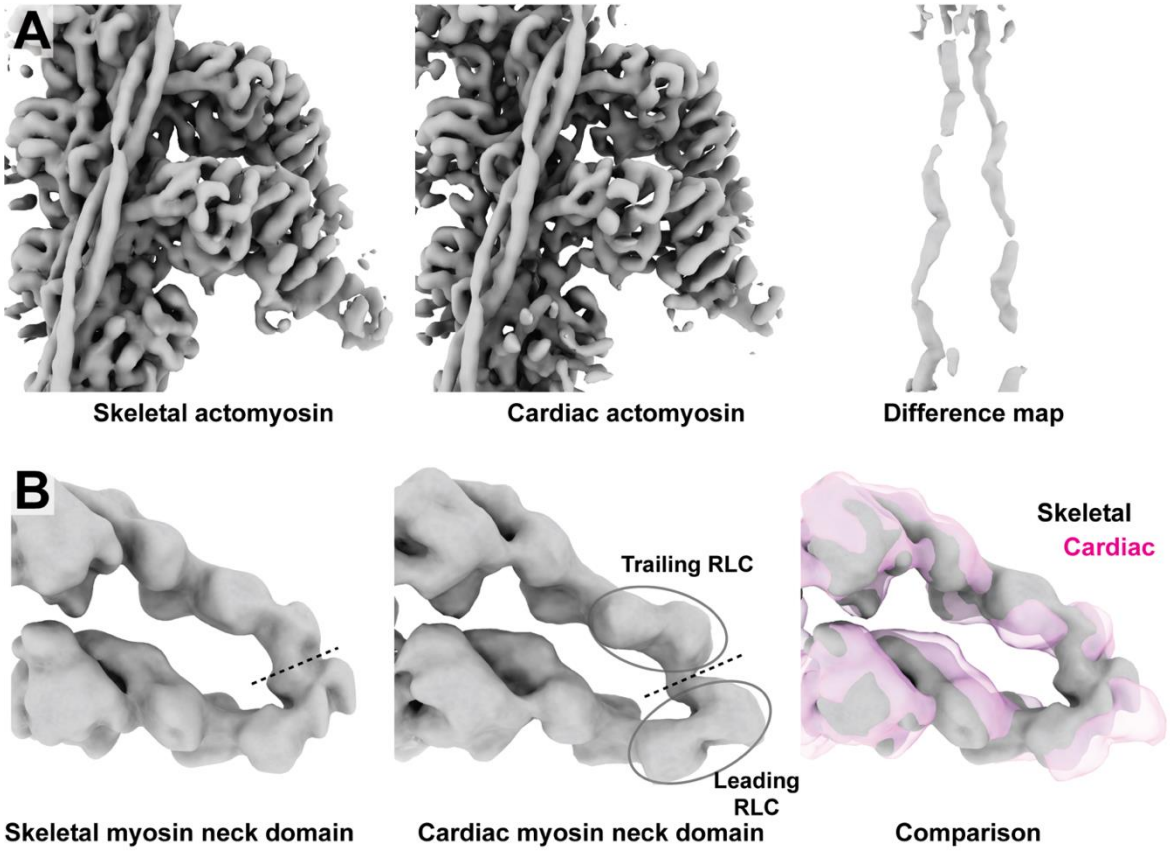

Fig. 4.26 Comparison between cardiac and skeletal actomyosin structures.
(A) *EM density maps of skeletal and cardiac actomyosin, both filtered to 7.8 Å, as well as the difference maps between them. The densities in the difference map correspond to nebulin.* ***(B)*** *EM density maps of skeletal and cardiac myosin double head, with a focus on the neck domain, both filtered to 15 Å. Dotted lines mark the interfaces between trailing and leading RLCs. The comparison between the skeletal and cardiac map is shown on the right.*

We noticed that 18% of the skeletal double-heads had a different conformation in which both neck domains are bent by ~20° perpendicular to the direction of the myosin power stroke (Fig. 4.25D,E, Fig. 4.27A). This different structural arrangement increases the range within which myosin can bind to the thin filament by ~ 5 nm without interfering with force transmission during the power stroke (Fig. 4.25F). Thus, the bending contributes additional adaptability on top of what is provided by the flexibility of the S2 domain for cross-bridge formation between actin and myosin filaments (Fig. 4.25G). The myosin "arm" can thus hold on tightly to a thin filament, but at the same time have enough freedom to cooperate the mismatch between helical

pitches of thick and thin filaments and account for local deformation of the sarcomere. Indeed, the double-heads with bent neck domains are randomly distributed in the A-band of the sarcomere (Fig. 4.27B-D), ensuring efficient binding of myosin during contraction.

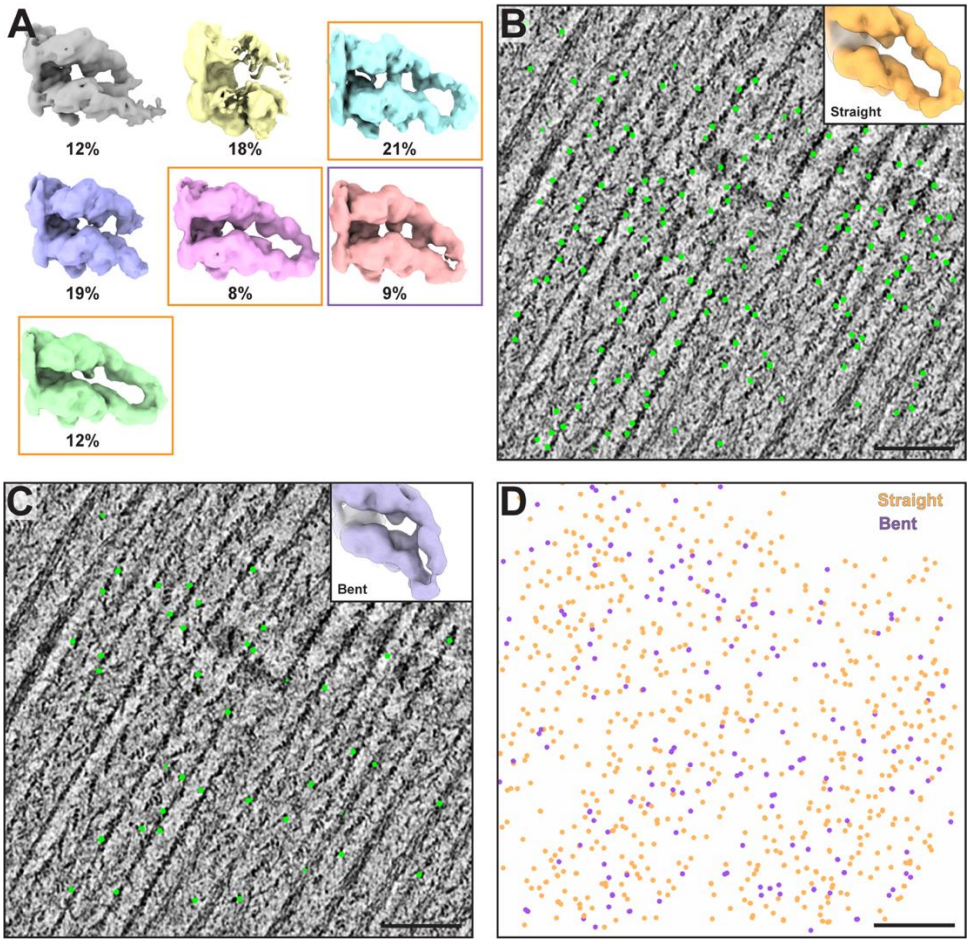

Fig. 4.27 Distribution of the two conformations of myosin double-head.

(A) *3D classification of a myosin double-head. Classes marked in orange and purple are selected as the straight and bent form for further refinement, respectively.* ***(B)*** *Distribution of myosin double-head in the straight conformation in a tomogram. A slice image of the tomogram with a thickness of 14 nm and particles within it (orange) are shown.* ***(C)*** *Distribution of myosin double-head in the bent conformation in the same slice of tomogram as (B). Particle positions are represented in purple dots.* ***(D)*** *Distribution of both straight and bent forms in the entire tomographic volume. Scale bars: 100 nm.*

4.3.5 Nebulin structure and localisation of residues

While nebulin consists of repetitive simple repeats, each simple repeat has different sequences, with a few conserved charged residues and a putative actin-binding SDxxYK motif (Fig. 4.28A,H, see also Appendix, Fig. 6.8). Owing to the nature of sub-tomogram averaging, the obtained EM density map of nebulin is an averaged density of all repeats in the A-band. Taking advantage of the 4.5 Å map, where bulky side chains are typically resolved (Fig. 4.20), we were able to build an atomic model for actin and refine a poly-alanine nebulin model into its density. Using a published convention (Labeit and Kolmerer, 1995), we defined the start of a simple repeat at two residues preceding a conserved aspartic acid, resulting in the SDxxYK motif residing at position 18-23.

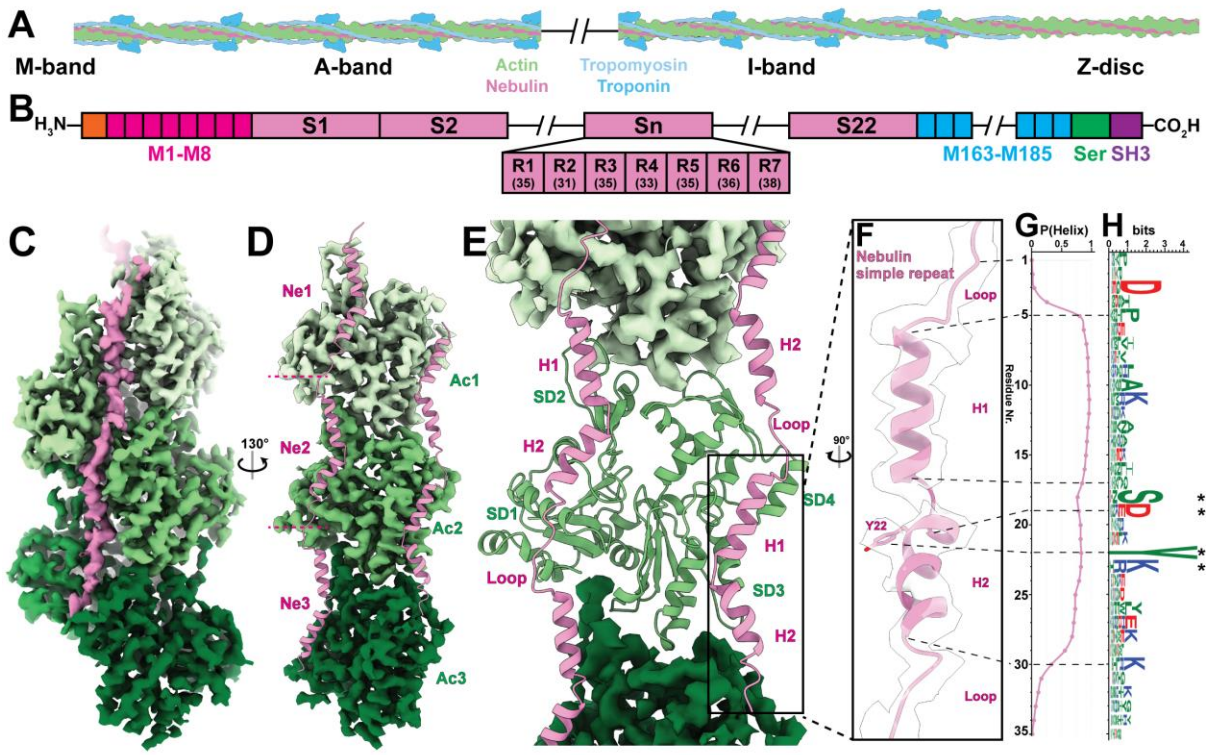

Fig. 4.28 Nebulin structure and its binding to the actin filament.

(A) *Schematic drawing of the nebulin-bound thin filament.* ***(B)*** *Modular organisation of the primary sequence of nebulin demonstrating its super repeats and simple repeats. Nebulin contains an N-terminal sequence (orange), repeats 1-8 (M1-M8, bright magenta), a super repeat region (magenta), repeat 163-185 (M163-M185, blue), a serine-rich region (Ser, green) and a C-terminal Src homology-3 domain (SH3, purple). The number below each simple repeat indicates its most common size, in number of amino acids.* ***(C)*** *Sub-tomogram averaged structure of the actin filament in complex with nebulin (magenta) at a resolution of 4.5 Å. Different actin subunits are coloured in different shades of green with darker green towards the*

barbed end. ***(D)*** *Rotated view of (C) highlighting both nebulin molecules (shown as structural models of three and two simple repeats) on the actin filament. Only one strand of the actin filament is shown. Nebulin simple repeats are labelled on one strand to show 1:1 stoichiometry with actin subunits.* ***(E)*** *Structural model of one actin subunit and two nebulin molecules. One nebulin binds along actin subdomain 1 and 2 (SD1 and SD2) while the other binds along actin subdomain 3 and 4 (SD3 and SD4). The cryo-EM map of the neighbouring actin subunits is shown.* ***(F)*** *Zoom-in view of one nebulin simple repeat. The side chain of residue Y22 is highlighted.* ***(G)*** *Averaged predicted score for an α-helix at each residue position of a simple repeat.* ***(H)*** *Graphical representation of sequence alignment of all simple repeats (M1-M163). A larger amino acid symbol corresponds to a greater occurrence at a certain position. Positive, negative and neutral residues are coloured in blue, red and green, respectively. Dotted lines map the sequence to the structural model in (F) and (G). Asterisks mark the conserved SDxxYK motif.*

The model of nebulin consists of a repetitive structure of two α-helices (H1 and H2), with a short kink of 46° in between, followed by a loop region spanning around SD1 of actin (Fig. 4.28C-F). As validation, and in order to map the sequence to our structural model, we predicted the average secondary structure to highlight structured and unstructured regions from the sequences of nebulin simple repeats (see Appendix, Fig. 6.8). The prediction implied each nebulin simple repeat should form a long helix, with a drop in probability in the middle of this helix (Fig. 4.28F). By matching the predicted start of the helix in the sequence with the start of H1 in the structure, the predicted end of the helix matched the end of H2 and the dip in probability matched the position of the kink in our model (Fig. 4.28E, F). Based on this registry, a noticeable bulky side chain density aligned with position 22, corresponding to a fully conserved tyrosine residue. We attributed this density as the phenyl group of this tyrosine (Fig. 4.28E, Fig. 4.20D). This observation further validates the sequence-structure mapping. As such, H1 starts at position 5, which is often occupied by a proline (Fig. 4.28E-G). The SDxxYK motif, where the exon boundaries are, is located at the beginning of H2, among which the serine is positioned at the kink between H1 and H2. This registry allowed us to assign the location of other conserved residues, and further investigate their roles in the interactions between nebulin and the thin filament.

4.3.6 Nebulin as a “molecular ruler” of the thin filament

A molecular ruler for the actin filament should coordinate two main functions: capping of the barbed and pointed end of the filament at a defined distance and being in close association with

actin subunits along the filament length. Although the general concept of nebulin being a "molecular ruler" is supported by its size being proportional to the length of the thin filament in different muscle fibres (Kruger et al., 1991; Labeit et al., 1991), it has been speculated that the interaction of nebulin with the thin filament differ at the N- and C-termini (McElhinny et al., 2001; Pappas et al., 2008). Because we averaged over all nebulin repeats, our study does not give insights into the ends of nebulin. However, the structures of the native thin filaments clearly depict a 1:1 stoichiometry between nebulin repeats and actin subunits in both A-band and I-band (Fig. 4.21D, Fig. 4.28D). Furthermore, the repeats are distinct structural units rather than part of a contiguous α-helix, as previously suggested (Pfuhl et al., 1994). Thus, each nebulin repeat likely denotes the "gradation" of a ruler in measuring the number of actin subunits.

While most nebulin simple repeats contain 35 amino acids (as is modelled above), some repeats can be as short as 31 aa or as long as 38 aa (Fig. 4.29A). Different sizes of nebulin repeats typically correspond to different positions in a super repeat (Fig. 4.28B). The predicted secondary structure implies that in the shorter repeats, the helix ends earlier than in an average-length repeat and in the longer repeats, the loop is longer (Fig. 4.29B). Although we did not observe separate classes within our cryo-ET data for these repeats owing to their low abundancy, it is noticeable that the density corresponding to H2 and the first half of the loop has lower occupancy compared to H1 (Fig. 4.29C). This suggests that in the shorter nebulin repeats, part of H2 is extruded into the loop along segments of actin to compensate for fewer amino acids while in the longer nebulin repeats, the extra amino acids reside flexibly in the loop (Fig. 4.29D). This ensures that in all regions of the sarcomere, nebulin repeats have the same physical length to span an actin subunit to maintain a 1:1 binding stoichiometry which is one of the main functions of a "molecular ruler".

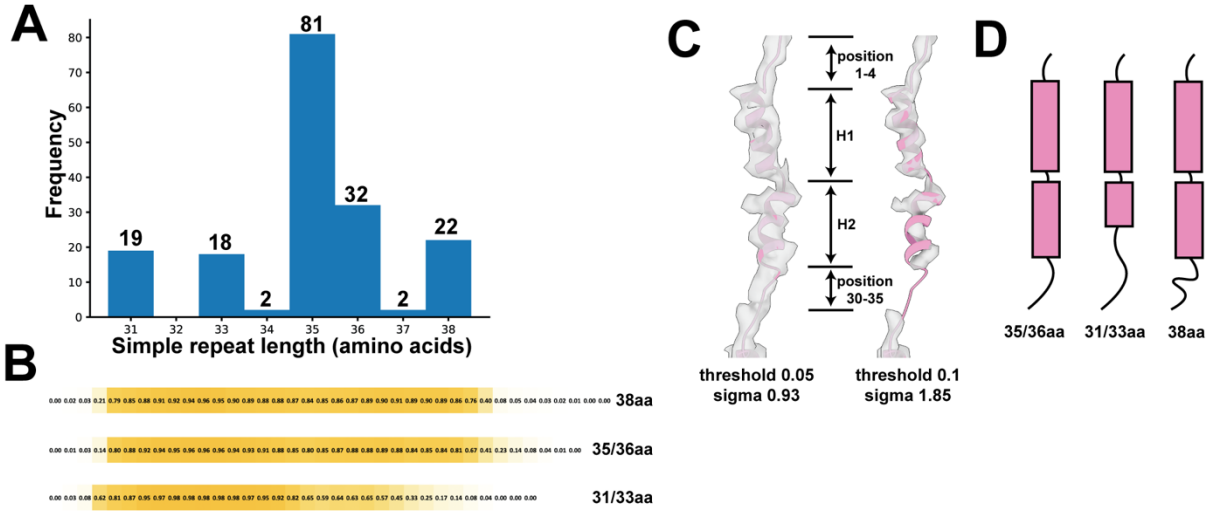

Fig. 4.29 Length of individual nebulin simple repeats.

(A) *Histogram of the length of simple repeats.* ***(B)*** *Averaged secondary structure prediction of normal (35/36 aa), short (31/33 aa) and long (38 aa) simple repeats.* ***(C)*** *Cryo-EM density map of one nebulin repeat at low and high surface threshold.* ***(D)*** *Schematic model of the nebulin simple repeats with different numbers of amino acids but the same physical length. α-helices are represented in magenta rectangles. Loops are shown as lines.*

4.3.7 Interactions between nebulin and the thin filament

Based on our model, we were able to show that the interactions between actin and nebulin are mediated by residues throughout one nebulin simple repeat and three adjacent actin subunits (Fig. 4.30A). In the SDxxYK motif, Y22 forms a potential cation-pi interaction with K68 on SD1 of one actin subunit (N) (Fig. 4.30C). S18 likely forms a hydrogen bond with E276 on SD3 of the laterally adjacent actin subunit on the other strand (N+1). D19 and K23 interact with residues on SD1 and SD2 of actin subunit N through electrostatic attractions. In addition, other highly conserved charged residues outside the SDxxYK motif are also involved in the interactions between actin and nebulin. D3, K11 and K30 can form electrostatic interactions with SD1 of actin subunit N+2, SD4 of actin subunit N+1 and SD1 of actin subunit N, respectively (Fig. 4.30C). Every nebulin repeat interacts with all three neighbouring actin subunits (Fig. 4.30A), which prevents them from depolymerisation and confers rigidity and mechanical stability to the thin filament.

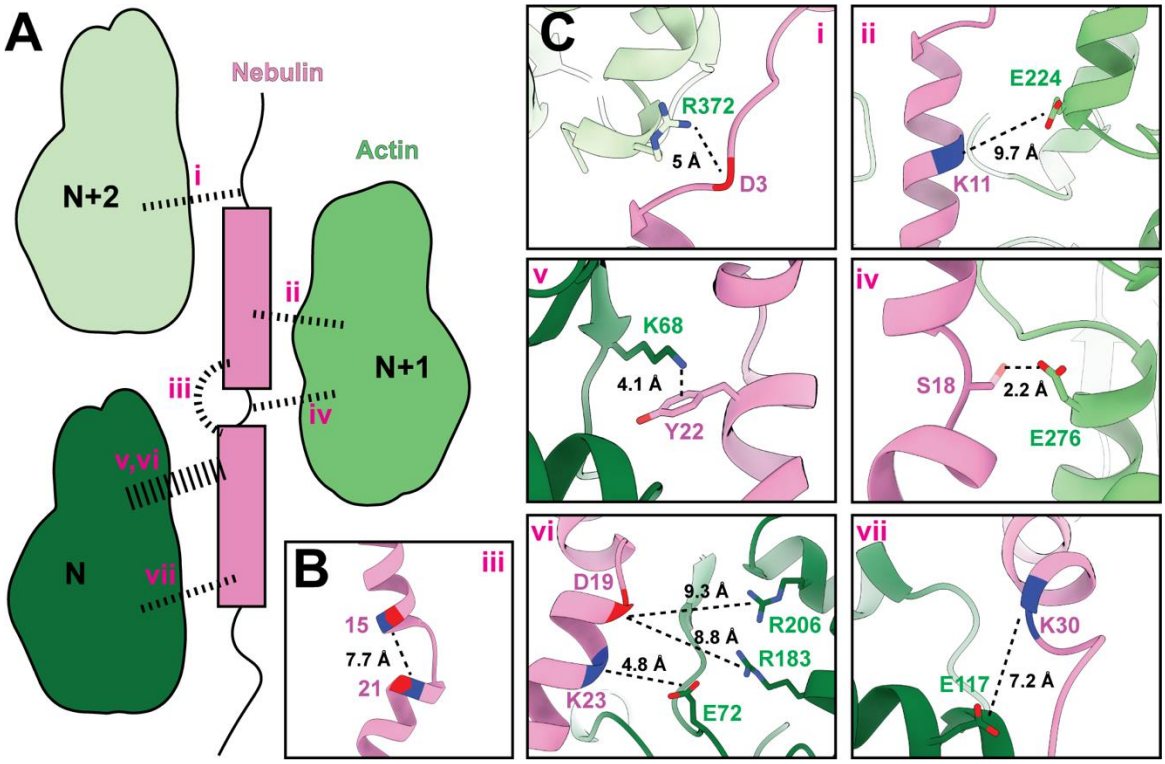

Fig. 4.30 Interactions between nebulin and actin.

(A) *Schematic depiction of interactions between nebulin (magenta) and three adjacent actin (green) subunits. Interactions are marked as dotted lines.* ***(B)*** *Intra-nebulin interactions (iii in (A)) between residues with complementary charges at position 15 and 21.* ***(C)*** *Details of interactions i-vii in (A). Distances were measured between actin residues and the Cβ of the poly-alanine model of nebulin where side chain is not resolved. A potential side chain conformation of S18 is shown for visualisation although it was not determined from the map.*

We noted that an intra-molecule interaction occurs between position 15 and 21 on nebulin at the position of the kink between H1 and H2 (Fig. 4.30A,B). Although both positions can accommodate either positively or negatively charged residues, they appear to be often complementary to each other among all repeat sequences (Fig. 4.31A-C). Their interaction is also supported by weak side-chain densities in our averaged reconstruction (Fig. 4.31D). This intra-molecular interaction stabilises the kink conformation of the two helices, which is necessary for positioning charged residues near actin.

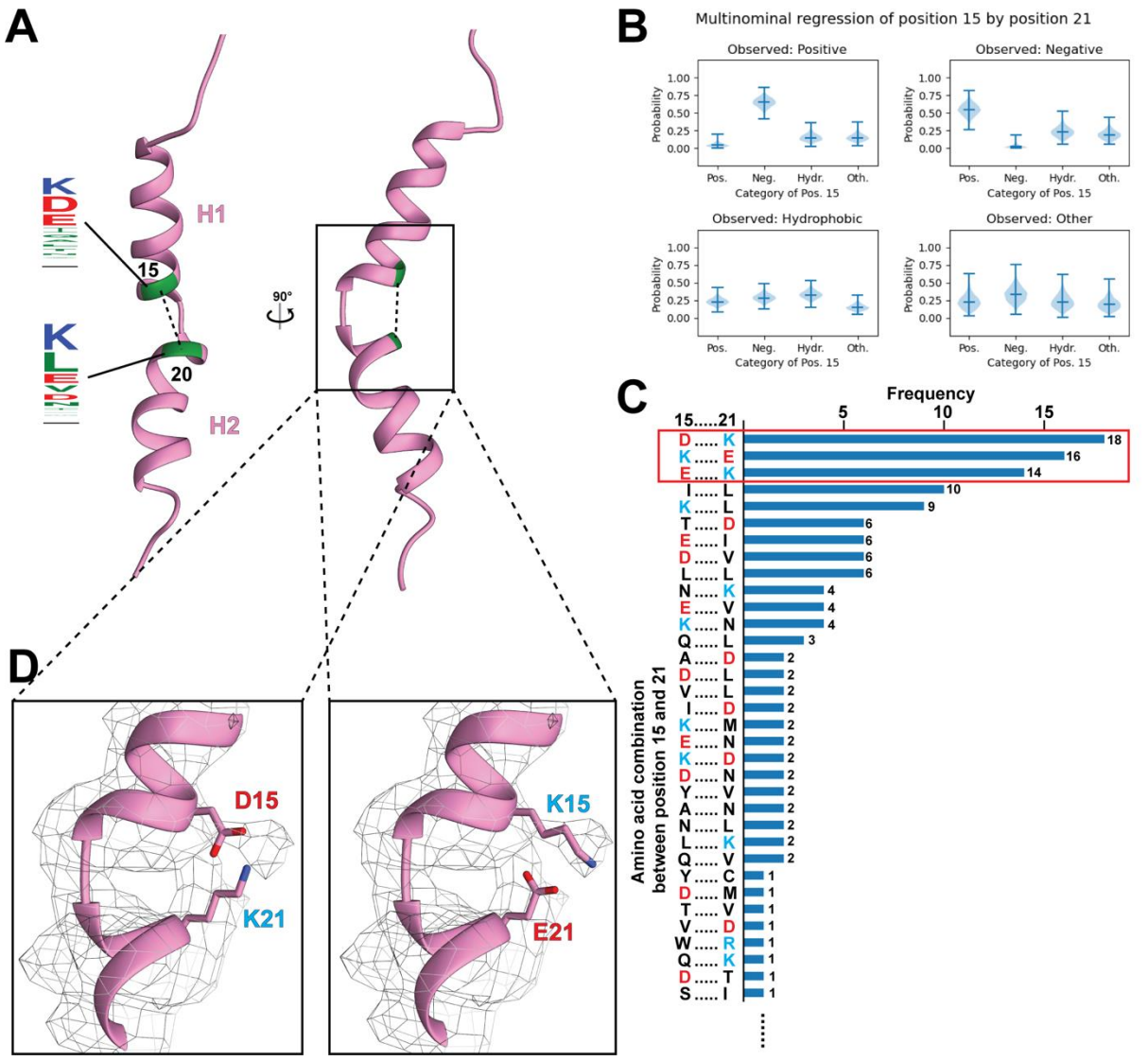

Fig. 4.31 Intra-nebulin interactions between position 15 and 21 and location of pathogenic missense mutations on a simple repeat.

(A) *Location of residue number 15 and 21 on a simple repeat including the possible amino acids at these two positions. Larger amino acid letter represents higher occurrence.* ***(B)*** *Violin plot of Bayesian multinominal regression depicting the conditional probability of a certain amino acid type on position 15 given the amino acid residue type on position 21. The median, minimum and maximum estimated probability values for each category are shown. The shaded area shows the probability density of the model within the respective category.* ***(C)*** *Histogram of amino acid combinations of position 15 and 21. Charged amino acids are coloured in blue (positive) and red (negative). Other combinations with only one occurrence are not shown.* ***(D)*** *Weak side chain densities at position 15 and 21. Fitted structural models are mutated to the two most populated amino acid combinations at position 15 and 21 showing possible side chain conformations.*

Nebulin simple repeats share a higher sequence similarity with the repeats that are six repeats apart, forming a seven-repeat super repeat pattern (Fig. 4.21A). This modular structure suggests an interaction with the troponin-tropomyosin regulatory complex, which also has a 1:7 stoichiometry ratio to actin. The physical separation by actin between nebulin and tropomyosin has ruled out their interactions. The core of troponin, including troponin C (TnC), troponin I (TnI) and the majority of troponin T (TnT) are also located away from nebulin (Fig. 4.32A). On the other hand, a linker region in TnT between R134 and R179 is likely to be the binding partner of nebulin (Fig. 4.32C). It was hypothesised to cross the groove between two actin stands (Manning et al., 2011). Although nebulin and this TnT linker could not be resolved in a structure of the thin filament containing troponin determined from our data (Fig. 4.33), previous structures of troponin with actin, reported from cardiac thin filament (Risi et al., 2021b; Yamada et al., 2020), show that this TnT linker is localised close to the region where nebulin resides in our structure. Despite the lack of a structural model for the linker owing to its flexibility, superimposing previous EM densities for TnT with our structural model of actin and nebulin suggests the location of two contact sites between TnT and nebulin (Fig. 4.32A,B). One site is located at the end of H2 (Fig. 4.32A-C box I). This site is consistent with the position of a WLKGIGW motif in nebulin, which has previously been proposed to be the tropomyosin-troponin binding motif at the end of repeat 3 (Labeit and Kolmerer, 1995). The other site is located downstream of the first site at the start of H1, indicating another potential troponin-binding motif, ExxK, at the beginning of repeat 4 (Fig. 4.32A-C box II). The TnT linker region contains a hydrophobic C-terminus and a highly charged N-terminus matching the orientation of the two binding sites, suggesting the WLKGIGW motif and ExxK motif interact with TnT through hydrophobic and electrostatic interactions, respectively (Fig. 4.32D).

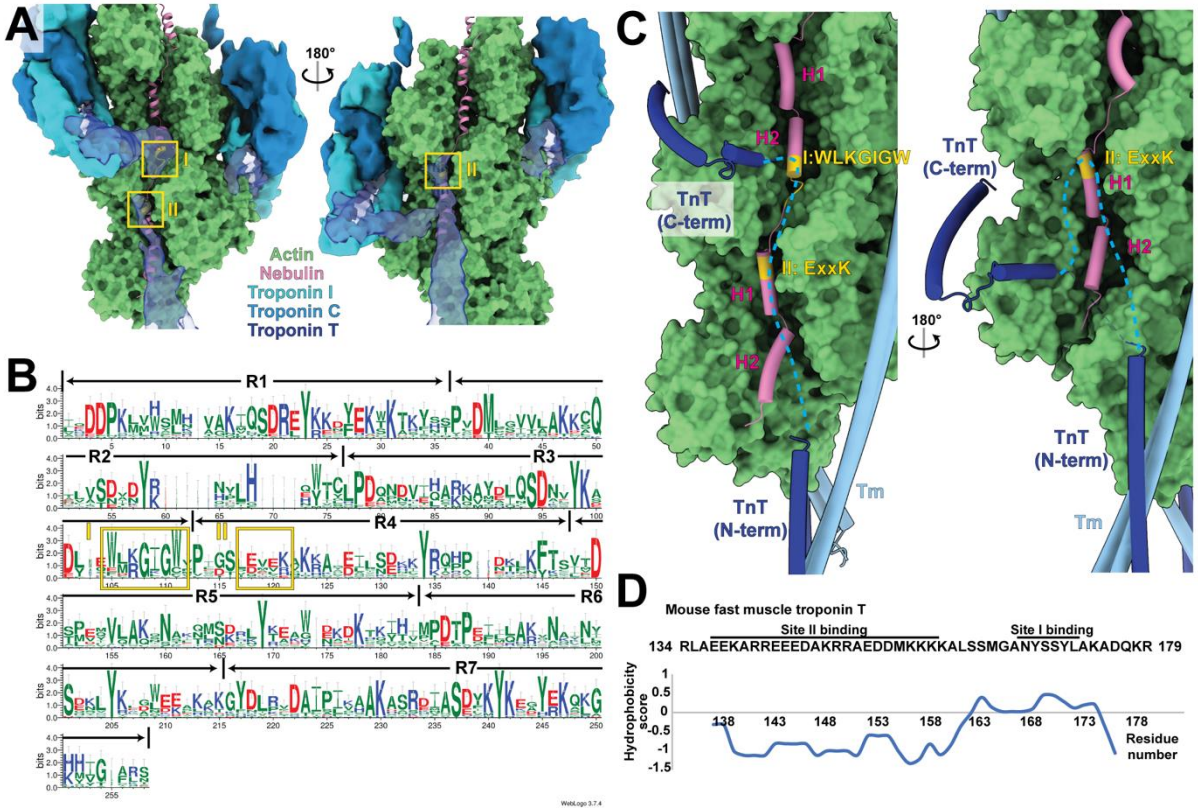

Fig. 4.32 Potential interactions between nebulin and troponin T (TnT).

(A). *The actin-nebulin complex superimposed with the cryo-EM densities of the troponin complex (EMD-0729). Two contact sites between nebulin and troponin T are marked in yellow as I and II.* ***(B)*** *Graphical representation of the sequence alignment of all nebulin super repeats (each super repeat contains the simple repeats R1-R7). A larger amino acid symbol corresponds to a greater occurrence at a certain position. The troponin binding sites I and II are marked corresponding to the WLKGIGW and ExxK motif.* ***(C)*** *Two different TnT models (dark blue) that bind to opposite sides of the actin filament (PDB: 6KN8) are shown. The linker region between R134 and R179 (corresponding to R151 and S198 in the original model) is missing in the structural model. Possible shapes of the TnT linkers are marked as cyan dotted lines based on weak EM densities (EMD-0729). Potential TnT binding sites on nebulin are highlighted in yellow. Tropomyosin (Tm) is shown in light blue.* ***(D)*** *Hydrophobicity of the linker in mouse fast muscle troponin T (TNNT3). Potential regions that can bind to site I and II are marked.*

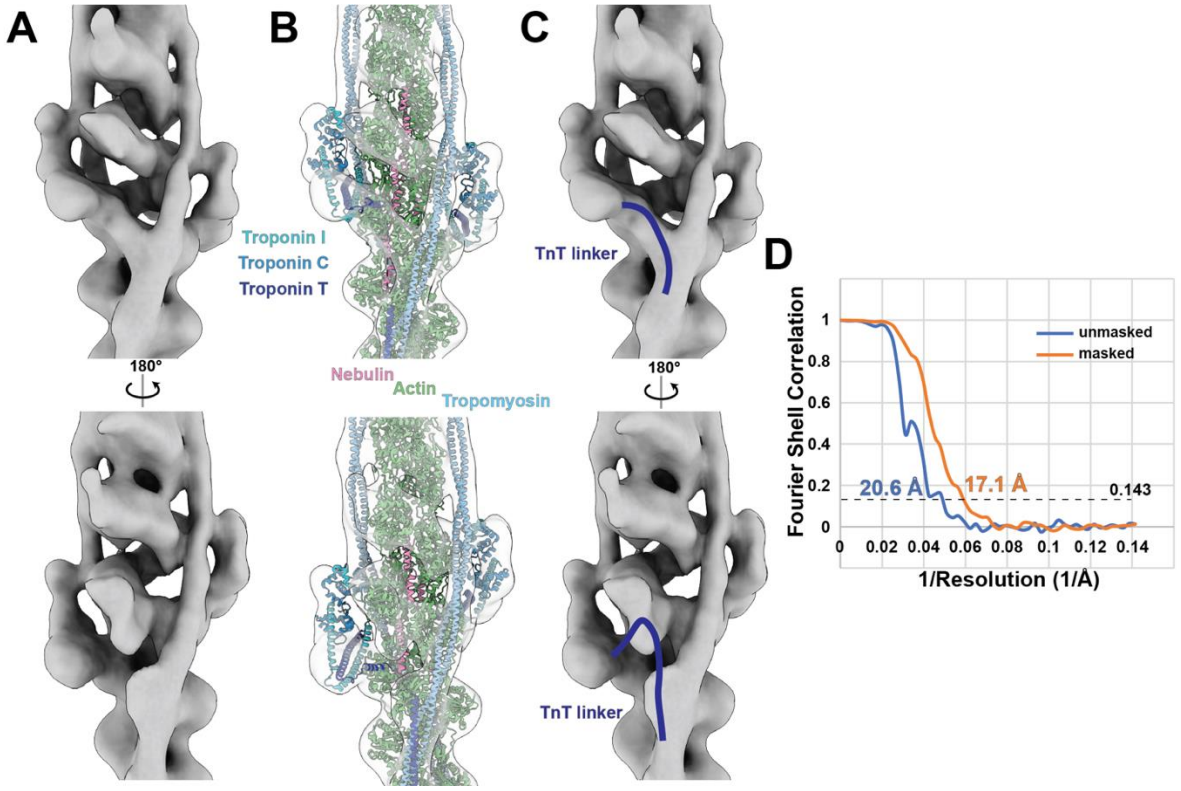

Fig. 4.33 Thin filament structure with troponin obtained from sub-tomogram averaging

*(**A**) EM density map depicting the thin filament including the troponin. (**B**) Atomic models of actin, nebulin, tropomyosin and troponin fitted into the EM density map. (**C**) The position of the TnT linkers from EMD-0729 depicted on our map obtained from sub-tomogram averaging. (**D**) Gold-standard FSC curve of the troponin-containing thin filament structure.*

Although missense mutations have not been localised to this linker, TnT is the only Tn component where mutations can lead to nemaline myopathy (Sewry et al., 2019). For example, Amish nemaline myopathy, a severe type, is caused by a TNNT1 (slow muscle troponin) truncation (Johnston et al., 2000) and a splicing variant of TNNT3 (fast muscle troponin) can also lead to nemaline myopathy (Sandaradura et al., 2018). This is in agreement with our proposed interactions between nebulin and TnT. Based on our observation that nebulin does not interact with myosin or tropomyosin, the role nebulin plays in regulating myosin binding is likely to be a downstream effect of its interaction with the TnT linker. This interaction in skeletal muscle may rigidify the linker and thus help to maintain efficient calcium regulation and the subsequent binding of myosin. It can also increase the cooperativity in calcium regulation across the two actin strands, which has been recently observed in cardiac muscle (Risi et al., 2021b).

4.3.8 Human nebulin and insights into nemaline myopathy

Nebulin in mouse shares more than 90% sequence similarity with human nebulin (Kazmierski et al., 2003). Key residues involved in the interactions between nebulin and the thin filament are conserved among repeats of mouse and human nebulin (Fig. 4.34). Our structural model of nebulin derived from mouse is thus also applicable to human and enables the understanding of the mechanism underlying the pathogenicity caused by recessive mutations in the NEB gene, which is the major cause of nemaline myopathies (Sewry et al., 2019). Nemaline myopathy mutations are usually compound heterozygous, in some cases with one truncating and one missense variant (Sewry et al., 2019). Two missense NEB mutations, Ser6366Ile and Thr7382Pro, have been identified as founder mutations in the Finnish population (Lehtokari et al., 2014). The locations of the two sites on a simple repeat correspond to Ser18 and Thr14 (Fig. 4.35A). A mutation of Ser18 into a hydrophobic isoleucine would disrupt its potential hydrogen bond with actin (Fig. 4.30C, Fig. 4.35F). A mutation of Thr14 to proline, despite not being at a conserved residue position, can lead to the disruption of H1 helical secondary structure and thus alter the local conformation of nebulin and interfere with actin binding (Fig. 4.35F).

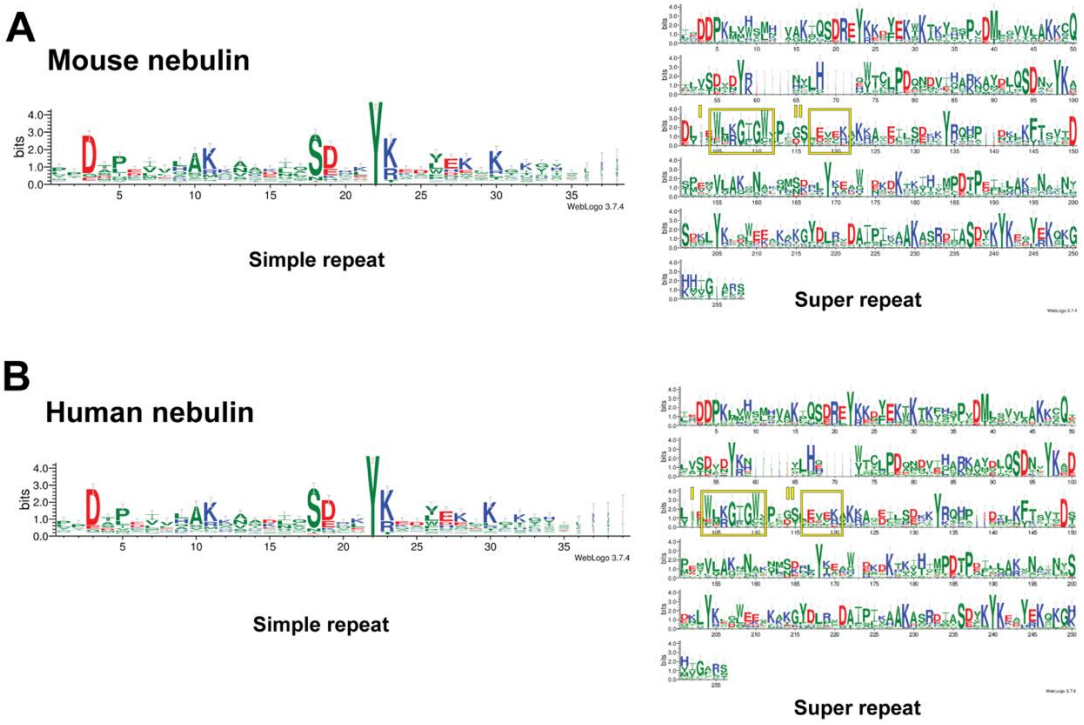

Fig. 4.34 Similarities between mouse nebulin and human nebulin.

(A) *Sequence logos of mouse nebulin simple repeats (left) and super repeats (right) after multiple sequence alignment.* ***(B)*** *Sequence logos of human nebulin simple repeats (left) and super repeats (right) after multiple sequence alignment.*

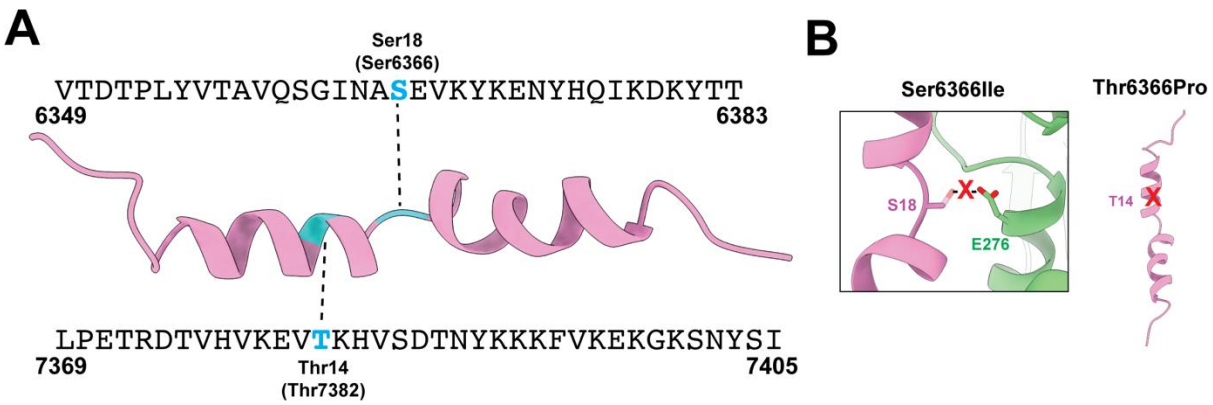

Fig. 4.35 Intra-nebulin interactions between position 15 and 21 and location of pathogenic missense mutations on a simple repeat.

(A) *Location of the two founder mutations of nemaline myopathies in the Finnish population, S6366I and T7382P, on a simple repeat.* ***(B)*** *Potential disruption of a hydrogen bond between nebulin and E276 on actin due to the mutation S6366I and potential disruption of the H1 helix structure due to the mutation T7382P.*

Our structural model of actin and nebulin maps residues crucial in maintaining the interactions between nebulin and the thin filament. When also applied to clinical genetics, this information should help to determine additional pathogenic interfaces of nebulin variants. This is especially crucial when considering missense variants, where the pathogenicity is often difficult to determine (Lehtokari et al., 2014) and will thus aid the early diagnosis of nemaline myopathies and genetic counselling of variant carriers.

4.3.9 Conclusions

Our structural reconstruction of nebulin within a native skeletal sarcomere provides the basis of interaction between nebulin and thin filaments. Our structures determined across several tissue types and regions enable a comparative analysis of nebulin in its native context. It reveals the mechanism underlying the roles nebulin plays in regulating thin filament length, as a thin filament stabiliser, as well as in regulating myosin-binding through its interaction with TnT. Our approach using cryo-FIB milling and cryo-ET, provides a high-resolution structural approach within an isolated tissue. Our findings highlight different conformations of myosin and illustrates similarities and differences from in vitro structures. Together with the recent study reporting the high-resolution structure of bacterial ribosomes (O'Reilly et al., 2020), our

structures showcase the full potential of in situ structural biology using cryo-ET. In the context of the sarcomere where several flexible proteins, such as titin and myosin-binding protein-C, are present and still lack structural visualisation, our approach is a general tool for structural analysis where other methods are limited. Determining the structure of these key players in the context of native sarcomeres will enable better modelling of skeletal muscle in the future, directly impacting also the understanding of disease. The structure of nebulin presented here is one such case, where the molecular interactions described might help to establish a foundation for future developments of the treatment of nemaline myopathies.

4.4 Discussions and future perspectives

The grand objective for this thesis was to elucidate the mechanism underlying muscle contraction and muscle diseases. Therefore, I aimed to obtain a molecular picture of the entire sarcomere and determining *in situ* structures of nebulin, which is closely related to the disease nemaline myopathy, and actomyosin. The results presented in section 4.2 and 4.3 demonstrate that the goals have been accomplished successfully.

Throughout my doctoral thesis, in addition to advancing the scientific understanding of muscle contraction, I established a cryo-FIB-ET workflow for studying muscle. I was also actively involved in improving the software and hardware used in the workflow together with Dr. Thorsten Wagner and Dr. Sebastian Tacke. Dr. Wagner implemented tools for automatic filament picking, where I contributed to testing and designing from a user perspective. In addition, I have developed numerous scripts used for different processing steps (see Chapter 3, Appendix). Dr. Tacke designed anti-contamination devices such as a cryo-shield inside the cryo-FIB-SEM microscope and a glovebox for sample transfer, where I contributed to testing and collecting datasets for benchmarking (Tacke et al., 2021). These devices reduce ice formation on lamellae and thus increase the success rate of FIB-milling.

In this section, I will first discuss the implication of my results (section 4.4.1). Then, the future challenges in the muscle field will be addressed in section 4.4.2. In the end, future developments of cryo-FIB-ET that will further enlarge the arsenal to tackle these challenges will be discussed in section 4.4.3.

4.4.1 New approach for investigating muscle structures

A “bridge” between the grand picture of a sarcomere and the atomic structures of individual components obtained from previous studies was required. This bridge has been constructed by the new cryo-FIB-ET workflow used in this thesis. The results from the first half of this thesis describe the first 3D molecular organisation of a sarcomere (section 4.2). This high-resolution picture of the entire sarcomere enabled unambiguous identification and localisation of different components. It illustrates the arrangement of filaments in the A-band (section 4.2.2), I-band (section 4.2.5), and Z-disc (section 4.2.6) as well as the cross-links formed by myosin (section 4.2.4) and α-actinin (section 4.2.6). On the molecular level, various structures of actin, myosin,

tropomyosin, troponin, and α-actinin obtained through sub-tomogram averaging shed lights on the cooperativity of the two myosin heads (section 4.2.3), the local regulation of tropomyosin (section 4.2.5), and different confirmation of α-actinin binding to actin (section 4.2.6). Overall, these discoveries clarified previous misconception of a sarcomere as a strictly ordered crystal-like structure. The sarcomere is a magnificent system with both regularity and stochasticity. While it certainly contains ordered patterns (such as the hexagonal arrangement of filaments in the A-band and M-band, the 37-nm-spaced cross-bridge clusters, and the tetragonal arrangement in the Z-disc), it also contains irregular features (such as the stochastic binding of myosin, the irregular rearrangement of filaments in the I-band, and the varying spacing between α-actinins in the Z-disc). This combination of regularity and stochasticity provides a plasticity that is crucial, especially for high-level mammals that are adapted for different environment, to function properly at the same time of tolerating external disturbance.

Building upon the first half of this thesis, the second part on high-resolution *in situ* structures of nebulin and actomyosin showcases the power of cryo-ET over other structural methods (section 4.3). The large size and elongated shape of nebulin render the purification of the full-length protein while keeping it in a functional state nearly impossible (Chitose et al., 2010; Zhang et al., 1998). In addition, recombinant nebulin fragments bundle F-actin and thus hinder a reconstitution for cryo-EM SPA (Gonsior et al., 1998). This makes cryo-ET and sub-tomogram averaging the best and only approach for investigating the structure of nebulin. The *in situ* structure of nebulin provides insights into the mechanism underlying it function as a molecular ruler (section 4.3.6), in stabilising thin filaments (section 4.3.7), and regulating myosin binding through troponin (section 4.3.7). It eventually serves as a foundation for the diagnosis of nemaline myopathy and development of treatment (section 4.3.8). Our structure of actin-nebulin at 4.5Å, being the highest resolution achieved after cryo-FIB to date, demonstrates the possibility of widely applicable *in situ* structural biology that can determine protein structures without the need for isolation.

The cryo-FIB-ET workflow for investigating muscle samples established in this thesis pave the way for future research on muscles of different species, of different types, and in different diseased states. Concurrently with this thesis, neonatal rat cardiomyocytes were also investigated using the cryo-FIB-ET workflow, which depicted a semi-striated organisation of the thin and thick filaments inside immature sarcomeres (Burbaum et al., 2021). Undoubtably, in the next few years, more mysteries in the muscle field will be unveiled using the cryo-FIB-

ET workflow from both our lab and other groups. Cryo-ET will become a mainstream technique for muscle structural biology.

4.4.2 More challenges ahead in muscle research

Cryo-FIB-ET opens a new era of investigating the structures of muscle proteins. It allows direct characterisation of proteins, which are flexible when isolated, in their native environment. The in situ structures of nebulin and actomyosin are the first high-resolution structures in muscle determined by cryo-FIB-ET, but certainly would not be the last ones. Although the organisation of the thick filaments in the M-band has been characterised in this thesis (section 4.2.2), the cross-linking proteins between the thick filaments, supposedly myomesin and possibly also obscurin and titin (Lange et al., 2020), still remain to be identified. These proteins all share similar a domain architecture that is made of tandem repeats of Ig or Fn domains (sections 2.1.2.2 and 2.1.3). Therefore, it will be challenging to visualise and distinguish these proteins unambiguously. A reliable labelling method to tag these proteins with electron-dense particles is a pre-requisite to investigate them (see later in section 4.4.3). Similarly, MyBP-C in the A-band is also composed of Ig repeats (section 2.1.2.3). In this thesis where the sarcomere was in the rigor state, The identification of MyBP-C was largely hindered by the overwhelming densities of myosin cross-bridges in the same region. One solution to this problem is keep myosin in a super-relaxed state (reviewed by (Nag and Trivedi, 2021)), where the heads retract to the thick filament, forming a compact IHM motif (Scarff et al., 2020; Yang et al., 2020). This will leave the MyBP-C as the only cross-links (Luther et al., 2011) and thus to be identified easily.

The structure of nebulin still has a few missing puzzles in order for its function to be fully understood. In principle, the resolution of nebulin can still be improved with a much larger amount of data, which has been made possible with the rapid development in automation and software. However, this is unlikely to provide more insights into the structure as the sequences are different among simple repeats. Thus, side chain densities will not be resolved even at a higher nominal resolution. Nevertheless, the structure of nebulin together with troponin was limited in resolution in this thesis (section 4.3.7). This can be certainly improved with more data to provide an experimental proof on the detailed interactions between nebulin and troponin, as well as its regulatory role. As a bonus, as the similarities among super repeats are much higher than those among simple repeats (Fig. 4.33), a structure of nebulin-troponin can

eventually reach a resolution where the side chains of nebulin can be more resolved compared to the structure in this thesis. In addition, the structure of the central super-repeat region has been determined (section 4.3), but it still remains unclear what the structure of the ends of nebulin in the Z-disc and close to the M-band is. It would also be interesting to ascertain whether and how nebulin interacts with the capping proteins, tropomodulin (McElhinny et al., 2001) and CapZ (Pappas et al., 2008), to understand how it realises the "range" function of a ruler.

Titin is another key player in sarcomere that remains to be characterised. It plays major roles in the regulating length and elasticity of a sarcomere (section 2.1.2.2) and its defects are the most frequent cause for dilated cardiomyopathy. Being the largest known protein, there has been no structure of the full titin except for a few domains (von Castelmur et al., 2008; Pernigo et al., 2010; Pinotsis et al., 2006) due to its enormous size. Other than located in the M-band as mentioned earlier in this subsection, titin is present in every region, likely with different morphologies. In the A-band, titin is suggested to tightly bind to myosin and be part of the thick filament. This was also indicated by the 4-nm periodicity in the sub-tomogram averaged structure of the thick filament in this thesis (section 4.2.3). A high-resolution structure of the thick filament will shed light on the structure and interactions with myosin of the A-band titin. In this thesis, it has been shown that averaging of the thick filament in the rigor state is difficult without surface features for alignment (section 4.2.3). Therefore, the thick filaments from the relaxed sarcomere would be an easier start, where the myosin heads in a IHM configuration can facilitate alignment during sub-tomogram averaging. In the I-band, titin is suggested to have structurally distinct Ig-repeat and PEVK regions (Linke et al., 1999). While the Ig-repeat region may be directly visualised in a tomogram, the PEVK domain is likely to be too thin and thus will require specific labelling to be identified. The Z-disc titin is suggested to bind to actin. If this interaction between titin and actin is not transient, the structure of the Z-disc titin can be determined by averaging thin filaments in the Z-disc. Otherwise, as the Z-disc is similarly crowded as the M-band, it will also need labelling to recognise titin in this region.

4.4.3 The future of cryo-FIB-ET

With cryo-FIB, cryo-ET is no longer restricted to very thin specimens such as bacteria or viruses. However, there is still a limitation to the thickness of the specimen due to limited freezing rate if the specimen is plunge frozen (section 4.1). This limitation of a few micrometres

can be expanded to 100-200 µm if a high pressure is applied during freezing. This approach is called high-pressure freezing (HPF) ((Moor and Riehle, 1968) reviewed by (Kaech and Ziegler, 2014; McDonald, 2009)). Practically, this method involves enclosing the specimen within aluminium carriers and applying a pressure ~2100 Pa when the specimen is cooled to ~-180°C rapidly. While HPF was typically combined with freeze substitution (Steinbrecht and Müller, 1987) as well as CEMOVIS (Al-Amoudi et al., 2004) and used for convention EM, it has been recently employed to combine with cryo-FIB-ET for structural investigations of *C. elegans* (Fuest et al., 2019; Harapin et al., 2015; Mahamid et al., 2015). HPF provides the power to vitrify a large volume, but at the same rises a challenge on how to deal with this large volume. Although in principle Ga^+ FIB can be used to mill HPF specimen, it would take hours or even days to produce a single lamella from a thick HPF specimen. Therefore, a more powerful beam is desired to tackle the large chunk frozen via HPF. Extending from the material science field, plasma FIB (PFIB) using species such as oxygen, nitrogen, argon, or xenon can be a good candidate (Burnett et al., 2016; Garnier et al., 2015). Initial results from (Gorelick et al., 2019) have already demonstrated the possibility to use PFIB to process biological specimen once embedded. In addition, a lift-out procedure has been recently developed for cryo-FIB (Klumpe et al., 2022; Mahamid et al., 2015; Schaffer et al., 2019). A small chunk is first cut from the HPF grid. Then it can be lifted out and transferred to another grid for being trimmed into a thin lamella. The lift-out procedure not only speeds up processing a large volume, but also provides an approach to produce the lamella in different orientations as a result of the flexible attachment to the second grid. Combing the aforementioned newly techniques in a cryo-HPF-PFIB workflow in the future, cryo-ET will be applicable to an even broader range of samples than single cells or myofibrils. Tissues or organoids will be possible to be investigated to elucidate mechanisms at a higher level such as cell-cell interactions or development of organs.

An inherent limitation of cryo-EM/cryo-ET is that it can only capture “snapshot” images. The core of cryo-EM is the cryo-immobilisation of the specimen. Thus, it lacks the ability to visualise biological events as they happen (i.e. live imaging). However, like a movie is produced by frames, as long as there are enough “snapshots”, a dynamic picture can still be obtained. This requires precise control to freeze the specimen at certain states. Biochemically, cells or proteins can be arrested or stabilised at different stages. However, there are important stages that are only transient and short-lived. This requires cryo-immobilisation to occur quickly after the cells or proteins change their states (Frank, 2017). In cryo-EM SPA, this concept of time-resolved cryo-EM has been proposed and successfully implemented in a few

systems (Dandey et al., 2020; Klebl et al., 2021; Mäeots et al., 2020). It typically involves a microfluidic device that mixes two solutions, such as proteins and ligands, immediately before spraying the mixture onto the grid (Lu et al., 2009). Similarly, cryo-ET specimens should be investigated in a time-resolved approach in order to understand cellular processes at different stages. Recent studies have shown a microfluidic system coupled with light microscopy and HPF that demonstrated the potential for time-resolved cryo-ET (Fuest et al., 2018, 2019; Mejia et al., 2014). Certainly, specimens for cryo-ET are more diverse than those for SPA, thus would require specific designs for different cell types and experiments in the future.

Another challenge in cryo-ET at the moment is the specific labelling of a certain protein. As already discussed in section 4.4.2, many proteins in the sarcomere share the similar domain organisation and likely the similar shape. Specific and efficient tagging is the only way to identify these proteins in order for subsequent characterisations. Numerous methods for labelling proteins *in situ* have been proposed. The most commonly used tagging approach for conventional EM is immunogold labelling (Page Faulk and Malcolm Taylor, 1971), as gold is electron-dense and easily recognisable within a micrograph or tomogram. The protein-of-interest is first bound by a specific primary antibody. Then the secondary antibody with gold attached binds to the primary antibody. For conventional EM, the labelling is often performed after fixation of the specimen (reviewed in (D'Amico and Skarmoutsou, 2008; Roth, 1996)). This method has also been extended to cryo-ET in recent years (Jiang et al., 2021; Yi et al., 2015), where the binding to the tag occurs prior to cryo-immobilisation. Recently, DNA origami with an RNA aptamer was also employed to detect GFP-fused proteins on the cell surface (Silvester et al., 2021). However, most labelling reagents cannot enter the cell efficiently. One solution is to genetically modify the protein-of-interest to incorporate protein tags that are capable of binding metals, such as metallothionein (Jiang et al., 2020; Mercogliano and DeRosier, 2007) or ferritin (Wang et al., 2011). Alternatively, labelling reagents can be potentially delivered into the cell using electroporation (Alex et al., 2019). Another possible method to identify a protein-of-interest is the "negative tagging" through the deletion of the protein. For example, in this thesis, nebulin was identified through comparing the structures of the skeletal thin filament and the nebulin-absent cardiac thin filament (section 4.3.3). It has also been used to identified components of the bacterial flagellar motor (Beeby et al., 2016). However, this method is not widely applicable. On the one hand, deletion of the protein-of-interest is likely to lead to the perturbation of the native environment or even cell death. On the other hand, if the protein-of-interest is in a crowded environment and lacks a characteristic

shape, it remains challenging to visualise the disappearance of its density in a tomogram. The loss of density is likely to be only visible in the structure after sub-tomogram averaging. In the end, thanks to the high-quality images obtained from cryo-ET and the rapid development of machine learning, it is getting possible to computationally recognise the small proteins simply based on their shape to circumvent the need of labelling (Moebel et al., 2021; Rice et al., 2022).

Other than these major challenges currently being tackled, the cryo-FIB-ET field is also growing rapidly with new developments that automate and speed up sample preparation (Buckley et al., 2020; Klumpe et al., 2021; Tacke et al., 2021; Zachs et al., 2020), data acquisition (Bouvette et al., 2021; Chreifi et al., 2019; Eisenstein et al., 2022; Khavnekar et al., 2022) and processing (Zheng et al., 2022). Given time, cryo-FIB-ET will be as streamlined as conventional EM or even light microscopy. In the future, cryo-FIB-ET will be not only a tool for basic research, but also used as an imaging tool at a much higher resolution than the current histopathology for clinical diagnosis and precision medicine.

CHAPTER 5 REFERENCES

Ababou, A., Rostkova, E., Mistry, S., Masurier, C. le, Gautel, M., and Pfuhl, M. (2008). Myosin Binding Protein C Positioned to Play a Key Role in Regulation of Muscle Contraction: Structure and Interactions of Domain C1. J Mol Biol *384*, 615–630. https://doi.org/10.1016/j.jmb.2008.09.065.

Abraham, D.J., and Leo, A.J. (1987). Extension of the fragment method to calculate amino acid zwitterion and side chain partition coefficients. Proteins: Structure, Function, and Bioinformatics *2*, 130–152. https://doi.org/10.1002/prot.340020207.

Afonine, P. V, Klaholz, B.P., Moriarty, N.W., Poon, B.K., Sobolev, O. V, Terwilliger, T.C., Adams, P.D., and Urzhumtsev, A. (2018). New tools for the analysis and validation of cryo-EM maps and atomic models. Acta Crystallographica Section D *74*, 814–840. https://doi.org/10.1107/S2059798318009324.

Agarkova, I., and Perriard, J.C. (2005). The M-band: An elastic web that crosslinks thick filaments in the center of the sarcomere. Trends Cell Biol *15*, 477–485. https://doi.org/10.1016/j.tcb.2005.07.001.

Alamo, L., Wriggers, W., Pinto, A., Bártoli, F., Salazar, L., Zhao, F.Q., Craig, R., and Padrón, R. (2008). Three-Dimensional Reconstruction of Tarantula Myosin Filaments Suggests How Phosphorylation May Regulate Myosin Activity. J Mol Biol *384*, 780–797. https://doi.org/10.1016/j.jmb.2008.10.013.

Al-Amoudi, A., Chang, J.J., Leforestier, A., McDowall, A., Salamin, L.M., Norlén, L.P.O., Richter, K., Blanc, N.S., Studer, D., and Dubochet, J. (2004). Cryo-electron microscopy of vitreous sections. EMBO Journal *23*, 3583–3588. https://doi.org/10.1038/sj.emboj.7600366.

Alex, A., Piano, V., Polley, S., Stuiver, M., Voss, S., Ciossani, G., Overlack, K., Voss, B., Wohlgemuth, S., Petrovic, A., et al. (2019). Electroporated recombinant proteins as tools for in vivo functional complementation, imaging and chemical biology. Elife *8*, e48287. https://doi.org/10.7554/eLife.48287.001.

AL-Khayat, H.A., Kensler, R.W., Squire, J.M., Marston, S.B., and Morris, E.P. (2013). Atomic model of the human cardiac muscle myosin filament. Proceedings of the National Academy of Sciences *110*, 318–323. https://doi.org/10.1073/pnas.1212708110.

Andersen, A.H., and Kak, A.C. (1984). Simultaneous Algebraic Reconstruction Technique (SART): A Superior Implementation of the ART Algorithm. Ultrason Imaging *6*, 81–94. .

Ao, X., and Lehrer, S.S. (1995). Phalloidin unzips nebulin from thin filaments in skeletal myofibrils. J Cell Sci *108*, 3397–3403. https://doi.org/10.1242/jcs.108.11.3397.

Bang, M.L., Li, X., Littlefield, R., Bremner, S., Thor, A., Knowlton, K.U., Lieber, R.L., and Chen, J. (2006). Nebulin-deficient mice exhibit shorter thin filament lengths and reduced contractile function in skeletal muscle. Journal of Cell Biology *173*, 905–916. https://doi.org/10.1083/jcb.200603119.

Bang, M.-L., Caremani, M., Brunello, E., Littlefield, R., Lieber, R.L., Chen, J., Lombardi, V., and Linari, M. (2009). Nebulin plays a direct role in promoting strong actin-myosin interactions. The FASEB Journal *23*, 4117–4125. https://doi.org/10.1096/fj.09-137729.

Barad, B.A., Echols, N., Wang, R.Y.R., Cheng, Y., Dimaio, F., Adams, P.D., and Fraser, J.S. (2015). EMRinger: Side chain-directed model and map validation for 3D cryo-electron microscopy. Nat Methods *12*, 943–946. https://doi.org/10.1038/nmeth.3541.

Baumann, B.A.J., Taylor, D.W., Huang, Z., Tama, F., Fagnant, P.M., Trybus, K.M., and Taylor, K.A. (2012). Phosphorylated smooth muscle heavy meromyosin shows an open conformation linked to activation. J Mol Biol *415*, 274–287. https://doi.org/10.1016/j.jmb.2011.10.047.

Beeby, M., Ribardo, D.A., Brennan, C.A., Ruby, E.G., Jensen, G.J., Hendrixson, D.R., and Hultgren, S.J. (2016). Diverse high-torque bacterial flagellar motors assemble wider stator rings using a conserved protein scaffold. Proc Natl Acad Sci U S A *113*, E1917–E1926. https://doi.org/10.1073/pnas.1518952113.

Behrmann, E., Müller, M., Penczek, P.A., Mannherz, H.G., Manstein, D.J., and Raunser, S. (2012). Structure of the rigor actin-tropomyosin-myosin complex. Cell *150*, 327–338. https://doi.org/10.1016/j.cell.2012.05.037.

Bennett, P.M. (1974). Decrease in section thickness on exposure to the electron beam; the use of tilted sections in estimating the amount of shrinkage. J Cell Sci *15*, 693–701. .

Bennett, P., Rees, M., and Gautel, M. (2020). The Axial Alignment of Titin on the Muscle Thick Filament Supports Its Role as a Molecular Ruler. J Mol Biol *432*, 4815–4829. https://doi.org/10.1016/j.jmb.2020.06.025.

Bertoni, M., Kiefer, F., Biasini, M., Bordoli, L., and Schwede, T. (2017). Modeling protein quaternary structure of homo- and hetero-oligomers beyond binary interactions by homology. Sci Rep *7*, 1–15. https://doi.org/10.1038/s41598-017-09654-8.

Betts, J.G., Young, K.A., Wise, J.A., Johnson, E., Poe, B., Kruse, D.H., Korol, O., Johnson, J.E., Womble, M., and DeSaix, P. (2013). Anatomy and Physiology (Houston, Texas: OpenStax).

Bharat, T.A.M., and Scheres, S.H.W. (2016). Resolving macromolecular structures from electron cryo-Tomography data using subtomogram averaging in RELION. Nat Protoc *11*, 2054–2065. https://doi.org/10.1038/nprot.2016.124.

Bienert, S., Waterhouse, A., De Beer, T.A.P., Tauriello, G., Studer, G., Bordoli, L., and Schwede, T. (2017). The SWISS-MODEL Repository-new features and functionality. Nucleic Acids Res *45*, D313–D319. https://doi.org/10.1093/nar/gkw1132.

Blanchoin, L., and Pollard, T.D. (2002). Hydrolysis of ATP by polymerized actin depends on the bound divalent cation but not profilin. Biochemistry *41*, 597–602. https://doi.org/10.1021/bi011214b.

Blanchoin, L., Boujemaa-Paterski, R., Sykes, C., and Plastino, J. (2014). Actin Dynamics, Architecture, and Mechanics in Cell Motility. Physiol Rev *94*, 235–263. https://doi.org/10.1152/physrev.00018.2013.-Tight.

Blankenfeldt, W., Thomä, N.H., Wray, J.S., Gautel, M., and Schlichting, I. (2006). Crystal structures of human cardiac β-myosin II S2-Δ provide insight into the functional role of the S2 subfragment. Proc Natl Acad Sci U S A *103*, 17713–17717. https://doi.org/10.1073/pnas.0606741103.

Bouvette, J., Liu, H.F., Du, X., Zhou, Y., Sikkema, A.P., da Fonseca Rezende e Mello, J., Klemm, B.P., Huang, R., Schaaper, R.M., Borgnia, M.J., et al. (2021). Beam image-shift accelerated data acquisition for near-atomic resolution single-particle cryo-electron tomography. Nat Commun *12*. https://doi.org/10.1038/s41467-021-22251-8.

Bower, S.M., Wang, Y., and Chantler, P.D. (1992). Regulatory light-chain Cys-55 sites on the two heads of myosin can come within 2Å of each other. FEBS Lett *310*, 132–134. https://doi.org/10.1016/0014-5793(92)81313-B.

Briegel, A., Dias, D.P., Li, Z., Jensen, R.B., Frangakis, A.S., and Jensen, G.J. (2006). Multiple large filament bundles observed in Caulobacter crescentus by electron cryotomography. Mol Microbiol *62*, 5–14. https://doi.org/10.1111/j.1365-2958.2006.05355.x.

Brown, J.H., Kumar, V.S.S., O'Neall-Hennessey, E., Reshetnikova, L., Robinson, H., Nguyen-McCarty, M., Szent-Györgyi, A.G., and Cohen, C. (2011). Visualizing key hinges and a potential major source of compliance in the lever arm of myosin. Proc Natl Acad Sci U S A *108*, 114–119. https://doi.org/10.1073/pnas.1016288107.

Buckley, G., Gervinskas, G., Taveneau, C., Venugopal, H., Whisstock, J.C., and de Marco, A. (2020). Automated cryo-lamella preparation for high-throughput in-situ structural biology. J Struct Biol *210*, 107488. https://doi.org/https://doi.org/10.1016/j.jsb.2020.107488.

Burbaum, L., Schneider, J., Scholze, S., Böttcher, R.T., Baumeister, W., Schwille, P., Plitzko, J.M., and Jasnin, M. (2021). Molecular-scale visualization of sarcomere contraction within native cardiomyocytes. Nat Commun *12*, 1–12. https://doi.org/10.1038/s41467-021-24049-0.

Burgoyne, T., Muhamad, F., and Luther, P.K. (2008). Visualization of cardiac muscle thin filaments and measurement of their lengths by electron tomography. Cardiovasc Res *77*, 707–712. https://doi.org/10.1093/cvr/cvm117.

Burgoyne, T., Morris, E.P., and Luther, P.K. (2015). Three-Dimensional Structure of Vertebrate Muscle Z-Band: The Small-Square Lattice Z-Band in Rat Cardiac Muscle. J Mol Biol *427*, 3527–3537. https://doi.org/10.1016/j.jmb.2015.08.018.

Burgoyne, T., Heumann, J.M., Morris, E.P., Knupp, C., Liu, J., Reedy, M.K., Taylor, K.A., Wang, K., and Luther, P.K. (2019). Three-dimensional structure of the basketweave Z-band

in midshipman fish sonic muscle. Proc Natl Acad Sci U S A *116*, 15534–15539. https://doi.org/10.1073/pnas.1902235116.

Burnett, T.L., Kelley, R., Winiarski, B., Contreras, L., Daly, M., Gholinia, A., Burke, M.G., and Withers, P.J. (2016). Large volume serial section tomography by Xe Plasma FIB dual beam microscopy. Ultramicroscopy *161*, 119–129. https://doi.org/10.1016/j.ultramic.2015.11.001.

Cantino, M.E., Brown, L.D., Chew, M., Luther, P.K., and Squire, J.M. (2000). A-band architecture in vertebrate skeletal muscle: Polarity of the myosin head array. J Muscle Res Cell Motil *21*, 681–690. https://doi.org/10.1023/A:1005661123914.

Carlier, M.F., and Pantaloni, D. (1988). Binding of phosphate to F-ADP-actin and role of F-ADP-Pi-actin in ATP-actin polymerization. Journal of Biological Chemistry *263*, 817–825. https://doi.org/https://doi.org/10.1016/S0021-9258(19)35428-6.

Casella, J.F., Craig, S.W., Maack, D.J., and Brown, A.E. (1987). Cap Z(36/32), a barbed end actin-capping protein, is a component of the Z-line of skeletal muscle. Journal of Cell Biology *105*, 371–379. https://doi.org/10.1083/jcb.105.1.371.

von Castelmur, E., Marino, M., Svergun, D.I., Kreplak, L., Ucurum-Fotiadis, Z., Konarev, P. v., Urzhumtsev, A., Labeit, D., Labeit, S., and Mayans, O. (2008). A regular pattern of Ig super-motifs defines segmental flexibility as the elastic mechanism of the titin chain. Proc Natl Acad Sci U S A *105*, 1186–1191. https://doi.org/10.1073/pnas.0707163105.

Castillo, A., Nowak, R., Littlefield, K.P., Fowler, V.M., and Littlefield, R.S. (2009). A nebulin ruler does not dictate thin filament lengths. Biophys J *96*, 1856–1865. https://doi.org/10.1016/j.bpj.2008.10.053.

Chakrabarty, T., Xiao, M., Cooke, R., and Selvin, P.R. (2002). Holding two heads together: Stability of the myosin II rod measured by resonance energy transfer between the heads. Proc Natl Acad Sci U S A *99*, 6011–6016. https://doi.org/10.1073/pnas.082024299.

Chandra, M., Manidi, R., Ford, S., Hidalgo, C., Witt, C., Ottenheijm, C., Labeit, S., and Granzier, H. (2009). Nebulin alters cross-bridge cycling kinetics and increases thin filament activation. A novel mechanism for increasing tension and reducing tension cost. Journal of Biological Chemistry *284*, 30889–30896. https://doi.org/10.1074/jbc.M109.049718.

Chantler, P.D., Tao, T., and Stafford, W.F. (1991). On the relationship between distance information derived from cross-linking and from resonance energy transfer, with specific reference to sites located on myosin heads. Biophys J *59*, 1242–1250. https://doi.org/10.1016/S0006-3495(91)82339-6.

Chen, M., Bell, J.M., Shi, X., Sun, S.Y., Wang, Z., and Ludtke, S.J. (2019). A complete data processing workflow for cryo-ET and subtomogram averaging. Nat Methods *16*, 1161–1168. https://doi.org/10.1038/s41592-019-0591-8.

Chen, V.B., Arendall III, W.B., Headd, J.J., Keedy, D.A., Immormino, R.M., Kapral, G.J., Murray, L.W., Richardson, J.S., and Richardson, D.C. (2010). {\it MolProbity}: all-atom structure validation for macromolecular crystallography. Acta Crystallographica Section D *66*, 12–21. https://doi.org/10.1107/S0907444909042073.

Chesarone, M.A., and Goode, B.L. (2009). Actin nucleation and elongation factors: mechanisms and interplay. Curr Opin Cell Biol *21*, 28–37. https://doi.org/10.1016/j.ceb.2008.12.001.

Chew, M.W.K., and Squire, J.M. (1995). Packing of α-Helical Coiled-Coil Myosin Rods in Vertebrate Muscle Thick Filaments. J Struct Biol *115*, 233–249. https://doi.org/https://doi.org/10.1006/jsbi.1995.1048.

Chitose, R., Watanabe, A., Asano, M., Hanashima, A., Sasano, K., Bao, Y., Maruyama, K., and Kimura, S. (2010). Isolation of nebulin from rabbit skeletal muscle and its interaction with actin. J Biomed Biotechnol *2010*. https://doi.org/10.1155/2010/108495.

Chou, S.Z., and Pollard, T.D. (2019). Mechanism of actin polymerization revealed by cryo-EM structures of actin filaments with three different bound nucleotides. Proc Natl Acad Sci U S A *116*, 4265–4274. https://doi.org/10.1073/pnas.1807028115.

Chreifi, G., Chen, S., Metskas, L.A., Kaplan, M., and Jensen, G.J. (2019). Rapid tilt-series acquisition for electron cryotomography. J Struct Biol *205*, 163–169. https://doi.org/https://doi.org/10.1016/j.jsb.2018.12.008.

Craig, R., and Offer, G. (1976). The location of C protein in rabbit skeletal muscle. Proceedings of the Royal Society of London - Biological Sciences *192*, 451–461. https://doi.org/10.1098/rspb.1976.0023.

Craig, R., Greenet, L.E., and Eisenbergt, E. (1985). Structure of the actin-myosin complex in the presence of ATP (electron microscopy/negative staining/crosslinked actomyosin/cross-bridge cycle/arrowhead structure).

Croll, T.I. (2018). {\it ISOLDE}: a physically realistic environment for model building into low-resolution electron-density maps. Acta Crystallographica Section D *74*, 519–530. https://doi.org/10.1107/S2059798318002425.

Crooks, G.E., Hon, G., Chandonia, J.M., and Brenner, S.E. (2004). WebLogo: A sequence logo generator. Genome Res *14*, 1188–1190. https://doi.org/10.1101/gr.849004.

D'Amico, F., and Skarmoutsou, E. (2008). Quantifying immunogold labelling in transmission electron microscopy. J Microsc *230*, 9–15. https://doi.org/10.1111/j.1365-2818.2008.01949.x.

Dandey, V.P., Budell, W.C., Wei, H., Bobe, D., Maruthi, K., Kopylov, M., Eng, E.T., Kahn, P.A., Hinshaw, J.E., Kundu, N., et al. (2020). Time-resolved cryo-EM using Spotiton. Nat Methods *17*, 897–900. https://doi.org/10.1038/s41592-020-0925-6.

Daneshparvar, N., Taylor, D.W., O'Leary, T.S., Rahmani, H., Abbasiyeganeh, F., Previs, M.J., and Taylor, K.A. (2020). CryoEM structure of Drosophila flight muscle thick filaments at 7 A resolution. Life Sci Alliance *3*. https://doi.org/10.26508/LSA.202000823.

Danev, R., and Nagayama, K. (2001). Transmission electron microscopy with Zernike phase plate. Ultramicroscopy *88*, 243–252. .

Danev, R., Buijsse, B., Khoshouei, M., Plitzko, J.M., and Baumeister, W. (2014). Volta potential phase plate for in-focus phase contrast transmission electron microscopy. Proc Natl Acad Sci U S A *111*, 15635–15640. https://doi.org/10.1073/pnas.1418377111.

Dominguez, R., and Holmes, K.C. (2011). Actin structure and function. Annu Rev Biophys *40*, 169–186. https://doi.org/10.1146/annurev-biophys-042910-155359.

Dominguez, R., Freyzon, Y., Trybus, K.M., and Cohen, C. (1998). Crystal Structure of a Vertebrate Smooth Muscle Myosin Motor Domain and Its Complex with the Essential Light Chain: Visualization of the Pre–Power Stroke State. Cell *94*, 559–571. https://doi.org/https://doi.org/10.1016/S0092-8674(00)81598-6.

Donner, K., Sandbacka, M., Lehtokari, V.L., Wallgren-Pettersson, C., and Pelin, K. (2004). Complete genomic structure of the human nebulin gene and identification of alternatively spliced transcripts. European Journal of Human Genetics *12*, 744–751. https://doi.org/10.1038/sj.ejhg.5201242.

Dubochet, J. (2007). The Physics of Rapid Cooling and Its Implications for Cryoimmobilization of Cells. Methods Cell Biol *2007*, 7–21. https://doi.org/10.1016/S0091-679X(06)79001-X.

Dubochet, J., Chang, J.-J., Freeman, R., Lepault, J., and McDowall, A.W. (1982). Frozen aqueous suspensions. Ultramicroscopy *10*, 55–61. https://doi.org/https://doi.org/10.1016/0304-3991(82)90187-5.

von der Ecken, J., Müller, M., Lehman, W., Manstein, D.J., Penczek, P.A., and Raunser, S. (2015). Structure of the F-actin-tropomyosin complex. Nature *519*, 114–117. https://doi.org/10.1038/nature14033.

von der Ecken, J., Heissler, S.M., Pathan-Chhatbar, S., Manstein, D.J., and Raunser, S. (2016). Cryo-EM structure of a human cytoplasmic actomyosin complex at near-atomic resolution. Nature *534*, 724–728. https://doi.org/10.1038/nature18295.

Edgar, R.C. (2004). MUSCLE: Multiple sequence alignment with high accuracy and high throughput. Nucleic Acids Res *32*, 1792–1797. https://doi.org/10.1093/nar/gkh340.

Eisenstein, F., Yanagisawa, H., Kashihara, H., Kikkawa, M., Tsukita, S., and Danev, R. (2022). Parallel cryo electron tomography on in situ lamellae. BioRxiv 2022.04.07.487557. https://doi.org/10.1101/2022.04.07.487557.

Emsley, P., Lohkamp, B., Scott, W.G., and Cowtan, K. (2010). Features and development of Coot. Acta Crystallogr D Biol Crystallogr *66*, 486–501. https://doi.org/10.1107/S0907444910007493.

Eswar, N., Eramian, D., Webb, B., Shen, M.-Y., and Sali, A. (2008). Protein Structure Modeling with MODELLER. In Structural Proteomics: High-Throughput Methods, B. Kobe, M. Guss, and T. Huber, eds. (Totowa, NJ: Humana Press), pp. 145–159.

Eulitz, S., Sauer, F., Pelissier, M.C., Boisguerin, P., Molt, S., Schuld, J., Orfanos, Z., Kley, R.A., Volkmer, R., Wilmanns, M., et al. (2013). Identification of Xin-repeat proteins as novel ligands of the SH3 domains of nebulin and nebulette and analysis of their interaction during myofibril formation and remodeling. Mol Biol Cell *24*, 3215–3226. https://doi.org/10.1091/mbc.E13-04-0202.

Farabella, I., Vasishtan, D., Joseph, A.P., Pandurangan, A.P., Sahota, H., and Topf, M. (2015). TEMPy: A Python library for assessment of three-dimensional electron microscopy density fits. J Appl Crystallogr *48*, 1314–1323. https://doi.org/10.1107/S1600576715010092.

Fisher, A.J., Smith, C.A., Thoden, J., Smith, R., Sutoh, K., Holden, H.M., and Rayment, I. (1995). X-ray Structures of the Myosin Motor Domain of Dictyostelium discoideum Complexed with MgADP.cntdot.BeFx and MgADP.cntdot.AlF4-. Biochemistry *34*, 8960–8972. https://doi.org/10.1021/bi00028a004.

Frank, J. (1975). Averaging of low exposure electron micrographs of non-periodic objects. Ultramicroscopy *1*, 159–162. https://doi.org/https://doi.org/10.1016/S0304-3991(75)80020-9.

Frank, J. (2017). Time-resolved cryo-electron microscopy: Recent progress. J Struct Biol *200*, 303–306. https://doi.org/10.1016/j.jsb.2017.06.005.

Fuest, M., Nocera, G.M., Modena, M.M., Riedel, D., Mejia, Y.X., and Burg, T.P. (2018). Cryofixation during live-imaging enables millisecond time-correlated light and electron microscopy. J Microsc *272*, 87–95. https://doi.org/10.1111/jmi.12747.

Fuest, M., Schaffer, M., Nocera, G.M., Galilea-Kleinsteuber, R.I., Messling, J.E., Heymann, M., Plitzko, J.M., and Burg, T.P. (2019). In situ Microfluidic Cryofixation for Cryo Focused Ion Beam Milling and Cryo Electron Tomography. Sci Rep *9*, 1–10. https://doi.org/10.1038/s41598-019-55413-2.

Funk, J., Merino, F., Schaks, M., Rottner, K., Raunser, S., and Bieling, P. (2021). A barbed end interference mechanism reveals how capping protein promotes nucleation in branched actin networks. Nat Commun *12*. https://doi.org/10.1038/s41467-021-25682-5.

Galaz-Montoya, J.G., and Ludtke, S.J. (2017). The advent of structural biology in situ by single particle cryo-electron tomography. Biophys Rep *3*, 17–35. https://doi.org/10.1007/s41048-017-0040-0.

Garnier, A., Filoni, G., Hrnčíř, T., and Hladík, L. (2015). Plasma FIB: Enlarge your field of view and your field of applications. Microelectronics Reliability *55*, 2135–2141. https://doi.org/10.1016/j.microrel.2015.07.016.

Gasteiger, E., Hoogland, C., Gattiker, A., Duvaud, S., Wilkins, M.R., Appel, R.D., and Bairoch, A. (2005). Protein Identification and Analysis Tools on the ExPASy Server. In The Proteomics Protocols Handbook, J.M. Walker, ed. (Totowa, NJ: Humana Press), pp. 571–607.

Gautel, M. (2011). The sarcomeric cytoskeleton: Who picks up the strain? Curr Opin Cell Biol *23*, 39–46. https://doi.org/10.1016/j.ceb.2010.12.001.

Gautel, M., and Djinović-Carugo, K. (2016). The sarcomeric cytoskeleton: From molecules to motion. Journal of Experimental Biology *219*, 135–145. https://doi.org/10.1242/jeb.124941.

Gautel, M., Goulding, D., Bullard, B., Weber, K., and Furst, D.O. (1996). The central Z-disk region of titin is assembled from a novel repeat in variable copy numbers. J Cell Sci *109*, 2747–2754. https://doi.org/10.1242/jcs.109.11.2747.

Giganti, D., Yan, K., Badilla, C.L., Fernandez, J.M., and Alegre-Cebollada, J. (2018). Disulfide isomerization reactions in titin immunoglobulin domains enable a mode of protein elasticity. Nat Commun *9*. https://doi.org/10.1038/s41467-017-02528-7.

Gilbert, P. (1972). Iterative methods for the three-dimensional reconstruction of an object from projections. J Theor Biol *36*, 105–117. https://doi.org/https://doi.org/10.1016/0022-5193(72)90180-4.

Goddard, T.D., Huang, C.C., Meng, E.C., Pettersen, E.F., Couch, G.S., Morris, J.H., and Ferrin, T.E. (2018). UCSF ChimeraX: Meeting modern challenges in visualization and analysis. Protein Science *27*, 14–25. https://doi.org/10.1002/pro.3235.

Gokhin, D.S., Kim, N.E., Lewis, S.A., Hoenecke, H.R., D'Lima, D.D., and Fowler, V.M. (2012). Thin-filament length correlates with fiber type in human skeletal muscle. Am J Physiol Cell Physiol *302*, 555–565. https://doi.org/10.1152/ajpcell.00299.2011.

Goldstein, J.I., Newbury, D.E., Echlin, P., Joy, D.C., Lyman, C.E., Lifshin, E., Sawyer, L., and Michael, J.R. (2003). Scanning Electron Microscopy and X-ray Microanalysis (Boston, MA: Springer US).

Goldstein, M.A., Schoeter, J.P., and Sass, R.L. (1990). Two structural states of the vertebrate Z band. Electron Microsc Rev *3*, 227–248. https://doi.org/10.1016/0892-0354(90)90003-B.

Gonsior, S.M., Gautel, M., and Hinssen, H. (1998). A six-module human nebulin fragment bundles actin filaments and induces actin polymerization. J Muscle Res Cell Motil *19*, 225–235. https://doi.org/10.1023/A:1005372915268.

Goody, R.S., Reedy, M.C., Hofmann, W., Holmes, K.C., and Reedy, M.K. (1985). Binding of myosin subfragment 1 to glycerinated insect flight muscle in the rigor state. Biophys J *47*, 151–169. https://doi.org/10.1016/S0006-3495(85)83889-3.

Gordon, A.M., Homsher, E., and Regnier, M. (2000). Regulation of Contraction in Striated Muscle. Physiol Rev *80*, 853–924. .

Gorelick, S., Buckley, G., Gervinskas, G., Johnson, T.K., Handley, A., Caggiano, M.P., Whisstock, J.C., Pocock, R., and de Marco, A. (2019). PIE-scope, integrated cryo-correlative light and FIB/SEM microscopy. Elife *8*, e45919. https://doi.org/10.7554/eLife.45919.

Grant, T., and Grigorieff, N. (2015). Measuring the optimal exposure for single particle cryo-EM using a 2.6 Å reconstruction of rotavirus VP6. Elife *4*. https://doi.org/10.7554/eLife.06980.001.

Granzier, H.L., and Labeit, S. (2004). The Giant Protein Titin: A Major Player in Myocardial Mechanics, Signaling, and Disease. Circ Res *94*, 284–295. https://doi.org/10.1161/01.RES.0000117769.88862.F8.

Green, D.W., Ingram, V.M., Perutz, M.F., and Bragg, W.L. (1954). The structure of haemoglobin - IV. Sign determination by the isomorphous replacement method. Proc R Soc Lond A Math Phys Sci *225*, 287–307. https://doi.org/10.1098/rspa.1954.0203.

Griggs, R., Vihola, A., Hackman, P., Talvinen, K., Haravuori, H., Faulkner, G., Eymard, B., Richard, I., Selcen, D., Engel, A., et al. (2007). Zaspopathy in a large classic late-onset distal myopathy family. Brain *130*, 1477–1484. https://doi.org/10.1093/brain/awm006.

Gruen, M., Prinz, H., and Gautel, M. (1999). cAPK-phosphorylation controls the interaction of the regulatory domain of cardiac myosin binding protein C with myosin-S2 in an on-o¡ fashion. FEBS Lett *453*, 254–259. .

Grünewald, K., Desai, P., Winkler, D.C., Heymann, J.B., Belnap, D.M., Baumeister, W., and Steven, A.C. (2003). Three-Dimensional Structure of Herpes Simplex Virus from Cryo-Electron Tomography. Science (1979) *302*, 1396–1398. .

Guex, N., Peitsch, M.C., and Schwede, T. (2009). Automated comparative protein structure modeling with SWISS-MODEL and Swiss-PdbViewer: A historical perspective. Electrophoresis *30*, 162–173. https://doi.org/10.1002/elps.200900140.

Gurel, P.S., Kim, L.Y., Ruijgrok, P. v, Omabegho, T., Bryant, Z., and Alushin, G.M. (2017). Cryo-EM structures reveal specialization at the myosin VI-actin interface and a mechanism of force sensitivity. Elife *6*, e31125. https://doi.org/10.7554/eLife.31125.

Hagen, W.J.H., Wan, W., and Briggs, J.A.G. (2017). Implementation of a cryo-electron tomography tilt-scheme optimized for high resolution subtomogram averaging. J Struct Biol *197*, 191–198. https://doi.org/10.1016/j.jsb.2016.06.007.

Hampton, C.M., Taylor, D.W., and Taylor, K.A. (2007). Novel Structures for α-Actinin:F-Actin Interactions and their Implications for Actin-Membrane Attachment and Tension Sensing in the Cytoskeleton. J Mol Biol *368*, 92–104. https://doi.org/10.1016/j.jmb.2007.01.071.

Harapin, J., Börmel, M., Sapra, K.T., Brunner, D., Kaech, A., and Medalia, O. (2015). Structural analysis of multicellular organisms with cryo-electron tomography. Nat Methods *12*, 634–636. https://doi.org/10.1038/nmeth.3401.

Hartman, M.A., and Spudich, J.A. (2012). The myosin superfamily at a glance. J Cell Sci *125*, 1627–1632. https://doi.org/10.1242/jcs.094300.

Heissler, S.M., Arora, A.S., Billington, N., Sellers, J.R., and Chinthalapudi, K. (2021). Cryo-EM structure of the autoinhibited state of myosin-2.

Heling, L.W.H.J., Geeves, M.A., and Kad, N.M. (2020). MyBP-C: one protein to govern them all. J Muscle Res Cell Motil *41*, 91–101. https://doi.org/10.1007/s10974-019-09567-1.

Heumann, J.M., Hoenger, A., and Mastronarde, D.N. (2011). Clustering and variance maps for cryo-electron tomography using wedge-masked differences. J Struct Biol *175*, 288–299. https://doi.org/10.1016/j.jsb.2011.05.011.

Himes, B.A., and Zhang, P. (2018). emClarity: software for high-resolution cryo-electron tomography and subtomogram averaging. Nat Methods *15*, 955–961. https://doi.org/10.1038/s41592-018-0167-z.

Himmel, D.M., Mui, S., O'Neall-Hennessey, E., Szent-Györgyi, A.G., and Cohen, C. (2009). The On-Off Switch in Regulated Myosins: Different Triggers but Related Mechanisms. J Mol Biol *394*, 496–505. https://doi.org/10.1016/j.jmb.2009.09.035.

Hirose, K., and Wakabayashi, T. (1993). Structural change of crossbridges of rabbit skeletal muscle during isometric contraction. J Muscle Res Cell Motil *14*, 432–445. https://doi.org/10.1007/BF00121295.

Hodge, A.J., Huxley, H.E., and Spiro, D. (1954). Electron microscope studies on ultrathin sections of muscle. Journal of Experimental MEDICINE *99*, 201–206. .

Holmes, K.C. (1997). The swinging lever-arm hypothesis of muscle contraction. Current Biology *7*, 112–118. https://doi.org/10.1016/s0960-9822(06)00051-0.

Holmes, K.C., Angert, I., Kull, F.J., Jahn, W., and Schröder, R.R. (2003). Electron cryo-microscopy shows how strong binding of myosin to actin releases nucleotide. Nature *425*, 423–427. https://doi.org/10.1038/nature01927.

Hooijman, P., Stewart, M.A., and Cooke, R. (2011). A new state of cardiac myosin with very slow ATP turnover: A potential cardioprotective mechanism in the heart. Biophys J *100*, 1969–1976. https://doi.org/10.1016/j.bpj.2011.02.061.

Hoppe, W., Schramm, H.J., Sturm, M., Hunsmann, N., and Gaßmann, J. (1976). Three-Dimensional Electron Microscopy of Individual Biological Objects Part I. Methods. Z. Naturforsch *31*, 645–655. .

Houdusse, A., Szent-Györgyi, A.G., and Cohen, C. (2000). Three conformational states of scallop myosin S1. Proc Natl Acad Sci U S A *97*, 11238–11243. https://doi.org/10.1073/pnas.200376897.

Hu, Z., Taylor, D.W., Reedy, M.K., Edwards, R.J., and Taylor, K.A. (2016). Structure of myosin filaments from relaxed Lethocerus flight muscle by cryo-EM at 6 Å resolution. Sci Adv *2*. https://doi.org/10.1126/sciadv.1600058.

Hutchings, J., Stancheva, V., Miller, E.A., and Zanetti, G. (2018). Subtomogram averaging of COPII assemblies reveals how coat organization dictates membrane shape. Nat Commun *9*. https://doi.org/10.1038/s41467-018-06577-4.

Huxley, H. (1957). The Double Array of Filaments in Cross-Striated Muscle. Journal of Biophysical and Biochemical Cytology *3*, 631–648. .

Huxley, H.E. (1969). The Mechanism of Muscular Contraction. Science (1979) *164*, 1356–1366. https://doi.org/10.1016/0002-8703(59)90238-8.

Huxley, A.F., and Niedergerke, R. (1954). Structural changes in muscle during contraction. Nature *173*, 971–973. https://doi.org/10.1038/nrm1308.

Huxley, H., and Hanson, J. (1954). Changes in the Cross-Striations of Muscle during Contraction and Stretch and their Structural Interpretation. Nature *173*, 973–976. .

Huxley, H.E., and Brown, W. (1967). The low-angle X-ray diagram of vertebrate striated muscle and its behaviour during contraction and rigor. J Mol Biol *30*, 383–434. https://doi.org/10.1016/S0022-2836(67)80046-9.

Huxley, H.E., Simmonst, R.M., Faruqi, A.R., Kress, M., Bordast, J., and Kocht, M.H.J. (1981). Millisecond time-resolved changes in x-ray reflections from contracting muscle during rapid mechanical transients, recorded using synchrotron radiation (cross-bridge movement/contraction mechanism/high-intensity x-ray beams). Proc. Natl. Acad. Sci. USA *78*, 2297–2301. .

Huxley, H.E., Faruqi, A.R., Kresx, M., Rordas, J., and Koch, M.H.J. (1982). Time-resolved X-ray Diffraction Studies of the Myosin Layer-line Reflections during Muscle Contraction.

Inkson, B.J. (2016). Scanning Electron Microscopy (SEM) and Transmission Electron Microscopy (TEM) for Materials Characterization. In Materials Characterization Using Nondestructive Evaluation (NDE) Methods, (Elsevier Inc.), pp. 17–43.

Iwamoto, D. v., Huehn, A., Simon, B., Huet-Calderwood, C., Baldassarre, M., Sindelar, C. v., and Calderwood, D.A. (2018). Structural basis of the filamin A actin-binding domain interaction with F-actin. Nat Struct Mol Biol *25*, 918–927. https://doi.org/10.1038/s41594-018-0128-3.

Jiang, J., Cheong, K.Y., Falkowski, P.G., and Dai, W. (2021). Integrating on-grid immunogold labeling and cryo-electron tomography to reveal photosystem II structure and spatial distribution in thylakoid membranes. J Struct Biol *213*, 107746. https://doi.org/https://doi.org/10.1016/j.jsb.2021.107746.

Jiang, Z., Jin, X., Li, Y., Liu, S., Liu, X.M., Wang, Y.Y., Zhao, P., Cai, X., Liu, Y., Tang, Y., et al. (2020). Genetically encoded tags for direct synthesis of EM-visible gold nanoparticles in cells. Nat Methods *17*, 937–946. https://doi.org/10.1038/s41592-020-0911-z.

Jin, J.P., and Wang, K. (1991). Cloning, expression, and protein interaction of human nebulin fragments composed of varying numbers of sequence modules. Journal of Biological Chemistry *266*, 21215–21223. https://doi.org/10.1016/s0021-9258(18)54843-2.

Joel, P.B., Trybus, K.M., and Sweeney, H.L. (2001). Two Conserved Lysines at the 50/20-kDa Junction of Myosin Are Necessary for Triggering Actin Activation. Journal of Biological Chemistry *276*, 2998–3003. https://doi.org/10.1074/jbc.M006930200.

Johnston, J.J., Kelley, R.I., Crawford, T.O., Morton, D.H., Agarwala, R., Koch, T., Schäffer, A.A., Francomano, C.A., and Biesecker, L.G. (2000). A novel nemaline myopathy in the Amish caused by a mutation in troponin T1. Am J Hum Genet *67*, 814–821. https://doi.org/10.1086/303089.

Jumper, J., Evans, R., Pritzel, A., Green, T., Figurnov, M., Ronneberger, O., Tunyasuvunakool, K., Bates, R., Žídek, A., Potapenko, A., et al. (2021). Highly accurate protein structure prediction with AlphaFold. Nature https://doi.org/10.1038/s41586-021-03819-2.

Kabsch, W., Mannherz, H.G., Suck, D., Pai, E.F., and Holmes, K.C. (1990). Atomic structure of the actin: DNase I complex. Nature *347*, 37–44. .

Kaech, A., and Ziegler, U. (2014). High-Pressure Freezing: Current State and Future Prospects. In Electron Microscopy: Methods and Protocols, J. Kuo, ed. (Totowa, NJ: Humana Press), pp. 151–171.

Kazmierski, S.T., Antin, P.B., Witt, C.C., Huebner, N., McElhinny, A.S., Labeit, S., and Gregorio, C.C. (2003). The complete mouse nebulin gene sequence and the identification of cardiac nebulin. J Mol Biol *328*, 835–846. https://doi.org/10.1016/S0022-2836(03)00348-6.

Kendrew, J.C., Bodo, G., Dintzis, H.M., Parrish, R.G., Wyckoff, H., and Phillips, D.C. (1958). A Three-Dimensional Model of the Myoglobin Molecule Obtained by X-Ray Analysis. Nature *181*, 662–666. https://doi.org/10.1038/181662a0.

Khavnekar, S., Wan, W., Majumder, P., Wietrzynski, W., Erdmann, P.S., and Plitzko, J.M. (2022). Multishot Tomography for High-Resolution In Situ Subtomogram Averaging. BioRxiv 2022.04.10.487763. https://doi.org/10.1101/2022.04.10.487763.

Kiss, B., Lee, E.J., Ma, W., Li, F.W., Tonino, P., Mijailovich, S.M., Irving, T.C., and Granzier, H.L. (2018). Nebulin stiffens the thin filament and augments cross-bridge interaction in skeletal muscle. Proc Natl Acad Sci U S A *115*, 10369–10374. https://doi.org/10.1073/pnas.1804726115.

Kiss, B., Gohlke, J., Tonino, P., Hourani, Z., Kolb, J., Strom, J., Alekhina, O., Smith, J.E., Ottenheijm, C., Gregorio, C., et al. (2020). Nebulin and Lmod2 are critical for specifying thin-filament length in skeletal muscle. Sci Adv *6*, 1–18. https://doi.org/10.1126/sciadv.abc1992.

Klebl, D.P., White, H.D., Sobott, F., and Muench, S.P. (2021). On-grid and in-flow mixing for time-resolved cryo-EM. Acta Crystallogr D Struct Biol *77*, 1233–1240. https://doi.org/10.1107/S2059798321008810.

Klumpe, S., Fung, H.K.H., Goetz, S.K., Zagoriy, I., Hampoelz, B., Zhang, X., Erdmann, P.S., Baumbach, J., Müller, C.W., Beck, M., et al. (2021). A Modular Platform for Automated Cryo-FIB Workflows. Elife *10*, 1–29. https://doi.org/10.7554/eLife.70506.

Klumpe, S., Kuba, J., Schioetz, O.H., Erdmann, P.S., Rigort, A., and Plitzko, J.M. (2022). Recent Advances in Gas Injection System-Free Cryo-FIB Lift-Out Transfer for Cryo-

Electron Tomography of Multicellular Organisms and Tissues. Micros Today *30*, 42–47. https://doi.org/10.1017/s1551929521001528.

Knight, P.J., and Trinick, J.A. (1982). Preparation of Myofibrils. Methods Enzymol *85*, 9–12. https://doi.org/10.1016/0076-6879(82)85004-0.

Knoll, M., and Ruska, E. (1931). Beitrag zur geometrischen Elektronenoptik. I. Ann Phys *404*, 607–661. https://doi.org/10.1002/andp.19324040506.

Knupp, C., Luther, P.K., and Squire, J.M. (2002). Titin organisation and the 3D architecture of the vertebrate-striated muscle I-band. J Mol Biol *322*, 731–739. https://doi.org/10.1016/S0022-2836(02)00819-7.

Knupp, C., Morris, E.P., and Squire, J.M. (2019). The Interacting Head Motif Structure Does Not Explain the X-Ray Diffraction Patterns in Relaxed Vertebrate (Bony Fish) Skeletal Muscle and Insect (Lethocerus) Flight Muscle. Biology (Basel) *8*, 67. https://doi.org/10.3390/biology8030067.

Kremer, J.R., Mastronarde, D.N., and McIntosh, J.R. (1996). Computer visualization of three-dimensional image data using IMOD. J Struct Biol *116*, 71–76. https://doi.org/10.1006/jsbi.1996.0013.

Krüger, M., and Linke, W.A. (2011). The giant protein titin: A regulatory node that integrates myocyte signaling pathways. Journal of Biological Chemistry *286*, 9905–9912. https://doi.org/10.1074/jbc.R110.173260.

Kruger, M., Wright, J., and Wang, K. (1991). Nebulin as a length regulator of thin filaments of vertebrate skeletal muscles: Correlation of thin filament length, nebulin size, and epitope profile. Journal of Cell Biology *115*, 97–107. https://doi.org/10.1083/jcb.115.1.97.

Kudryashov, D.S., and Reisler, E. (2013). ATP and ADP actin states. Biopolymers *99*, 245–256. https://doi.org/10.1002/bip.22155.

von Kügelgen, A., Tang, H., Hardy, G.G., Kureisaite-Ciziene, D., Brun, Y. v., Stansfeld, P.J., Robinson, C. v., and Bharat, T.A.M. (2020). In Situ Structure of an Intact Lipopolysaccharide-Bound Bacterial Surface Layer. Cell *180*, 348-358.e15. https://doi.org/10.1016/j.cell.2019.12.006.

Kühlbrandt, W. (2014). The resolution revolution. Science (1979) *343*, 1443–1444. https://doi.org/10.1126/science.1251652.

Kühne, W. (1864). Untersuchungen über das Protoplasma und die Contractilität.

Labeit, S., and Kolmerer, B. (1995). The Complete Primary Structure of Human Nebulin and its Correlation to Muscle Structure. Mol Biol 308–315. .

Labeit, S., Gibson, T., Lakey, A., Leonard, K., Zeviani, M., Knight, P., Wardale, J., and Trinick, J. (1991). Evidence that nebulin is a protein-ruler in muscle thin filaments. FEBS Lett *282*, 313–316. https://doi.org/10.1016/0014-5793(91)80503-U.

Labeit, S., Gautel, M., Lakey, A., and Trinick', J. (1992). Towards a molecular understanding of titin.

Lange, S., Ehler, E., and Gautel, M. (2006). From A to Z and back? Multicompartment proteins in the sarcomere. Trends Cell Biol *16*, 11–18. https://doi.org/10.1016/j.tcb.2005.11.007.

Lange, S., Pinotsis, N., Agarkova, I., and Ehler, E. (2019). The M-band: The underestimated part of the sarcomere. Biochim Biophys Acta Mol Cell Res *1867*. https://doi.org/10.1016/j.bbamcr.2019.02.003.

Lange, S., Pinotsis, N., Agarkova, I., and Ehler, E. (2020). The M-band: The underestimated part of the sarcomere. Biochimica et Biophysica Acta (BBA) - Molecular Cell Research *1867*, 118440. https://doi.org/https://doi.org/10.1016/j.bbamcr.2019.02.003.

Larkin, M.A., Blackshields, G., Brown, N.P., Chenna, R., Mcgettigan, P.A., McWilliam, H., Valentin, F., Wallace, I.M., Wilm, A., Lopez, R., et al. (2007). Clustal W and Clustal X version 2.0. Bioinformatics *23*, 2947–2948. https://doi.org/10.1093/bioinformatics/btm404.

van Leeuwenhoek, A. (1682). An account of several curious Discoveries about the internal texture of the flesh of Muscles, of strange motions in the Finns or Beard of Oysters; of the manner of the production of Oyster shells; and several other late Observations made by Mr. Anth. Leuw. Philosophical Collections *5*. .

Lehtokari, V.L., Kiiski, K., Sandaradura, S.A., Laporte, J., Repo, P., Frey, J.A., Donner, K., Marttila, M., Saunders, C., Barth, P.G., et al. (2014). Mutation update: The spectra of nebulin

variants and associated myopathies. Hum Mutat *35*, 1418–1426. https://doi.org/10.1002/humu.22693.

Li, M., Ma, J., Li, X., and Sui, S.F. (2021). In situ cryo-et structure of phycobilisome–photosystem ii supercomplex from red alga. Elife *10*, 1–19. https://doi.org/10.7554/eLife.69635.

Linke, W.A., Rudy, D.E., Centner, T., Gautel, M., Witt, C., Labeit, S., and Gregorio, C.C. (1999). I-band titin in cardiac muscle is a three-element molecular spring and is critical for maintaining thin filament structure. Journal of Cell Biology *146*, 631–644. https://doi.org/10.1083/jcb.146.3.631.

Liu, J., Reedy, M.C., Goldman, Y.E., Franzini-Armstrong, C., Sasaki, H., Tregear, R.T., Lucaveche, C., Winkler, H., Baumann, B.A.J., Squire, J.M., et al. (2004). Electron tomography of fast frozen, stretched rigor fibers reveals elastic distortions in the myosin crossbridges. J Struct Biol *147*, 268–282. https://doi.org/10.1016/j.jsb.2004.03.008.

Llinas, P., Isabet, T., Song, L., Ropars, V., Zong, B., Benisty, H., Sirigu, S., Morris, C., Kikuti, C., Safer, D., et al. (2015). How Actin Initiates the Motor Activity of Myosin. Dev Cell *33*, 401–412. https://doi.org/10.1016/j.devcel.2015.03.025.

Lu, Z., Shaikh, T.R., Barnard, D., Meng, X., Mohamed, H., Yassin, A., Mannella, C.A., Agrawal, R.K., Lu, T.M., and Wagenknecht, T. (2009). Monolithic microfluidic mixing-spraying devices for time-resolved cryo-electron microscopy. J Struct Biol *168*, 388–395. https://doi.org/10.1016/j.jsb.2009.08.004.

Lučić, V., Rigort, A., and Baumeister, W. (2013). Cryo-electron tomography: The challenge of doing structural biology in situ. Journal of Cell Biology *202*, 407–419. https://doi.org/10.1083/jcb.201304193.

Lukoyanova, N., VanLoock, M.S., Orlova, A., Galkin, V.E., Wang, K., and Egelman, E.H. (2002). Each actin subunit has three nebulin binding sites: Implications for steric blocking. Current Biology *12*, 383–388. https://doi.org/10.1016/S0960-9822(02)00678-4.

Luther, P.K. (2009). The vertebrate muscle Z-disc: Sarcomere anchor for structure and signalling. J Muscle Res Cell Motil *30*, 171–185. https://doi.org/10.1007/s10974-009-9189-6.

Luther, P.K., and Squire, J.M. (2002). Muscle Z-band ultrastructure: Titin Z-repeats and Z-band periodicities do not match. J Mol Biol *319*, 1157–1164. https://doi.org/10.1016/S0022-2836(02)00372-8.

Luther, P.K., Winkler, H., Taylor, K., Zoghbic, M.E., Craig, R., Padrón, R., Squire, J.M., and Liu, J. (2011). Direct visualization of myosin-binding protein C bridging myosin and actin filaments in intact muscle. Proc Natl Acad Sci U S A *108*, 11423–11428. https://doi.org/10.1073/pnas.1103216108.

Lymn, R.W., and Taylor, E.W. (1971). Mechanism of adenosine triphosphate hydrolysis by actomyosin. Biochemistry *10*, 4617–4624. https://doi.org/10.1021/bi00801a004.

Ma, W., and Irving, T.C. (2022). Small Angle X-ray Diffraction as a Tool for Structural Characterization of Muscle Disease. Int J Mol Sci *23*. https://doi.org/10.3390/ijms23063052.

Mäeots, M.E., Lee, B., Nans, A., Jeong, S.G., Esfahani, M.M.N., Ding, S., Smith, D.J., Lee, C.S., Lee, S.S., Peter, M., et al. (2020). Modular microfluidics enables kinetic insight from time-resolved cryo-EM. Nat Commun *11*, 1–14. https://doi.org/10.1038/s41467-020-17230-4.

Mahamid, J., Schampers, R., Persoon, H., Hyman, A.A., Baumeister, W., and Plitzko, J.M. (2015). A focused ion beam milling and lift-out approach for site-specific preparation of frozen-hydrated lamellas from multicellular organisms. J Struct Biol *192*, 262–269. https://doi.org/10.1016/j.jsb.2015.07.012.

Mahamid, J., Pfeffer, S., Schaffer, M., Villa, E., Danev, R., Cuellar, L.K., Förster, F., Hyman, A.A., Plitzko, J.M., and Baumeister, W. (2016). Visualizing the molecular sociology at the HeLa cell nuclear periphery. Science (1979) *351*, 969–972. https://doi.org/10.1126/science.aad8857.

Manning, E.P., Tardiff, J.C., and Schwartz, S.D. (2011). A model of calcium activation of the cardiac thin filament. Biochemistry *50*, 7405–7413. https://doi.org/10.1021/bi200506k.

Manring, H.R., Carter, O.A., and Ackermann, M.A. (2017). Obscure functions: the location–function relationship of obscurins. Biophys Rev *9*, 245–258. https://doi.org/10.1007/s12551-017-0254-x.

Marko, M., Hsieh, C., Schalek, R., Frank, J., and Mannella, C. (2007). Focused-ion-beam thinning of frozen-hydrated biological specimens for cryo-electron microscopy. Nat Methods *4*, 215–217. https://doi.org/10.1038/nmeth1014.

Marston, S., and Zamora, J.E. (2020). Troponin structure and function: a view of recent progress. J Muscle Res Cell Motil *41*, 71–89. https://doi.org/10.1007/s10974-019-09513-1.

Marttila, M., Hanif, M., Lemola, E., Nowak, K.J., Laitila, J., Grönholm, M., Wallgren-Pettersson, C., and Pelin, K. (2014). Nebulin interactions with actin and tropomyosin are altered by disease-causing mutations. Skelet Muscle *4*, 1–10. https://doi.org/10.1186/2044-5040-4-15.

Maruyama, K., Natori, R., and Nonomura, Y. (1976). New elastic protein from muscle. Nature *262*, 58–60. .

Mastronarde, D.N. (2005). Automated electron microscope tomography using robust prediction of specimen movements. J Struct Biol *152*, 36–51. https://doi.org/10.1016/j.jsb.2005.07.007.

McDonald, K.L. (2009). A review of high-pressure freezing preparation techniques for correlative light and electron microscopy of the same cells and tissues. J Microsc *235*, 273–281. https://doi.org/10.1111/j.1365-2818.2009.03218.x.

McDowall, A.W., Hofmann, W., Lepault, J., Adrian, M., and Dubochet, J. (1984). Cryo-electron microscopy of vitrified insect flight muscle. J Mol Biol *178*, 105–111. https://doi.org/https://doi.org/10.1016/0022-2836(84)90233-X.

McElhinny, A.S., Kolmerer, B., Fowler, V.M., Labeit, S., and Gregorio, C.C. (2001). The N-terminal end of nebulin interacts with tropomodulin at the pointed ends of the thin filaments. Journal of Biological Chemistry *276*, 583–592. https://doi.org/10.1074/jbc.M005693200.

McKillop, D.F., and Geeves, M.A. (1993). Regulation of the interaction between actin and myosin subfragment 1: evidence for three states of the thin filament. Biophys J *65*, 693–701. https://doi.org/10.1016/S0006-3495(93)81110-X.

McNamara, J.W., Singh, R.R., and Sadayappan, S. (2019). Cardiac myosin binding protein-C phosphorylation regulates the super-relaxed state of myosin. Proc Natl Acad Sci U S A *116*, 11731–11736. https://doi.org/10.1073/pnas.1821660116.

Mejia, Y.X., Feindt, H., Zhang, D., Steltenkamp, S., and Burg, T.P. (2014). Microfluidic cryofixation for correlative microscopy. Lab Chip *14*, 3281–3284. https://doi.org/10.1039/c4lc00333k.

Mentes, A., Huehn, A., Liu, X., Zwolak, A., Dominguez, R., Shuman, H., Ostap, E.M., and Sindelar, C. v. (2018). High-resolution cryo-EM structures of actin-bound myosin states reveal the mechanism of myosin force sensing. Proc Natl Acad Sci U S A *115*, 1292–1297. https://doi.org/10.1073/pnas.1718316115.

Mercogliano, C.P., and DeRosier, D.J. (2007). Concatenated metallothionein as a clonable gold label for electron microscopy. J Struct Biol *160*, 70–82. https://doi.org/10.1016/j.jsb.2007.06.010.

Merino, F., Pospich, S., Funk, J., Wagner, T., Küllmer, F., Arndt, H.D., Bieling, P., and Raunser, S. (2018). Structural transitions of F-actin upon ATP hydrolysis at near-atomic resolution revealed by cryo-EM. Nat Struct Mol Biol *25*, 528–537. https://doi.org/10.1038/s41594-018-0074-0.

Merino, F., Pospich, S., and Raunser, S. (2020). Towards a structural understanding of the remodeling of the actin cytoskeleton. Semin Cell Dev Biol *102*, 51–64. https://doi.org/10.1016/j.semcdb.2019.11.018.

Millevoi, S., Trombitas, K., Kolmerer, B., Kostin, S., Schaper, J., Pelin, K., Granzier, H., and Labeit, S. (1998). Characterization of Nebulette and Nebulin and Emerging Concepts of Their Roles for Vertebrate Z-Discs. J. Mol. Bio. *282*, 111–123. .

Moebel, E., Martinez-Sanchez, A., Lamm, L., Righetto, R.D., Wietrzynski, W., Albert, S., Larivière, D., Fourmentin, E., Pfeffer, S., Ortiz, J., et al. (2021). Deep learning improves macromolecule identification in 3D cellular cryo-electron tomograms. Nat Methods *18*, 1386–1394. https://doi.org/10.1038/s41592-021-01275-4.

Moncman, C.L., and Wang, K. (1995). Nebulette: A 107 kD nebulin-like protein in cardiac muscle. Cell Motil Cytoskeleton *32*, 205–225. https://doi.org/10.1002/cm.970320305.

Moor, H., and Riehle, U. (1968). Freeze-etching, Snap-freezing under high pressure: A new fixation technique for. In Proc. Fourth Europ. Reg. Conf. Elect. Microsc, pp. 33–34.

Moriya, T., Saur, M., Stabrin, M., Merino, F., Voicu, H., Huang, Z., Penczek, P.A., Raunser, S., and Gatsogiannis, C. (2017). High-resolution single particle analysis from electron cryo-microscopy images using SPHIRE. Journal of Visualized Experiments *2017*, 1–11. https://doi.org/10.3791/55448.

Morris, E.P., Nneji, G., and Squire, J.M. (1990). The three-dimensional structure of the nemaline rod Z-band. Journal of Cell Biology *111*, 2961–2978. https://doi.org/10.1083/jcb.111.6.2961.

Mukund, K., and Subramaniam, S. (2020). Skeletal muscle: A review of molecular structure and function, in health and disease. Wiley Interdiscip Rev Syst Biol Med *12*. https://doi.org/10.1002/wsbm.1462.

Mun, J.Y., Previs, M.J., Yu, H.Y., Gulick, J., Tobacman, L.S., Previs, S.B., Robbins, J., Warshaw, D.M., and Craig, R. (2014). Myosin-binding protein C displaces tropomyosin to activate cardiac thin filaments and governs their speed by an independent mechanism. Proceedings of the National Academy of Sciences *111*, 2170–2175. https://doi.org/10.1073/pnas.1316001111.

Nag, S., and Trivedi, D. v. (2021). To lie or not to lie: Super-relaxing with myosins. Elife *10*, 1–21. https://doi.org/10.7554/eLife.63703.

Nicastro, D., Frangakis, A.S., Typke, D., and Baumeister, W. (2000). Cryo-electron tomography of Neurospora mitochondria. J Struct Biol *129*, 48–56. https://doi.org/10.1006/jsbi.1999.4204.

Nicastro, D., Schwartz, C., Pierson, J., Gaudette, R., Porter, M.E., and Mcintosh, J.R. (2006). The Molecular Architecture of Axonemes Revealed by Cryoelectron tomography. Science (1979) *313*, 944–948. .

Nowak, K.J., Ravenscroft, G., Jackaman, C., Filipovska, A., Davies, S.M., Lim, E.M., Squire, S.E., Potter, A.C., Baker, E., Clément, S., et al. (2009). Rescue of skeletal muscle α-actin-null mice by cardiac (fetal) α-actin. Journal of Cell Biology *185*, 903–915. https://doi.org/10.1083/jcb.200812132.

O'Connell, C.B., Tyska, M.J., and Mooseker, M.S. (2007). Myosin at work: Motor adaptations for a variety of cellular functions. Biochim Biophys Acta Mol Cell Res *1773*, 615–630. https://doi.org/10.1016/j.bbamcr.2006.06.012.

Oda, T., and Yanagisawa, H. (2020). Cryo-electron tomography of cardiac myofibrils reveals a 3D lattice spring within the Z-discs. Commun Biol *3*, 1–9. https://doi.org/10.1038/s42003-020-01321-5.

Oda, T., Iwasa, M., Aihara, T., Maéda, Y., and Narita, A. (2009). The nature of the globular- to fibrous-actin transition. Nature *457*, 441–445. https://doi.org/10.1038/nature07685.

Oda, T., Yanagisawa, H., and Wakabayashi, T. (2020). Cryo-EM structures of cardiac thin filaments reveal the 3D architecture of troponin. J Struct Biol *209*, 107450. https://doi.org/10.1016/j.jsb.2020.107450.

Offer, G., and Elliott, A. (1978). Can a myosin molecule bind to two actin filaments? Nature *271*, 325–329. https://doi.org/10.1038/271325a0.

Ohtsuki, I. (1974). Localization of Troponin in Thin Filament and Tropomyosin Paracrystal. J. Biochem. *75*, 753–765. .

Onishi, H., Mikhailenko, S. v, and Morales, M.F. (2006). Toward understanding actin activation of myosin ATPase: The role of myosin surface loops.

Oosterheert, W., Klink, B.U., Belyy, A., Pospich, S., and Raunser, S. (2022). Structural basis of actin filament assembly and aging. BioRxiv https://doi.org/10.1101/2022.03.29.486216.

O'Reilly, F.J., Xue, L., Graziadei, A., Sinn, L., Lenz, S., Tegunov, D., Blötz, C., Singh, N., Hagen, W.J.H., Cramer, P., et al. (2020). In-cell architecture of an actively transcribing-translating expressome. Science (1979) *369*, 554–557. https://doi.org/10.1126/science.abb3758.

Page Faulk, W., and Malcolm Taylor, G. (1971). An immunocolloid method for the electron microscope. Immunochemistry *8*, 1081–1083. https://doi.org/10.1016/0019-2791(71)90496-4.

Pappas, C.T., Bhattacharya, N., Cooper, J.A., and Gregorio, C.C. (2008). Nebulin Interacts with CapZ and Regulates Thin Filament Architecture within the Z-Disc. Mol Biol Cell *19*, 1837–1847. https://doi.org/10.1091/mbc.E07.

Pappas, C.T., Krieg, P.A., and Gregorio, C.C. (2010). Nebulin regulates actin filament lengths by a stabilization mechanism. Journal of Cell Biology *189*, 859–870. https://doi.org/10.1083/jcb.201001043.

Pask, H.T., Jones, K.L., Luther, P.K., and Squire, J.M. (1994). M-band structure, M-bridge interactions and contraction speed in vertebrate cardiac muscles.

Pavlov, I., Novinger, R., and Rassier, D.E. (2009). The mechanical behavior of individual sarcomeres of myofibrils isolated from rabbit psoas muscle. Am J Physiol Cell Physiol *297*, 1211–1219. https://doi.org/10.1152/ajpcell.00233.2009.

Pepe, F.A. (1975). Structure of muscle filaments from immunohistochemical and ultrastructural studies. Journal of Histochemistry and Cytochemistry *23*, 543–562. .

Pernigo, S., Fukuzawa, A., Bertz, M., Holt, M., Rief, M., Steiner, R.A., and Gautel, M. (2010). Structural insight into M-band assembly and mechanics from the titin-obscurin-like-1 complex. Proc Natl Acad Sci U S A *107*, 2908–2913. https://doi.org/10.1073/pnas.0913736107.

Perrin, B.J., and Ervasti, J.M. (2010). The actin gene family: Function follows isoform. Cytoskeleton *67*, 630–634. https://doi.org/10.1002/cm.20475.

Perz-Edwards, R.J., and Reedy, M.K. (2011). Electron microscopy and X-ray diffraction evidence for two Z-band structural states. Biophys J *101*, 709–717. https://doi.org/10.1016/j.bpj.2011.06.024.

Pettersen, E.F., Goddard, T.D., Huang, C.C., Couch, G.S., Greenblatt, D.M., Meng, E.C., and Ferrin, T.E. (2004). UCSF Chimera - A visualization system for exploratory research and analysis. J Comput Chem *25*, 1605–1612. https://doi.org/10.1002/jcc.20084.

Pfuhl, M., Winder, S.J., and Pastore, A. (1994). Nebulin, a helical actin binding protein. EMBO Journal *13*, 1782–1789. https://doi.org/10.1002/j.1460-2075.1994.tb06446.x.

Pfuhl, M., Winder, S.J., Morelli, M.A.C., Labeit, S., and Pastore, A. (1996). Correlation between conformational and binding properties of nebulin repeats. J Mol Biol *257*, 367–384. https://doi.org/10.1006/jmbi.1996.0169.

Pinotsis, N., Petoukhov, M., Lange, S., Svergun, D., Zou, P., Gautel, M., and Wilmanns, M. (2006). Evidence for a dimeric assembly of two titin/telethonin complexes induced by the telethonin C-terminus. J Struct Biol *155*, 239–250. https://doi.org/10.1016/j.jsb.2006.03.028.

Pinotsis, N., Chatziefthimiou, S.D., Berkemeier, F., Beuron, F., Mavridis, I.M., Konarev, P. v., Svergun, D.I., Morris, E., Rief, M., and Wilmanns, M. (2012). Superhelical architecture of the myosin filament-linking protein myomesin with unusual elastic properties. PLoS Biol *10*. https://doi.org/10.1371/journal.pbio.1001261.

Pöge, M., Mahamid, J., Imanishi, S.S., Plitzko, J.M., Palczewski, K., and Baumeister, W. (2021). Determinants shaping the nanoscale architecture of the mouse rod outer segment. Elife.

Politou, A.S., Millevoi, S., Gautel, M., Kolmerer, B., and Pastore, A. (1998). SH3 in Muscles: Solution Structure of the SH3 Domain from Nebulin. J. Mol. Biol. *276*, 189–202. .

Pollard, T.D. (1986). Rate constants for the reactions of ATP- and ADP-actin with the ends of actin filaments. Journal of Cell Biology *103*, 2747–2754. https://doi.org/10.1083/jcb.103.6.2747.

Pollard, T.D., and Cooper, J.A. (2009). Actin, a central player in cell shape and movement. Science (1979) *326*, 1208–1212. https://doi.org/10.1126/science.1175862.

Poole, K.J.V., Lorenz, M., Evans, G., Rosenbaum, G., Pirani, A., Craig, R., Tobacman, L.S., Lehman, W., and Holmes, K.C. (2006). A comparison of muscle thin filament models obtained from electron microscopy reconstructions and low-angle X-ray fibre diagrams from non-overlap muscle. J Struct Biol *155*, 273–284. https://doi.org/10.1016/j.jsb.2006.02.020.

Pospich, S., Merino, F., and Raunser, S. (2020). Structural Effects and Functional Implications of Phalloidin and Jasplakinolide Binding to Actin Filaments. Structure *28*, 437-449.e5. https://doi.org/10.1016/j.str.2020.01.014.

Pospich, S., Sweeney, H.L., Houdusse, A., and Raunser, S. (2021). High-resolution structures of the actomyosin-v complex in three nucleotide states provide insights into the force generation mechanism. Elife *10*. https://doi.org/10.7554/eLife.73724.

Potter, J.D. (1974). The content of troponin, tropomyosin, actin, and myosin in rabbit skeletal muscle myofibrils. Arch Biochem Biophys *162*, 436–441. https://doi.org/https://doi.org/10.1016/0003-9861(74)90202-1.

Punjani, A., Rubinstein, J.L., Fleet, D.J., and Brubaker, M.A. (2017). CryoSPARC: Algorithms for rapid unsupervised cryo-EM structure determination. Nat Methods *14*, 290–296. https://doi.org/10.1038/nmeth.4169.

van Putten, M., Lloyd, E.M., de Greef, J.C., Raz, V., Willmann, R., and Grounds, M.D. (2020). Mouse models for muscular dystrophies: an overview. Dis Model Mech *13*. https://doi.org/10.1242/dmm.043562.

Pyle, E., and Zanetti, G. (2021). Current data processing strategies for cryo-electron tomography and subtomogram averaging. Biochemical Journal *478*, 1827–1845. https://doi.org/10.1042/BCJ20200715.

Pyle, W.G., and Solaro, R.J. (2004). At the Crossroads of Myocardial Signaling: The Role of Z-Discs in Intracellular Signaling and Cardiac Function. Circ Res *94*, 296–305. https://doi.org/10.1161/01.RES.0000116143.74830.A9.

Quentin, D., and Raunser, S. (2018). Electron cryomicroscopy as a powerful tool in biomedical research. J Mol Med *96*, 483–493. https://doi.org/10.1007/s00109-018-1640-y.

Rao, J.N., Madasu, Y., and Dominguez, R. (2014). Mechanism of actin filament pointed-end capping by tropomodulin. Science (1979) *345*, 463–467. https://doi.org/10.1126/science.1256159.

Ratti, J., Rostkova, E., Gautel, M., and Pfuhl, M. (2011). Structure and interactions of myosin-binding protein C domain C0: Cardiac-specific regulation of myosin at its neck? Journal of Biological Chemistry *286*, 12650–12658. https://doi.org/10.1074/jbc.M110.156646.

Rayment, I., Rypniewski, W.R., Schmidt-Bäse, K., Smith, R., Tomchick, D.R., Benning, M.M., Winkelmann, D.A., Wesenberg, G., and Holden, H.M. (1993a). Three-Dimensional Structure of Myosin Subfragment-1: A Molecular Motor. Science (1979) *261*, 50–58. https://doi.org/10.1126/science.8316857.

Rayment, I., Holden, H., Whittaker, M., Yohn, C., Lorenz, M., Holmes, K., and Milligan, R. (1993b). Structure of the actin-myosin complex and its implications for muscle contraction. Science (1979) *261*, 58–65. https://doi.org/10.1126/science.8316858.

Reedy, M.K. (1968). Ultrastructure of insect flight muscle. J Mol Biol *31*, 155-IN16. https://doi.org/10.1016/0022-2836(68)90437-3.

Ribeiro, E.D.A., Pinotsis, N., Ghisleni, A., Salmazo, A., Konarev, P. v., Kostan, J., Sjöblom, B., Schreiner, C., Polyansky, A.A., Gkougkoulia, E.A., et al. (2014). The structure and regulation of human muscle α-Actinin. Cell *159*, 1447–1460. https://doi.org/10.1016/j.cell.2014.10.056.

Rice, G., Wagner, T., Stabrin, M., and Raunser, S. (2022). TomoTwin: Generalized 3D Localization of Macromolecules in Cryo-electron Tomograms with Structural Data Mining. BioRxiv 2022.06.24.497279. https://doi.org/10.1101/2022.06.24.497279.

Risal, D., Gourinath, S., Himmel, D.M., Szent-Györgyi, A.G., and Cohen, C. (2004). Myosin subfragment 1 structures reveal a partially bound nucleotide and a complex salt bridge that helps couple nucleotide and actin binding. Proc Natl Acad Sci U S A *101*, 8930–8935. https://doi.org/10.1073/pnas.0403002101.

Risi, C., Belknap, B., Forgacs-Lonart, E., Harris, S.P., Schröder, G.F., White, H.D., and Galkin, V.E. (2018). N-Terminal Domains of Cardiac Myosin Binding Protein C Cooperatively Activate the Thin Filament. Structure *26*, 1604-1611.e4. https://doi.org/10.1016/j.str.2018.08.007.

Risi, C.M., Patra, M., Belknap, B., Harris, S.P., White, H.D., and Galkin, V.E. (2021a). Interaction of the C2 Ig-like Domain of Cardiac Myosin Binding Protein-C with F-actin: Interaction of C2 Domain of cMyBP-C with F-actin. J Mol Biol *433*. https://doi.org/10.1016/j.jmb.2021.167178.

Risi, C.M., Pepper, I., Belknap, B., Landim-Vieira, M., White, H.D., Dryden, K., Pinto, J.R., Chase, P.B., and Galkin, V.E. (2021b). The structure of the native cardiac thin filament at systolic Ca2+ levels. Proc Natl Acad Sci U S A *118*, 2–9. https://doi.org/10.1073/pnas.2024288118.

Romero, N.B., Sandaradura, S.A., and Clarke, N.F. (2013). Recent advances in nemaline myopathy. Curr Opin Neurol *26*, 519–526. https://doi.org/10.1097/WCO.0b013e328364d681.

Root, D.D., and Wang, K. (1994). Calmodulin-Sensitive Interaction of Human Nebulin Fragments with Actin and Myosin. Biochemistry 12581–12591. .

de Rosier, D.J., and Klug, A. (1968). Reconstruction of Three Dimensional Structures from Electron Micrographs. Nature *217*, 130–134. https://doi.org/10.1038/217130a0.

Roth, J. (1996). The silver anniversary of gold: 25 Years of the colloidal gold marker system for immunocytochemistry and histochemistry. Histochem Cell Biol *106*, 1–8. https://doi.org/10.1007/BF02473197.

Ruff, C., Furch, M., Brenner, B., Manstein, D.J., and Meyhöfer, E. (2001). Single-molecule tracking of myosins with genetically engineered amplifier domains. Nat Struct Biol *8*, 226–229. https://doi.org/10.1038/84962.

Rusu, M., Hu, Z., Taylor, K.A., and Trinick, J. (2017). Structure of isolated Z-disks from honeybee flight muscle. J Muscle Res Cell Motil *38*, 241–250. https://doi.org/10.1007/s10974-017-9477-5.

Ryan, M.M., Schnell, C., Strickland, C.D., Shield, L.K., Morgan, G., Iannaccone, S.T., Laing, N.G., Beggs, A.H., and North, K.N. (2001). Nemaline myopathy: A clinical study of 143 cases. Ann Neurol *50*, 312–320. https://doi.org/10.1002/ana.1080.

Sandaradura, S.A., Bournazos, A., Mallawaarachchi, A., Cummings, B.B., Waddell, L.B., Jones, K.J., Troedson, C., Sudarsanam, A., Nash, B.M., Peters, G.B., et al. (2018). Nemaline myopathy and distal arthrogryposis associated with an autosomal recessive TNNT3 splice variant. Hum Mutat *39*, 383–388. https://doi.org/10.1002/humu.23385.

Savarese, M., Palmio, J., Poza, J.J., Weinberg, J., Olive, M., Cobo, A.M., Vihola, A., Jonson, P.H., Sarparanta, J., García-Bragado, F., et al. (2019). Actininopathy: A new muscular

dystrophy caused by ACTN2 dominant mutations. Ann Neurol *85*, 899–906. https://doi.org/10.1002/ana.25470.

Scarff, C.A., Carrington, G., Casas-Mao, D., Chalovich, J.M., Knight, P.J., Ranson, N.A., and Peckham, M. (2020). Structure of the shutdown state of myosin-2. Nature *588*, 515–520. https://doi.org/10.1038/s41586-020-2990-5.

Schaffer, M., Mahamid, J., Engel, B.D., Laugks, T., Baumeister, W., and Plitzko, J.M. (2017). Optimized cryo-focused ion beam sample preparation aimed at in situ structural studies of membrane proteins. J Struct Biol *197*, 73–82. https://doi.org/10.1016/j.jsb.2016.07.010.

Schaffer, M., Pfeffer, S., Mahamid, J., Kleindiek, S., Laugks, T., Albert, S., Engel, B.D., Rummel, A., Smith, A.J., Baumeister, W., et al. (2019). A cryo-FIB lift-out technique enables molecular-resolution cryo-ET within native Caenorhabditis elegans tissue. Nat Methods *16*, 757–762. https://doi.org/10.1038/s41592-019-0497-5.

Scheres, S.H.W. (2012). RELION: Implementation of a Bayesian approach to cryo-EM structure determination. J Struct Biol *180*, 519–530. https://doi.org/10.1016/j.jsb.2012.09.006.

Schindelin, J., Arganda-Carreras, I., Frise, E., Kaynig, V., Longair, M., Pietzsch, T., Preibisch, S., Rueden, C., Saalfeld, S., Schmid, B., et al. (2012). Fiji: An open-source platform for biological-image analysis. Nat Methods *9*, 676–682. https://doi.org/10.1038/nmeth.2019.

Schmitz, H., Reedy, M.C., Reedy, M.K., Tregear, R.T., Winkler, H., and Taylor, K.A. (1996). Electron tomography of insect flight muscle in rigor and AMPPNP at 23°C. J Mol Biol *264*, 279–301. https://doi.org/10.1006/jmbi.1996.0641.

Schneider, C.A., Rasband, W.S., and Eliceiri, K.W. (2012). NIH Image to ImageJ: 25 years of image analysis. Nat Methods *9*, 671–675. https://doi.org/10.1038/nmeth.2089.

Schur, F.K.M., Obr, M., Hagen, W.J.H., Wan, W., Jakobi, A.J., Kirkpatrick, J.M., Sachse, C., Kräusslich, H.-G., and Briggs, J.A.G. (2016). An atomic model of HIV-1 capsid-SP1 reveals structures regulating assembly and maturation. Science (1979) *353*, 506–508. https://doi.org/10.1126/science.aaf9620.

Selcen, D., and Engel, A.G. (2011). Myofibrillar myopathies (Elseview B.V.).

Sewry, C.A. (2002). Electron microscopy of human skeletal muscle: role in diagnosis. Curr Diagn Pathol *8*, 225–231. https://doi.org/10.1054/ycdip.2002.0121.

Sewry, C.A., Laitila, J.M., and Wallgren-Pettersson, C. (2019). Nemaline myopathies: a current view. J Muscle Res Cell Motil *40*, 111–126. https://doi.org/10.1007/s10974-019-09519-9.

Silvester, E., Vollmer, B., Pražák, V., Vasishtan, D., Machala, E.A., Whittle, C., Black, S., Bath, J., Turberfield, A.J., Grünewald, K., et al. (2021). DNA origami signposts for identifying proteins on cell membranes by electron cryotomography. Cell *184*, 1110-1121.e16. https://doi.org/10.1016/j.cell.2021.01.033.

Smith, F.H. (1954). Two Half-shade Devices for Optical Polarizing Instruments. Nature *173*, 362–363. .

Smyth, M.S., and Martin, J.H.J. (2000). X Ray crystallography. J Clin Pathol: Mol Pathol *53*, 8–14. .

Spudich, J.A. (2001). The myosin swinging cross-bridge model. Nat Rev Mol Cell Biol *2*, 387–392. .

Squire, J.M. (2009). Muscle myosin filaments: Cores, crowns and couplings. Biophys Rev *1*, 149–160. https://doi.org/10.1007/s12551-009-0017-4.

Stan Development Team (2019). Stan Modeling Language Users Guide and Reference Manual, version 2.27.

Steffen, W., Smith, D., Simmons, R., and Sleep, J. (2001). Mapping the actin filament with myosin. Proc Natl Acad Sci U S A *98*, 14949–14954. https://doi.org/10.1073/pnas.261560698.

Steinbrecht, R.A., and Müller, M. (1987). Freeze-Substitution and Freeze-Drying. In Cryotechniques in Biological Electron Microscopy, K. Steinbrecht Rudolf Alexander and Zierold, ed. (Berlin, Heidelberg: Springer Berlin Heidelberg), pp. 149–172.

Steinbrecht, R.A., and Zierold, K. (1987). Cryotechniques in Biological Electron Microscopy (Berlin: Springer-Verlag).

Stewart, M.A., Franks-Skiba, K., Chen, S., and Cooke, R. (2010). Myosin ATP turnover rate is a mechanism involved in thermogenesis in resting skeletal muscle fibers. Proc Natl Acad Sci U S A *107*, 430–435. https://doi.org/10.1073/pnas.0909468107.

Straub, F.B. (1942). Actin. Stud. Inst. Med. Chem. Univ. Szeged. *2*. https://doi.org/10.1007/bf01599277.

Studer, G., Rempfer, C., Waterhouse, A.M., Gumienny, R., Haas, J., and Schwede, T. (2020). QMEANDisCo-distance constraints applied on model quality estimation. Bioinformatics *36*, 1765–1771. https://doi.org/10.1093/bioinformatics/btz828.

Sutton, G., Sun, D., Fu, X., Kotecha, A., Hecksel, C.W., Clare, D.K., Zhang, P., Stuart, D.I., and Boyce, M. (2020). Assembly intermediates of orthoreovirus captured in the cell. Nat Commun *11*, 1–7. https://doi.org/10.1038/s41467-020-18243-9.

Sweeney, H.L., Houdusse, A., and Robert-Paganin, J. (2020). Myosin Structures. In Myosins: A Superfamily of Molecular Motors, L.M. Coluccio, ed. (Cham: Springer International Publishing), pp. 7–19.

Szent-Györgyi, A. (1943). The crystallization of myosin and some of its properties and reactions. Stud. Inst. Med. Chem. Univ. Szeged. 76–85. .

Szent-Györgyi, A.G. (1953). Meromyosins, the subunits of myosin. Arch Biochem Biophys *42*, 305–320. https://doi.org/https://doi.org/10.1016/0003-9861(53)90360-9.

Tacke, S., Erdmann, P., Wang, Z., Klumpe, S., Grange, M., Kříž, R., Dolník, M., Mitchels, J., Plitzko, J., and Raunser, S. (2020). A streamlined workflow for automated cryo focused ion beam milling. BioRxiv 2020.02.24.963033. https://doi.org/10.1101/2020.02.24.963033.

Tacke, S., Erdmann, P., Wang, Z., Klumpe, S., Grange, M., Plitzko, J., and Raunser, S. (2021). A streamlined workflow for automated cryo focused ion beam milling. J Struct Biol 107743. https://doi.org/10.1016/j.jsb.2021.107743.

Takahashi, K., and Hattori, A. (1989). α-actinin is a component of the Z-filament, a structural backbone of skeletal muscle Z-disks. J Biochem *105*, 529–536. https://doi.org/10.1093/oxfordjournals.jbchem.a122701.

Takeda, S., Yamashita, A., Maeda, K., and Maéda, Y. (2003). Structure of the core domain of human cardiac troponin in the Ca^{2+}-saturated form. Nature *424*, 35–41. https://doi.org/10.1038/nature01780.

Tanaka, K., Takeda, S., Mitsuoka, K., Oda, T., Kimura-Sakiyama, C., Maéda, Y., and Narita, A. (2018). Structural basis for cofilin binding and actin filament disassembly. Nat Commun *9*. https://doi.org/10.1038/s41467-018-04290-w.

Tang, G., Peng, L., Baldwin, P.R., Mann, D.S., Jiang, W., Rees, I., and Ludtke, S.J. (2007). EMAN2: An extensible image processing suite for electron microscopy. J Struct Biol *157*, 38–46. https://doi.org/10.1016/j.jsb.2006.05.009.

Taylor, K.A., Reedy, M.C., Cordova, L., and Reedy, M.K. (1984). Three-dimensional reconstruction of rigor insect flight muscle from tilted thin sections. Nature *310*, 285–291. https://doi.org/10.1038/310285a0.

Tegunov, D., and Cramer, P. (2019). Real-time cryo-electron microscopy data preprocessing with Warp. Nat Methods *16*, 1146–1152. https://doi.org/10.1038/s41592-019-0580-y.

Tegunov, D., Xue, L., Dienemann, C., Cramer, P., and Mahamid, J. (2021). Multi-particle cryo-EM refinement with M visualizes ribosome-antibiotic complex at 3.5 Å in cells. Nat Methods *18*, 186–193. https://doi.org/10.1038/s41592-020-01054-7.

Terwilliger, T.C., Ludtke, S.J., Read, R.J., Adams, P.D., and Afonine, P. V. (2020). Improvement of cryo-EM maps by density modification. Nat Methods *17*, 923–927. https://doi.org/10.1038/s41592-020-0914-9.

Tinevez, J.Y., Perry, N., Schindelin, J., Hoopes, G.M., Reynolds, G.D., Laplantine, E., Bednarek, S.Y., Shorte, S.L., and Eliceiri, K.W. (2017). TrackMate: An open and extensible platform for single-particle tracking. Methods *115*, 80–90. https://doi.org/10.1016/j.ymeth.2016.09.016.

Trombitas, K., Frey, L., and Pollack, G.H. (1993). Filament lengths in frog semitendinosus and tibialis anterior muscle fibres. J Muscle Res Cell Motil *14*, 167–172. .

Turoňová, B., Schur, F.K.M., Wan, W., and Briggs, J.A.G. (2017). Efficient 3D-CTF correction for cryo-electron tomography using NovaCTF improves subtomogram averaging resolution to 3.4 Å. J Struct Biol *199*, 187–195. https://doi.org/10.1016/j.jsb.2017.07.007.

Tyska, M.J., Dupuis, D.E., Guilford, W.H., Patlak, J.B., Waller, G.S., Trybus, K.M., Warshaw, D.M., and Lowey, S. (1999). Two heads of myosin are better than one for generating force and motion. Proc Natl Acad Sci U S A *96*, 4402–4407. .

Ullrick, W.C., Toselli, P.A., Saide, J.D., and Phear, W.P.C. (1977). Fine structure of the vertebrate Z-disc. J Mol Biol *115*, 61–74. https://doi.org/10.1016/0022-2836(77)90246-7.

Vibert, P., Craig, R., and Lehman, W. (1997). Steric-model for Activation of Muscle Thin Filaments. J. Mol. Biol. *268*, 8–14. .

Villa, E., Schaffer, M., Plitzko, J.M., and Baumeister, W. (2013). Opening windows into the cell: Focused-ion-beam milling for cryo-electron tomography. Curr Opin Struct Biol *23*, 771–777. https://doi.org/10.1016/j.sbi.2013.08.006.

Vinogradova, M. v., Stone, D.B., Malanina, G.G., Karatzaferi, C., Cooke, R., Mendelson, R.A., and Fletterick, R.J. (2005). Ca^{2+}-regulated structural changes in troponin. Proc Natl Acad Sci U S A *102*, 5038–5043. https://doi.org/10.1073/pnas.0408882102.

Volkmann, N., Ouyang, G., Trybus, K.M., DeRosier, D.J., Lowey, S., and Hanein, D. (2003). Myosin isoforms show unique conformations in the actin-bound state. Proceedings of the National Academy of Sciences *100*, 3227–3232. https://doi.org/10.1073/pnas.0536510100.

Wagner, T., Merino, F., Stabrin, M., Moriya, T., Antoni, C., Apelbaum, A., Hagel, P., Sitsel, O., Raisch, T., Prumbaum, D., et al. (2019). SPHIRE-crYOLO is a fast and accurate fully automated particle picker for cryo-EM. Commun Biol *2*, 1–13. https://doi.org/10.1038/s42003-019-0437-z.

Wallgren-Pettersson, C., Sewry, C.A., Nowak, K.J., and Laing, N.G. (2011). Nemaline myopathies. Semin Pediatr Neurol *18*, 230–238. https://doi.org/10.1016/j.spen.2011.10.004.

Wang, H.W., and Fan, X. (2019). Challenges and opportunities in cryo-EM with phase plate. Curr Opin Struct Biol *58*, 175–182. https://doi.org/10.1016/j.sbi.2019.06.013.

Wang, K., and Williamson, C.L. (1980). Identification of an N2 line protein of striated muscle. Proc Natl Acad Sci U S A *77*, 3254–3258. https://doi.org/10.1073/pnas.77.6.3254.

Wang, K., McClure, J., and Tu, A. (1979). Titin: Major myofibrillar components of striated muscle. Proc Natl Acad Sci U S A *76*, 3698–3702. https://doi.org/10.1073/pnas.76.8.3698.

Wang, Q., Mercogliano, C.P., and Löwe, J. (2011). A ferritin-based label for cellular electron cryotomography. Structure *19*, 147–154. https://doi.org/10.1016/j.str.2010.12.002.

Wang, S., Li, W., Liu, S., and Xu, J. (2016). RaptorX-Property: a web server for protein structure property prediction. Nucleic Acids Res *44*, W430–W435. https://doi.org/10.1093/nar/gkw306.

Wang, Z., Grange, M., Wagner, T., Kho, A.L., Gautel, M., and Raunser, S. (2021). The molecular basis for sarcomere organization in vertebrate skeletal muscle. Cell *184*, 2135-2150.e13. https://doi.org/10.1016/j.cell.2021.02.047.

Wang, Z., Grange, M., Pospich, S., Wagner, T., Kho, A.L., Gautel, M., and Raunser, S. (2022). Structures from intact myofibrils reveal mechanism of thin filament regulation through nebulin. Science *375*, eabn1934. https://doi.org/10.1126/science.abn1934.

Waterhouse, A., Bertoni, M., Bienert, S., Studer, G., Tauriello, G., Gumienny, R., Heer, F.T., De Beer, T.A.P., Rempfer, C., Bordoli, L., et al. (2018). SWISS-MODEL: Homology modelling of protein structures and complexes. Nucleic Acids Res *46*, W296–W303. https://doi.org/10.1093/nar/gky427.

Weber, A., Pennise, C.R., Babcock, G.G., and Fowler, V.M. (1994). Tropomodulin Caps the Pointed Ends of Actin Filaments. Journal of Cell Biology *127*, 1627–1635. .

Wegner, A. (1976). Head to Tail Polymerization of Actin.

Wells, C., and Bagshaw, C.R. (1985). Calcium regulation of molluscan myosin ATPase in the absence of actin. Nature *313*, 696–697. https://doi.org/10.1038/313696a0.

Wendt, T., Taylor, D., Trybus, K.M., and Taylor, K. (2001). Three-dimensional image reconstruction of dephosphorylated smooth muscle heavy meromyosin reveals asymmetry in the interaction between myosin heads and placement of subfragment 2. Proc Natl Acad Sci U S A *98*, 4361–4366. https://doi.org/10.1073/pnas.071051098.

Williams, D.B., and Carter, C.B. (2009). Transmission Electron Microscopy (Springer).

Winkler, J., Lunsdorf, H., and Jockusch, B.M. (1997). Flexibility and fine structure of smooth-muscle a-actinin. Eur. J. Biochem *248*. .

Witt, C.C., Burkart, C., Labeit, D., McNabb, M., Wu, Y., Granzier, H., and Labeit, S. (2006). Nebulin regulates thin filament length, contractility, and Z-disk structure in vivo. EMBO Journal *25*, 3843–3855. https://doi.org/10.1038/sj.emboj.7601242.

Wolff, G., Limpens, R.W.A.L., Zheng, S., Snijder, E.J., Agard, D.A., Koster, A.J., and Bárcena, M. (2019). Mind the gap: Micro-expansion joints drastically decrease the bending of FIB-milled cryo-lamellae. J Struct Biol *208*, 0–3. https://doi.org/10.1016/j.jsb.2019.09.006.

Woodhead, J.L., Zhao, F.Q., Craig, R., Egelman, E.H., Alamo, L., and Padrón, R. (2005). Atomic model of a myosin filament in the relaxed state. Nature *436*, 1195–1199. https://doi.org/10.1038/nature03920.

Wulf, S.F., Ropars, V., Fujita-Becker, S., Oster, M., Hofhaus, G., Trabuco, L.G., Pylypenko, O., Sweeney, H.L., Houdusse, A.M., and Schröder, R.R. (2016). Force-producing ADP state of myosin bound to actin. Proceedings of the National Academy of Sciences *113*, E1844–E1852. https://doi.org/10.1073/pnas.1516598113.

Xiong, Q., Morphew, M.K., Schwartz, C.L., Hoenger, A.H., and Mastronarde, D.N. (2009). CTF determination and correction for low dose tomographic tilt series. J Struct Biol *168*, 378–387. https://doi.org/10.1016/j.jsb.2009.08.016.

Yamada, Y., Namba, K., and Fujii, T. (2020). Cardiac muscle thin filament structures reveal calcium regulatory mechanism. Nat Commun *11*, 1–3. https://doi.org/10.1038/s41467-019-14008-1.

Yang, S., Woodhead, J.L., Zhao, F.Q., Sulbarán, G., and Craig, R. (2016). An approach to improve the resolution of helical filaments with a large axial rise and flexible subunits. J Struct Biol *193*, 45–54. https://doi.org/10.1016/j.jsb.2015.11.007.

Yang, S., Tiwari, P., Lee, K.H., Sato, O., Ikebe, M., Padrón, R., and Craig, R. (2020). Cryo-EM structure of the inhibited (10S) form of myosin II. Nature *588*, 521–525. https://doi.org/10.1038/s41586-020-3007-0.

Yang, Y., Gourinath, S., Kovács, M., Nyitray, L., Reutzel, R., Himmel, D.M., O'Neall-Hennessey, E., Reshetnikova, L., Szent-Györgyi, A.G., Brown, J.H., et al. (2007). Rigor-like Structures from Muscle Myosins Reveal Key Mechanical Elements in the Transduction Pathways of This Allosteric Motor. Structure *15*, 553–564. https://doi.org/10.1016/j.str.2007.03.010.

Yang, Z., Fang, J., Chittuluru, J., Asturias, F.J., and Penczek, P.A. (2012). Iterative stable alignment and clustering of 2D transmission electron microscope images. Structure *20*, 237–247. https://doi.org/10.1016/j.str.2011.12.007.

Yasuda, M., Koshida, S., Sato, N., and Obinata, T. (1995). Complete Primary Structure of Chicken Cardiac C-protein (MyBP-C) and its Expression in Developing Striated Muscles.

Yi, H., Strauss, J.D., Ke, Z., Alonas, E., Dillard, R.S., Hampton, C.M., Lamb, K.M., Hammonds, J.E., Santangelo, P.J., Spearman, P.W., et al. (2015). Native Immunogold Labeling of Cell Surface Proteins and Viral Glycoproteins for Cryo-Electron Microscopy and Cryo-Electron Tomography Applications. Journal of Histochemistry and Cytochemistry *63*, 780–792. https://doi.org/10.1369/0022155415593323.

Young, P., Ehler, E., and Gautel, M. (2001). Obscurin, a giant sarcomeric Rho guanine nucleotide exchange factor protein involved in sarcomere assembly. Journal of Cell Biology *154*, 123–136. https://doi.org/10.1083/jcb.200102110.

Zachs, T., Schertel, A., Medeiros, J., Weiss, G.L., Hugener, J., Matos, J., and Pilhofer, M. (2020). Fully automated, sequential focused ion beam milling for cryo-electron tomography. Elife *9*, 1–14. https://doi.org/10.7554/eLife.52286.

Zernike, F. (1955). How I Discovered Phase Contrast. Science (1979) *121*, 345–349. .

Zhang, J.Q., Weisberg, A., and Horowits, R. (1998). Expression and purification of large nebulin fragments and their interaction with actin. Biophys J *74*, 349–359. https://doi.org/10.1016/S0006-3495(98)77792-6.

Zheng, S., Wolff, G., Greenan, G., Chen, Z., Faas, F.G.A., Bárcena, M., Koster, A.J., Cheng, Y., and Agard, D. (2022). AreTomo: An integrated software package for automated marker-free, motion-corrected cryo-electron tomographic alignment and reconstruction. BioRxiv 2022.02.15.480593. https://doi.org/10.1101/2022.02.15.480593.

Zheng, S.Q., Palovcak, E., Armache, J.P., Verba, K.A., Cheng, Y., and Agard, D.A. (2017). MotionCor2: Anisotropic correction of beam-induced motion for improved cryo-electron microscopy. Nat Methods *14*, 331–332. https://doi.org/10.1038/nmeth.4193.

Zivanov, J., Otón, J., Ke, Z., Qu, K., Morado, D., Castaño-Díez, D., von Kügelgen, A., Bharat, T.A.M., Briggs, J.A.G., and Scheres, S.H.W. (2022). A Bayesian approach to single-particle electron cryo-tomography in RELION-4.0. BioRxiv 2022.02.28.482229. https://doi.org/10.1101/2022.02.28.482229.

Zoghbi, M.E., Woodhead, J.L., Moss, R.L., and Craig, R. (2008). Three-dimensional structure of vertebrate cardiac muscle myosin filaments. Proc Natl Acad Sci U S A.

CHAPTER 6 APPENDIX

Methods specific to section 4.2

Sub-volume averaging of the thick filament

Tomograms were initially 4x binned and lowpass-filtered to 60 Å using EMAN2 for visualization. To pick filaments accurately without the interference from signals from cross-bridges, an equatorial mask in the Fourier transform of XY slices of tomograms was applied. CrYOLO (Wagner et al., 2019) was afterwards employed to detect the shape of thick filaments in the XZ planes of the filtered tomogram. The detected points were then traced by a python script and generate the coordinates for thick filaments. In total, 13,700 segments of thick filaments (sub-volumes) were picked from 8 tomograms from multiple myofibrils with an inter-segment distance of 105 Å. These segments were extracted from unbinned and 2x binned tomograms with a box size of 128 pixels (450 Å) using RELION (Bharat and Scheres, 2016). Prior information of the orientations of the thick filaments in a tomogram was used to generate a featureless cylinder-like reference using PEET (Heumann et al., 2011; Nicastro et al., 2006). The sub-volumes were then aligned and averaged using RELION. Three different strategies were used during alignment. First, the sub-volumes were aligned without any symmetry imposed and a global refinement was enabled. This resulted in aligning the missing wedge and a map with anisotropic resolution was generated (Fig. 6.1B). Then, a C3 symmetry was imposed during refinement according to a previous structural study of the relaxed human cardiac myosin filament (AL-Khayat et al., 2013). Although the averaged map had an isotropic resolution, the quality of the map did not improve (Fig. 6.1C). In the end, without any symmetry imposed, only local refinement was enabled to prevent aligning the missing wedges (Fig. 6.1D). This averaged structure has an estimated resolution of 30.4 Å based on the "gold-standard" FSC with 0.143 criterion. The map was used as a model for the thick filament in Fig. 4.13 and Fig. 4.15.

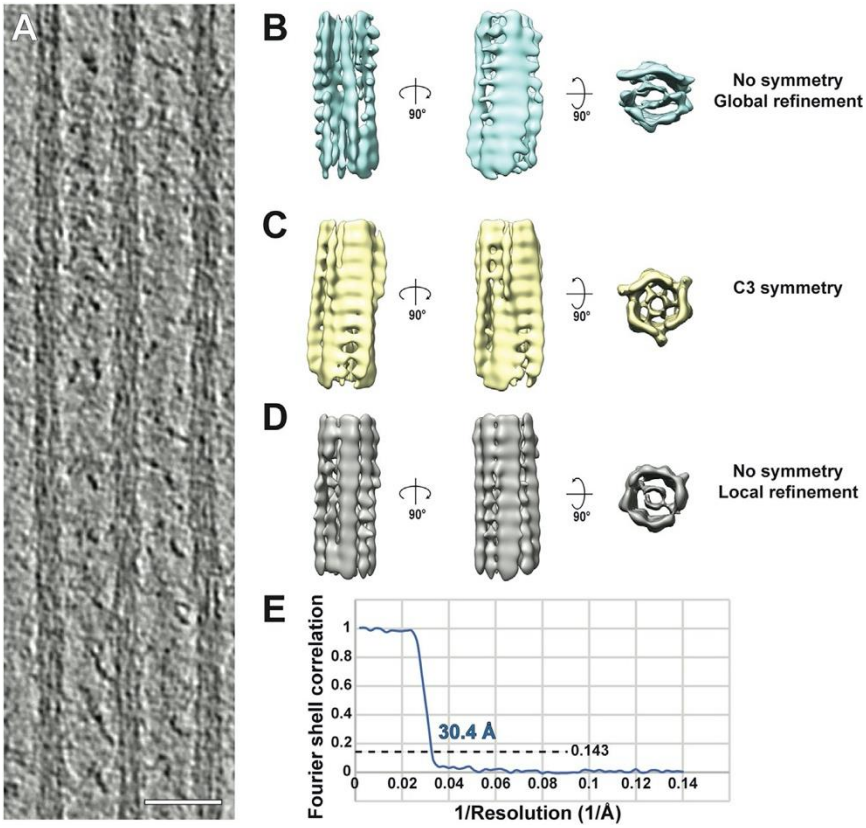

Fig. 6.1 Sub-volume averaging of thick filaments

*(**A**) Slice through a tomogram depicting three adjacent thick filaments. Scale bar, 50 nm. (**B**) Averaged structure from a global refinement. The map suffers from missing wedge artifacts, indicating alignment focused on the missing wedge instead of actual structural features. (**C**) The distribution of myosin heads when retracted to the thick filaments in the relaxed state has a C3 symmetry. We therefore performed a refinement and reconstruction applying C3 symmetry. However, this did not improve the quality of the map, indicating that the core of vertebrate thick filaments is not C3 symmetric. (**D**) A local refinement with restricted possible rotation angles reduced alignment errors and thereby missing wedge artifacts. This reconstruction was used as a model for thick filament later in Fig. 4.13 and Fig. 4.15. (**E**) The estimated resolution of the reconstruction in (D) is 30.4 Å using the 0.143 criterion.*

Sub-volume averaging of the actomyosin complex and fitting of atomic model

Thin filaments were picked automatically in a similar method as described above. Instead of using crYOLO, thin filaments, which appeared as dense dots from the XZ view (Fig. 4.10E), were recognized and traced by the TrackMate plug-in (Tinevez et al., 2017) in Fiji (Schindelin et al., 2012; Schneider et al., 2012). In total, 32,421 segments (sub-volumes) were picked from 8 tomograms from multiple myofibrils with an inter-segment distance of 63 Å. These segments were extracted from unbinned and unfiltered tomograms with a box size of 200 pixels (351 Å) using RELION (Bharat and Scheres, 2016). In order to exclude low-quality sub-volumes using

2D classification, the extracted sub-volumes were first rotated to orient thin filaments parallel the XY plane based on filament orientations calculated from particle positions. Projection images along Z-axis were then generated from the central 100 slices (175 Å) of each particle and subsequently classified using 2D classification in the ISAC software (Yang et al., 2012) from the SPHIRE package (Moriya et al., 2017). This approach, compared to using the entire sub-volume for projection, excluded signals from other filaments at the corner of the sub-volume and thus enabled a more reliable assessment of particle quality (Fig. 6.2B). 21,130 selected good sub-volumes were aligned, averaged, and classified in 3D using RELION, based on a cylinder-like reference generated from averaging all sub-volumes after aligning the longitudinal axis of segments using PEET (Fig. 6.2C). In each 3D class, translation and rotation parameters were modified to align the most prominent double-head of myosin (Fig. 6.2D). After combining the modified good classes and removing duplicate particles, 18,090 sub-volumes were refined locally with a mask including the thin filament and one pair of myosin double-head. Final average has an estimated resolution of 10.2 Å based on the "gold-standard" FSC with 0.143 criterion. Local resolution was estimated in SPHIRE using the two half-maps and the mask used during averaging. The final map was sharpened with a B-factor of -250 and filtered to the nominal resolution (Fig. 6.2F).

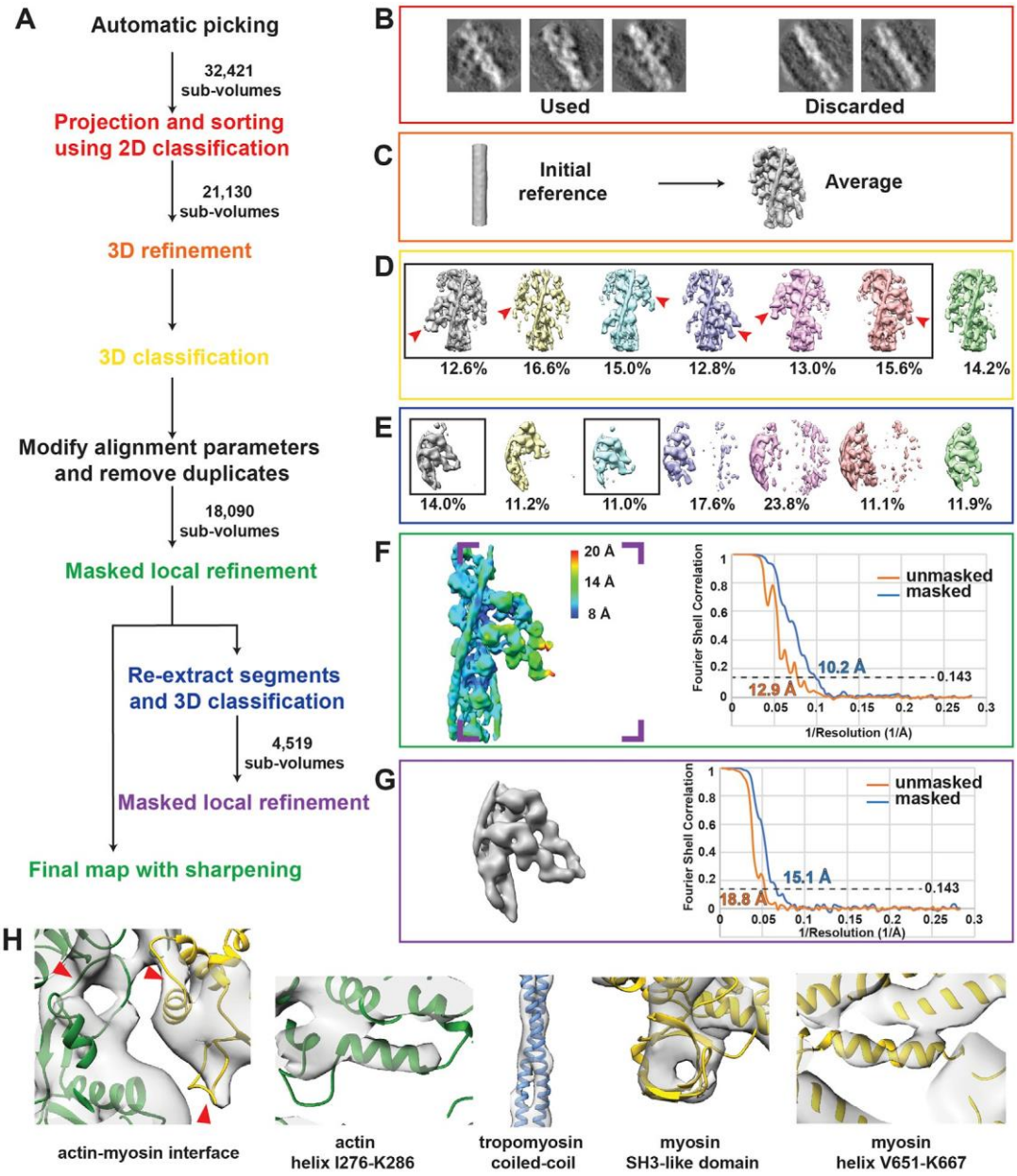

Fig. 6.2 Strategies of sub-volume averaging of the in situ actomyosin complex.

*(**A**) Workflow of sub-volume averaging leading to the final structures of the in situ actomyosin complex and double-head myosin. Details of the coloured steps are shown in (B-G). (**B**) Examples of selected and discarded 2D class averages. After cleaning by 2D sorting, 21,130 out of 32,421 sub-volumes were selected for subsequent processing. (**C**) Initial reference and the average after the first 3D refinement with only a spherical mask with a diameter of 340 Å applied. (**D**) Classes of the actomyosin complex after 3D classification. Prominent myosin double head pairs in each class are indicated by red arrow heads. These pairs were later aligned to each other during merging the classes by modifying the alignment parameters. The classes in the black box were selected and used for subsequent processing. (**E**) Classes of the myosin double-heads after the 3D classification applied on the sub-volumes re-centred on myosin heads. The two classes in the black boxes showing clear densities for the double-*

*head were selected for the final averaging. (**F**) Left: final reconstruction of the actomyosin complex generated from the local refinement with a mask around the thin filament and a pair of myosin heads after merging the classes in (D). The map is coloured based on local resolution. The purple inset shows the area of the re-centred sub-volumes for double-head analysis in (E) and (**G**). Right: The estimated resolution of the reconstruction is 10.2 Å using the 0.143 criterion. (**G**)Left: final average of the complete myosin double-head including RLC. Right: The estimated resolution of the reconstruction is 15.1 Å using the 0.143 criterion. (**H**) Example details showing secondary structures that are visible in the averaged structure in F. The red arrow heads indicate the D-loop of actin, helix-loop-helix motif and loop 3 of myosin from left to right at the interface between actin and myosin.*

In order to resolve the light chain domains of myosin heads, sub-volumes centered on myosin the double-heads (shifted 90 pixels along x axis compared to original sub-volumes) were extracted. The positions of these new sub-volumes in tomograms were calculated by a python script using the original sub-volume coordinates and their alignment parameters. The new sub-volumes were sorted through 3D classification in RELION. 4,519 particles from the two good classes were refined locally with masking out the thin filament and myosin double-head (Fig. 6.2E, G).

An initial atomic model of the *in situ* actomyosin complex was first built by rigid-body fitting of actin subunits and myosin motor domains from the atomic model of the *in vitro* actomyosin complex (von der Ecken et al., 2016) (PDB: 5JLH), tropomyosin from the atomic model of isolated cardiac thin filament (Yamada et al., 2020) (PDB: 6KN8) and myosin lever arms from the crystal structure of rigor-like squid myosin S1 (Yang et al., 2007) (PDB: 3I5G) using 'Fit in Map' in Chimera (Pettersen et al., 2004). Essential light chains (ELCs) and the regulatory light chain (RLCs) were fitted separately into the averaged map after removing 5 amino acids (M796-Y800) at the hinge on the α-helix between ELC and RLC. The model of RLC together with part of the heavy chain lever arm (K801-L839) was rigid-body fitted a segmented map generated by "Color Zone" in Chimera. Based on this initial atomic model and the sequences of actin, myosin and tropomyosin in mouse fast skeletal muscle, a homology model was calculated using SWISS-MODEL (Bertoni et al., 2017; Bienert et al., 2017; Guex et al., 2009; Studer et al., 2020; Waterhouse et al., 2018) (Fig. 4.11). Comparison of lever arms in the *in-situ* rigor upper head, lower head, squid myosin S1 fragment, and the blocked and free heads from relaxed insect flight muscle (PDB: 6SO3) (Knupp et al., 2019) (Fig. 6.2I, J) was performed by aligning the RLC of the heads using the "MatchMaker" function in Chimera.

Annotation of A-band and fitting of molecular model

In order to visualize the organization of cross-bridges between thin and thick filaments, the densities of a complete A-band were annotated manually using Amira (Thermo Fischer Scientific) on a slice-by-slice basis. A user-defined mask based on grey values was used during manual annotation to prevent the picking of weaker densities. The 2D annotation stacked to form a 3D segmented volume depicting the arrangement of thin and thick filaments as well as the cross-bridges formed by myosin heads (Fig. 4.13A). During sub-tomogram averaging, a structure of thin filament fully decorated with myosin heads (Fig. 6.2C) was obtained prior to 3D classification. This was low-pass filtered to 17 Å and extended to a length of 1,755 Å (~63 actin subunits) based on the helical symmetry detected in the structure (-166.6° turn and 27.9 Å rise) using RELION helix toolbox. This long fully-decorated thin filament model was then fitted into each segmented volume corresponding to a thin filament with bound myosin heads using "Fit in Map" in Chimera. The myosin heads that matched segmented volume were kept and colored depending on which thick filament they originated from while the other myosin heads were removed. This generated a complete map of myosin heads bound to thin filaments in the A-band (Fig. 4.13B, Fig. 4.15).

The models of double-head and split-head conformations were made from initially fitting our actomyosin structure into the segmented volume (Fig. 4.13C, D, Fig. 6.3). For the split-head conformation, the upper head from the double-head conformation was fitted into densities for both heads. The S2 domain from segments of a crystal structure (Blankenfeldt et al., 2006) (PDB: 2FXM) was manually placed at the interface between the two regulatory light chains for its speculated position and orientation. Surface models were generated with the "molmap" command in Chimera at a resolution of 15 Å.

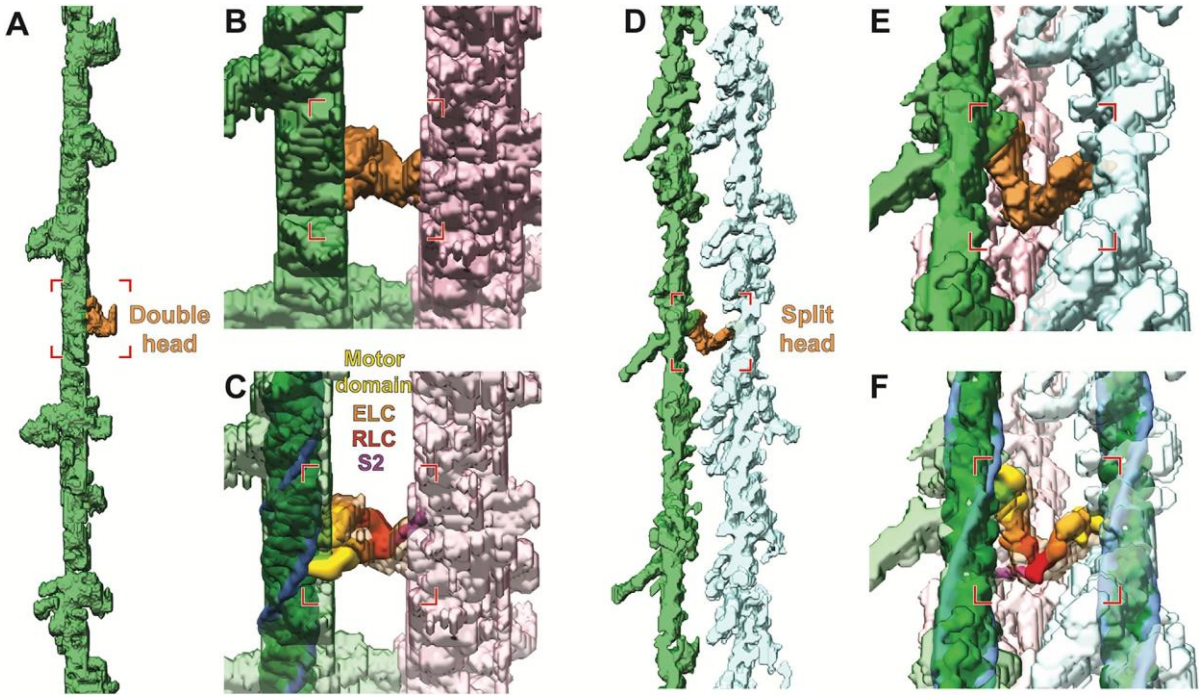

Fig. 6.3 Annotation and fitting of split and double heads of myosin between thin and thick filaments from A-band tomograms

*(**A**) Annotated density of a thin filament including the myosin heads (green), with the annotated density for a myosin double-head highlighted in orange. (**B**) Oblique and zoomed-in view of the double-head density and its associated thick filament segmentation (pink). (**C**) Same view as in (B) including the fitted thin filament and myosin double-head models from sub-volume averaging. (**D**) Annotated density of two thin filaments including the myosin heads (green and light blue), highlighting annotated density corresponding split-head in orange. (**E**) Oblique and zoomed-in view of the split-head density and its associated thick filament segmentation. (**F**) Same view as in (E) including the fitted thin filament and myosin split-head models. The split-head is composed of two heads in the upper head conformation in order to be fitted into the density.*

Analysis of preferred binding positions of myosin on thin filament

In order to investigate the relation between myosin binding and the orientation of their bound actin subunit relative to the neighboring thick filament, the corresponding angle of each actin position relative to the first actin subunit in the thin filament was calculated based on actin helical parameters determined from the averaged structure. The angles where there was a myosin bound were divided into three groups depending the original thick filaments and plotted as a circular histogram. Values of angles from different filaments were combined by aligning the average of one myosin group (represented as red color in Fig. 4.14), resulting a final histogram representing all myosin-bound actin positions (Fig. 4.14).

In addition, the molecular model of each thin filament was converted to a myosin-binding profile sequence consisting of R, G, B, and E representing actin bound by myosin from three different thick filaments and non-bound actin, respectively. The sequences of all 30 annotated filaments were aligned by multiple sequence alignment using the "msa" package in R with the MUSCLE algorithm (Edgar, 2004) utilizing a customized weighting matrix (Table 6.1, Fig. 6.4). When a thin filament was treated as a single strand, adjacent actin subunits had a huge change in orientation (166.6°) and thus very different preference for myosin binding, resulting in nonoptimal multiple sequence alignment. Therefore, each thin filament was considered as two actin strands and only one strand was used for multiple sequence alignment. The other strands were aligned using the same alignment as the first strands. The occurrence of myosin binding at each actin position was summed up for myosin from each thick filament and then used to color actin filament models in Chimera, showing averaged hotspots for myosin binding on a thin filament (Fig. 6.4B).

Score	R	G	B	E
R	10	-1	-1	-1
G	-1	0	-1	-1
B	-1	-1	0	-1
E	-1	-1	-1	0

Table 6.1 Weight matrix used for multiple sequence alignment with MUSCLE algorithm

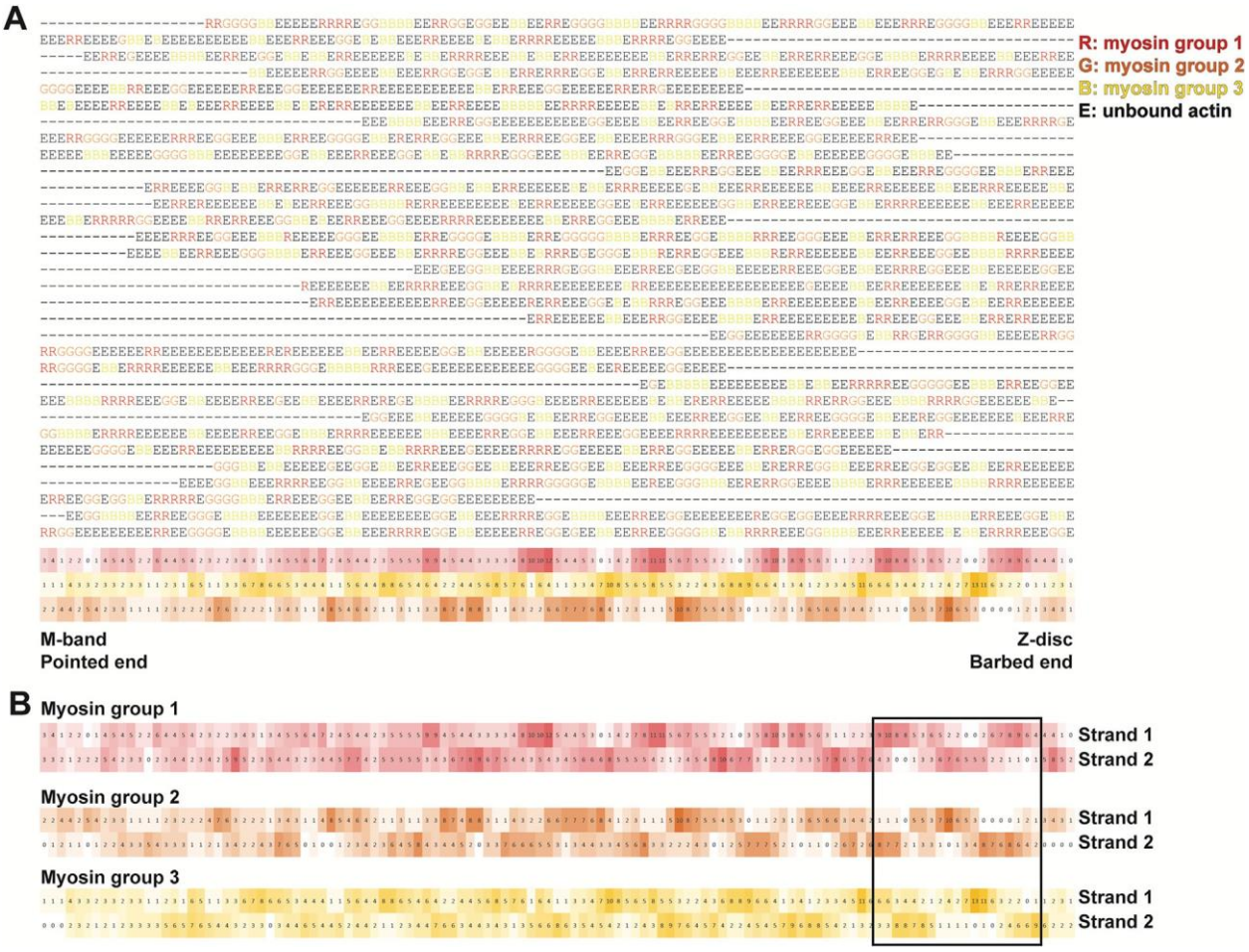

Fig. 6.4 Overall myosin binding profile generated from multiple sequence alignment of myosin binding profiles of 30 thin filaments

*(**A**) The fitted myosin head model in Fig. 4.13B was converted to myosin binding profile sequences on thin filaments, with ''R,'' ''G,'' ''B'' representing actin subunits bound by three groups of myosin heads originating from three neighboring thick filaments and ''E'' representing myosin-free actin subunits. These sequences were aligned using multiple sequence alignment with a customized weight matrix. Only the sequence of one actin strand for each thin filament was used for alignment. The sum of occurrence of each myosin group at each actin subunit position is shown at the bottom and colored accordingly. Darker color indicates higher occurrence. (**B**) The colored overall myosin binding profile on both actin strands for each myosin group. Sequences of strand 2 were combined using the alignment of strand 1 shown in (A). The overall myosin binding profiles depict hotspots for myosin binding on a thin filament and the region highlighted in the black box is used to color the models shown in Fig. 4.14B.*

To further investigate whether myosin prefers to bind at shorted distances between thin and thick filaments, the distances between thin and thick filaments at the positions where there is a myosin head bound and where myosin is absent were calculated using a python script. For each actin subunit not bound by a myosin head, three measurements were taken between the actin

and three different neighboring thick filaments. For an actin subunit that is bound by a myosin head, the distance between the actin subunit and the corresponding thick filament is considered as the myosin-bound measurement while the distances between this actin subunit and the other two neighboring thick filaments are considered as the myosin-free measurements. All measurements were plotted in a histogram (Fig. 4.14C).

Sub-volume averaging of the I-band thin filaments

Thin filaments in the I-band were picked automatically as described in the previous sections with crYOLO. 15,153 sub-volumes from 4 tomograms from multiple myofibrils showing I-band in the field of view were aligned with calculated priors (phi and theta angles) and refined in 3D with using RELION. Helical processing was used to minimize missing wedge artefacts using the helical parameters determined in the A-band thin filament structure. This resulted to a final structure of I-band thin filament without troponin with an estimated resolution of 10.6 Å using the 0.143 criterion. The map was sharpened with a B-factor of -600 and filtered to the nominal resolution. Thin filament segments decorated by troponin densities was picked manually in IMOD. In total, 704 sub-volumes were aligned to an initial reference generated by averaging all sub-volumes without alignment in PEET. The averaged structure of the I-band thin filament including troponin has an estimated resolution of 19.8 Å after masking. A homology atomic model of the I-band thin filament was calculated using SWISS-MODEL based on the atomic model of isolated cardiac thin filament (Yamada et al., 2020) and rigid-body fitted into the averaged maps (Fig. 4.16, Fig. 4.17).

To investigate the location where the transition of tropomyosin from the M-state to C-state occurs, three tomograms containing both A-band and I-band were analyzed. Particles around the A/I junction in these tomograms were divided into 37-nm sections. Four sections (one in A-band and three in I-band) were selected using a customized script. Sections 1-4 contains 1206, 1126, 988 and 947 particles, respectively. The particles from the four sections were averaged separately using the same strategy as described above (Fig. 4.17D,F). The averages were aligned to an undecorated actin filament structure for the comparison of tropomyosin positions. The particles colored by their tropomyosin states were visualized in the 3D view in IMOD to depict their distribution (Fig. 4.17E).

Analysis of I-band and Z-disc organization

Different Z-disc thicknesses were observed in different sarcomeres from multiple myofibrils. The thickness was measured between the sites where α-actinins start to bind to the antiparallel

thin filaments using IMOD (Fig. 4.18A, D, Fig. 4.19A). The relative angle between α-actinin and actin was measured as the obtuse angle between the pointed end of actin filament and α-actinin using Fiji (Fig. 4.19A). From our observation, the Z-discs from the same myofibril have a similar thickness.

A tomogram showing both I-band and Z-disc were 4x binned and filtered initially with a SIRT-like filter using IMOD, followed by a low-pass filter at 60 Å. Thin filaments in the tomogram were first picked automatically as described in the previous section. The segments in the Z-disc were further curated manually and merged into the originally picked filaments. The polarities of the filaments were determined based on the location of the ends of the filaments. 3D organization of these filaments was generated in Fiji and shown in Chimera (Fig. 4.16F). To analyze the organization of α-actinin in the thin-form Z-disc, potential positions of α-actinin were sampled between ends of filaments with opposite polarities. The exact location of α-actinin was searched for by aligning sub-volumes extracted at these positions to a cylinder using a limited search range with PEET. The new positions and the corresponding orientation of sub-volumes representing the location of α-actinin were clustered based on the determined new position. Obvious false-positive and false-negative positions were then curated manually. In the thick-form and intermediate Z-discs, 12 α-actinins were picked in each tomogram manually in IMOD. The angles between the pointed end of actin and the long axis α-actinin and the lengths of α-actinins in both types of Z-discs were calculated and plotted as histograms using python scripts. The 3D organization of the thin-form Z-disc was generated in Fiji and shown in Chimera (Fig. 4.18H, I). A local 3D model of one thin filament with its neighboring thin filaments and α-actinins was generated by fitting models of actin filament and plotting back a map from the crystal structure of α-actinin (Ribeiro et al., 2014) (PDB: 4D1E) according to their 3-dimensional positions and orientations using tools developed as part of the TEMPy software package (Farabella et al., 2015) (Fig. 4.18K).

Sub-volumes at the position of α-actinin were extracted from the 4x binned tomogram with a box size of 80 pixels (560 Å). An initial reference was obtained by averaging all 384 sub-volumes without refinement using PEET based on their orientation calculated from the coordinates of the α-actinin and the connected thin filaments. These sub-volumes were aligned to this reference during 3D refinement using RELION to generate a final average. The central rod domain from the crystal structure of α-actinin (PDB: 4D1E) was fitted into the averaged

density manually. The actin binding domain, together with actin filaments was fitted into the density based on the atomic model of actin filament decorated by the first calponin homology (CH1) domain of filamin A (PDB: 6D8C), which shares a similar structure to the CH1 domain of α-actinin (Fig. 4.19H).

Parameter	Actomyosin complex (EMDB-12289)	re-centered myosin double-head (EMDB-12291)	I-band thin filament (without troponin) (EMDB-12292)	I-band thin filament (with troponin) (EMDB-12293)
Data collection and processing				
Magnification	81000	81000	81000	81000
Voltage (kV)	300	300	300	300
Exposure dose ($e^-/Å^2$)	130-155	130-155	130-155	130-155
Defocus range (μm)	2.4-3.4	2.4-3.4	3.3-4	3.3-4
Pixel size (Å)	1.76	1.76	1.76	1.76
No. of tomograms	8	8	4	4
Initial no. of particles	32,421	32,421	15,153	704
Final no. of particles	18,090	4,519	15,153	704
Symmetry imposed	C1	C1	Helical (-166.6° twist, 27.9 Å rise)	C1
FSC threshold	0.143	0.143	0.143	0.143
Map resolution (Å)	10.2	15.1	10.6	19.8

Table 6.2 Cryo-ET data collection and sub-tomogram averaging statistics

Methods specific to section 4.3

Sub-tomogram averaging

Skeletal A-band thin filament: Sub-tomogram averaging of the skeletal A-band thin filaments first followed a previously published approach (Wang et al., 2021). Briefly, the determined positions for filaments within the tomograms were used to extract sub-tomograms in RELION (Bharat and Scheres, 2016) using a box size of 200 voxels (346 Å), which were then projected (central 100 slices) and sorted into good and bad particle classes through 2D classification in ISAC (Yang et al., 2012). Good particles were then subject to three-dimensional refinement using a cylindrical reference in RELION, achieving a global resolution (0.143 criterion) of 8.8 Å.

In order to increase resolution, the particles were then subjected to further refinement in the program M (Tegunov et al., 2021). Tilt movies and image stacks were motion-corrected and CTF-estimated within Warp (Tegunov and Cramer, 2019) and new tomograms were reconstructed. The original particle position information obtained from the final step of refinement in RELION was then transformed to match the output geometry of tomograms from Warp. The new particles were extracted in Warp for subsequent averaging in RELION using a 2x down-sampling. After 3D refinement in RELION, the structure of the thin filament was determined to 7.8 Å (Fig. 6.5). The final half-maps and alignment parameters were subjected to M for refinement. The strategy for refinement in M followed previously published regimens (Tegunov et al., 2021). After this refinement, the structure reached a global resolution of 6.7 Å. The core of the thin filament, including actin and nebulin, was masked and reached a resolution of 4.5 Å (Fig. 6.5, Fig. 4.20), which was used for model building of actin and nebulin.

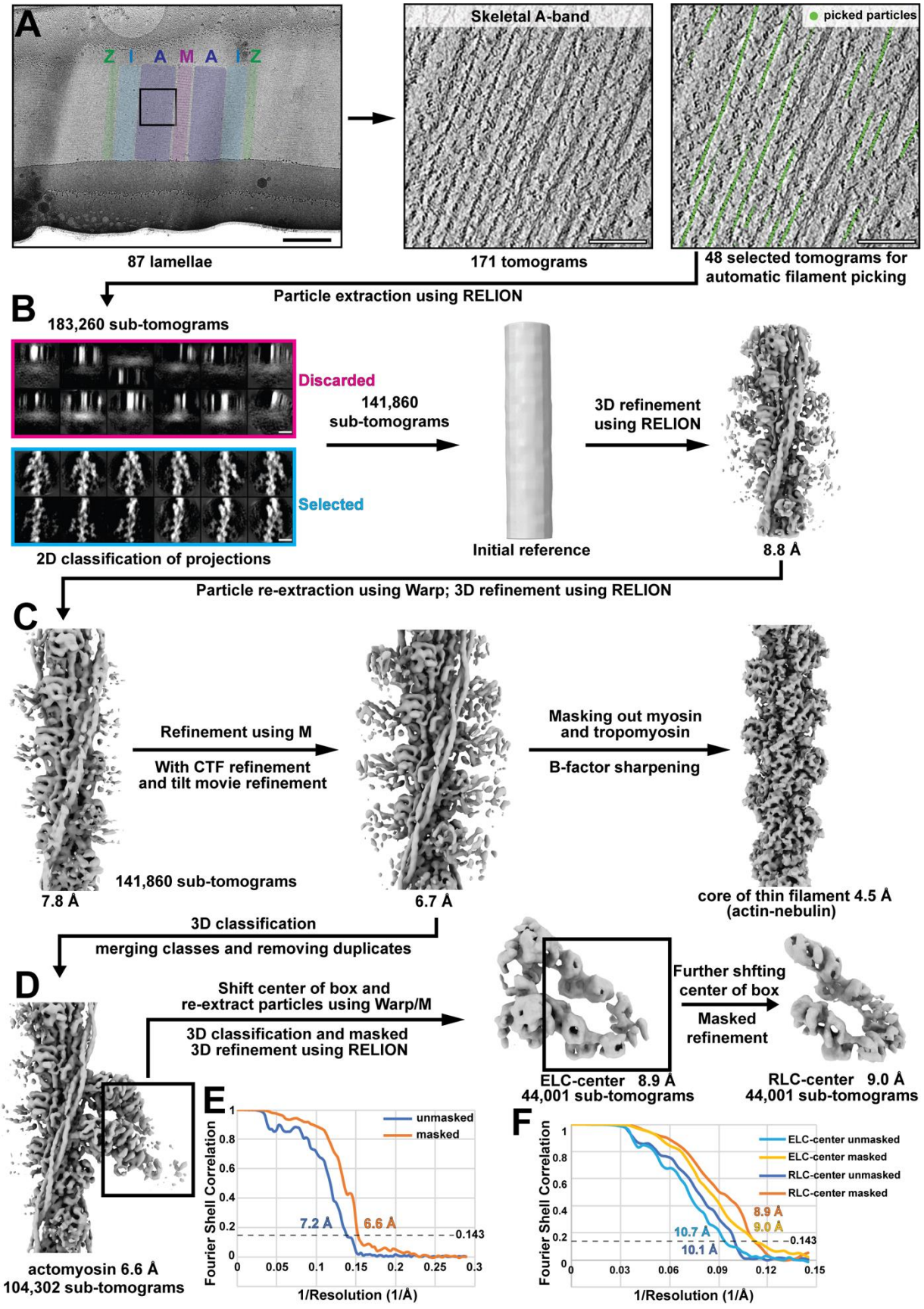

Fig. 6.5 Cryo-FIB-ET and processing workflow of A-band thin filament structures from mouse psoas muscle.

(A) *Examples of a lamella of mouse psoas myofibrils and a slice of tomogram depicting the sarcomeric A-band, where the thin filaments are picked automatically. Different zones (Z-disc, I-band, A-band, M-band) of a sarcomere on the lamella are highlighted in different colours. Scale bars: 1 µm (left), 100 nm (right).* ***(B)*** *Cleaning of particles using 2D classification of projection images and initial refinement using RELION. Scale bar: 10 nm.* ***(C)*** *Improving the resolution of the thin filament structure using the Warp-M packages.* ***(D)*** *Actomyosin structure (including a thin filament and two myosin heads) and structures of the myosin neck domain obtained through further classification and re-centring of particle boxes.* ***(E)*** *Gold-standard FSC curve of the actomyosin complex.* ***(F)*** *Gold-standard FSC curve of the ELC and RLC centred myosin double head structures.*

Skeletal A-band actomyosin and myosin neck domain. In order to resolve the actomyosin structure, including thin filament and a bound myosin double-head, a 3D classification approach similar to the one previously published (Wang et al., 2021) was used. After the refinement in M, sub-tomograms were re-extracted and classified in RELION. Classes were translated and rotated to a common double-head configuration and re-refined in M. The final reconstruction at a resolution of 6.6 Å was used for model building of myosin heavy chain. In order to increase the resolution of the myosin neck domains (predominantly the ELC and RLC), the sub-tomograms were first re-centred towards ELC and re-refined in RELION with a mask containing only myosin. This resulted in an ELC-centred myosin double-head structure with a resolution of 8.9 Å (Fig. 6.5). Afterwards, the sub-tomograms were further re-centred towards RLC and re-refined with a smaller mask containing ELCs and RLCs to reconstruct a structure of RLC-centred myosin double-head with a resolution of 9 Å. The ELC- and RLC-centred myosin double-head maps were used for rigid-body docking of ELC and RLC models, respectively.

Cardiac A-band thin filament, actomyosin and myosin neck domain: Sub-tomogram averaging of the cardiac A-band thin filament followed the same strategy as for the A-band of skeletal muscle and resulted in a structure of thin filament resolved to a global resolution of 8 Å, with the core of thin filament (actin) resolved to 6.3 Å (Fig. 6.6A,B). Structures of cardiac actomyosin and myosin neck domain were determined using the same classification and re-centring approach as for skeletal structures, resulting in resolutions of 7.7 Å and 12 Å, respectively.

Skeletal I-band thin filament: Sub-tomogram averaging of the skeletal I-band thin filament excluding troponin was performed largely as described for the A-band structures, except for using helical symmetry (twist -167.4°, rise 28.8 Å) during the initial refinement in RELION to reduce alignment error due to the missing wedge artefacts. The final structure of the I-band thin filament was determined to a global resolution of 9.4Å, with the core (actin and nebulin) resolved to 7.4 Å (Fig. 6.6C,D). Sub-tomogram averaging of the thin filament including troponin was performed as previously described (Wang et al., 2021). 2,030 manually-picked sub-tomograms were used for averaging using a cylinder-like reference generated from averaging all particles without alignment.

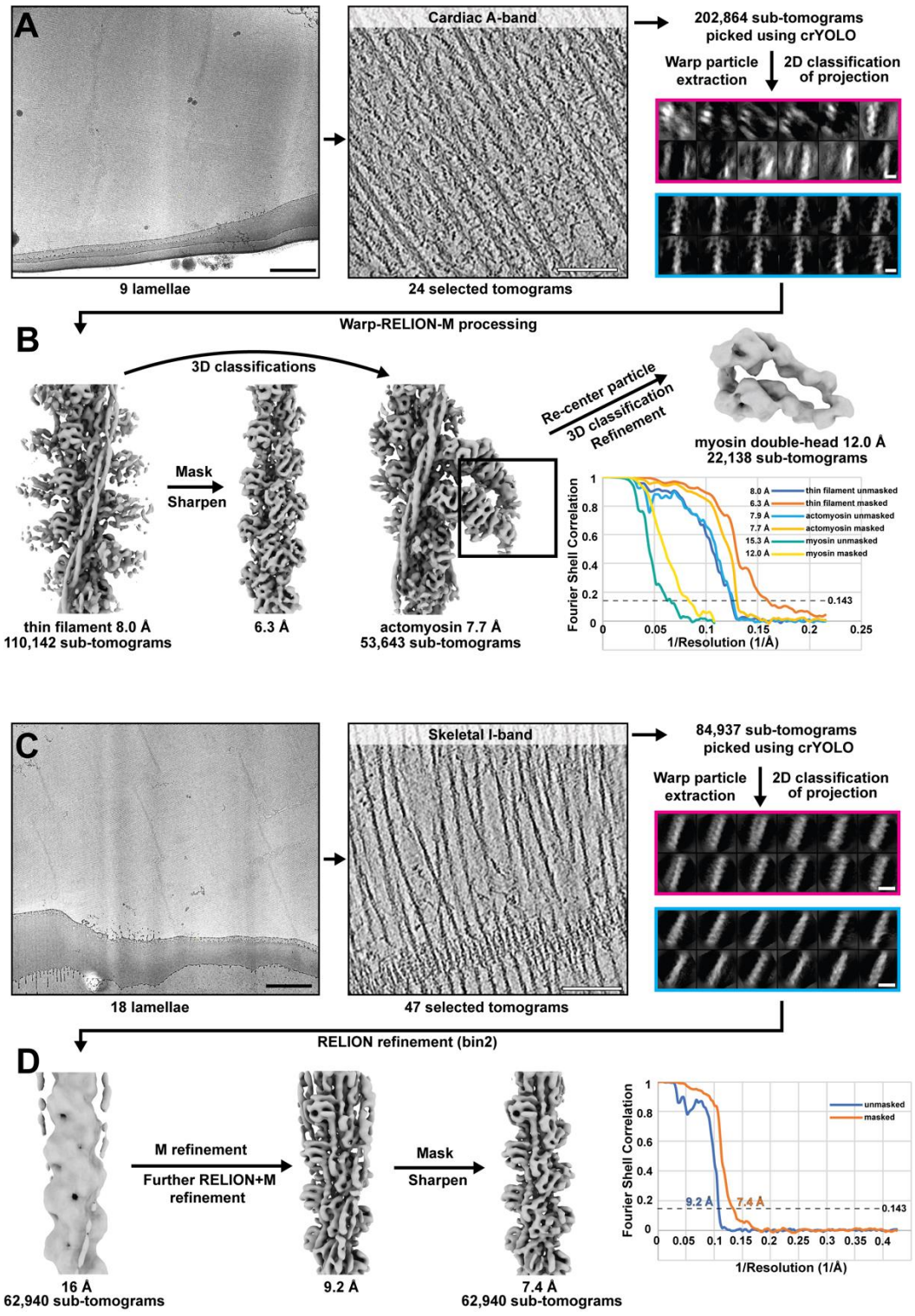

Fig. 6.6 Cryo-FIB-ET and processing workflow of A-band thin filament structures from mouse cardiac muscle and I-band thin filament structures from mouse psoas muscle.

(A) *Examples of a lamellae of mouse cardiac myofibrils, a slice through a tomogram of mouse cardiac sarcomere A-band and particle-cleaning using 2D classification.* ***(B)*** *EM density maps and gold-standard FSC curves of the thin filament, actomyosin and re-centred myosin double-head structures. The processing workflow is similar to the processing of mouse skeletal A-band structures.* ***(C)*** *Examples of a lamellae of mouse psoas myofibrils, a slice through a tomogram of mouse skeletal sarcomere I-*

band (also depicting a Z-disc at the bottom) and particle-cleaning using 2D classification. ***(D)*** *Processing workflow of the I-band thin filament and gold-standard FSC curve of the structure.*
Scale bar: 1 µm (lamella), 100 nm (tomogram), 10 nm (2D classes)

Model building of actin, nebulin and myosin heavy chain

To reduce the risk of over-refinement and account for the heterogenous resolution of our structures, several density maps, which were masked to different areas, filtered to nominal or local resolution as determined by SPHIRE (Moriya et al., 2017) and sharpened using various B-factors, were used for model building. In addition, density modified maps were calculated from half maps providing the reported nominal resolution (Terwilliger et al., 2020).

An initial model for actin was generated by homology modelling using Modeller (Eswar et al., 2008) in Chimera based on a previous atomic model (PDB: 5JLH (von der Ecken et al., 2016), chain A) and a sequence alignment from Clustal Ω. The unresolved N-terminus of actin (aa 1-6) was removed and Mg^{2+}-ADP was added from PDB 5LJH. HIS 73 was replaced by HIC (4-methyl-histidine) and regularized in Coot (Emsley et al., 2010). A pentameric composite model was assembled by rigid-body fitting in Chimera including an initial model of nebulin (see below). Model building was performed in ISOLDE (Croll, 2018) in ChimeraX (Goddard et al., 2018). A total of four density maps were loaded (filtered to nominal resolution and sharpened with B-factors -70 and -150; filtered to local resolution and sharpened to B-factor -100; and the density modified map). Only the central actin chain and residues in close contact were included in the simulation and rebuilt. Unresolved side chains are in the most likely positions. After a first pass through the complete molecule, Ramachandran and rotamer issues were addressed locally. Based on the refined central chain, the composite actin-nebulin pentamer was updated. Hydrogens were removed and the resulting model was real-space refined against the map filtered to nominal resolution in Phenix (Afonine et al., 2018). To avoid large deviations from the input model, the ISOLDE model was used as a reference, while local grid search, rotamer and Ramachandran restraints were deactivated. The actin model was further improved by a second round of model building in ISOLDE.

Modeling of nebulin was performed in analogy. An initial poly-alanine model for nebulin was built manually in Coot based on the density of the central repeat (4.5 Å resolution). In order to cover the connection between two nebulin repeats, a peptide of 56 aa (instead of 35 aa) was initially built. The density corresponding to residue 22 was consistent with a consensus tyrosine residue and thus tyrosine was used instead of alanine. A segmented post-processed map (filtered to nominal resolution and sharpened with B-factor -70) was loaded for further modelling in ISOLDE. Secondary structure and rotamer restraints were applied where appropriate. Based on the resulting model, a continuous model of nebulin was created by first cutting the model to 35 aa and rigid-body fitting into the density. The termini of three consecutive nebulin chains were then manually connected. To address geometry issues due to the connection, the combined nebulin chain was real-space refined in Phenix against the segmented map and subjected to another round of refinement in ISOLDE.

Refined models of actin and nebulin were finally combined into one pentameric model. Minor adjustments to the orientation of side chains were done in Coot where necessary. The composite model was real-space refined against the 4.5 Å-resolution map filtered to local resolution (B-factor -100) in Phenix using the same settings as before.

An initial model of the actin-nebulin-tropomyosin-myosin (actomyosin) complex was assembled from the refined actin-nebulin model, a homology model of myosin (Yang et al., 2007) (PDB: 3I5G, chain A), and a polyalanine model of tropomyosin (von der Ecken et al., 2016) (PDB: 5JLH chains J and K) using rigid-body fitting. Only the heavy chain of myosin (up to residue 788) was modelled. After addition of hydrogens, the central myosin chain was refined in ISOLDE using four segmented density maps of actomyosin, as described for actin. All applicable secondary structure restraints and many rotamer restraints were applied. Manual building was started from the acto-myosin interface, as it is best resolved. Unresolved residues including loop I (aa 207-215), loop 2 (626-643) and the N-terminus (1-11) were removed. After deletion of hydrogens, the resulting atomic model was real-space refined in Phenix and further improved by a second round of refinement in ISOLDE. The refined atomic model of the central myosin chain, was finally used to assemble an updated composite model of the actomyosin complex. This model was addressed to a final round of real-space refinement in Phenix against a 6.6 Å-resolution density map filtered to nominal resolution (B-factor -75) using the same settings as before, but with both Ramachandran and Rotamer restraints applied.

As the resolution was not sufficient to reliably model Mg^{2+} ions, they were replaced with the ones from PDB 5JLH by superposition of actin subunits. The final atomic models of actin-nebulin and actomyosin complexes were assessed by Molprobity (Chen et al., 2010) and EMRinger (Barad et al., 2015) statistics (Appendix).

Rigid-body docking of myosin light chains

As the density for the C-terminus of the myosin heavy chain lever arm as well as the ELC and RLC is of insufficient quality for reliable model building with refinement, rigid-body docking of previously published structural models(Yang et al., 2007) (PDB: 3I5G) was performed. First, the ELC model together with the ELC-binding lever arm helix (aa 785-802 in PDB 3I5G) were docked into both myosin ELC densities in the ELC-centred myosin double-head map (8.9 Å, B-factor -500) in Chimera (Fig. 6.7B). Then, the RLC model together with RLC-binding HC helices (aa 809-839) were docked into the RLC density of the leading myosin head in the RLC-centred myosin double head map (9 Å, B-factor -300) (Fig. 6.7C). For the RLC of the trailing head, the C-lobe of RLC (together with HC helix aa 809-824) and the N-lobe of RLC (together with HC helix aa 826-839) were docked separately into a segmented map of trailing myosin RLC (Fig. 6.7D). The maps of actomyosin, ELC-centred myosin double-head and RLC-centred myosin double-head were aligned in Chimera in order to unify the coordinate system of all models. In the end, a final homology model was calculated based on these initial models and the sequences of mouse myosin heavy chain and light chains from mouse fast muscle using SWISS-MODEL (Waterhouse et al., 2018). In order to compare the difference of RLC-RLC interface between active and inactive myosin, this model was compared to previous structures of myosin IHM (Yang et al., 2020) (PDB: 6XE9) through aligning the leading head RLC from our model to the free head RLC from IHM in Chimera.

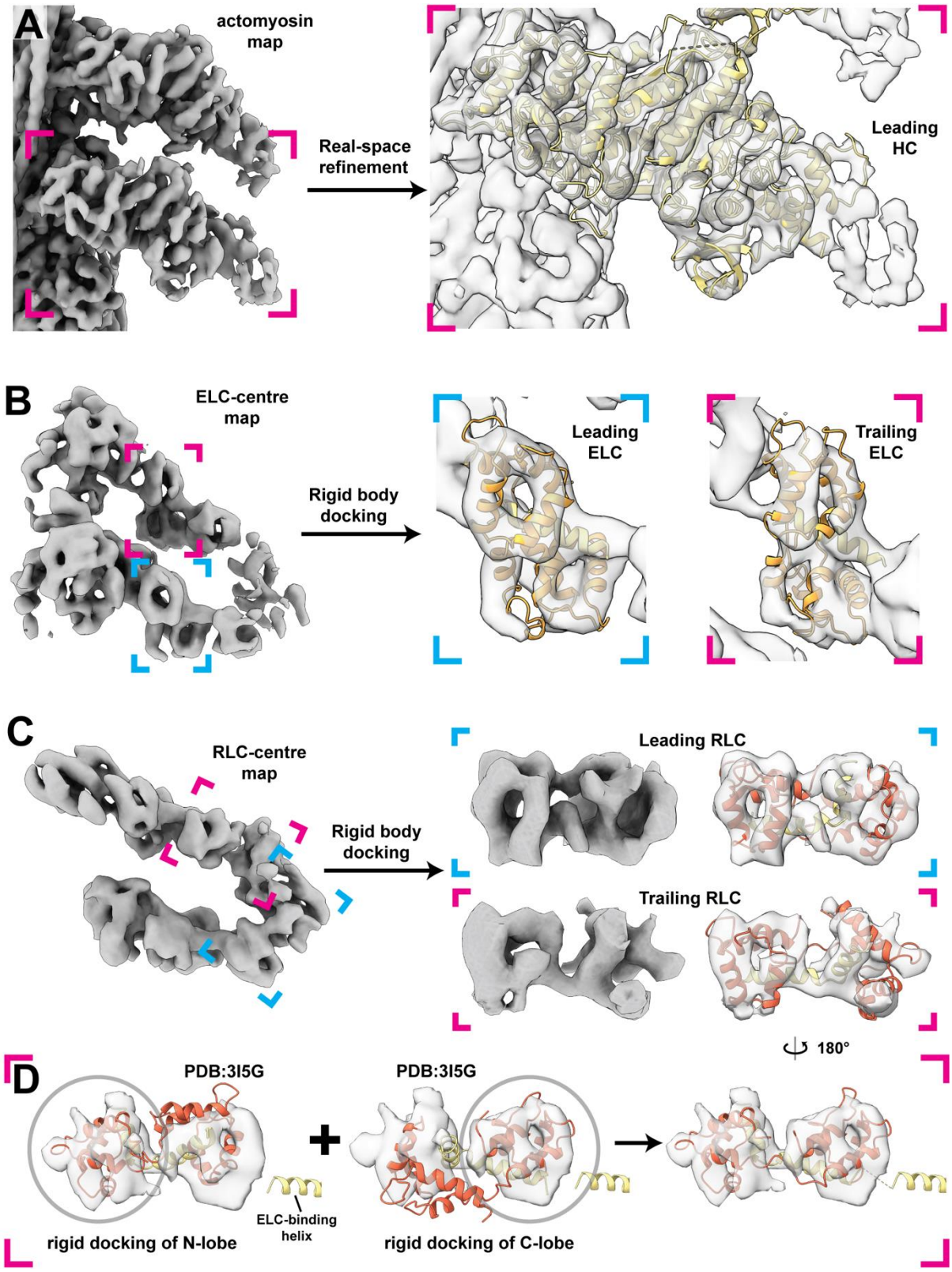

Fig. 6.7 Model building of myosin heads.

(A) *Cryo-EM density map of myosin motor domain with structural models (yellow) refined into the map.* ***(B)*** *Cryo-EM density map of myosin heads with a focus on the ELC. Myosin ELC (orange) and HC LH2 (yellow) from PDB 3I5G were docked into the map as rigid bodies.* ***(C)*** *EM density map of myosin heads*

with a focus on the RLC. The leading RLC density was directly fitted with the myosin RLC model (red; with HC LH3-4, yellow) from PDB 3I5G. The trailing RLC density was fitted with a modified model of RLC and HC LH3-4, as shown in (F). ***(D)*** *Separate rigid body docking of the N-lobe (red; with HC LH4, yellow) and the C-lobe (red; with HC LH3, yellow) of the RLC in the trailing head. The final structural model was obtained combining the two docked models.*

Sequence analysis of nebulin and troponin T

As a defined boundary on nebulin sequence between A-band and I-band is not present, the nebulin sequence of M1-8 and the entire super repeat region (Fig. 4.28B) from mouse (Uniprot: E9Q1W3) was considered as the A-band nebulin sequence and divided into 176 simple repeats (M1-162) through placing the SDxxYK motif at position 18-23. Multiple sequence alignment was performed using ClustalW (Larkin et al., 2007) with gaps disabled (Fig. 6.8A) and visualised in WebLogo (Crooks et al., 2004). Secondary structure of each simple repeat was predicted using RaptorX-Property (Wang et al., 2016). Probability values for being α-helix at each residue position were averaged and used for Fig. 4.28 and Fig. 4.29.

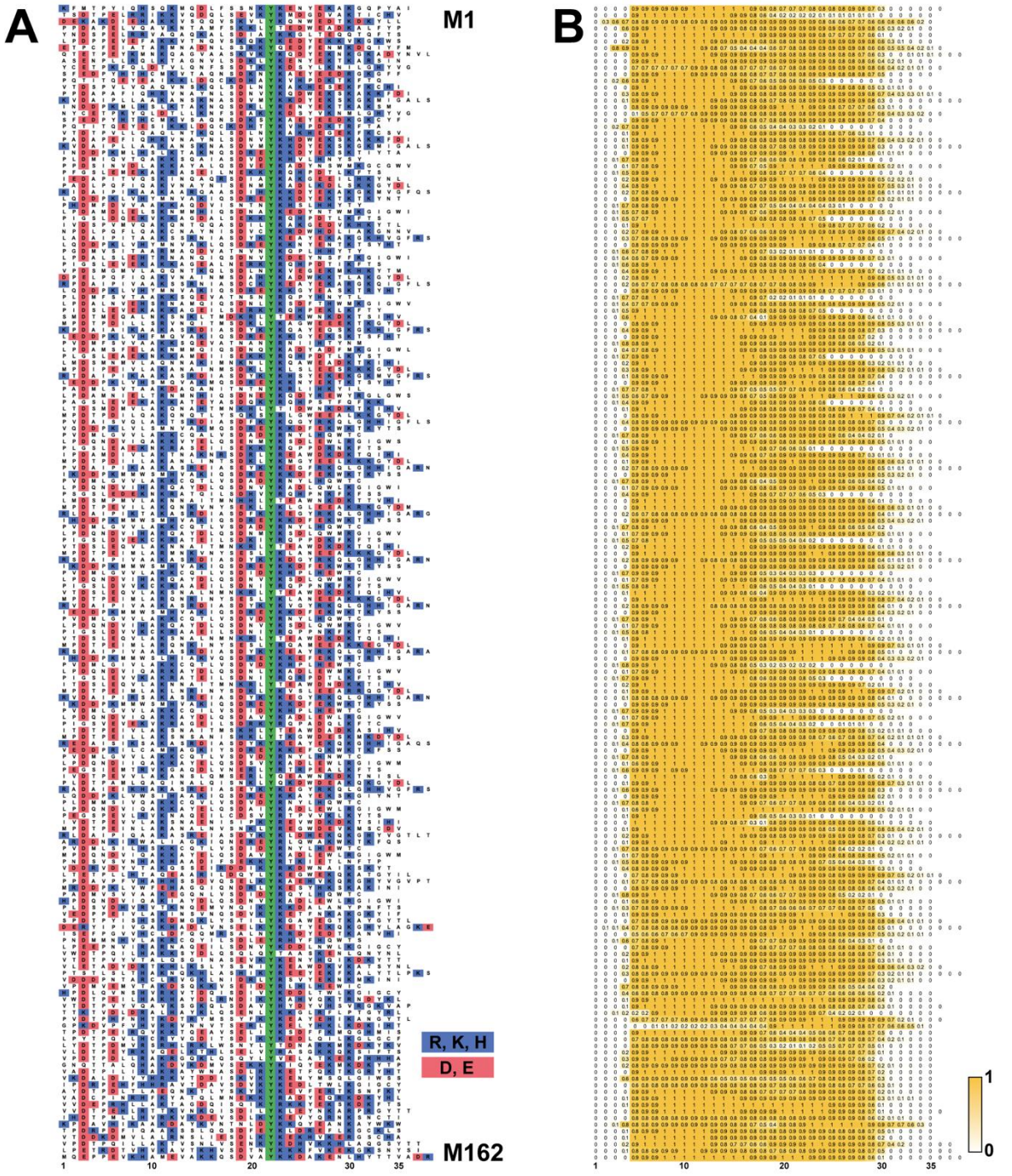

Fig. 6.8 Sequence and secondary structure prediction of individual nebulin simple repeats.
(A) *Sequence alignment of nebulin repeats M1-M162. Positively and negatively charged residues are highlighted in blue and red, respectively. The fully conserved tyrosine at position 22 is highlighted in green.* ***(B)*** *Secondary structure prediction of repeats M1-M162, coloured based on the probability of an α-helix.*

To estimate relationship between the charge of the amino acid at position 15 and 21 a Bayesian multi-nominal regression was performed. For both positions and for each of the 176 sequences, the amino acid type was assigned a number, representing one of four categories which are 1 (Positive), 2 (Negative), 3 (Hydrophobic) and 4 (Other). With this, the categorical variables $y_{i,j}^{15}$ and $y_{i,j}^{21}$ were constructed, representing the category i at position 15 and 21 for sequence j respectively. The hierarchical Bayesian model was then modelled the following way and fitted with Stan (Stan Development Team, 2019):

$$\begin{aligned} a_i &\sim normal(0,1) \\ \beta_i &\sim normal(-0.3,1.5) \\ y_{i,j}^{21} &= softmax\left(a_i + \sum_{k=1}^{4} \beta_k \, x_{i,j}^{15}\right) \\ p_{i,j}^{15} &= cat\left(y_{i,j}^{21}\right) \end{aligned}$$

Where a_i is the intercept, β_i the regression coefficients and $p_{i,j}^{15}$ the probability of seeing category i in sequence j. The variable $x_{i,j}^{15}$ is an indicator variable which is one when sequence j at position 15 is of class i. The priors for a_i and β_i were chosen in a way to that the prior predictive distribution of $p_{i,j}^{15}$ has mean probability for each class of 0.18. After fitting, 1000 samples were drawn from the posterior distribution for each possible state of category of amino acid 21 (Fig. 4.31B).

Troponin T linker sequence was from mouse fast skeletal muscle troponin T (UniProt: Q9QZ47-1) after sequence alignment with the sequence of the missing segment of troponin T (R151-S198) in PDB: 6KN8 (Yamada et al., 2020). Hydrophobicity score (Fig. 4.32D) was calculated through ProtScale (Gasteiger et al., 2005) using the scale from Abraham & Leo (Abraham and Leo, 1987).

	Skeletal A-band				**Cardiac A-band**			**Skeletal I-band**
Microscopy								
Microscope	Titan Krios				Titan Krios			Titan Krios
Voltage (kV)	300				300			300
Camera	Gatan K2 Summit				Gatan K3			Gatan K3
Slit width (eV)	20				20			20
Pixel size (Å)	1.73				2.32			1.18
Defocus range (μm)	2.4-5.0				3.2-5.0			2.5-5.5
Tilt range[a]	-54°/+54° (3°)				-54°/+54° (3°)			-54°/+54° (3°)
Tilt scheme	Dose-symmetric				Dose-symmetric			Dose-symmetric
Total dose (e^-/Å^2)	130-150				130-150			130-150
Number of lamellae	87				9			18
Number of tomograms[b]	48 (171)				24 (24)			47 (115)
3D refinement statistics	**Actin-nebulin**	**Acto-myosin**	**Myosin (ELC-centred)**	**Myosin (RLC-centred)**	**Actin**	**Acto-myosin**	**Myosin (neck-domain)**	**Actin-nebulin**
Number of sub-tomograms	141,860	104,302	44,001	44,001	110,142	53,643	22,138	62,940
Symmetry	C1	C1	C1	C1	C1	C1	C1	C1, Helical[d] (-167.4°, 28.8Å)
Resolution[c] (Å)	4.5 (6.7)	6.6 (7.2)	8.9 (10.7)	9.0 (10.1)	6.3 (8.0)	7.7 (7.9)	12.0 (15.3)	7.4 (9.2)
B-factor	-100	-75	-500	-300	-300	-200	-300	-250
EMDB deposition	EMD-13990	EMD-13991	EMD-13992	EMD-13993	EMD-13995	EMD-13996	EMD-13997	EMD-13994
Atomic model statistics								
Non-hydrogen atoms	15,550	29,589	Homology model					
Cross correlation masked	0.72	0.82						
Molprobity score	1.75	1.97						
Clashscore	17.88	30.61						
EMRinger score	0.86	0.20						
Bond RMSD (Å)	0.010	0.007						
Angle RMSD (°)	1.535	1.415						

Rotamer outliers (%)	0.00	0.00					
Ramachandran favored (%)	100.00	99.69					
Ramachandran outliers (%)	0.00	0.20					
CaBLAM outliers (%)	2.15	2.33					
PDB deposition	PDB: 7QIM	PDB: 7QIN	PDB: 7QIO				

[a]Tilt angle is relative to the pre-tilt of each lamella. In parenthesis is the tilt angle increment.

[b]In parenthesis is the initial number of tomograms

[c]Resolution is based on 0.143 FSC threshold. In parenthesis is the global resolution without mask applied.

[d]Helical refinement was used for initial refinement in RELION. No helical symmetry was applied during local refinement in RELION and M.

Table 6.3 Data collection, refinement and model building statistics

Scripts developed and used in this thesis

The scripts developed and used in this thesis have been deposited on Zenodo (https://zenodo.org/) with DOI: 10.5281/zenodo.7084180.

Including:

DS_ultimate.tcl	SerialEM script for batch tomography (section 3.4)
serialEM2etomo.py	Script for pre-processing (section 3.5.1)
setpriors.py	Script for obtaining the prior ψ and θ for filaments (section 3.5.4.2)
subtomo22d.py	Script for rotating and projecting sub-tomograms (section 3.5.4.3)

CHAPTER 7 PUBLICATIONS AND CONFERENCE CONTRIBUTIONS

Publications

[1] **Wang, Z.** and Raunser, S. (in press). Structural biochemstry of muscle contraction. Annual Review Biochemistry *92*.

[2] **Wang, Z.***, Grange, M.*, Pospich, S., Wagner, T., Kho, A.L., Gautel, M., and Raunser, S. (2022). Structures from intact myofibrils reveal mechanism of thin filament regulation through nebulin. Science *375*, eabn1934.

[3] **Wang, Z.***, Grange, M.*, Wagner, T., Kho, A.L., Gautel, M., and Raunser, S. (2021). The molecular basis for sarcomere organization in vertebrate skeletal muscle. Cell *184*, 2135-2150.e13.

[4] Tacke, S.*, Erdmann, P.*, **Wang, Z.**, Klumpe, S., Grange, M., Plitzko, J., and Raunser, S. (2021). A streamlined workflow for automated cryo focused ion beam milling. Journal of Structural Biology *213*, 107743.

[5] Káčeriková, R., Godočíková, J., **Wang, Z.**, Kutejová, E., Raunser, S., and Farkašovský, M. (2018). Modulation of septin higher-order structure by the Cdc28 protein kinase. Biologia (Bratisl). *73*, 1025–1033.

*Co-first author

Conference contributions

09.2022 Gesellschaft für Biochemie und Molekularbiologie Fall Meeting 2022, Düsseldorf, Germany
Biomol PhD Award – Award talk
Structural insights into muscle organisation by cryo-electron tomography

09.2022 9th Electron Tomography Congress, Egmond aan Zee, The Netherlands
Poster presentation
In situ structures of muscle sarcomere and sarcomeric proteins

06.2022 Gordon Research Conference – Three-Dimensional Electron Microscopy, Barcelona, Spain
Poster presentation
In situ structures of muscle sarcomere and sarcomeric proteins

09.2021 European Muscle Conference 2021, Online
Oral and poster presentation – Marcus C. Schaub Award
The molecular basis for sarcomere organisation in vertebrate skeletal muscle

08.2021 Microscopy and Microanalysis (M&M) Meeting, Online
Oral presentation
The molecular basis for sarcomere organisation in vertebrate skeletal muscle

04.2021 8th International Max Planck Research School (IMPRS) of Living Matter PhD Symposium, Online
Poster presentation – Best Poster Award
The molecular basis for sarcomere organisation in vertebrate skeletal muscle

12.2020 EMBO Workshop: In situ Structural Biology: From Cryo-EM to Integrative Modelling, Online
Poster presentation
The molecular basis for sarcomere organisation in vertebrate skeletal muscle

11.2018 7th IMPRS for Chemical Molecular Biology PhD Symposium, Dortmund, Germany
Poster presentation
Complete molecular architecture of in situ mammalian sarcomeres by cryo-electron tomography

09.2018 8th International Conference on Electron Tomography, Les Diablerets, Switzerland
Active participation

10.2017 EMBO Workshop: Molecular and Cellular Biology of Septins, Berlin, Germany
Active participation

CHAPTER 8 ACKNOWLEDGEMENTS

First, I would like to express my deepest gratitude to my supervisor Prof. Dr. Stefan Raunser for initially providing me the opportunity to work on this exciting thesis research. Throughout the journey of my PhD, he guided my research in the right direction while giving me enough freedom to explore in the world of cryo-ET. He has shaped my understanding of good research and helped me grow as a scientist.

I would like to also thank Prof. Dr. Roland Winter for being the second referee of this thesis.

Many thanks to my colleagues at MPI Dortmund. Particularly, I would like to first thank Markus Stabrin not only for his help with data processing, but also for brighten my life outside the institute. Secondly, I would like to thank the "Tomo buddies", Dr. Michael Grange, Dr. Sebastian Tacke, and Dr. Oleg Sitsel, for the fun cooperation in establishing the entire tomography workflow from scratch. Additionally, I would like to thank the officemates in the "successful office": Dr. Sabrina Pospich, Dr. Julian von der Ecken, Dr. Daniel Roderer, Dr. Felipe Merino, and Dr. Toshio Moriya. Being around these excellent scientists truly motivated me as a first-year PhD student. I am also grateful to Dr. Tobias Raisch for the help with Zusammenfassung in this thesis. Special thanks to Dr. Thorsten Wagner for the brainstorm in developing tools for data processing and to Dr. Oliver Hofnagel and Dr. Daniel Prumbaum for the EM support. Last but not least, I would like to thank all current and previous members in Department III for creating such a friendly and inspiring environment.

I would like to thank my collaborators Dr. Ay Lin Kho and Prof. Dr. Mathias Gautel for the fruitful collaboration. I would like to also acknowledge our IMPRS coordinators, Christa Hornemann and Dr. Lucia Sironi, for their effort in organising wonderful events and training courses.

I am extremely grateful to my parents, Hui Wang and Dr. Xia Li, for years of emotional support and their early education to make me a person that I am proud of. Special thanks also to my friend and brother, Dr. Boning Ding, for the joyful experience outside of work and the mutual encouragement in the early stage of my PhD.

ACKNOWLEDGEMENTS

In the end, I would like to especially thank my girlfriend, Dr. Liyang Wang, who added sweetness to my life and supported me through the most stressful moments. This journey could not be finished without you by my side. I love you.